DECLARATION

This work has not previously been accepted in substance for any degree and is not being concurrently submitted in candidature for any degree.

Signed ..... (candidate)

Date 04/12/2019

STATEMENT 1

This thesis is the result of my own investigations, except where otherwise stated. Where correction services have been used the extent and nature of the correction is clearly marked in a footnote(s). Other sources are acknowledged by footnotes giving explicit references. A bibliography is appended.

Signed ..... (candidate)

Date 04/12/2019

STATEMENT 2

I hereby give consent for my thesis, if accepted, to be available for photocopying and for inter-library loan, and for the title and summary to be made available to outside organisations.

Signed ..... (candidate)

Date 04/12/2019

STATEMENT 3

I hereby give consent for my thesis, if accepted, to be available for deposit in the University's digital repository.

Signed ..... (candidate)

Date 04/12/2019

Virtual Source Aperture Ultrasonic Imaging for Non Destructive Testing

Ewan Hoyle

Supervised by: Profesor Peter Charlton, Professor John Rees and Dr Mark Sutcliffe

Submitted in partial fulfilment for the award of Doctor of Philosophy

University of Wales Trinity Saint David

2019

Acknowledgements

This work is a result of a partnership between TWI ltd and the University of Wales Trinity Saint David, thanks to sponsorship from the Knowledge Economy Skills Scholarships (KESS 2) scheme. I'd also like to thank TWI Wales for providing much of the equipment and software packages used in this work. I'd like to thank Professor Peter Charlton and Professor John Rees of the University of Wales Trinity Saint David and Dr Mark Sutcliffe of TWI ltd for their support and guidance throughout this project.

Abstract

Ultrasonic testing is of huge importance when it comes to assessing the integrity of a huge variety of structures and components. Virtual Source Aperture (VSA) is an new advanced method of testing and is considered to be a hybrid between traditional phased array (PA) techniques and full matrix capture (FMC). VSA overcomes the shortcoming of PA by using the Total Focussing Method (TFM) to synthesise a PA focussing point at every single point in the image. This allows for easier data interpretation than PA and also allows for several extra views, not applicable to PA such as the self tandem and multimode views. VSA overcomes the slow imaging rate of FMC-TFM imaging by using phased array like delay laws on transmission are used to generate a divergent wavefront that behaves as if it had originated from a singular point behind the aperture. Each element recieves individually as with FMC. However the higher signal to noise ratios at the Ascan level obtained by the virtual source allows a comparable image to FMC to be generated in fewer firings. Therefore an increased acquisition speed can be achieved. Therefore

Therefore, VSA is of significant interest in non destructive testing (NDT). This work takes forward four main areas of investigation in ultrasound NDT:

- Evaluation of the strengths and shortcomings of FMC, PWI and VSA in a comparative study.
- Investigate of the VSA frequency domain algorithm and establish whether it is a viable alternative solution.
- Development of VSA ‘multi-mode‘ and self-tandem algorithms to improve the probability of defect detection by use of the different propagation modes.

- Creation of a surface mapping algorithm for VSA inspections of components with nonplanar surfaces (complex geometry).

The FMC algorithm provides the highest quality images overall. However, for a relatively small loss (a few dB) in image quality, much higher frame rates can be achieved using either VSA or PWI. VSA offered slightly higher SNR than PWI. For a typical setup, FMC achieved 18fps while VSA and PWI could deliver up to 250fps.

The PWI performed better than VSA for the Array Performance Indicator Measurements (API), indicating that in general the PWI transmissions were more tightly focussed. However the measured values for SNR and API varied massively across the imaging region for PWI, correlating to how many transmissions had covered each particular point in space. Where wave fronts overlapped, the images were higher intensity and more tightly focussed. To avoid this problem the number of transmissions must be higher to offer a more uniform distribution of energy. The energy values for VSA were overall more uniform, and resembled those of FMC. Therefore, for high speed inspections, VSA is likely to be the preferred option if a wider angle range must be covered.

The VSA frequency domain algorithm gave a narrower range of angular coverage compared to the time domain equivalent. Time domain was easier to implement through a refractive boundary, a common issue in NDT. Accordingly, the time domain VSA algorithm was used in the main testing.

The VSA self tandem and multimode algorithms benefit from the ability to reprocess the data acquired to exploit a wider range of sound paths, including mode conversions, for imaging. The probability of detection and classification for certain defect categories can be improved, including vertically aligned flaws. Examples were developed illustrating

ability of the self-tandem and multimode algorithms to image vertically aligned flaws using high amplitude specular responses rather than the low amplitude tip diffracted signals used by the half skip and full-skip algorithms.

A VSA surface mapping method was created, the method being compared to the dipping reflector and plane wave surface mapping algorithms. For less complex surface geometry the algorithm was very comparable to the established algorithms. The VSA data can be used to extract surface information such that the surface mapping and imaging algorithm can be performed with a single transmission sequence.

Contents

1 Introduction **16**

1.1 Motivation for Research 16

1.2 Ultrasonic Testing 17

1.3 Aims and Objectives 18

1.4 Research Methodology 19

1.5 Summary of the Contribution to Knowledge 20

1.6 Organisation of Thesis 22

1.6.1 Critical Evaluation of Current State of the Art Ultrasonic Imaging Techniques 22

1.6.2 Evaluation of the Frequency Domain VSA Algorithm . 23

1.6.3 VSA Multi-Mode and Self Tandem 23

1.6.4 VSA Surface Mapping Algorithm 24

2 Ultrasonic Non-Destructive Testing and Imaging **25**

2.1 Introduction 25

2.2 Basic Wave Theory 26

2.2.1 Phase and Interference 27

2.2.2 The Wave Equation 29

2.2.3 Propagation Modes 30

2.3 Generating Ultrasound - Piezo Electric Effect 31

2.4 Huygens Principle 33

2.4.1 Near and Far Field Zones 33

2.4.2 Grating Lobes . . . 34
2.4.3 Reflection and Transmission . . . 36
2.5 Ultrasonic Testing . . . 38
2.5.1 Conventional UT, A-scans, B-scans and C-scans . . . 38
2.5.2 Phased Array Ultrasonic Testing . . . 39
2.6 Fully Focussed Imaging . . . 42
2.6.1 Data Acquisition Methods . . . 42
2.6.2 Total Focussing Method . . . 45
2.6.3 Hilbert Transform . . . 47
2.6.4 Adaptions of the TFM, other Imaging Methods and Coherence Weighting . . . 47
2.7 Refractive Boundary . . . 49
2.7.1 Imaging Approaches to Consider . . . 52
2.7.2 Unknown Geometry . . . 53
2.8 Acceleration of Post Processing Methods . . . 55
2.8.1 Frequency Domain Imaging . . . 55
2.9 Conclusions . . . 57

3 A Comparative Study Between VSA, PWI and FMC 58
3.1 Introduction . . . 58
3.2 Experimental Setup and Configuration . . . 60
3.2.1 FMC Setup . . . 60
3.2.2 VSA Setup . . . 61
3.2.3 PWI Setup . . . 69
3.3 Results . . . 70
3.3.1 Signal to Noise Ratio . . . 70
3.3.2 Indication Intensity Map . . . 72
3.3.3 Array Performance Indicator (API) . . . 74
3.3.4 Inspection Rate . . . 76

3.4 Conclusion 78
3.5 Further Work 80

4 Virtual Source Aperture Algorithms - Time and Frequency Domain 87
4.1 Introduction 87
4.2 Virtual Source Aperture 89
4.2.1 Time Domain VSA 90
4.2.2 Frequency Domain VSA 91
4.3 Results and Discussion 98
4.3.1 Array Performance Indicator (API) 99
4.4 Implementation Complexity of the Time and Frequency Domain Algorithms 101
4.5 Conclusion 103

5 Self Tandem and Multi-Mode Imaging 105
5.1 Introduction 105
5.2 Imaging Algorithm 108
5.2.1 Multi-Mode Time of Flight Calculation 109
5.3 Experimental Setup 112
5.4 Conclusion 120

6 VSA Surface Mapping for Components with Complex Geometry 122
6.1 Introduction 123
6.2 Virtual Source Surface Mapping Method 125
6.2.1 First Responses 127
6.2.2 Constructing the Ellipses 128
6.2.3 Estimating the Surface 130
6.2.4 Least Means Squared Interpolation 132
6.2.5 Outlying Points + Other Errors 134
6.3 TFM Imaging Algorithm through Dual Layered Media 135

6.3.1 Time of Flight Calculation - Gradient Method 136
6.4 Other Surface mapping methods 138
6.4.1 Dipping Reflector Algorithm 138
6.4.2 Plane Wave Surface Mapping Algorithm 139
6.5 Testing the VSA Surface Mapping Technique 140
6.5.1 Setup 141
6.5.2 Testing Components 142
6.5.3 Accurately Determining the Surface Relative to the Transducer 143
6.6 Results 144
6.7 Conclusions 147

7 Thesis Conclusion **160**
7.1 Review of Thesis 160
7.2 Main Conclusions 161
7.3 Further Work 163

List of Figures

2.1 Depicting the interference as two waves overlap. 28

2.2 Mass On Springs 29

2.3 Example of Different wave modes: Top - Compressional/Longitudinal. Middle - Shear/Transverse. Bottom - Surface/Rayleigh. 31

2.4 Image depicting the wavelet sources predicted by Huygens principle. 33

2.5 Depiction of how side lobes are generated. 35

2.6 Intensity with angle for a $8mm$ wide probe generating a $2mm$ sound beam. 36

2.7 Image depicting sound originating from a point source through refractive boundary. 37

2.8 Depiction of a single element 0^o scan. 39

2.9 Depiction of how a linear array is used to generate a Planar Wavefront (left) and Phased Array Focussing Point (right). . . 40

2.10 Top - unfocussed phased array inspection: left - linear scan and right - sector scan. Bottom - focussed phased array inspection: left - linear scan and right - sector scan. 41

2.11 Left: Beam Profile for a Virtual Source. Right: Beam Profile from an Angled Plane Wave 44

2.12 Paths for the TFM algorithm. Left: direct contact inspection, Right: refractive boundary inspection. 46

2.13 Image depicting inspection circumstances where imaging through a refractive boundary is required. Left - wedge inspection, Right - immersion inspection. 50
2.14 Imaging modes: Left - Half Skip, Middle - Full Skip, Right - Self Tandem. 52

3.1 Figures Showing the Different Virtual Source Distances Behind the Aperture 64
3.2 Amplitude of a Virtual Source Wavefront for Different Distances of the Source Behind the Aperture 65
3.3 Virtual Source Wavefronts from Sub Apertured Containing Different Number of Elements 67
3.4 Depicting the wavefront generated by a virtual source at half aperture using 16 elements. 68
3.5 Full Matrix Capture Intensity Maps 79
3.6 Intensity Maps for the PWI Techniques. 80
3.7 Intensity Maps for the VSA Techniques. 81
3.8 FMC API images. 82
3.9 PWI API images. 82
3.10 VSA API Images. 83
3.11 API for PWI at a Depth of 20mm 84
3.12 API for VSA at a Depth of 20mm 84
3.13 API for PWI at a Depth of 40mm 85
3.14 API for VSA at a Depth of 40mm 85
3.15 API for PWI at a Depth of 60mm 86
3.16 API for VSA at a depth of 60mm 86

4.1 Generating a Virtual Source Using an Ultrasonic Array 89
4.2 Depiction of the transmitting virtual source and receiving element. 91

4.3 Depiction of the wavelength of a planar wave in the direction of propagation and the vertical and horizontal direction. . . . 93
4.4 Left - Depiction of the time domain reconstruction. Right - Depiction of the frequency domain reconstruction. 97
4.5 Image of the SDHs using the time domain TFM algorithm. . . 100
4.6 Image of the SDHs using the frequency domain TFM algorithm.101
4.7 API map of the time domain TFM algorithm. 102
4.8 API map of the frequency domain algorithm. 103

5.1 Depicting different inspection paths that can be considered using the TFM. 106
5.2 Depicting some of the resultant wave modes generated by an incident longitudinal wave crossing a refractive boundary. . . 108
5.3 Depiction of the coordinates. 110
5.4 Image Depicting the Experimental Setup and the Fatigue Crack.112
5.5 Figure Depicting the Potential Use of a Multimode Algorithm in Detecting a Vertically Aligned Flaw 114
5.6 Half Skip Algorithm on the Vertical Fatigue Crack Originating from the Bottom of the Part. 115
5.7 Full Skip Algorithm on the Vertical Fatigue Crack Originating from the Bottom of the Part. 115
5.8 Self Tandem Algorithm on the Vertical Fatigue Crack Originating from the Bottom of the Part. 116
5.9 Multi-Mode Algorithm on the Vertical Fatigue Crack Originating from the Bottom of the Part. 116
5.10 Half Skip Algorithm on the Vertical Fatigue Crack Originating from the Top of the Part. 117
5.11 Full Skip Algorithm on the Vertical Fatigue Crack Originating from the Top of the Part. 118

5.12 Self Tandem Algorithm on the Vertical Fatigue Crack Originating from the Top of the Part. 118
5.13 Multi-Mode Algorithm on the Vertical Fatigue Crack Originating from the Top of the Part. 119

6.1 Depiction of how ellipses can be used to map the surface. . . . 126
6.2 Figure Depicting the Intercept Error. 131
6.3 Depiction of the Fast Fermat method on an arbitrary surface. . 137
6.4 Depiction of how the Dipping Reflector Algorithm can be used to map the surface of an inspected component. 139
6.5 Depiction of how a planar wave may be used to map the surface of an inspected component. 140
6.6 Depicting the component with the sinusoidal surface. 143
6.7 Depicting the component with the quadratic surface. 143
6.8 Showing the errors in the DR, VSSM and PWSM techniques using adjacent receivers (6.8a) and non-adjacent receivers (6.8b). 148
6.9 Figure showing the surface point fluctuation in the DR, VSSM and PWSM techniques using adjacent receivers (6.9a) and non-adjacent receivers (6.9b). 149
6.10 Surface mapping of $\pm 1mm$ Sinusoidal Peak 150
6.11 Surface mapping of $\pm 1mm$ Sinusoidal Middle 151
6.12 Surface mapping of $\pm 1mm$ Sinusoidal Trough 152
6.13 Surface mapping of $\pm 2mm$ Sinusoidal Peak 153
6.14 Surface mapping of $\pm 2mm$ Sinusoidal Middle 154
6.15 Surface mapping of $\pm 2mm$ Sinusoidal Trough 155
6.16 Surface mapping of $\pm 4mm$ Sinusoidal Peak 156
6.17 Surface mapping of $\pm 4mm$ Sinusoidal Middle 157
6.18 Surface mapping of $\pm 4mm$ Sinusoidal Trough 158

6.19 Surface mapping of $\pm 4mm$ Sinusoidal Trough 159

List of Tables

3.1 Showing the VSA parameters used for the study. 69
3.2 Showing the PWI parameters used for the study. 70
3.3 Table Showing the FMC, VSA, and PWI set up for the comparison, and displaying the SNR of a SDH using this technique. 71
3.4 Showing the inspections speeds of the different modes considered. 77

5.1 Modes Considered for different inspection views. T-Transverse, L-Longitudinal. 113
5.2 Table showing the Intensity (dB) of different Indications Relative to a Side Drilled Hole. 120

List of Acronyms Commonly Used in this Thesis

A-scan - Amplitude Scan

API - Array performance Indicator

DR - Dipping Reflector

FMC - FullMatrix Capture

NDT - Non Destructive Testing

PA - Phased Array

PAUT - Phased Array Ultrasonic Testing

PWI - Plane Wave Imaging

PWSM - Plane Wave Surface Mapping

SDH - Side Drilled Hole

SAFT - Synthetic Aperture Focussing Technique

SNR - Signal to Noise

TFM - Total Focussing Method

UT - Ultrasonic Testing

VSA - Virtual Source Aperture

VSSM - Virtual Source Surface Mapping

Chapter 1

Introduction

1.1 Motivation for Research

On a daily basis society relies on engineering components to be functioning reliably safely. Many components need to be regularly tested for faults that could be cause the component to fail, risking safety and economic loss. Non Destructive Testing (NDT) is a term referring to a collection of methods used to test components for faults such as these. The methods for testing include radiography, ultrasonic, magnetic particle, eddy current and visual inspection, along with others. These techniques are applicable to a range of applications including: mechanical, civil, aeronautical, forensic, systems and petroleum engineering.

Virtual Source Aperture (VSA) is an advanced method of ultrasonic testing. VSA allows for ultra-fast, high quality inspections however, the technique has been overshadowed by Plane Wave Imaging (PWI), a similar fast method of inspection. Consequently VSA has not been subject to much research. The aim of this thesis is to asses VSA as a viable inspection technique by developing the capability of the technique for the use in various inspection scenarios.

1.2 Ultrasonic Testing

Ultrasonic Testing (UT) is particularly useful in NDT as it is a versatile technique, that can performed easily with relatively portable equipment. It is also completely safe, which gives it an edge over methods such as radiography, where high energy radiation can potentially cause harm to the user. The basic concept is that sound is generated in the testing component. The wave propagates through the material via mechanical oscillations in the particles. If the wave encounters a boundary in the material where the impedance is different, then a certain part of the wave energy is reflected. The ultrasonic transducer may record these echos if the sound returns to the probe. Using the time of flight and the known velocity of sound in the material, the distance of the reflector from the transducer can be measured. All ultrasonic testing stems from this basic concept.

Conventional single crystal ultrasonic inspection involves single crystal transducers that produce a non divergent narrow beam of sound into the material. The angle of the beam can be changed using an angled wedge. Using trigonometry, the known beam angle and the travel distance of the sound, the indications can be located. Conventional UT can be difficult and required a skilled user with suitable knowledge in order to correctly detect, identify and size defects.

Phased Array (PA) was designed to make this process easier. PA uses multiple ultrasonic elements, and by delaying the transmission time of each element, it is possible or focus the beam at a certain place, or steer the beam at a particular angle. By using multiple transmissions it is possible focus in multiple different places, and to manipulate this data to generate an image. Images are generally easier for the user to interpret, making the inspection process easier and reduces user error. Unfortunately, the images are only

focussed at the designated focussing positions, and poor focussing in other areas reduce the reliability of the technique.

Full Matrix Capture (FMC) was developed in order to generate fully focussed images that are easier for the user to interpret. To acquire the full matrix of data, each element is fired individually, while all elements simultaneously receive. The resulting data is then delayed and summed using an algorithm named the Total Focussing Method (TFM) in order to synthetically focus at every point in the image. This is known as the 'gold standard' in ultrasonic imaging. Unfortunately, the scale of the data required to be collected and the vast amount of processing required to form an image limits the FMC-TFM and even when the algorithm in parallelised using graphics hardware, it still is a relatively slow method of inspection compared to PA.

VSA and PWI have been developed in order to try to retain the focussed images allowed by the TFM algorithm, but to improve imaging rate and reduce data sizes. Both techniques use delay laws similar to phased array in order to increase the energy of sound used to insonify the inspected region. Each element receives individually in the same manner as FMC. The TFM is then used to image. Because more energy is used to insonify the region, the signal to noise ratios of the returned scans are higher, meaning that a similar image to FMC can be achieved in fewer transmissions, allowing for faster data acquisition and image generation.

1.3 Aims and Objectives

The aim of this thesis is to investigate the ultrasonic imaging technique VSA. VSA has the potential to exceed inspection speeds currently achieved by FMC, and offers an alternative to PWI. The has been significant interest in the two latter techniques, with significantly less research being conducted

on using virtual sources as a method of transmission, rather than a single element or a plane wave. This thesis aims to develop that understanding of the VSA technique, to better characterise our understanding of the benefits and drawbacks of the technique and to develop VSA to the level of other TFM based imaging techniques. In order to address the aims, a literature review was conducted and four main areas of investigation were identified to form the basis of this thesis:

- To perform a comparative study of FMC, PWI and VSA to evaluate the strengths and shortcomings of each technique.
- To investigate the VSA frequency domain algorithm to evaluate the strengths and shortcomings of the techniques and establish whether it is a viable option to pursue.
- To develop a VSA 'multi-mode' and self tandem algorithms to improve the probability of defect detection by making full use of the different propagation modes of the data acquired.
- To conceive a surface mapping algorithm for VSA inspections of components with non planar surfaces (complex geometry).

1.4 Research Methodology

The purpose of this was to investigate new methods to perform non-destructive testing on sample components by manipulating ultrasound. The literature was studied and experimental tests were performed in order to understand the physical behaviour of the propagation ultrasound, and the techniques designed to manipulate sound for the benefit of the user. These are documented in the introduction chapter. This led to the development of a library of MATLAB scripts used

for controlling the instruments used to produce sound, to perform known imaging techniques such as FMC, VSA and PWI and to implement several simulation methods such as basic finite element and Rayleigh-Sommerfield models to perform simulations.

Data was collected through a collection of experimental and simulated methods. The experimental data was generally collected using a 64 channel LT-PA unit manufactured by Peak NDT in Derby and a collection of transducers manufactured by Olympus NDT. The simulated data was generated by the ultrasound simulation software CIVA 2015. CIVA was chosen as it is a reliable and accepted method of generating data in the field of NDT.

The data was captured using FMC, PWI or VSA acquisition techniques and reconstructed using the TFM imaging algorithm. The indication was evaluated primarily based on its Signal to Noise Ratio (SNR) and other known analysis methods. The inspection speed was judged by the number of frames that could be generated in a second. These methods were used as they are widely known and accepted in the industry.

1.5 Summary of the Contribution to Knowledge

- It was found that FMC overall provides the highest quality images. However for a small compromise in image quality (a few dB) it is possible to achieve much higher frame rates using either VSA or PWI. For a typical setup, FMC achieved 18fps while VSA and PWI could achieve up to 250fps. The frame rate depended on the amount of data that needed to be processed as the bottleneck in the algorithm occurred during the data processing stage.

- The PWI and VSA techniques gave comparable signal to noise values for the images, with VSA slightly higher. However both of these were

a few dB less than FMC. The PWI performed better than VSA for the array Performance Indicator Measurements (API), meaning that in general the PWI transmissions were more tightly focussed. However the measured values for SNR and API varied massively across the imaging region for PWI, correlating to how many transmissions had covered each particular point in space. Where wavefronts overlapped, the images were higher intensity and more tightly focussed. To avoid this problem the number of transmissions must be higher such that the distribution of energy is more uniform. The values for VSA were overall more uniform, and resembled the FMC values. Therefore, for high speed inspections, it could be argued that VSA is the more successful method if a wider angle range must be covered.

- The VSA frequency domain algorithm was implemented and compared to the time domain. It was found that the frequency domain gave a narrower range of angular coverage compared to the time domain. Also the time domain was easier to implement through a refractive boundary, which is often an issue in NDT. Therefore the remaining chapters were carried out using the time domain VSA algorithm.

- The VSA self tandem and multi-mode algorithms was investigated. It was found that these algorithms, the data acquired can be reprocessed in a number of ways to exploit all possible sound paths, including mode conversions, for imaging. Therefore, probability of detection and classification for certain defects can be improved. A few examples were shown of how the self tandem and multi-mode algorithms were used to image a vertically aligned flaw using the

high amplitude specular responses rather than the low amplitude tip diffracted signals used by the half skip and full-skip algorithms.

- A VSA surface mapping method was introduced here. The method was compared to the existing dipping reflector and plane wave surface mapping algorithms and it was shown that for less complex surface geometry the algorithm was very comparable to existing algorithms. The advantage of using this algorithm is that VSA data can be used to extract surface information such that the surface mapping and imaging algorithm can be performed with a single transmission sequence.

1.6 Organisation of Thesis

The second chapter of this thesis introduces general ultrasonic inspection, before going into more detail about the TFM related imaging methods FMC, PWI and VSA. In order to evaluate the differences, advantages and disadvantages of these, a comparison of the techniques is performed for a simple case in Chapter 3. Chapter 4 investigates the frequency domain VSA imaging algorithm. Chapter 5 introduces the multi-mode VSA imaging algorithm, introduces an efficient method of calculating the time of flights and discusses the benefits of using the multi-mode algorithm. Chapter 5 introduces a surface mapping algorithm, designed for testing parts with complex surfaces. Chapter 7 is a short summary of the thesis.

1.6.1 Critical Evaluation of Current State of the Art Ultrasonic Imaging Techniques

The third chapter evaluates the three state of the art imaging techniques in NDT. A series of side drilled holes were used to evaluate the performance

of each technique at different points in a region below the ultrasonic transducer. A number of different set ups were used for FMC, VSA and PWI to evaluate the effect of the aperture size, number of transmissions and other parameters had on the imaging performance. The imaging performance was evaluated using the Signal to Noise Ratio (SNR), the Array Performance Indicator (API) and the frame rate of the inspection.

It was found that the VSA and PWI techniques can achieve significantly faster inspection rates at a small compromise to image quality.

1.6.2 Evaluation of the Frequency Domain VSA Algorithm

The VSA frequency domain algorithm was derived and implemented. The frequency domain algorithm uses Fourier transforms to obtain the spatial frequency components of the returned data, then a back migration algorithm is used to generate an image. There exists potential benefits of using the frequency domain algorithm, such as the use of fast Fourier transforms to increase the imaging rate an potentially higher SNR than the TFM.

As in the previous chapter, a series of side drilled holes, laid out in as a square lattice, was used to evaluate the performance of the algorithm at different locations. It was determined that due to the narrower view and the inability of the frequency domain algorithm to negotiate multiple mediums, the time domain algorithm would be used for the remainder of the work in this thesis.

1.6.3 VSA Multi-Mode and Self Tandem

Being able to account for the mode conversions that occur as sound propagates is likely to be beneficial for NDT. As the refraction and reflection angles are not equal to the incident angle when a wave mode

converts, it is likely that mode converted sound may be able to reach areas where non mode conversion may not. In this case it is useful to have an algorithm that accounts for this, in order to increase the likelihood of detecting a flaw.

The fifth chapter presents the multimode algorithm, including a efficient way to calculate the time of flight paths for multiple velocity changes. The potential benefits of the algorithm are demonstrated using vertically aligned flaws. It can be seen that the multimode algorithm illuminates areas of the flaw which were previously unseen.

1.6.4 VSA Surface Mapping Algorithm

The sixth chapter presents a VSA surface mapping algorithm for inspecting components with complex geometry. Current surface mapping algorithms use either data from the full matrix or plane wave data. The new algorithm uses VSA data to map the surface and image beneath. This allows the algorithm to use the same data for acquisition and imaging, removing the need for multiple firing sequences for VSA inspections and potentially increasing the imaging rate.

The algorithm is tested and compared to current surface mapping algorithms and it is shown that for simple surfaces, the algorithm performs as well as the current techniques. However the algorithm loses accuracy when the surfaces get more complicated.

Chapter 2

Ultrasonic Non-Destructive Testing and Imaging

2.1 Introduction

Ultrasonic testing is a large section of non destructive testing based on the propagation of ultrasonic waves in the testing component. It most commonly associated with the medical field, where sound is used to image the interior of bodies of humans and animals. A commonly known ultrasonic testing technique is often performed during pregnancy, where ultrasound is used to image unborn foetuses in order to check the health and well being of the baby. In Non Destructive Testing (NDT), ultrasound is generally performed on components made with steel or some other metal alloys, however it has also been known for testing composites, concrete and even wood.

This chapter aims to introduce wave theory, describe the propagation of waves through solids and how sound is generated. Current conventional and phased array ultrasonic testing technology is discussed before introducing the current state of the art of ultrasonic imaging: the Full

Matrix Capture technique. Then topic of this thesis, an advanced ultrasonic testing method named Virtual Source Aperture, is introduced.

2.2 Basic Wave Theory

Ultrasonic Testing (UT) is based on the propagation of waves through the inspected component. An acoustic wave is an organised mechanical vibration of atoms travelling through a medium, typical of cyclic behaviour. The frequency is defined as the number of cycles that happen with time. The standard unit of frequency is Hz, defined as one cycle per second. The period of a wave, defined as the time taken to complete a cycle, is equal to the inverse of the frequency:

$$T = \frac{1}{f} \tag{2.1}$$

Here, T is the time period of the wave and f is the frequency.

Ultrasonic waves typically have a frequency between 20kHz and a few GHz, above the range of the human ear. A bat uses ultrasound to navigate its way through the darkness by emitting a pulse of sound and listening for returned echos reflected from objects obstructing the flight path of sound. The time delay between emission of sound and the echo indicates the distance travelled by the sound. This is the basic principle of ultrasonic imaging. The exact distance can be calculated using the velocity of sound in the medium:

$$dx = v\ dt \tag{2.2}$$

Here, v is the velocity of sound in the medium, dx is the travelled distance and dt is the time delay between the emission and the recorded echo.

The wavelength (λ) is the distance travelled by the wave in a single cycle. Taking Equations 2.1 and 2.2, it can be seen that:

$$v = f\lambda \tag{2.3}$$

2.2.1 Phase and Interference

The phase is a measure of how far the wave is through its cycle. The unit for phase is radians (rad), and the phase goes through $0 \rightarrow 2\pi$ radians before repeating itself. The amplitude of the wave changes through the cycle and thus is phase dependent.

Interference happens when two waves overlap. The result is the summation of the amplitudes of the two waves. Consider Figure 2.1, this is a depiction of a line being held between two points, similar to the case if two people held a rope between them. If the two people were to displace (lift) the rope simultaneously in order to induce a wave, two waves would form travelling in opposite directions. Figure 2.1 follows the two waveforms as they travel along the rope, the red travelling to the right and the blue to the left. As these waves pass over each other, the resulting displacement of the rope is the sum of the two waveforms, highlighted in green.

Constructive interference is when the amplitudes of the two waveforms sum to form a larger displacement, as shown at time t_2 and t_4. Destructive interference is caused when the amplitudes of the two waveforms sum to generate a smaller overall displacement, as occurs at time t_3.

Understanding of the phase is extremely important in ultrasonic imaging, as it explains many different wave phenomena. A general rule to remember is that if two waves from two similar sources are in phase then

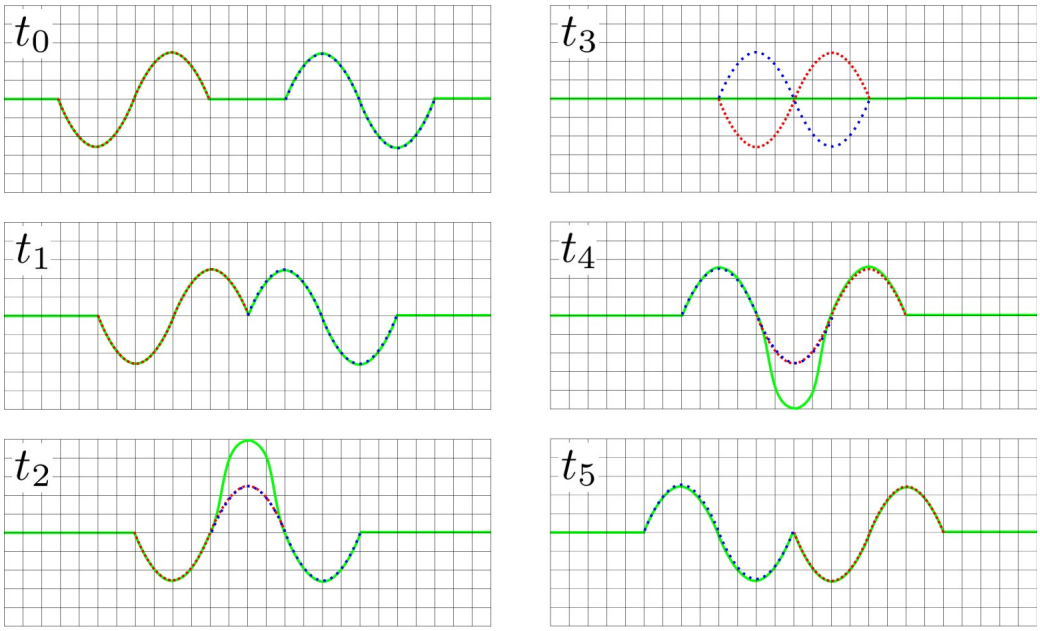


Figure 2.1: Depicting the interference as two waves overlap.

constructive interference happens. The two waveforms are in phase if:

$$\theta_1 - \theta_2 = 2n\pi \tag{2.4}$$

Where θ_1 and θ_2 are the phases of the first and second wave respectively and n is an arbitrary integer.

If the two waveforms are completely out of phase then destructive interference happens. The two waveforms are completely out of phase if:

$$\theta_1 - \theta_2 = (2n + 1)\pi \tag{2.5}$$

In between, either constructive or destructive interference can happen. The phase of a waveform at a given point depends on a many variables such as distance travelled, time, wave frequency and wavelength. The amplitude of a wave at a given point also depends on a number of factors such as attenuation, phase and energy. Both amplitude and phase need to be considered when working with ultrasound.

2.2.2 The Wave Equation

There are a number of different ways that an acoustic wave can propagate, as explained in Section 2.2.3. Each of these are caused by a different type of particle oscillation, all of which obey the wave equation. A good way to approximate the behaviour of particles is to consider the particles as a number of masses connected by springs. In this section the wave equation will be derived using the simple case of a string of masses that oscillate in one dimension by compression and tension the springs connecting them.

Hooke's law states that an extended/compressed spring will provide a resistant force to counter the change in length. The magnitude of this force is related to the extension/compression of the spring by the spring constant k, as shown in Equation 2.6.

$$F = -k\ du \tag{2.6}$$

Here, F is the force exerted by the spring, and du is the change in length. The units of k ($kg\ s^{-2}$) is seen using Equation 2.6. The acceleration of a mass at the end of the spring is derived using Newton's second law:

$$\frac{d^2u}{dt^2} = \frac{k\ du}{m} \tag{2.7}$$

Here the second derivative of position is the acceleration, and m is the mass of the spring. Consider a linear set of masses connected by a set of springs, and constrained to oscillate in a single dimension (x), as shown in Figure 2.2.

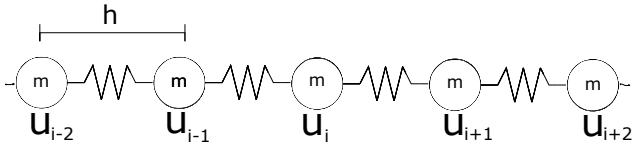


Figure 2.2: Mass On Springs

The equilibrium length of the spring (the length at which no force is exerted by the spring) is given by h. The acceleration of the centre mass positioned at U_i is proportional to the extension/compression of the springs attached to it and therefore the positions of its neighbouring masses at U_{i+1} and U_{i-1}, as shown in Equation 2.8.

$$m\frac{d^2u}{dt^2} = k[(u_{i+1} - h) - (u_i - h) + (u_{i-1} - h) - (u_i - h)] \tag{2.8}$$

Considering N particles spaced periodically by a distance h, the total length L is given as $L = Nh$. The total mass $M = mN$ and total stiffness $K = k/N$. Knowing this, Equation 2.8 can be rearranged to give:

$$\frac{d^2u}{dt^2} = \frac{KL^2}{M}\frac{[u_{i+1} - u_i + u_{i-1} - u_i]}{h^2} \tag{2.9}$$

It can be seen that the units of KL^2/M are: $kg\ s^{-2}m^2kg^{-1} = m^2s^{-2}$. Therefore the term KL^2/M is equal to the velocity of sound in the medium squared. Knowing this, and taking the case as $h \to 0$, Equation 2.9 is rearranged to get the well known wave equation:

$$\frac{d^2u}{dt^2} = v^2\frac{d^2u}{dx^2} \tag{2.10}$$

A wave can be described by any solution u that obeys Equation 2.10.

2.2.3 Propagation Modes

An acoustic wave travels through the oscillation of particles. Although the individual particles do not stray far from their resting position, energy is transferred through oscillation. There are a number of ways in which acoustic waves can propagate. Section 2.2.2 describes the simple case of longitudinal (compression) waves. In this case the particles oscillate parallel to the direction of the wave. However, other propagation modes

such as transverse (shear), surface (Rayleigh) and Lamb waves also exist. For a shear wave the particles oscillate perpendicular to the wave direction, as shown in Figure 2.3. For a surface wave, the particles close to the surface follow an elliptical pattern. Lamb waves occur in solid plates with thickness less than a few wavelengths and cause the entirety of the material to oscillate.

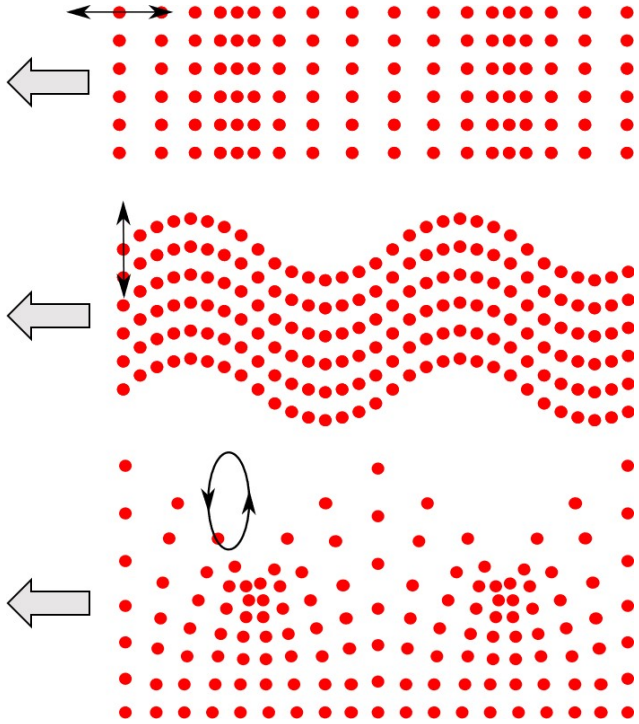


Figure 2.3: Example of Different wave modes: Top - Compressional/Longitudinal. Middle - Shear/Transverse. Bottom - Surface/Rayleigh.

Due to mechanical movement of the particles being different, the different wave modes propagate at different velocities in the material. Longitudinal waves are generally the quickest, with transverse being roughly half the speed and surface waves being roughly 90% of transverse.

2.3 Generating Ultrasound - Piezo Electric Effect

The Piezoelectric effect is used in ultrasonic transducers as a way of producing and detecting ultrasound waves. Electrostriction, the effect of

creating an electric field by changing the dimensions, was discovered by the Curie brothers in 1880 while investigating how materials form an electric field with change in Temperature, commonly known as the pyroelectric effect. The electrostatic effect occurs when polarised molecules in a piezo-electric material align themselves under mechanical pressure, changing to the lower entropic state. This creates a potential difference across the material.

Although the Piezo Electric effect was discovered in 1880, the development of ultrasonic technology for Non Destructive Testing (NDT) stagnated until the creation of the first piezo electric transducer, by Floyd Firestone at the University of Michigan in 1945 [1]. Ultrasonic transducers work by inducing an electric field or a voltage across the piezoelectric material. This causes the active (piezo-ceramic) element to expand. When the field is released, the crystal vibrates at its resonant frequency. The resonant frequency depends on the parameters of the crystal, the frequency can be carefully selected by cutting the crystal thickness to half the size of the desired wavelength: $\lambda/2$. Thinner transducer elements become fragile causing a limit to the highest frequency that can be produced. Common piezo-electric materials include Quarts (SiO2) and Barium Titanate (BaTiO3).

Ultrasonic Arrays were first developed by the University of Michigan [2]. The array is constructed of a number piezo-electric elements, each of which can have separate transmission times and can individually receive echo data. Phased Array inspection [3], where a B-scan can be generated by steering the beam without moving the probe as described in section 2.5.2, was the original purpose for developing ultrasonic arrays. However, due to the development in computer hardware enabling a large number of calculations to be done in a short space of time [4], arrays have been used to develop a wider variety of inspection techniques [5].

2.4 Huygens Principle

In 1678, the Dutch physicist Christiaan Huygens proposed a model that is still used today to predict the general behaviour of waves. He proposed that any point on a wave front could be treated as a source of wavelets propagating out from that point. The behaviour beyond a certain point could be described by the sum of an infinite number of point sources placed upon the beam front. Considering this, a number of different wave phenomenon can be explained such as the near field and far field zones, grating lobes, diffraction and refraction.

2.4.1 Near and Far Field Zones

Consider Figure 2.4. Figure 2.4 is a depiction of a 2 dimensional element capable of generating ultrasound. According to Huygen's principle, each infinitesimally small space on the surface of the element can be considered as a wavelet source. The wavelet source emits sound uniformly in all directions. The resultant element wave front is the summation or integration of the wave fronts of all individual wavelets across the surface of the element.

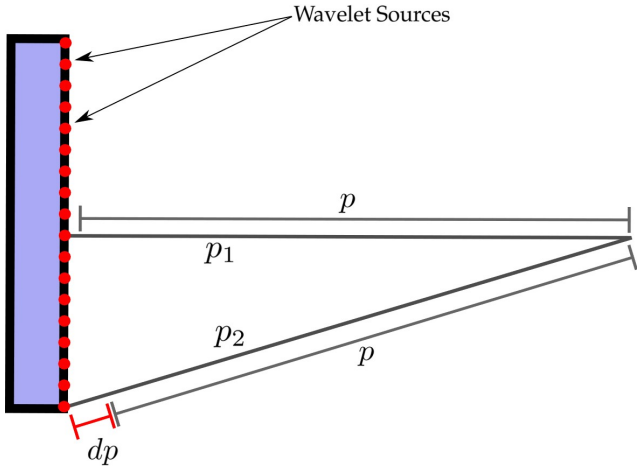


Figure 2.4: Image depicting the wavelet sources predicted by Huygens principle.

The near and far field can be found by considering the paths taken from different wavelet sources to a given point in space. The path from the wavelet at the centre of the element p_1, and at the edge of the element p_2, to a given point in space is depicted in Figure 2.4. As p_1 is shorter than p_2, sound that has been concurrently emitted from each source, have a difference in phase at a given point in space. The interference caused by this phase difference defines the nature of the near and far field.

The near field is defined as the area in which the difference in path length between a path p_1 that is perpendicular to the surface, and a path p_2 from the edge of the element, is greater than half of the wavelength of sound in that material ($dp > \lambda/2$). This tends to be in areas close to the element surface. In this region the phase of each wavelet source across the element at the point of interest has a range greater than pi, causing erratic interference between the wavelet sources, and an effectively random fluctuation of sound amplitude.

The far field is defined when the length of p_1 is such that: $dp < \lambda/2$. In this case, all of the wavelets begin to constructively interfere, giving a high amplitude signal. As the beam is far more predictable in the far field, this region is typically used in almost all practical applications of ultrasound.

2.4.2 Grating Lobes

Grating lobes are fluctuations in the amplitude of sound emitted from a source at different angles. These are a product of interfering wavelets. Grating lobes are famously seen with light in Young's single slit experiment, however the principle is the same with acoustic waves.

Consider Figure 2.5. This is a depiction of an ultrasonic source. Considering a point far away from the source, it can be assumed that p_1

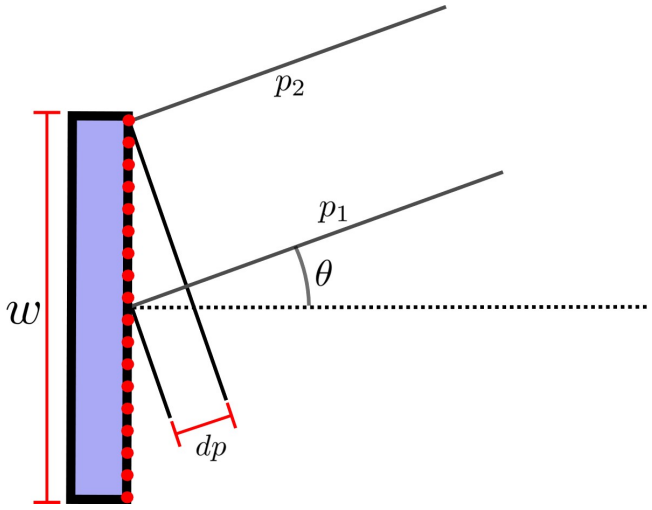


Figure 2.5: Depiction of how side lobes are generated.

and p_2 are parallel. Therefore:

$$2dp = w\ sin(\theta) \tag{2.11}$$

Here, w is the element width, and θ is the angle of the two paths from the surface. When $2dp = w\ sin(\theta) = \lambda$, the phase of the wavelets at the corresponding angle θ, are evenly distributed between $0 \rightarrow 2\pi$ across the probe surface. This leads to complete destructive interference as the summation of the wavelets is equal to zero.

At $w\ sin(\theta) = \lambda + \lambda/2$, the phase is evenly distributed over $0 \rightarrow 3\pi$. The wavelets with phase between $0 \rightarrow 2\pi$ cancel each other out, however constructive interference happens from the wavelets with phase between $2\pi \rightarrow 3\pi$, and so a peak can be seen. At $w\ sin(\theta) = 2\lambda$, complete destructive interference happens again.

It can be seen that at angles $w\ sin(\theta) = n\lambda$, where n is an arbitrary integer, complete destructive interference happens. However at $w\ sin(\theta) = n\lambda + \lambda/2$, minor constructive interference and a peak in the intensity is observed. These minor peaks at angles $\theta \neq 0$ are called grating lobes. Grating lobes

occur at $n \neq 0$:

$$\theta = sin^{-1}\left(\frac{(2n+1)\lambda}{2w}\right) \tag{2.12}$$

Figure 2.6 shows the intensity with angle for an element with width of $8mm$ and the wavelength of sound in the material being $2mm$. Peaks are observed at $\theta = 0^o, 21^o, 41^o$ and 61^o as expected.

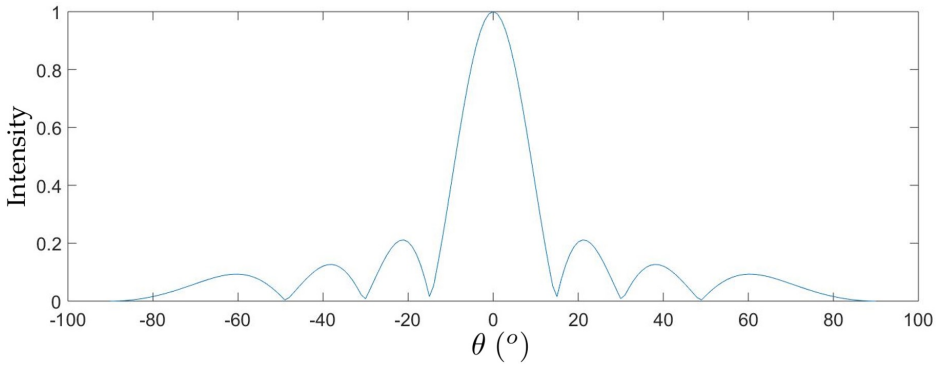


Figure 2.6: Intensity with angle for a $8mm$ wide probe generating a $2mm$ sound beam.

Probes are typically designed with a particular width in order to avoid grating lobes, however in NDT generally, probes are used in a variety of materials with different velocities of sound. Therefore grating lobes are often a problem.

2.4.3 Reflection and Transmission

The acoustic impedance of a material is the product of the velocity multiplied by the density of the material:

$$Z = \rho c \tag{2.13}$$

Here, Z is the material's impedance, ρ is the density of the material and c is the velocity of sound in the material. When a travelling sound wave meets an impedance boundary, part of the sound is reflected and part of it is transmitted. The percentage of of reflected energy varies with the incident

angle, for a 0^o incident angle the percentage of reflected energy is given by:

$$R = \left(\frac{Z_1 - Z_2}{Z_1 + Z_2}\right)^2 \times 100\% \tag{2.14}$$

Refraction and the Critical Angle

Refraction occurs on a boundary between two materials of different velocities. As sound passes through the boundary, the shape of the beam changes. This is depicted in Figure 2.7. Due to this, the path that the sounds takes between two points is not straight.

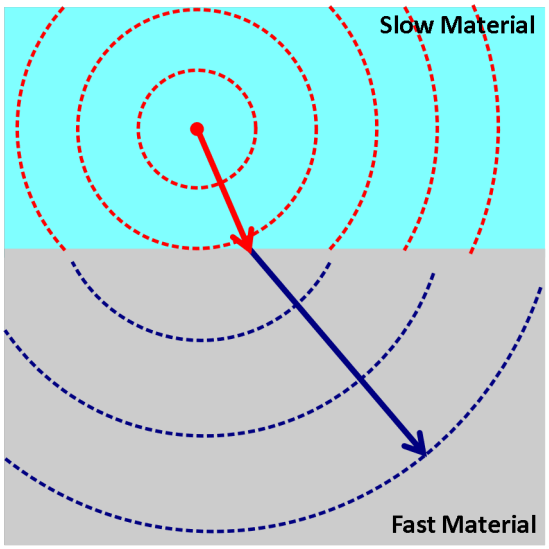


Figure 2.7: Image depicting sound originating from a point source through refractive boundary.

The refraction angle can be calculated using Snell's Law:

$$\frac{sin(\theta_1)}{sin(\theta_2)} = \frac{c_1}{c_2} \tag{2.15}$$

Here, θ_1 and θ_2 are the incident and refracted angles and c_1 and c_2 are the velocities of the incident and refracted material respectively.

The critical angle is defined as the incident angle required to make the refracted beam 90^o to the surface. At incident angles beyond the critical angle, all sound energy is reflected. Often in NDT, multiple critical angles

are often referred to, these are references to the critical angles of different wave modes. As the different wave modes have different velocities, each mode has its own critical angle. The first critical angle refers to the critical angle for longitudinal waves, the second critical angle is the critical angle for is for shear waves. In NDT, probe wedges are often designed to produce an incident angle that is beyond the longitudinal critical angle, so that only the shear wave mode enters the material. This way, confusing indications caused from multiple different incident wave modes can be eliminated, making a component simpler to inspect for the operator.

2.5 Ultrasonic Testing

The basic concept behind ultrasonic testing (UT) is that a probe is used to generate a pulse of sound which then propagates into the inspected material. The sound is then reflected off any impedance boundaries within the material which could be either material geometry or a flaw. The probe then receives the returning echo. The time of flight, between initial pulse and echo, and the known velocity of sound in the material is then used to calculate the distance travelled. Using this the location and size of the indication can be verified.

A brief description of conventional UT and phased array UT is given in this section. While not entirely applicable to the conducted research, it is useful for the reader to understand the basic concepts of methods currently used in order understand why the subject of this research (virtual source aperture) is applicable to the field.

2.5.1 Conventional UT, A-scans, B-scans and C-scans

Conventional Ultrasonic Testing uses single crystal elements. The element widths are designed to be larger than the wavelength of sound in the

material so that they produce a non divergent narrow beam in the material. Wedges are often used to produce an angled beam in the material. Common wedges are designed to produce a 45^o, 60^o or 70^o angle shear wave in Carbon Steel, and an inspection is performed using a combination of these three in order to find flaws within the material.

The information is displayed as an Amplitude scan (A-scan). This is a measure of the ultrasonic energy returned to the probe with time.

The probe is scanned over the surface of a probe, covering a rectangular area by a series of parallel lines, as depicted in Figure 2.8. This is called raster scanning. The B-scan is a 2D image of a cross section within the material showing the amplitude of the returned responses at a given depth and position.

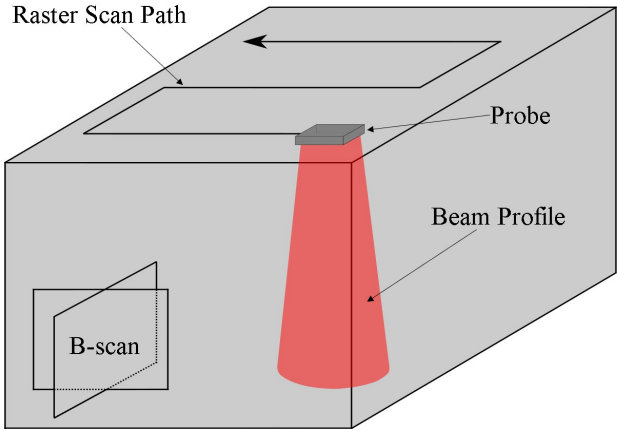


Figure 2.8: Depiction of a single element 0^o scan.

A C-scan is a 2D image is used to give a birds eye view over the top of the part. The amplitude of the maximum response is plotted over the entire surface area covered by the raster scan is displayed in the image.

2.5.2 Phased Array Ultrasonic Testing

Phased Array (PA/PAUT) is an advanced form of ultrasonic imaging. It uses an array of ultrasonic crystals, each which can transmit and receive ultrasound individually. The term 'delay law' applies to the transmission

delay applied to each element when groups of array elements are fired together. Delay laws are used to steer the beam or focus sound onto a given point or steer the beam to travel in a given direction, a depiction of this can be seen in Figure 2.9. PAUT allows the components to be inspected using multiple beam angles at once, eliminating the need for multiple probes required for conventional imaging. Focussing allows the resolution in a given region to be increased, however beyond that region, the beam diverges and the focus is lost. The resolution of an unfocussed scan is limited by the width of the active aperture, however the beam is more consistent over a greater distance.

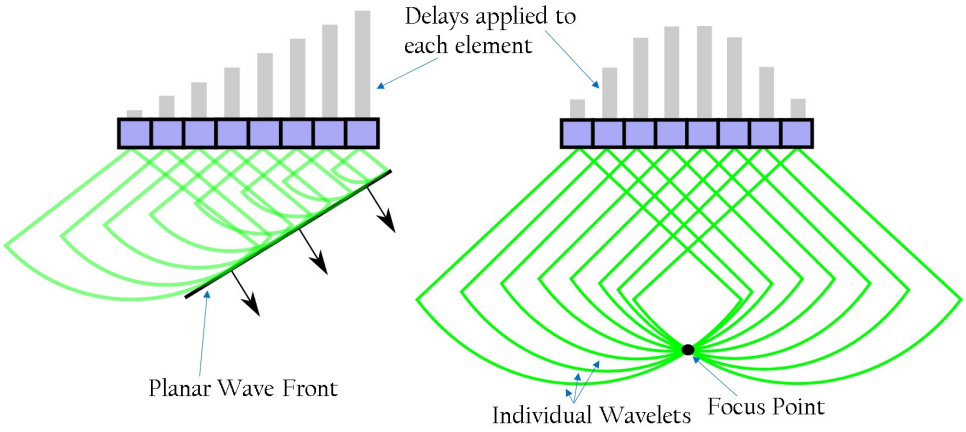


Figure 2.9: Depiction of how a linear array is used to generate a Planar Wavefront (left) and Phased Array Focussing Point (right).

Using delays laws on an ultrasonic array allow a large region to be inspected without moving the probe, giving PAUT an advantage over conventional ultrasound. A larger region can be inspected using a either linear or sector scan. A linear scan uses a small group of the array elements. The group is fired, focussed or unfocussed, and the A-scan collected. This process is repeated for new groups of elements incremented along the array, until last array element is included. A sector scan is where multiple A-scans are collected by steering the beam over a range of angles,

this can be focussed or unfocussed. These two scanning types are depicted in Figure 2.10.

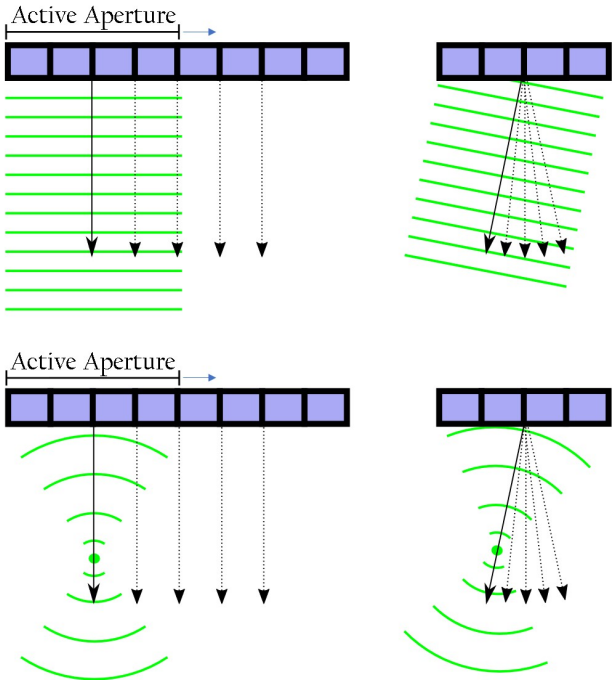


Figure 2.10: Top - unfocussed phased array inspection: left - linear scan and right - sector scan. Bottom - focussed phased array inspection: left - linear scan and right - sector scan.

The collected A-scans and their respective positions/angles are used to plot an ultrasonic intensity map. This image can then be interpreted by the user in order to find and classify flaws.

A brief description of PAUT is given in this section to give the reader a basic understanding of the technique as PAUT is often referred to in this thesis when discussing advantages and disadvantages of using different ultrasonic imaging techniques. As developments in computer processing power required for the real time implementation of more complicated algorithms has been developed only relatively recently [6], historically PAUT has been the most widely used UT technique in NDT [7, 8] and provides a good reference in which to develop future work.

2.6 Fully Focussed Imaging

Recent advances in computer hardware and processing power has allowed ultrasonic arrays to be used in for a variety of new techniques [5, 9]. The TFM is a post processing algorithm used to generate a fully focussed image of the inspected region and was first introduced for NDT in 2005 [10]. The TFM can be used with the Full Matrix Capture (FMC) [11], Plane Wave Imaging (PWI) [12] and Virtual Source Aperture (VSA) [13] data acquisition techniques in order to generate an image that is fully focussed across the entire region of interest. This section describes the methods used to acquire data and the TFM algorithm used to generate a fully focussed image.

2.6.1 Data Acquisition Methods

The TFM can be used for a variety of data acquisition methods. Each are subtly different, some favouring image quality and others that favour minimising the post processing in order to maximise inspection speed. SAFT, FMC, PWI and VSA are described here.

Synthetic Aperture

Synthetic aperture focussing was originally developed to improve the accuracy of B-scan images for single element transducers [14]. It can also be used along with an ultrasonic array. Each element fires and receives individually, for N element array, N^2 A-scans are collected.

Full Matrix Capture

FMC was introduced by the University of Bristol in 2005 [10]. Since then it has been developed as one of the leading ultrasonic inspection technique in

NDT [15]. The technique uses an ultrasonic array. Each element on the array is fired individually while receiving on all. This builds up what is known as the full matrix of data; for N_e element array, N_e^2 A-scans are collected. Then the TFM is used to generate a fully focussed image. FMC-TFM is commonly known as the 'gold standard' in ultrasonic imaging, due to its robustness [16], high signal to noise ratio (SNR) and the ease of interpretation of the image [17].

The quality of FMC-TFM is caused by vast amounts of data being processed and contributing to the image. However, this means that a single FMC image generates a comparatively large data file to that of PAUT, which has been a limiting factor for its adoption. There is also a huge difference in the processing required to generate the image, as millions of calculations are required. For an N_x by N_z pixel image using an N_e element array, $N_x N_z N_e^2$ calculations are required in order to gain a TFM image. This post processing has been a limiting factor in wide spread adoption of FMC-TFM until recent years where advances in computer hardware has been used to minimise the post processing burden [4].

Virtual Source Aperture

VSA is a technique that originates from medical imaging [18]. Each element of the array is fired at a slightly different time, named delay law, in order to produce a wave front as if it had originated from a virtual point behind the aperture [19], as shown in 2.11. The individual element wavelets, shown in green, are seen to behave as if the sound originated from a virtual source placed behind the aperture. All elements then receive individually in the same way as FMC. The delay on a given element required to produce a virtual source is given by:

$$t_e = \sqrt{(x_e - x_v)^2 + (z_e - z_v)^2} - v_z \tag{2.16}$$

Here, x_e and z_e are the x and z coordinates of the eth element, x_v and z_v are the x and z coordinates of the virtual source and v_z is the perpendicular distance of the virtual source behind the aperture.

The TFM is used to generate an image, with the virtual source point as the source location and the receiving element as the receive position [20]. As multiple elements are used in a single transmission, a higher amount of energy enters the material compared to a single element transmission used for FMC. As a consequence of this, the SNR of the A-scans for VSA is higher than FMC. Multiple virtual source transmissions may used for a single image [13]. The image SNR per transmission is higher and therefore an image can be constructed in fewer firings [21]. Therefore data files for an equivalent VSA inspection are smaller than FMC and there is less post processing allowing for a higher scanning speed.

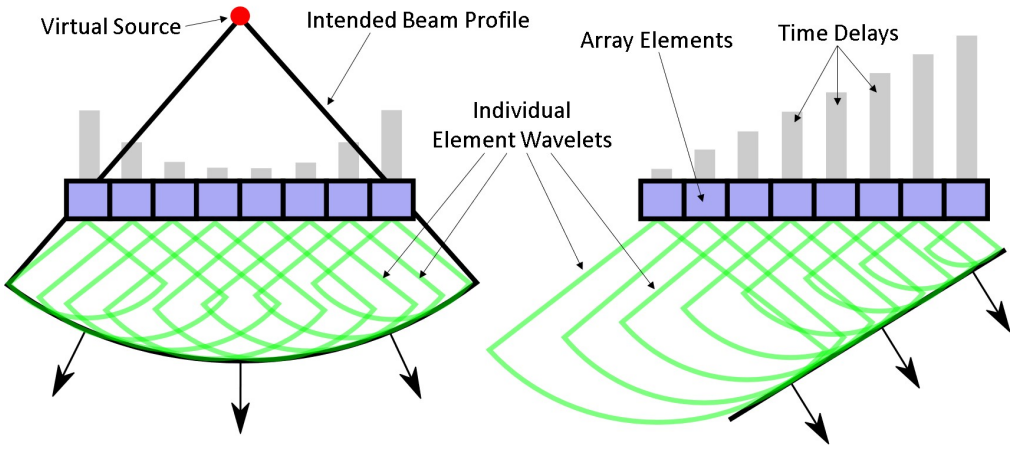


Figure 2.11: Left: Beam Profile for a Virtual Source. Right: Beam Profile from an Angled Plane Wave

Plane Wave Imaging

PWI is a technique that also originates from medicine [22, 23]. The technique uses a flat delay law to generate a planar wave front that propagates into the material. This is depicted in Figure 2.11. The delay laws required in order

to generate a planar wave front with an angle θ in the material is given in:

$$t_e = \frac{e\ p\ sin(\theta)}{c} \tag{2.17}$$

Here, t_e is the time delay on the eth element required to generate the planar beam, p is the array pitch, θ is the angle of the beam and c is the velocity of sound in the material.

The image is generated using a slightly modified TFM algorithm to the one that is described above, as the sound source is approximated to be an infinitely long line source [24] rather than the point sources used for FMC and VSA. However, the concept is the same and the image is fully focussed across the entire area of interest.

PWI and VSA are very similar techniques. Due to this they both exhibit the same advantages over FMC in minimal data and processing per image and therefore high inspection rates. The main difference between the two is the region insonified by the sound. PWI uses a high intensity narrow beam to insonify the region of interest whereas VSA uses a divergent beam originating from a virtual point source. The high intensity plane wave allows the SNR of an indication in the insonified region to be high comparatively to VSA. However this beam is narrow, and so multiple transmission different angles must be used to image a larger area.

2.6.2 Total Focussing Method

The TFM allows a fully focussed image to be generated. A modified version of the algorithm works with SAFT, FMC, VSA and PWI, although the basic concept is the same. The region of interest is flooded with sound and the echos are recorded on each individual element of the array. An area of interest is chosen and split up into pixels. In essence, the TFM synthesises a focussing point and returns the ultrasonic intensity for each

pixel in the image. This is done using Equation 2.18. The known velocity of sound in the material is used to calculate the time of flight from the sound source, to the pixel of interest and back to the receiving element is calculated. Then, the amplitude of the corresponding A-scan at that time is taken. The ultrasonic intensity is the sum of these A-scan amplitudes at the calculated time of flight, for every transmit receive combination. An image is made by using Equation 2.18 to focus at every pixel in the region of interest defined.

$$I(x,z) = \left| \sum_{i=1}^{N_t} \sum_{j=1}^{N_e} A_{i,j} \left(a_i(x,z) + b_j(x,z) \right) \right| \tag{2.18}$$

Here, $I(x,z)$ is the intensity of a pixel at position (x,z), N_t is the number of array transmissions and N_e is the number of elements on the array. a_i is the time of flight for the ith transmit path to the pixel at (x,z), b_j is the returning time of flight from the pixel at (x,z) to the jth element and $A_{i,j}$ is the amplitude of the corresponding A-scan.

Figure 2.12 depicts the paths a and b for the TFM algorithm using virtual sources. The TFM algorithm can be used to inspect through a refractive boundary as well as a direct contact inspection providing the path the sound takes is known.

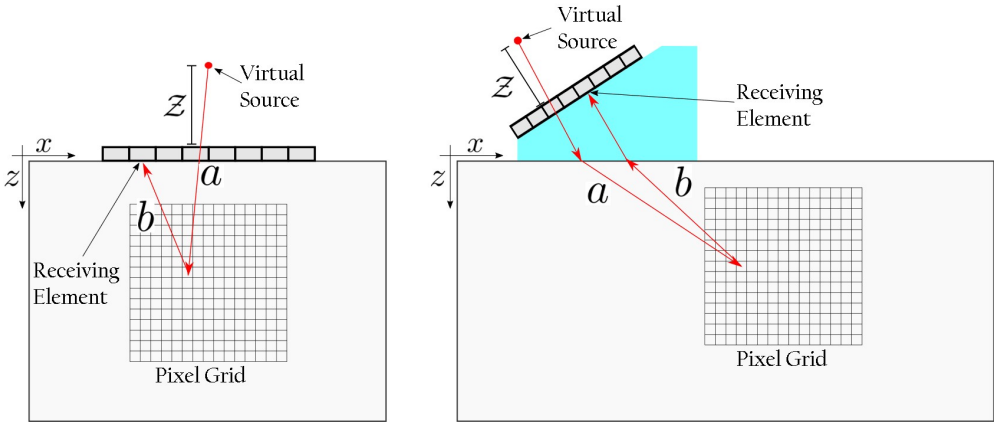


Figure 2.12: Paths for the TFM algorithm. Left: direct contact inspection, Right: refractive boundary inspection.

When the amplitudes are summed, the pixels containing reflectors have a higher intensity value than the surrounding ones due to A-scan amplitudes at the calculated times corresponding to peaks in the echo signal. Pixels that do not contain reflectors correspond mainly to low amplitude background noise and therefore the intensity of these pixels is lower.

2.6.3 Hilbert Transform

The Hilbert transform returns the real and imaginary parts of the signal [25]. This is done by applying a Fourier transform to the real signal, removing the negative frequencies and then performing the inverse Fourier transform on the signal. The magnitude of the returned complex number gives the envelope of the original signal. This is particularly useful in image processing to gain the phase information for the wave as well as improving image visualisation. Before performing the TFM, the Hilbert transform is applied on the returned echo signals. When the real and imaginary parts of the wave is summed, the absolute value is taken at the end of the process to give the final image.

2.6.4 Adaptions of the TFM, other Imaging Methods and Coherence Weighting

Coherence weighting is a phase dependent method of weighting the TFM image in order to improve SNR and visualisation. Coherence imaging uses phase information only in order to generate an image. Both have been studied and are useful in NDT. In [13], a coherence weighting function for VSA is introduced for improving SNR of the returned image. The principle of the coherence weighting function is that when the amplitudes of the TFM are summed, the selected amplitudes for a pixel that contains a

reflector have similar phase, as these amplitudes correspond to peaks at the calculated times that coherently sum to give a high intensity. Pixels that do no contain a reflector are a summation of random background noise with incoherent phase. The weighting function favours the phase coherent pixels while suppressing the incoherent pixels [26]. The weighting coefficient is calculated by modifying the TFM algorithm. The final intensity for a given pixel is divided the the sum of the magnitude of each of amplitude terms that contribute to that pixel, as shown in Equation 2.19.

$$C(x,z) = \frac{\left|\sum_{i=1}^{N_t}\sum_{j=1}^{N_e} A\left(a_i(x,z) + b_j(x,z)\right)\right|}{\sum_{i=1}^{N_t}\sum_{j=1}^{N_e}\left|A\left(a_i(x,z) + b_j(x,z)\right)\right|} \tag{2.19}$$

Here, $C(x,z)$ is the coherence weighting factor. The summation of signals with coherent phase have an intensity value close to the summation of the magnitudes and are favoured by the algorithm. Incoherent signals are suppressed. The coherence coefficient for each pixel is then multiplied by the TFM intensity in each pixel for the final image. A similar coherence weighting function exists for PWI [27]. Weighting functions can also be used to reduce the effect of side lobes when imaging [28].

While the TFM [10] and the coherence weighting function presented in [13] combines amplitude and phase information, coherence imaging focusses only on phase information [26]. Often when sizing planar flaws, the amplitude of the reflected signals from the middle of the flaw dwarfs the tip diffraction signals from the end of the flaw. Therefore, it is difficult to distinguish the size of the flaw from the TFM image only. However, tip diffracted signals behave more like point sources than the middle of a planar flaw. [29] presents a coherence imaging algorithm that focusses at the entire region of interest, much like the TFM algorithm, and displays only the phase coherence in the delayed signals [29]. This shows that tip

diffracted signals can be easily distinguished from reflected signals using the presented algorithm and therefore accurate sizing of flaws using this method can be achieved.

Discovering the orientation of a flaw is also of importance in NDT. In [30], the 'vector TFM' method is presented. The maximum amplitude of sound reflecting off a planar boundary is found where the reflected angle is equal to the angle of incidence. Using this knowledge, along with the transmit and receive positions of the array elements, the amplitude information from the full matrix is analysed in order to find the orientation of the surface vector of a series of planar flaws [30]. This is then plotted as a vector field. However, for point like sources, the original TFM algorithm works best.

The resolution of the TFM algorithm is limited by the wavelength of sound in that material, due to this, it is difficult to distinguish the orientation of sub-wavelength size flaws. The work presented in [30] has been developed in order to do this. Different types of flaws reflect sound differently and can be predicted by analysing the scatter matrix that they produce. Using the full matrix of data, the scatter matrix for a known flaw can be constructed [31]. The scatter matrix shows the amplitude of the reflected signal for different incident and reflection angles when focussing on a flaw and can be used for distinguishing sub-wavelength planar flaws from point like flaws [32].

2.7 Refractive Boundary

Often in NDT, inspection is done through multiple velocity mediums where refraction occurs. This is the case when inspecting using a wedge or immersion testing [33]. When refraction occurs, the path of the sound from the source in the first medium, through the boundary to the source in the

second medium is not straight. The point of incidence is required in order to calculate the path length and the time of flight for the TFM imaging algorithm. For a flat surface, it is possible to find an exact solution for the position of incidence using Snell's Law [34]. However, this method can be unstable. No exact solution exists for a curved boundary. In these situations, Fermat's principle may be used in order to find the position of incidence. Fermat's principle states that the path between the sound source and the receiver is the path that takes the least amount of time. Therefore, in order to find the correct path for the TFM algorithm, an exhaustive traversal of the boundary must be completed in order to find the minimum time of flight. [35], [36] and [37] both demonstrate how imaging using the TFM can be achieved through a refractive boundary using Fermat's principle. When imaging with PWI, the angle of incidence is known, and so calculating the position of incidence is simple using Snells Law for a flat surface [38]. However Fermat's principle must also be used for PWI in the case of a non flat surface.

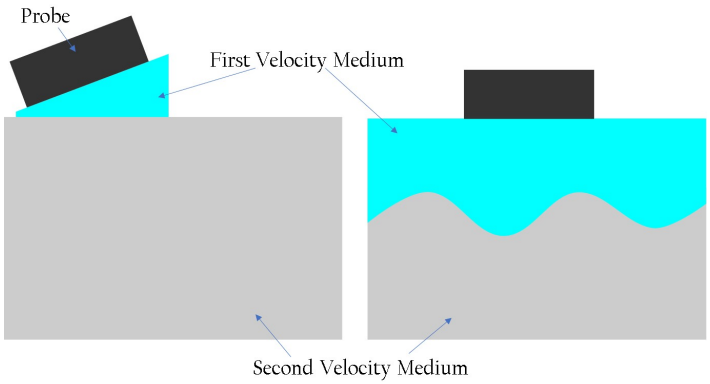


Figure 2.13: Image depicting inspection circumstances where imaging through a refractive boundary is required. Left - wedge inspection, Right - immersion inspection.

To perform the TFM, the path from every sound source and receiver to every pixel in the image must be pre calculated in order to generate an image. As each one of these requires an exhaustive traversal of the

boundary in order to find the least time, this can be computationally expensive. In some cases, this calculation may only be necessary at the start of imaging, if a fixed size medium is used such as a solid wedge. In which case the sound paths can be pre-calculated, saved and re-used for every image. However if the surface is dynamically changing, such is the case a probe is moved across the surface of a component when immersion testing, this can cause a drastic reduction in imaging speeds. Several methods exist in order to reduce this computational burden. In [39], a course grid of pixels is generated and the time of flight calculated using Fermat's principle. Then time of flight values for a finer grid of pixels is linearly interpolated using values for the course grid. The study [39] finds that linear interpolation is reasonably accurate providing the spacing of the pixels in the course grid is kept to below the length of a few wavelengths of sound in that material. Another study [40, 41] describes a Newton Raphson based technique in order to find the least time. The time of flight function is differentiated, the minimum occurs at the point at which the differential is zero. The Newton Raphson method is used to find the point at which the differential of the time of flight function is zero. At which point, the point of incidence is found. However this method is very unstable if the Newton Raphson technique fails to converge, and so a good original estimate is required [42].

Other methods attempt to reduce the problem to a single velocity medium by using an array of virtual sources and receivers on the surface [43]. However while focussing on transmission is perfectly reasonable, assuming a point on the surface as a virtual receiver is a poor assumption as diffraction occurs when sound meets an impedance boundary within the inspected material. Therefore focussing through the two boundaries is required upon receive, requiring the Fermat's principle method.

2.7.1 Imaging Approaches to Consider

Direct or half skip inspections consider sound that has travelled directly from the source, to the region of interest and back. If an inspected component has a known thickness, sound can be skipped off the back wall before insonifying the region of interest. Full skip is often referred to in NDT, this is the case where sound has skipped off the back wall, hit the region of interest, before returning along the same path to the probe. These two types of path are often used in conventional and phased array ultrasonic inspection and are depicted in Figure 2.14. Insonifying the region of interest from as many angles as possible is of vital importance in NDT in order to reduce the probability of missing a defect. A third mode, is introduced in [44, 45] using the TFM. This mode, referred to as 'self tandem' in this work, is when sound is skipped off the back wall, before hitting the region of interest and then returning directly to the probe. This mode is often ignored in conventional and phased array testing as the sound is often assumed to return back to the array along the same path as it had come from. The 'self tandem' method gives the TFM an extra approach to inspection, reducing the probability even further that a flaw is missed. This method is particularly useful when inspecting components with a known thickness, such as pipeline girth welds [46]. The 'self tandem' algorithm has been expanded for use with PWI [12] and VSA [47].

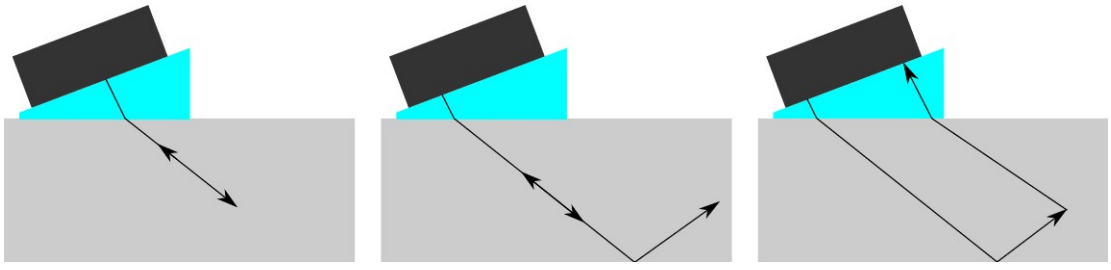


Figure 2.14: Imaging modes: Left - Half Skip, Middle - Full Skip, Right - Self Tandem.

Mode conversion occurs at any impedance mismatch. The more time sound spends in the material, the higher the probability that mode conversion occurs. If a constant velocity of sound is assumed, as it often is in NDT, mode conversion can cause confusing indications that could be misinterpreted as a flaw. This is because different wave modes of sound travel at different velocities. Consider a wedge designed with elevation beyond the critical angle in order to produce only shear waves into the material. For the half skip case, the sound may mode convert upon hitting the flaw. Therefore there are two forms in which the sound can return to the probe: shear-shear (*ss*) or shear-longitudinal (*sl*). As the longitudinal and the shear modes travel at different velocities, if shear velocity only is assumed for the imaging algorithm, then the same flaw may show two different indications. For the self tandem mode, mode conversion can occur after skipping off the back wall and when hitting the flaw, therefore four forms exist: *sss*, *sls*, *ssl*, *sll*. For full skip, eight different forms exist. This leaves a lot of room for unwanted false indications. The multi-mode TFM is introduced in [48], this is an edited version of the TFM which considers all the different mode conversion instances. The study shows that most of the modes described above are of low amplitude and often insignificant, however the algorithm is useful for explaining certain false indications that did show. This is important when finding and characterising flaws. The multi-mode TFM has since been developed for PWI [12].

2.7.2 Unknown Geometry

If a component has a non flat surface it can be inspected either using a flexible array that conforms to the surface [49], or the component and the probe can be immersed in a coupling fluid. If a flexible array is used, the

element positions on the surface must be known before focussing can be done [50, 51]. In [52] and [53], a technique for finding the element positions is introduced. The surface profile is described using a spline function and an initial estimate of the surface is made. The TFM is then used to generate an image. The spline function is edited and the process is repeated. The image contrast is measured each time. When the image contrast is at its maximum, the spline function best describes the surface geometry.

For the immersion case, refraction must be considered and the geometry of the component surface relative to the probe must be accurately known. Several methods exist to do this [54]. The TFM imaging algorithm may be used to generate an image of the surface [55], surface information can then be extrapolated in order to focus underneath. However this requires processing the TFM algorithm twice for every step which can be a burden, and the surface depth relative to the probe must be known in order for the TFM to image the surface in the first place.

The so called 'dipping reflector' introduced in [6] uses the first responses from the full matrix of data to obtain knowledge of the surface. The first responses from each element transmitting and receiving are recorded (a subset of the full matrix). Assuming that there is nothing between the probe and the surface that could interfere with the sound, it can be safely assumed that the first response comes from the surface reflection [56]. The difference in flight time between adjacent elements is then used to calculate the angle from which the sound originated from and the total time of flight is used to calculate the distance travelled by the sound. From this the surface profile may be estimated in a series of points. A similar method referred to as the 'pitch catch' method incorporates the rest of full matrix of data [57]. This method gives a larger number of points to describe the surface, however it is less accurate compared to the 'dipping reflector' method. Another method uses the first responses from

an incident 0^o plane wave [57] and trigonometry to find surface information. The same assumptions are made in [58] where surface information is obtained using an incident virtual source transmission. A slightly different method is introduced in [59] where the first response ellipses are plotted and a series or erosion techniques favouring intersecting point are used to map the surface.

Simple threshold crossing techniques can induce errors in the recorded first response time due to the long rise and fall times. Methods introduced in [60] and [61] can be used to reduce this error.

Once the surface profile is known, the interior of the component can be imaged.

2.8 Acceleration of Post Processing Methods

The acceleration of processing the TFM algorithm using graphics cards and other computer hardware is well documented [21]. This involves reducing the time taken for the computer to calculate the TFM algorithm and display an image. Graphics cards are used to parallelize the processing so that multiple calculations are done across a number of different cores at the same time. This has allowed FMC-TFM to become a real-time inspection technique [4] limited only by the time required for data acquisition for most inspection scenarios.

2.8.1 Frequency Domain Imaging

Frequency domain imaging originally was developed for radar, sonar and seismic exploration of the Earth's interior [62, 63]. A Fourier transform is used to acquire the phase and amplitude of the frequency domain components of the time domain signal (A-scan). The advantage of imaging in the frequency domain is that multiple frequency components (instead of

a single amplitude point from an A-scan) is used to contribute to the intensity of a pixel for a given transmit receive combination. This allows the destructive summation of the incoherent background noise to be reduced further in pixels not containing a reflector, increasing the overall SNR of the final image [64]. The amount of processing for the frequency domain algorithm therefore is higher than that of the time domain, however due to the efficient use of Fast Fourier transforms, the overall theoretical processing time for the frequency domain algorithm is lower [65].

The implementation of the frequency domain algorithm is difficult compared to the time domain TFM, and the fast Fourier transforms can only be used in a single velocity medium as the mathematics breaks down when a refractive boundary is introduced [66, 67]. Consequently, the algorithm isn't as widely used as the time domain equivalent in NDT, as the probe is rarely used in direct contact with the material. More often a wedge or a water path is used to couple the array to the material. Attempts have been made to implement the frequency algorithm using ray tracing techniques [68, 69], however much of the advantages from using fast Fourier transforms is lost and therefore generally people revert to using the time domain equivalent. In [70] an attempt is made to implement the algorithm using focussing laws to generate a virtual array of transmitters and receivers on the refractive boundary, converting it essentially into a single medium problem. However due to the dispersion after the sound enters the material, the assumption that a point on the surface can act as a virtual receiver breaks down and so ray tracing must be performed on receive for the imaging algorithm to be correct.

Most implementation examples of the frequency domain algorithm therefore uses a single velocity medium, where the probe is in direct contact with the material. In [71, 72], a frequency domain SAFT algorithm

is implemented. An implementation of the algorithm for a 2D array and a 3D volumetric image is seen in [73]. Hunter *et al* develop the algorithm further [65], allowing a different transmission and receive point ensuring that the algorithm can be used with the full matrix of data.

The frequency domain algorithm has gad great success in the medical field, as single medium inspection is common. However, multiple firings require a stable medium and therefore synthetic aperture algorithms have been avoided here, as the tissue of the patient might move while the data acquisition is taking place. PA techniques are generally the most commonly used imaging technique in medicine. However, PWI is developing interest, as the ultra fast frame rates allow for inspection of moving tissue and even blood flow [22, 23]. A recent paper [74] describes the frequency domain PWI algorithm in the medical field for a 0^o inspection. This allows high quality ultra fast imaging to be done in a single medium, ideal for the inspection of living tissue.

2.9 Conclusions

PAUT, FMC-TFM and PWI have been widely developed for ultrasonic imaging in NDT [10, 12], however there exists a void in research where virtual sources are concerned. Previous research investigates the use of VSA for direct contact and wedge inspection [19, 13] however it does not go further than that. VSA could be of great benefit to the NDT community as inspection speed is comparable to PAUT but with the advantage of fully focussed images, where PAUT fails. PWI is an existing ultra fast ultrasonic inspection technique however no study comparing PWI and VSA has been done, so there could exist potential advantages of using VSA over PWI.

To conclude, VSA has many potential benefits over existing techniques and consequently is the subject of interest for this thesis.

Chapter 3

A Comparative Study Between VSA, PWI and FMC

3.1 Introduction

A number of techniques exist that use ultrasonic arrays for NDT inspection [5]. PA uses time delays on the arrays to physically steer and focus the sound at the region of interest [75], however the resolution of this technique is limited by the focussing depth. The TFM is a post processing algorithm used to eliminate the depth of field problem by synthetically focussing at every point in the image. This sufficiently improves the resolution and allows the user to generate a fully focussed image of the test specimen interior [35]. The TFM was limited for a time by the computer processing power, however advances in hardware such as graphics cards have allowed real time TFM imaging [4].

The three main methods of acquiring data for the TFM algorithm are FMC, PWI and VSA. For an FMC acquisition, each array element is fired sequentially while simultaneously receiving on all. This provides the maximum amount of information possible that the array can give, as the region of interest is insonified from every possible angle that the array can

acquire. FMC is often referred to as the 'gold standard' for ultrasonic imaging [27], this is due to the sheer quantities of data that is acquired and processed leading to a high SNR and resolution in the generated image [10].

VSA uses multiple elements on transmission to generate a wavefront that behaves as if it originated from a virtual point behind the aperture [19, 20]. Often the array elements are divided into smaller sub-aperture groups, which are used to generate virtual source. The group is incremented along the array with each transmission [13]. With each transmission, all elements receive in the same manner as FMC and the TFM is used to generate an image. Generally the SNR of the returned A-scans is higher for a VSA transmission as multiple elements are used, allowing an image to be constructed in fewer firings than FMC [33, 21]. With fewer firings, there is less data to collect and process and therefore the scanning speed is higher [47].

PWI is a similar technique, multiple elements are used in order to increase the amount of sound energy used to insonify the material [24, 38]. PWI uses all elements on transmission and a flat delay law to generate a planar wavefront in the material [22]. The wavefront is steered over a range of angles to insonify the entire region of interest. The TFM is then used to generate an image [12].

Each technique is likely to have its own merits and disadvantages. For a given point in space, the FMC is likely to insonify the region with the largest range of angles that is possible for the array. The range of angles of the VSA inspection is likely to be smaller, given the position of the virtual sources behind the aperture. The PWI can insonify a given point using the same range of angles as FMC, however the number of transmissions chosen limit the angles actually used. The range of angles used to infonsify a given point is likely to impact the resolution of an indication and this can be quantified

by the Array Performance Indicator (API) [10]. The SNR is also likely to be affected by the range of angles used to insonify the reflector, as the angle of the reflector surface is likely to have an impact on whether sound returns to the transducer or not. The SNR is also likely to be affected by the number of transmissions, and the amplitude of the wavefront at the point where the wave hits the reflector.

The aim of this chapter is to investigate and compare the FMC, VSA and PWI imaging techniques. The number of set up parameters for each technique is discussed and the performance evaluated. To evaluate the performance of the different techniques, a simple direct contact inspection has been simulated. Side drilled hole (SDH) reflectors were used in order to determine the strength of the response from the TFM algorithm at different areas relative to the probe. An Olympus 5L64 transducer was used, with an element width of 0.6mm and a total number of 64 elements. The simulations were undertaken using the CIVA software.

3.2 Experimental Setup and Configuration

Each technique is set up differently with a various number of parameters to be considered. This section described the setup parameters used for each inspection case in order for a fair comparison to be established between the three techniques.

3.2.1 FMC Setup

As previously stated, FMC is an established technique that usually requires sequentially firing on each element while simultaneously receiving on all elements. N^2 A-scans are collected for an array of N elements. The FMC is often referred to as the maximum amount of information an ultrasonic array is able to collect. This is because every point of the region of interest

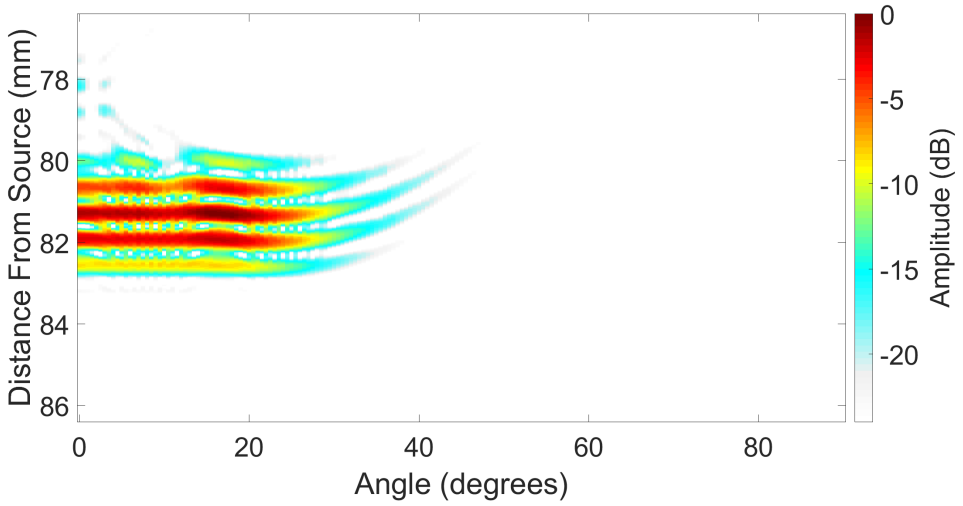
is insonified by every possible angle that the given transducer is able to in a given position. That information is combined by the TFM algorithm and shown in a single image, simplifying the detection and characterisation of flaws for the end user.

Due to symmetry between the time of flight paths, approximately half of the FMC data can be disregarded with negligible impact on the final image [4]. This is known as collecting the half matrix of the FMC data and is used to increase the imaging rate. The FMC full matrix often referred to as the 'gold standard' image quality [27] and the FMC half matrix has been used as a reference image in this study.

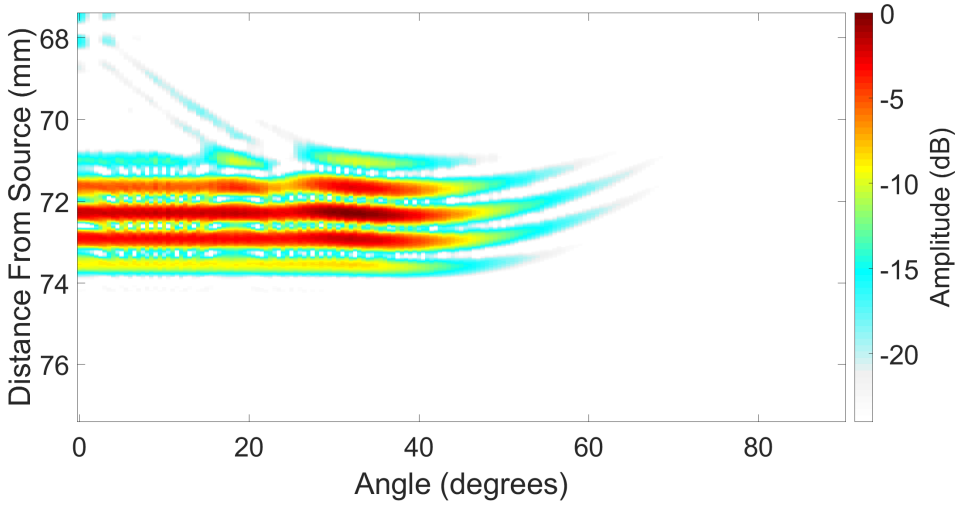
Much research has been conducted into FMC sparse arrays [76], where certain elements are removed from the imaging process in order to improve imaging speed without much detriment to the image quality. However these have not been considered in order to keep the focus of the study on the VSA and PWI techniques.

3.2.2 VSA Setup

There are a number of parameters that are required to be determined for a VSA inspection. A group of elements is chosen for transmission while every element on the array receives. The transmission group is incremented along the array to the end. The number of transmissions is determined by the total number of elements on the array, the size of the transmission group or 'sub aperture' and the incremented step size. The advantage of using a smaller sub aperture is that the inspected region can be insonified by a larger range of angles. However, using a smaller sub aperture reduces the power used to insonify the region. This study uses a variety of sub aperture sizes, and number of transmissions for the VSA inspections.



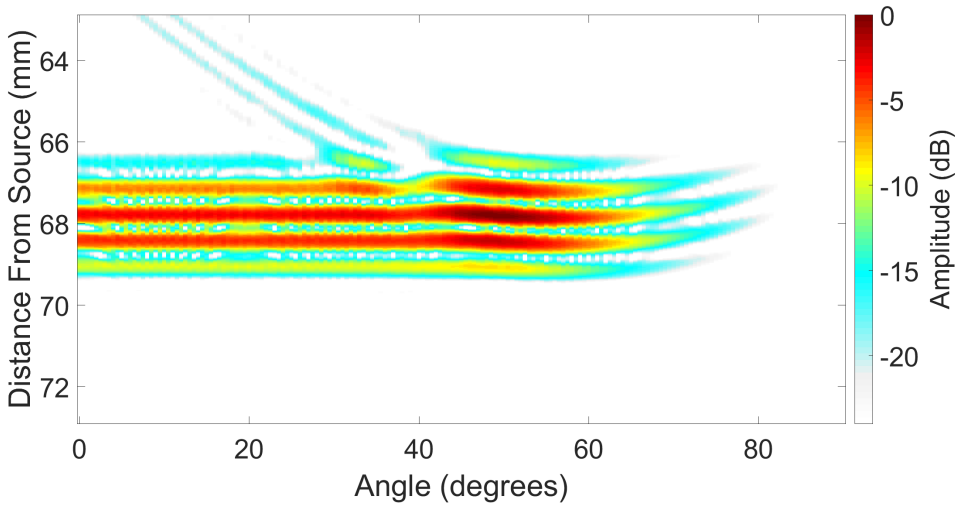
(a) Wavefront from a Virtual Source Placed at the Centre of the Array at Full Aperture Length Back



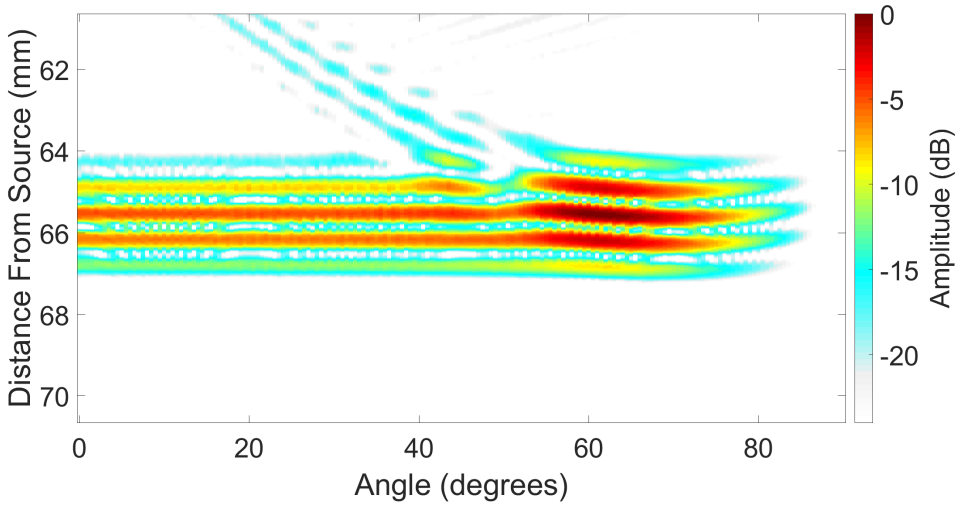
(b) Wavefront from a Virtual Source Placed at the Centre of the Array at Half Aperture Length Back

Virtual Source Positioning

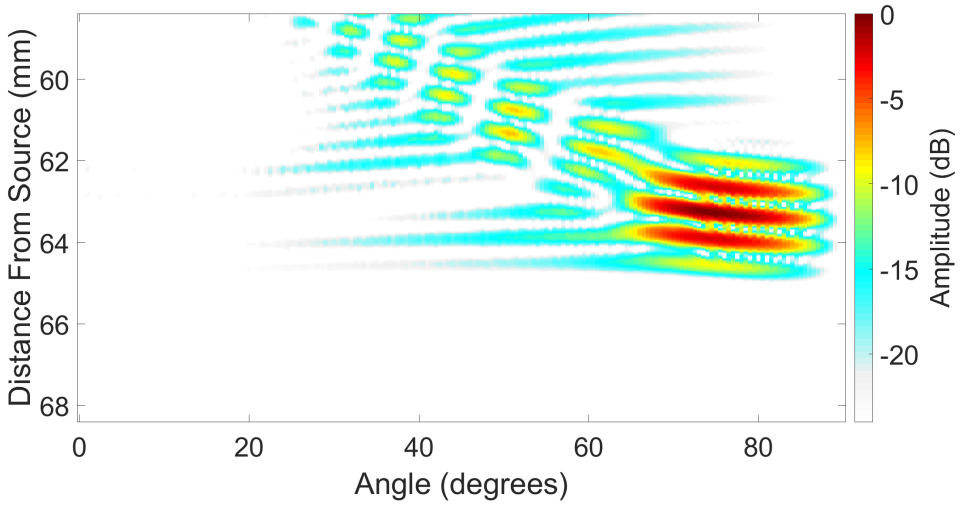
The distance of the virtual source behind the aperture has an effect on the divergence and power of the beam. To investigate this a sub aperture of 31 elements of the transducer chosen for this study was used. Using the CIVA software, a range of different distances of the virtual sources behind the aperture was investigated. Figures 3.1a - 3.1e show the wavefronts produced by different virtual source distances behind the aperture. The wavefront was captured $10\mu s$ after the first element was fired.



(c) Wavefront from a Virtual Source Placed at the Centre of the Array at Quarter Aperture Length Back



(d) Wavefront from a Virtual Source Placed at the Centre of the Array at Eighth Aperture Length Back



(e) Wavefront from a Virtual Source Placed at the Centre of the Array at No Distance Back

Figure 3.1: Figures Showing the Different Virtual Source Distances Behind the Aperture

Figure 3.1a shows the wavefront of the virtual source located at a perpendicular distance the size of the aperture away from the transducer. The figure shows distance from the virtual source location with angle from the vector perpendicular to the surface of the array. Figure 3.1b shows the beam produced at half aperture, Figure 3.1c at quarter aperture and Figure 3.1d at an eighth of the aperture length. Figure 3.1e is located on the array. The opening angle of each source is 27^o, 45^o, 63^o, 76^o and 90^o respectively. The opening angle is given by the $tan^{-1}(a/2z_v)$, where a is the aperture size and z_v is the distance of the virtual source behind the aperture. Each figure is normalised to the highest amplitude value of its wavefront.

The results show that the shape of wavefront produced by the virtual source is spherically divergent in the 2D plane as is expected from a point source, within the opening angle determined by the distance of the virtual source behind the aperture. The amplitude of the wavefront is strongly dependent on the angle from the perpendicular. The wavefronts generated by a source close to the aperture, or larger opening angle, covers a wider range of angles than the sources further away. This is due to the ratio of the

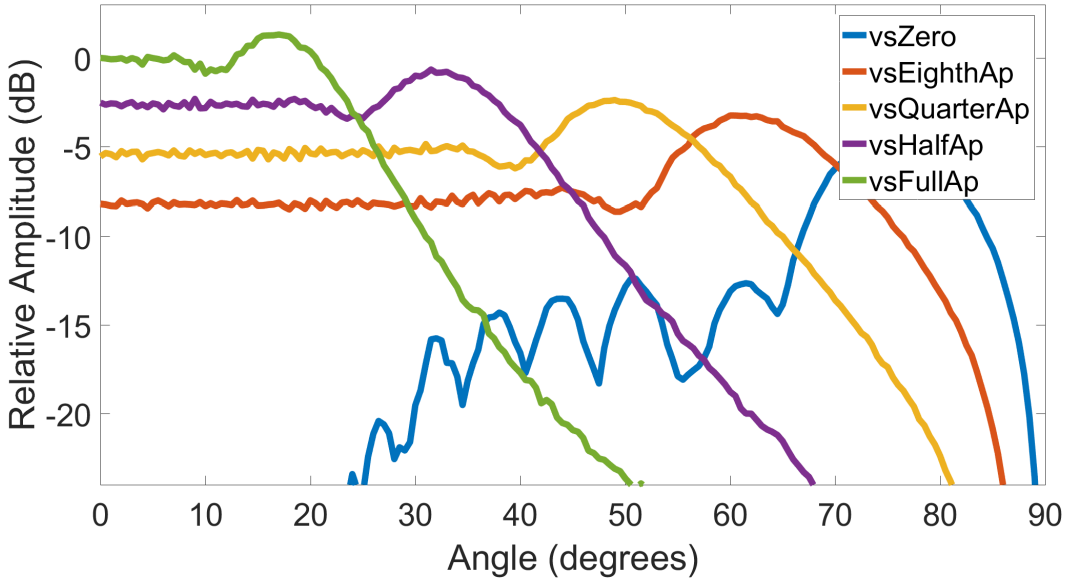


Figure 3.2: Amplitude of a Virtual Source Wavefront for Different Distances of the Source Behind the Aperture

aperture size relative to the distance of the source behind the aperture. For angles outside of the opening angle the shape and amplitude of the beam deteriorates rapidly.

It can also be seen, for every source, that at angles closer to the opening angles side lobes are generated. The side lobes increase the amplitude of the beam at this point and changes the shape slightly. The change of shape is only minor and therefore has negligible effect on the final image compared to other sources of error.

Figure 3.2 shows the maximum amplitude of the wavefront with angle for every opening angle of the probe. Each wavefront has been normalised to the wavefront with the highest amplitude. It can be seen that the wavefronts produced by the narrower opening angles have a higher relative amplitude to the other wavefronts. This is because the wave is less divergent and the power of the beam has been spread over a narrower range of angles.

It can be seen in 3.2 that for a wider opening angle, the difference between the side lobe amplitude and the main beam is greater. The side

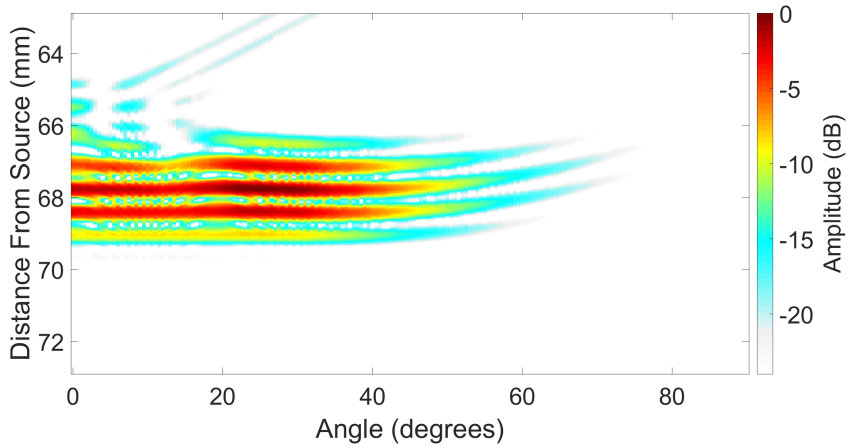
lobe is unavoidable as it occurs on every wavefront, however the effect is lessened by a narrower opening angle. It is possible to reduce the effect of the side lobe by applying a weighting function to the array elements [13], however this has been shown to reduce the divergence of the beam and is ignored in this work.

It can be seen in both Figure 3.1e and Figure 3.2 that there exists a limit to the opening angle of the virtual source as the wavefront fails to form properly for an opening angle of 90^o. This occurs when the opening angle is placed directly on the transducer. However this is a limitation for any technique as the transducer cannot physically steer sound at an angle of 90^o to the surface for a transducer in direct contact with the testing sample.

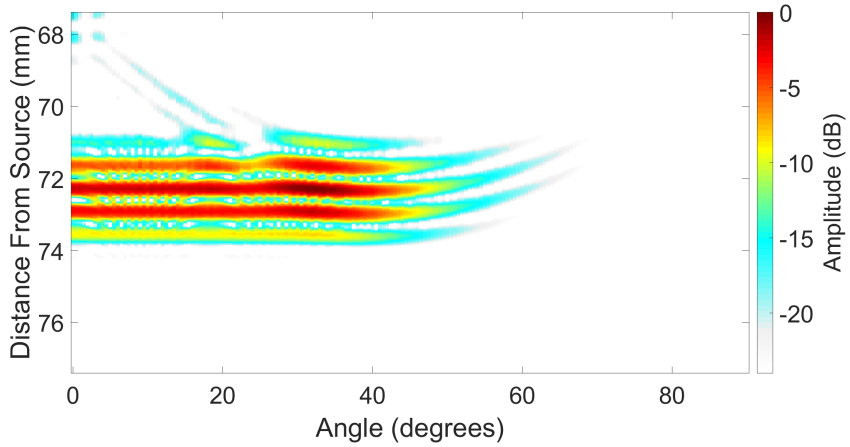
Number of Array Elements in the Sub Aperture

The number of elements used for the sub aperture may affect the shape of the wavefront and the images generated from the VSA algorithm. Figures 3.3a, 3.3b and 3.3c show the wavefront amplitude for virtual sources positioned in the centre of the array at a distance of half the aperture size back from the array. The wavefronts were taken $10\mu s$ after the first element was fired. It can be seen that the shape of the wavefront is more uniform using a higher number of elements, however the difference is negligible as it is much less than a wavelength, and is therefore unlikely to affect the imaging algorithm.

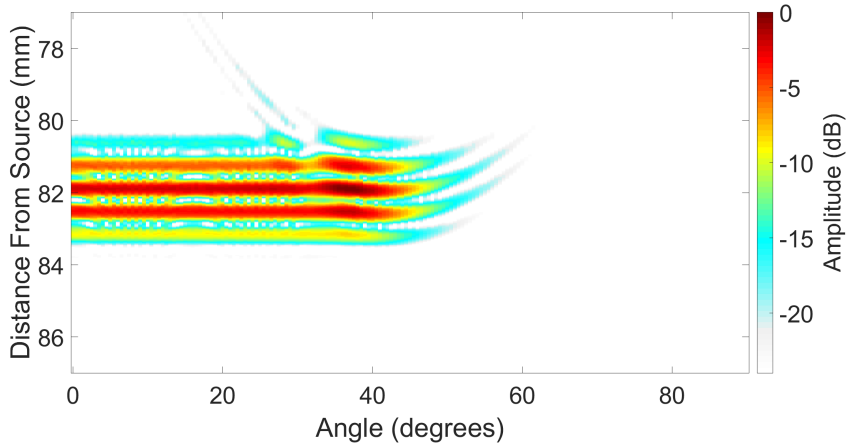
Figure 3.4 shows the relative amplitudes of the wavefronts produced by sub apertures with a different number of elements. The larger number of elements produces a more uniform amplitude across the entire wavefront. Using fewer elements narrows the wavefront and pulls in the side lobes. Although the delay laws calculated seem to generate a wavefront with an opening angle of 45^o, the number of elements has an impact on the



(a) Depicting the wavefront generated by a virtual source at half aperture using 16 elements.



(b) Depicting the wavefront generated by a virtual source at half aperture using 32 elements.



(c) Depicting the wavefront generated by a virtual source at half aperture using 64 elements.

Figure 3.3: Virtual Source Wavefronts from Sub Apertured Containing Different Number of Elements

wavefront, and only when using a large number of elements is the opening angle close to what is expected from the calculated delay laws.

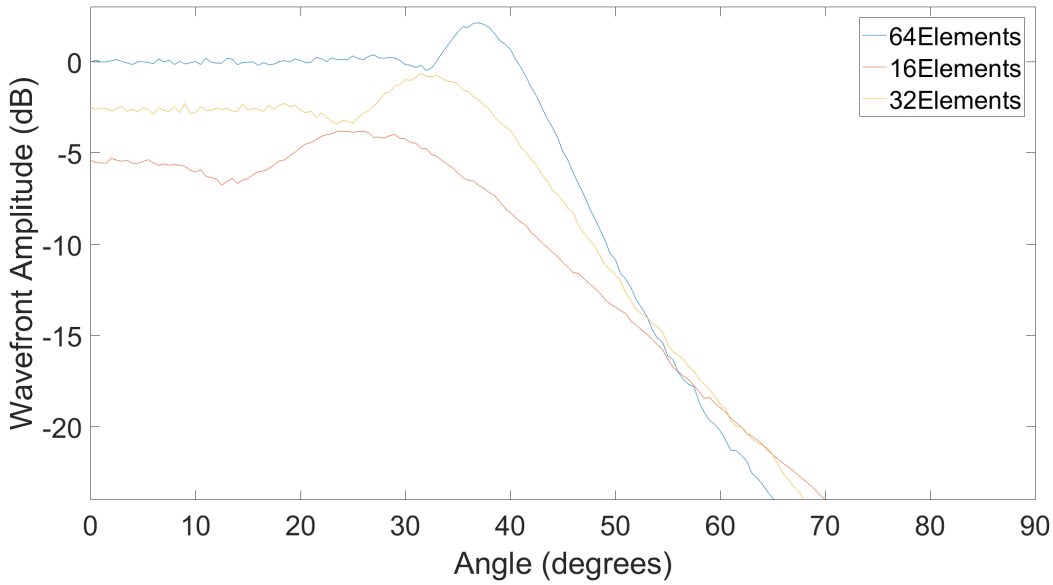


Figure 3.4: Depicting the wavefront generated by a virtual source at half aperture using 16 elements.

Although the amplitude varies with angle for a smaller number of elements in the sub aperture, the shape of the wavefront is circular as expected from a point source. Therefore the wavefront can still be used for an inspection. The VSA inspections in this study use different size sub apertures in order to see if the varying amplitude for the smaller number of elements has a significant impact on resulting images.

Parameters Used

The parameters selected for this study can be seen in Table 3.1. The sub aperture size is the number of elements used for each transmission. The sub aperture increment is the number of elements incremented across the array after each firing. For example, if a 64 element array is used, with the sub aperture size of 32 and the sub aperture increment of 8, then the element groups used on transmission are: [1-32], [9-40], [17-48], [25-56] and [33-64].

This gives a total of 5 transmissions. All array elements receive with each transmission.

Number Array Elements	Number Transmissions	Sub Aperture Size	Sub Aperture Increment
64	1	64	N/A
64	3	32	16
64	5	32	8
64	9	32	4
64	5	16	8
64	9	16	4

Table 3.1: Showing the VSA parameters used for the study.

An opening angle of 45^o was chosen for each inspection as in [13]. This was deemed to give sufficient coverage of the region of interest.

3.2.3 PWI Setup

An inspection with PWI typically uses all array elements on transmission. This is because there is no benefit of using fewer elements due to the nature of the wavefront formed. Therefore, only the number of transmissions and range of angles are required. In order to have a fair comparison, the number of firings has been selected to be the same as the VSA inspections. The range of angles covered is set to be the same as the opening angle of the virtual source, therefore the angle range has been selected to be $-45^o \rightarrow 45^o$, with equal angle increments depending on the number of firings.

The parameters used for the PWI are shown in Table 3.2. For example, if a given inspection has an angle range of $-45^o \rightarrow 45$ and the angle increment is 22.5, the transmission angles used are $-45^o, -22.5^o, 0^o, 22.5^o, 45^o$. If a single transmission is used then the steered angle is the average of the angle range limits.

Number Array Elements	Number Transmissions	Angle Range	Angle Increment
64	1	$-45^o \rightarrow 45^o$	N/A
64	3	$-45^o \rightarrow 45^o$	45^o
64	5	$-45^o \rightarrow 45^o$	22.5^o
64	9	$-45^o \rightarrow 45^o$	11.25^o

Table 3.2: Showing the PWI parameters used for the study.

3.3 Results

3.3.1 Signal to Noise Ratio

Initially an experimental test was run on a single SDH located at the centre of the array at a depth of 14mm to find the relative SNR for each technique. The SNR for each technique was calculated by taking the peak intensity value of this SDH, and the average intensity value of an image where the transducer was located above a region that did not contain any reflectors. The SNR was calculated using Equation 3.1.

$$SNR = 20 * log_{10}\left(\frac{A_{sdh}}{\bar{A}_n}\right) \tag{3.1}$$

Here, A_{sdh} is the peak intensity of the side drilled hole indication and $\bar{A}_n$ is the average intensity of the background noise. Table 3.3 shows the results for each technique.

The TWI Crystal software was utilised for this task. The hard gain for each technique was set such that the peak amplitude of all the signals from the reference signal was set at 80% of screen height. The results can be seen in Table 3.3.

Then a series of SDHs were inspected to investigate the performance of the techniques, the remaining results were simulated using the CIVA software. It was assumed that the intensity variation of the TFM image for the simulated results would correspond the experimental values, and that

Technique	Number Elements, Transmissions	Gain (dB)	SNR (dB)
FMC (Full Matrix)	64, 64	40	61
FMC (Half Matrix)	64, 64	40	61
PWI	64, 1	23	56
PWI	64, 3	23	43
PWI	64, 5	23	51
PWI	64, 9	23	52
VSA	64, 1	27	47
VSA	32, 3	28	55
VSA	32, 5	28	57
VSA	32, 9	28	59
VSA	16, 5	30	56
VSA	16, 9	28	57

Table 3.3: Table Showing the FMC, VSA, and PWI set up for the comparison, and displaying the SNR of a SDH using this technique.

the SNR of each simulated SDH could be calculated by measuring the intensity of each SDH relative to the simulated SDH at the position where the experimental data was taken. The holes were laid out in a square lattice with a spacing of 4mm. Each hole was simulated and processed separately in order to avoid interfering signals. The resulting images combine all the holes by taking the maximum intensity of indication at the given location. The intensity plots for FMC can be seen in Figure 3.5, VSA in Figure 3.7 and PWI in Figure 3.5.

It can be seen in Table 3.3 that FMC gives the highest SNR of the three techniques, the VSA and PWI giving the lowest SNR. Because the wavefront from a virtual source is divergent, it is more likely that sound from every transmission will insonify the entire region of interest. Therefore each transmission will contribute to an indication regardless of the position of the reflector. Therefore the indication will have a high intensity value. A planar wave insonifies a narrow corridor, therefore it is likely certain transmissions will not insonify a given reflector, therefore fewer transmissions will contribute to a given indication, reducing the intensity of the indication. However as the wavefront is less divergent than

a virtual source, the amplitude a reflector response on any given individual Ascan is greater for a plane wave, leading to a high intensity value. Another issue that is likely to occur using PWI is a poor distribution of sound across the region of interest, as certain regions will be subject to overlapping wavefronts, increasing the intensity of an indication relative to an area where there are fewer overlapping wavefronts. By comparison, VSA has a relatively uniform distribution of sound, as can be seen in Figures 3.5, 3.6 and 3.7. For formatting reasons, these figures are located at the end of the chapter.

3.3.2 Indication Intensity Map

The SDH indications were used to plot a sensitivity map for each of the chosen inspections. This indicates the sensitivity of the imaging technique to a generic reflector at different positions. The images generated can be seen in Figures 3.5a to 3.6d. The intensity of all figures is measured in dB and have been normalised to the side drilled hole value at 2mm from the centre of the array at a depth of 12mm. The background noise was set at the levels calculated in the previous section, however most of the indications proved to be above the noise level.

It can be seen in Figures 3.5a and 3.5b that the shape of the intensity map for the FMC full and half matrix approaches are almost exactly the same as expected. This indicates that half of the data is negligible due to the symmetry of transmit-receive pairs.

Figures 3.7a and 3.6a show the single transmission cases for VSA and PWI respectively. It can be seen that the singular virtual source covers a wider area than the single plane wave transmission. This is because the virtual source wavefront is divergent, and the indication intensity drops with a greater distance as the energy is spread out over a larger area. The

planar wavefront however confines the energy into a narrow corridor of sound and the intensity of the planar wave is more consistent with depth because of this. Reflectors outside this corridor may be missed and care must be taken in the set up to ensure that suitable inspection angles are chosen to properly insonify the region of interest. It must be noted that the signal to noise ratio of the singular virtual source is much less than the singular plane wave, with the plane wave 9dB higher.

Figures 3.7b and 3.6b shows the intensity maps using three transmissions for VSA and PWI respectively. It can be seen that the indication intensity at a shallow depth directly beneath the probe is similar. However, the VSA inspection covers a wide range of angles with the intensity decreasing with distance from the probe. Each transmission sends out a divergent beam so that it is likely that a reflector will be insonified with every transmission of the VSA inspection, such that most Ascans in the TFM image will contribute to an indication, leading to a higher intensity value. This causes the SNR to increase and is now comparable to the singular plane wave transmission. The large increment angle between each of the plane wave transmissions causes significant blind spots, as large regions of the material are not insonified by sound at all. The signal to noise ratio has also decreased significantly.

Figures 3.7c and 3.7d show the VSA intensity maps using 5 transmissions with a sub aperture of 32 and 16 elements respectively. There is little difference in the sensitivity map produced by these techniques with little difference in the SNR. Figure 3.6c shows the plane wave intensity map using 5 transmissions. The intensity profiles for the VSA and PWI inspections are comparable, the lower increment angle has had the effect of filling the blind spots that existed for the 3 transmissions, however the beam profile is not yet completely uniform with angle.

Figures 3.7e and 3.7f show the VSA intensity map using 9 transmissions with sub apertures of 32 and 16 elements respectively. Again, there is little difference in the sensitivity map and SNR. Figure 3.6d shows the PWI intensity map using 9 transmissions. The intensity profile is uniform with angle, as the difference in transmission angle is small enough to sufficiently cover the entire region.

3.3.3 Array Performance Indicator (API)

The API is a method of determining how tightly focussed the indication is [10, 65]. The API is given by:

$$API = \frac{A_{6dB}}{\lambda^2} \tag{3.2}$$

Here, A_{6dB} is the area of the indication that is within 6dB of the peak intensity and λ is the wavelength of sound in the inspected component.

This section investigates the API of the FMC, PWI and VSA imaging techniques. The API values of each indication is likely to vary across the region relative to the array. The amplitude of the wave at the measured position is also likely to have an impact. The amplitude of the wave can depend on a great number of factors such as, distance from the array, angle of the measured position from the transducer surface, the shape and divergence of the beam from the technique used. The amount of overlap at the measured position between the separate transmissions, and the respective angles of the incident wavefront, is also likely to have a significant effect on the API. In this section we aim to achieve a general overview of how the different imaging techniques perform with measured API values. The same imaging techniques and SDH reflectors as the previous section were used. The API of each SDH indication was taken

and plotted at its respective position, resulting in a map of the API across the imaging region. The results can be seen in Figures 3.8, 3.9 and 3.10.

It can be seen that there is little difference in the API of the FMC half and full matrix data acquisition, the results of which can be seen in Figures 3.8a and 3.8b. This is because the extra data used in the full matrix is symmetric to the data used in the half matrix. Although the inspected area is insonified by almost twice the amount of sound using the full matrix, the range of angles covered is the same. Therefore, this does not improve the imaging resolution.

The API data shown in Figures 3.9 and 3.10 was plotted at three different depths for a range of angles relative to the centre of the array. The data could be visualised easier this way. The PWI and VSA API values at a depth of 20mm can be seen in Figures 3.11 and 3.12, at a depth of 40mm in Figures 3.13 and 3.14 and at 60mm in Figures 3.15 and 3.16. In each image the FMC half matrix is included for reference.

It can be seen that at a low depth (20mm), the API for PWI is similar to that of FMC and actually maintains a more stable value across the entire range of angles compared to the FMC. This region is close to the array such that the planar wavefronts overlap, each contributing to the indication resulting in a high API value across the region. The optimum number of transmissions is 3 (-45^o, 0^o and 45^o), as this results in the highest API value across the region. This could be due to the large difference in the incident angle of the different transmissions causing the indications to be more sharply focussed than when more transmissions are added. By comparison it can be seen that the VSA results are lower than the PWI in this region. The optimum VSA set up for this region is with the smaller sub aperture and 5 transmissions, this could also indicate that a larger difference in incident angles could have a positive effect on the API.

At 40mm deep, shown in Figures 3.13 and 3.14 for PWI and VSA respectively, the API is lower for all techniques. Here, we begin to see less uniformity in API across the range of angles in the PWI set up. This is because the discrete transmission angles of the steered wavefronts cause variations between the total intensity of sound that covers a given position, causing large fluctuations in the SNR and the API of the indications. This effect is most notable in Figures 3.6b and 3.9b for three plane wave transmissions. A greater number of transmissions lessens this effect, and it can be seen that at 40mm, nine transmissions seems sufficient to cover the entire region with a uniform distribution of energy across all angles. In contrast, the VSA API is uniform across all angles for all number of transmissions, however these are slightly lower than the PWI.

The results for a depth of 60mm are similar to the 40mm depth. These can be seen in Figures 3.15 and 3.16 for PWI and VSA respectively. The PWI tends to higher, but less uniformly distributed across all angles than the VSA.

The results suggest that PWI is likely to give a higher API compared to VSA and FMC providing that the number of transmissions is enough to give sufficient angular coverage. However VSA gives a slightly more uniform distribution of API. This is because divergent wavefronts are generated, and all transmissions are likely to contribute to all indications across the region of interest.

3.3.4 Inspection Rate

The inspection rate was calculated using the TWI Crystal software. The software utilises graphics cards as described in [4] to enhance the efficiency of the TFM algorithm. The region of interest used contained 102400 pixels. A 50MHz sampling frequency was used and the signal time gates were

calculated corresponding to the maximum and minimum time of flight calculations in the TFM algorithm. The results are given in Table 3.4.

Technique	Number Elements, Transmissions	Inspection Rate (F s^{-1})
FMC (Full Matrix)	64, 64	9
FMC (Half Matrix)	64, 64	18
PWI	64, 1	250
PWI	64, 3	150
PWI	64, 5	100
PWI	64, 9	60
VSA	64, 1	250
VSA	32, 3	150
VSA	32, 5	100
VSA	32, 9	60
VSA	16, 5	100
VSA	16, 9	60

Table 3.4: Showing the inspections speeds of the different modes considered.

It can be seen from the results in Table 3.4 that the FMC techniques proved to be the slowest due to the large number of transmissions. The inspection rates for PWI and VSA proved to be the same for the same number of transmissions, all significantly faster than the FMC techniques.

There exists an inverse relationship between the number of transmissions and the frame rate of the inspection for most inspections. One exception is the FMC half matrix, where the frame rate is double that of the full matrix as half of the amount of data is captured and processed. Other exceptions are for the lowest number of transmissions. If an inverse relationship between the number of transmissions and the speed held true, one would expect the frame rate of the single transmission to be faster than the FMC full matrix by a factor of 64, giving a frame rate in the region of $550ms^{-1}$. However the difference is only a factor of 25. This suggests that there are other limiting factors that may affect the frame rate caused from the implementation. These factors may be negligible for a large number of transmissions, when the time taken to generate the image is the

dominating factor that affects the frame rate. However for a lower number of transmissions, these factors may have a larger relative impact on the algorithm.

3.4 Conclusion

In this chapter a comparative study between the imaging techniques FMC, VSA and PWI has been conducted. These techniques were studied for a particular case in which the transducer was in direct contact with the inspected component, and a series of side drilled holes were used to investigate the performance of the techniques in different areas relative to the transducer. The set up parameters for each technique and the reasoning behind why the these were chosen was discussed. The performance was evaluated using SNR, API and inspection speed.

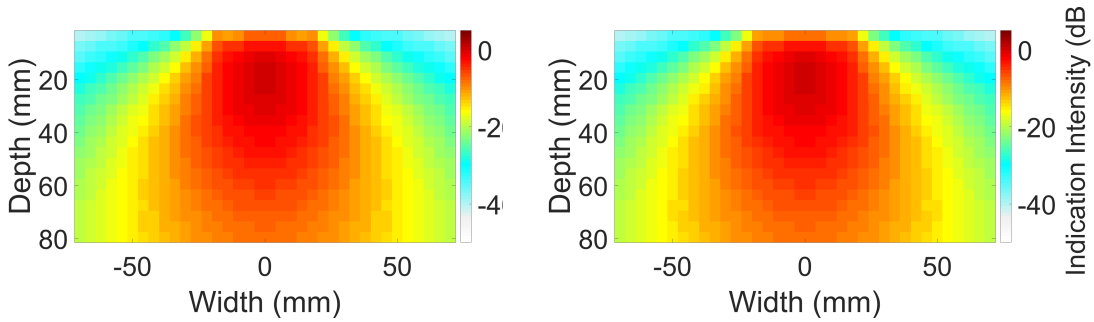
It was shown that FMC gives the highest SNR, followed by VSA and PWI showed the lowest SNR. As the virtual source is divergent, so for any given reflector position it is likely that the position would be insonified by every transmission using VSA. When forming the image, each transmissions would constructively contribute to the indication, giving a strong intensity value for the pixel containing the reflector. A PWI inspection involves sweeping the ultrasonic beam across the entire region of interest. Therefore the entire region of interest may not be infonified with every transmissions. Because of this the intensity value of the indications generally is lower than VSA or FMC, as fewer A-scans contribute to the value. This leads to a lower SNR. For this reason also, the SNR across the entire region is less uniform for a PWI inspection when compared to VSA or FMC as can be seen in Figures 3.5, 3.7 and 3.6.

The API results show that generally FMC gives more tightly focussed indications compared to VSA and most of the PWI set ups. It can be seen

that the API values are consistently lower than the FMC reference, however the PWI results for certain set ups exceed that of FMC. This is because the signal to noise ratio of the underlying Ascans is higher for PWI than the other techniques, as the energy of the sound is confined within a narrow corridor. This positively contributes to the API.

The scanning rates of each technique was estimated. It can be seen that PWI and VSA are vastly faster than FMC, as the frame rate corresponds to the number of transmissions (except for FMC half matrix which roughly corresponds to half the number of transmissions). It can be seen that frame rates of 60-250 fps can be achieved using these techniques.

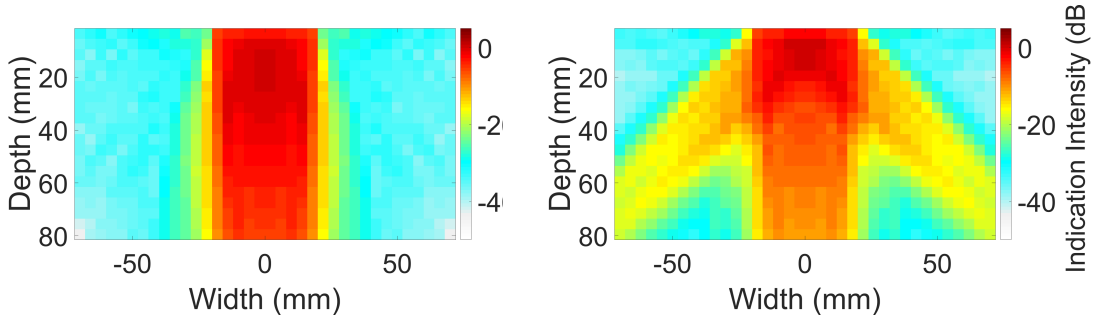
Although PWI shows higher SNR than VSA, the remainder of this thesis will investigate the VSA technique, due to its high SNR and its general uniform intensity across the entire imaging region. This is because generally all transmissions contribute to all indications across the region of interest. Using VSA it is largely unnecessary to ensure that the region is sufficiently covered by sufficient planar wavefront transmissions, and that energy is spread uniformly across the region of interest.



(a) FMC - Half Matrix SDH Intensity Map.

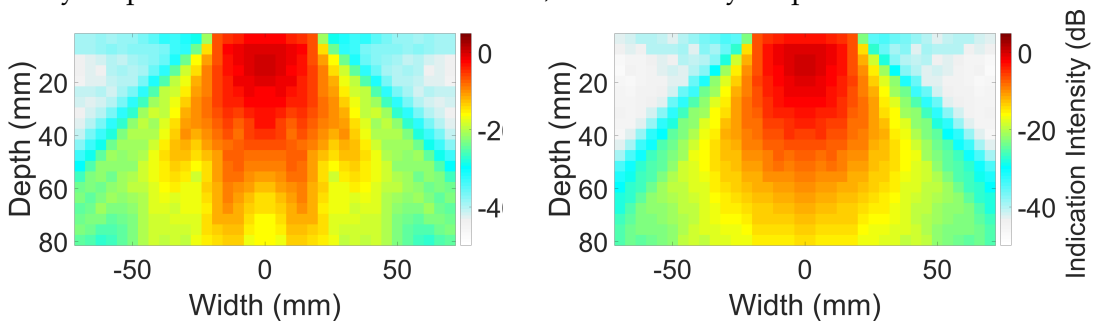
(b) FMC - Full Matrix SDH Intensity Map.

Figure 3.5: Full Matrix Capture Intensity Maps



(a) PWI - 1 Transmission at 0^o, SDH Intensity Map.

(b) PWI - 3 Transmissions at -45^o, 0^o and 45^o, SDH Intensity Map.



(c) PWI - 5 Transmissions at -45^o, -22.5^o, 0^o, 22.5^o, 45^o, SDH Intensity Map.

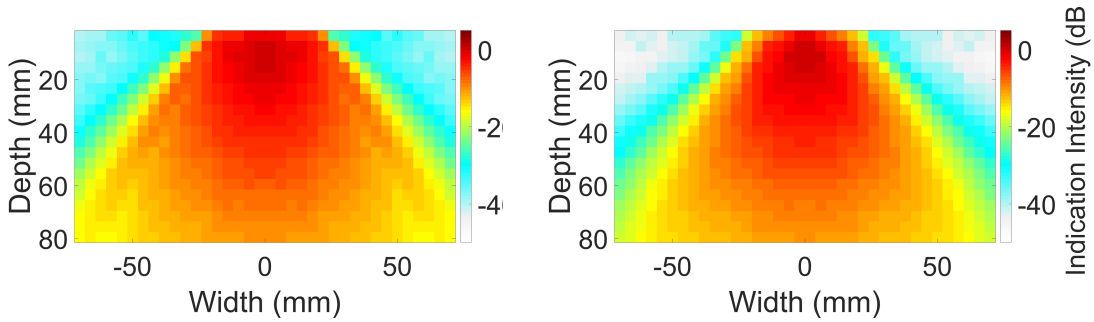
(d) PWI - 9 Transmissions at -45^o, -33.75^o, -22.5^o, 11.25^o, 0^o, 11.25^o, 22.5^o, 33.75^o, 45^o, SDH Intensity Map.

Figure 3.6: Intensity Maps for the PWI Techniques.

3.5 Further Work

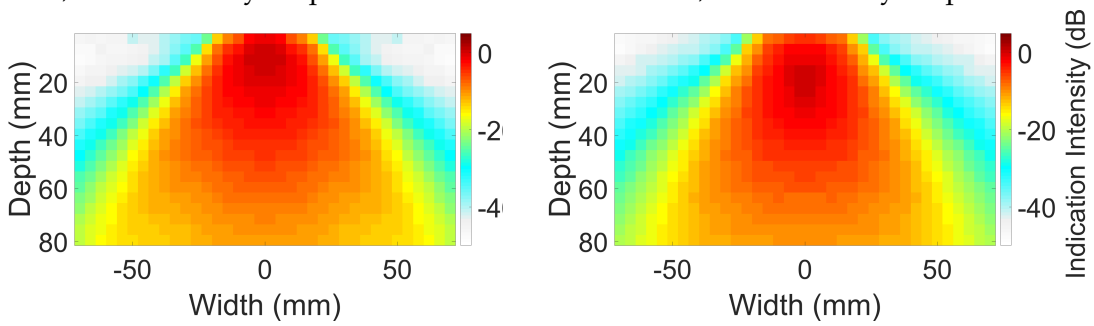
This study has compared FMC, VSA and PWI as ultrasonic imaging techniques. This study has looked at a specific use case, where an array is used in direct contact with a material and generic SDH reflectors were imaged. Further work must be undertaken in order to study the behaviour of these techniques with other reflectors such as planar flaws (fatigue cracks), small amplitude reflectors such as porosity and tip diffracted signals and other reflectors commonly seen in NDT. Perhaps these techniques may differ in their performance at evaluating these reflectors.

The performance of the algorithms especially must be evaluated using two mediums, such as an immersion testing or inspection through a wedge. The PWI may perform better than the other techniques through a wedge where the beam travels greater distances and the angle range



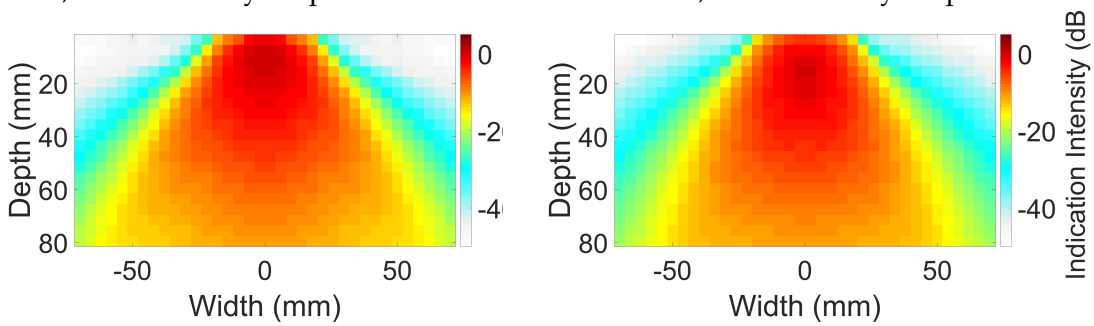
(a) VSA - 64 Elements Aperture, 1 Virtual Sources, SDH Intensity Map.

(b) VSA - 32 Elements Aperture, 3 Virtual Sources, SDH Intensity Map.



(c) VSA - 32 Elements Aperture, 5 Virtual Sources, SDH Intensity Map.

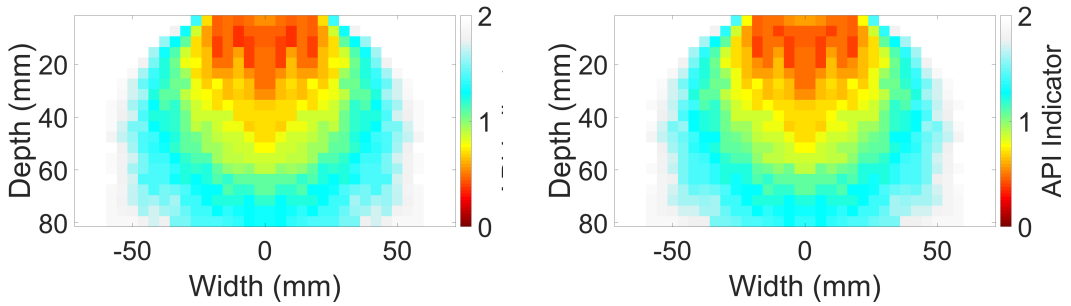
(d) VSA - 16 Elements Aperture, 5 Virtual Sources, SDH Intensity Map.



(e) VSA - 32 Elements Aperture, 9 Virtual Sources, SDH Intensity Map.

(f) VSA - 16 Elements Aperture, 9 Virtual Sources, SDH Intensity Map.

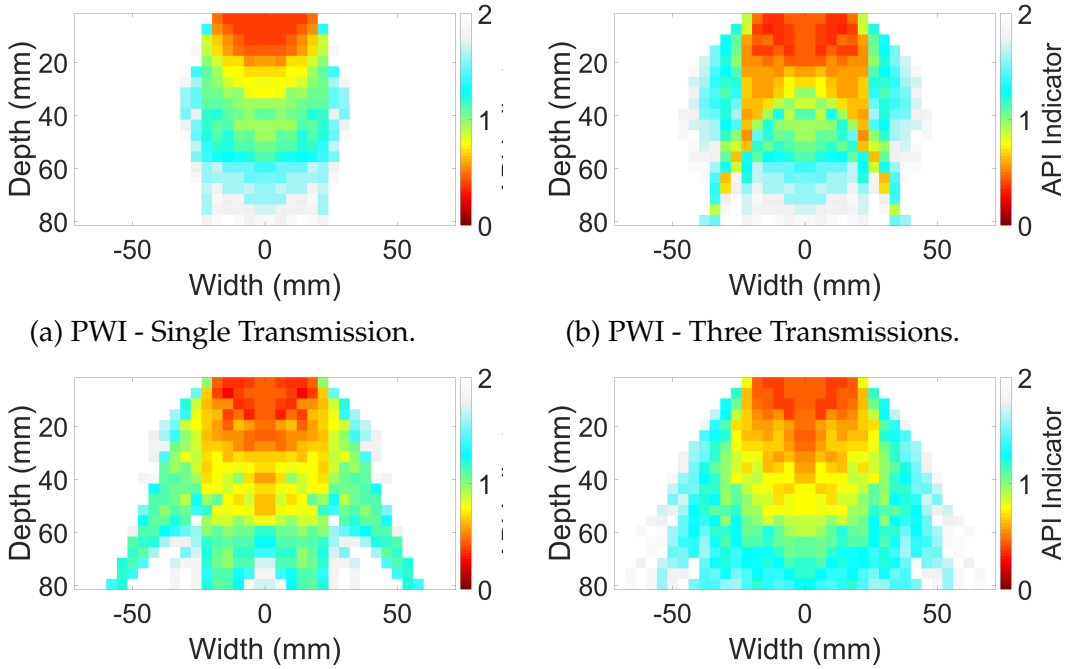
Figure 3.7: Intensity Maps for the VSA Techniques.



(a) FMC - Half Matrix API Indicator Map.

(b) FMC - Full Matrix API Indicator Map.

Figure 3.8: FMC API images.



(a) PWI - Single Transmission.

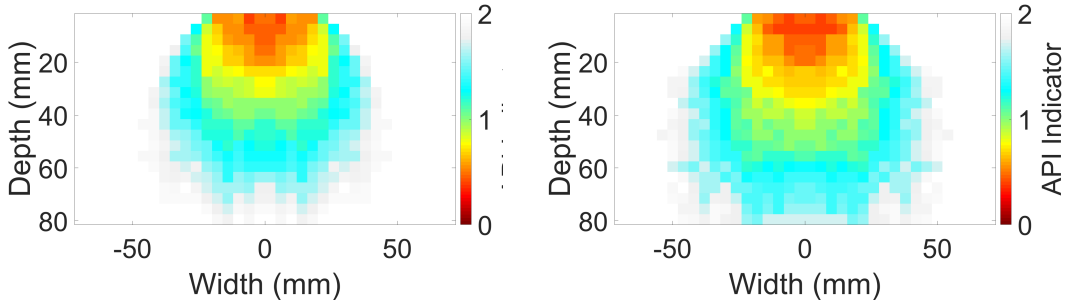
(b) PWI - Three Transmissions.

(c) PWI - Five Transmissions.

(d) PWI - Nine Transmissions.

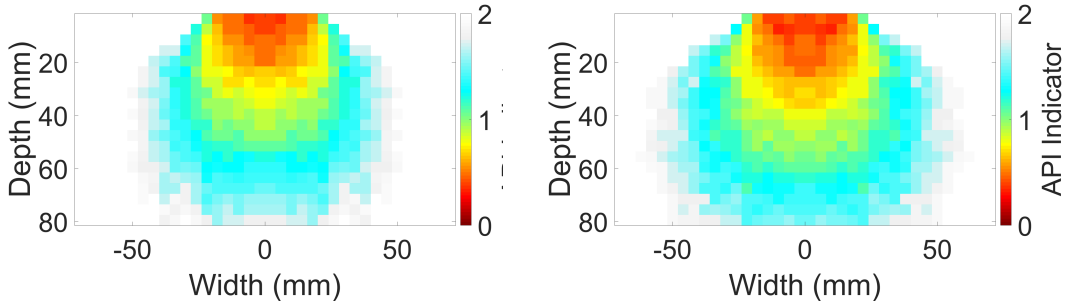
Figure 3.9: PWI API images.

required to insonify the region is smaller. In contrast the divergent wavefronts of the VSA and FMC techniques may be of use when inspecting components with complex geometry through a water path, as the continuous range of emission angles may help avoid blind spots like the ones seen in this study. This may also effect multi-mode imaging [24, 48], where many different wave modes and mode conversions must be considered to effectively study a region of interest.



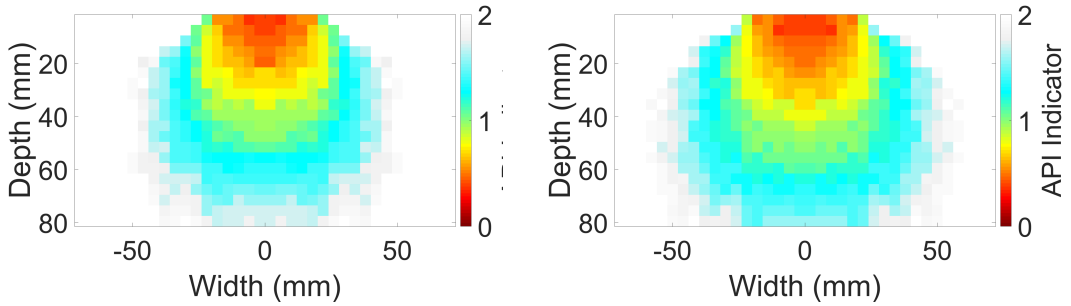
(a) VSA - One Transmission, 64 element aperture.

(b) VSA - Three Transmissions, 32 element sub aperture.



(c) VSA - Five Transmissions, 32 element sub aperture.

(d) VSA - Five Transmissions, 16 element sub aperture.



(e) VSA - Nine Transmissions, 32 element sub aperture.

(f) VSA - Nine Transmissions, 16 element sub aperture.

Figure 3.10: VSA API Images.

The TFM algorithm may be improved eliminating pixels that are outside of the coverage of the insonifying beam, this is likely to benefit the PWI algorithm much more than the FMC and VSA and could change the results of this study. The FMC algorithm could be made faster by using sparse arrays, and the performance of this compared to the VSA and PWI algorithms may be of interest.

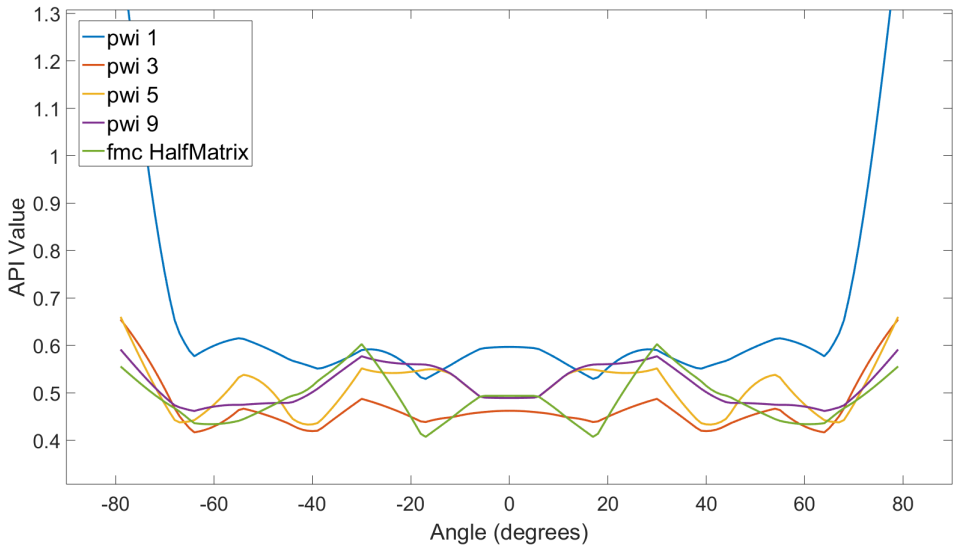


Figure 3.11: API for PWI at a Depth of 20mm

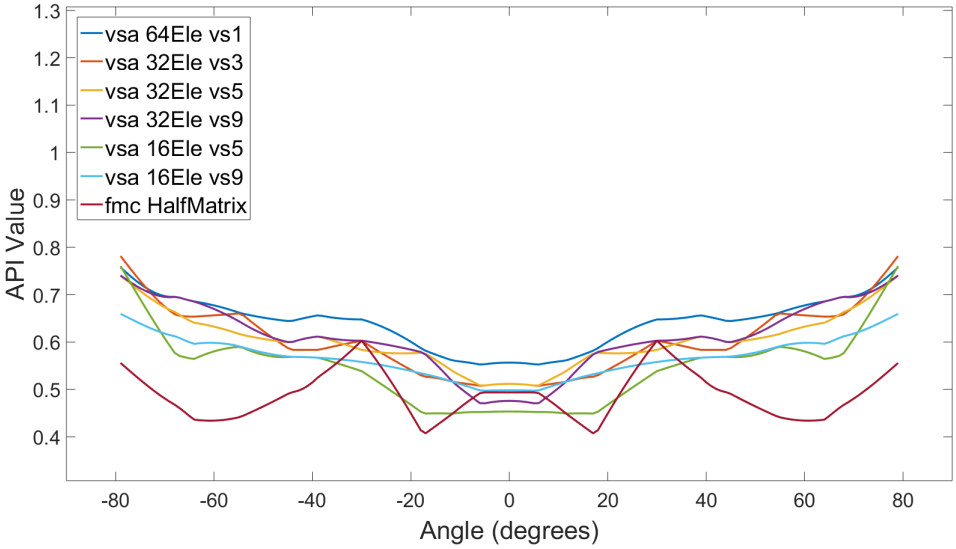


Figure 3.12: API for VSA at a Depth of 20mm

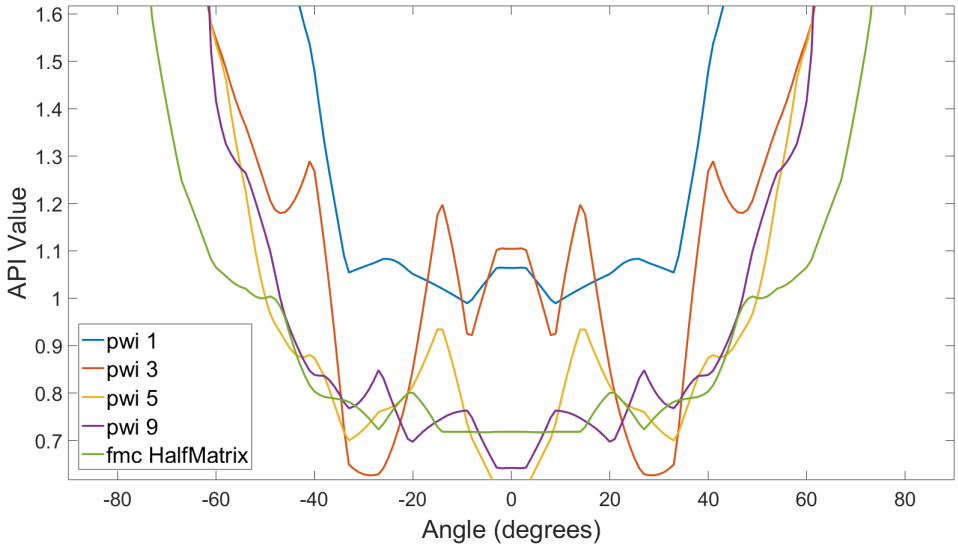


Figure 3.13: API for PWI at a Depth of 40mm

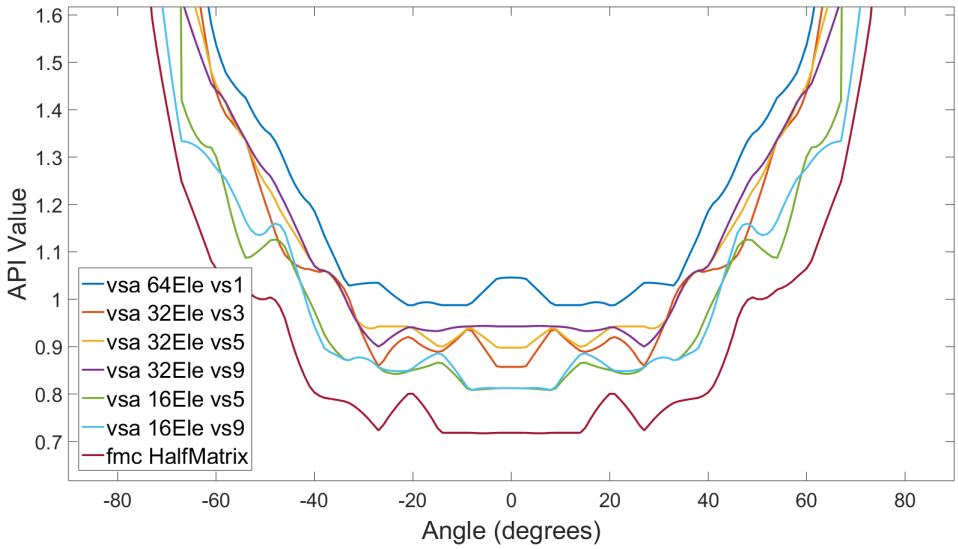


Figure 3.14: API for VSA at a Depth of 40mm

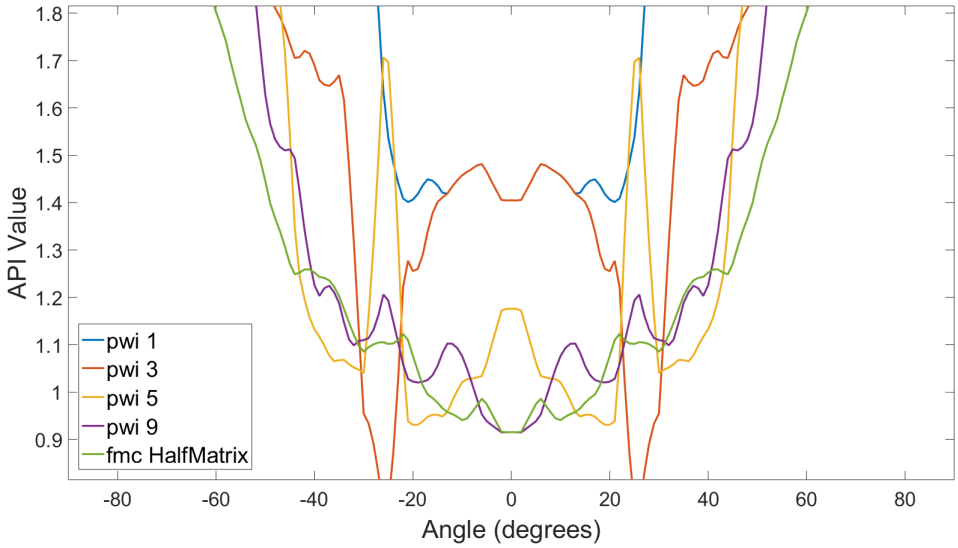


Figure 3.15: API for PWI at a Depth of 60mm

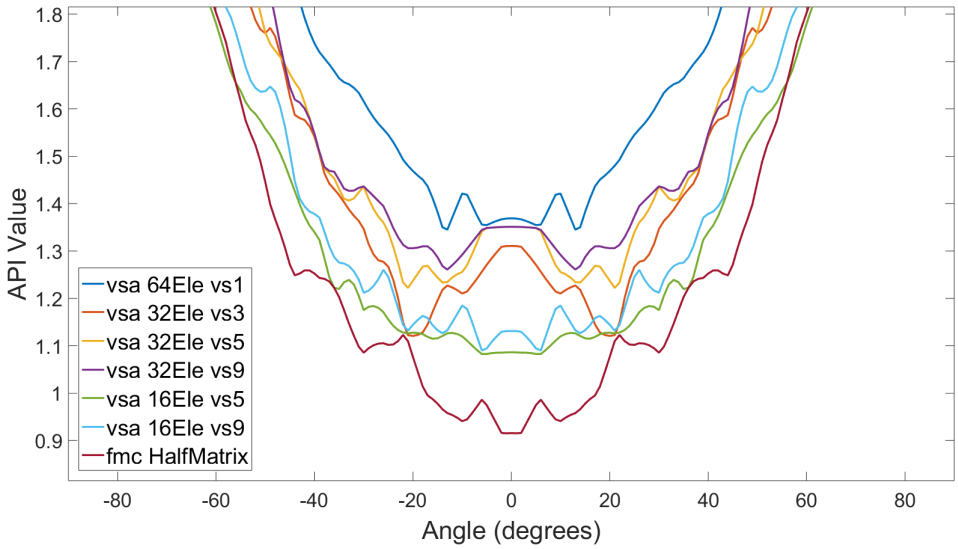


Figure 3.16: API for VSA at a depth of 60mm

Chapter 4

Virtual Source Aperture Algorithms - Time and Frequency Domain

4.1 Introduction

The two most prominent algorithms for generating a fully focussed image using data from a Full Matrix Capture (FMC), Virtual Source Aperture (VSA) or Plane Wave Imaging (PWI) data set exist in the time [10, 13, 12] and frequency [65, 77, 74] domain. The time domain TFM algorithm is a delay and sum approach and is the most commonly used in NDT. The frequency domain imaging algorithm involves multiple dimension Fourier transforms to obtain the spatial frequency components of the signal, then a coordinate transform known as Stolt mapping [63] is performed, finally a two dimensional inverse Fourier transform returns the image. These algorithms are described in Sections 4.2.1 and 4.2.2 of this chapter respectively.

The time domain TFM algorithm was originally developed as an extension to the SAFT algorithm and an alternative to PA in ultrasonic

testing [10]. However the algorithm was restricted due to the large amount of processing that is required to generate an image. The development of parallel processing using graphics cards has proved to significantly increase the inspection speed of the TFM algorithm, making real time TFM imaging a reality [4]. The algorithm is versatile and is able to be adapted to account for refraction when inspecting through multiple mediums [6, 58, 12]. This makes the algorithm particularly useful in Non Destructive Testing (NDT), when immersion inspection or inspection using a wedge is particularly common [35].

The frequency domain imaging technique was originally developed for terrain mapping using radar and sonar. The Synthetic Aperture Radar (SAR) or Synthetic Aperture Sonar (SAS) techniques [62, 73], used to map land terrain and the ocean floor, requires a single movable transmitter and receiver of waves. As the time signal is split up into each of the spatial frequencies that are considered separately, the frequency domain algorithm can lead to higher signal to noise ratios (SNR) [64] than the time domain equivalent. This frequency domain algorithm has since been adapted to NDT [71, 72] for direct contact inspection of components, using single elements to transmit and receive sound. Hunter *et al* [65] progressed this, by adapting the algorithm to account for the sound source and receiver to be at different locations. This is done using a coordinate transform known as Stolt mapping [63], originating from similar algorithms in geophysics. Due to the mathematical complexity of the frequency domain algorithm, there exist is difficulties when attempting to implement through multiple mediums, however progress is being made [68, 78].

In this chapter, the FMC frequency domain algorithm, presented in [65], is developed so that virtual sources may be used on transmission. Both frequency and time domain algorithms are used to process the same data

in order to evaluate their performance. Performance is measured using the 'array performance indicator' presented in [10].

4.2 Virtual Source Aperture

A virtual source can be generated by applying a delay to each transmitting element in the ultrasonic array, as seen in Figure 4.1. The time delay for the eth element is given by:

$$t_e = \frac{\sqrt{(v_e - u)^2 + \mathcal{Z}^2} - \mathcal{Z}}{c} \tag{4.1}$$

Here, t_e is the time delay on the eth element, v_e is the horizontal position of the eth element of the array, u is the horizontal distance of the virtual source from the origin and $\mathcal{Z}$ is vertical distance of the source behind the array. c is the velocity of sound in the medium.

The focal law is used to generate a virtual source and insonify the region of interest. Each element then receives individually. Either the time domain or the frequency domain VSA algorithm can then be used for imaging.

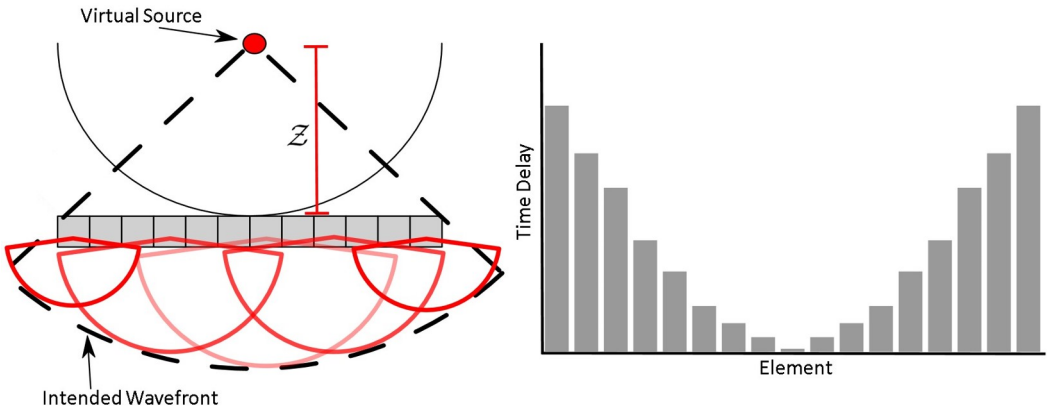


Figure 4.1: Generating a Virtual Source Using an Ultrasonic Array

4.2.1 Time Domain VSA

In the time domain, the well known Total Focussing Method (TFM) is adapted for virtual sources and used for imaging. Equation 4.2 shows the algorithm.

$$\sigma(x,z) = \int_{-\infty}^{\infty}\int E\left(\frac{\sqrt{(x-(u+u_0))^2+(z+\mathcal{Z})^2}+\sqrt{(x-v)^2+z^2}-\mathcal{Z}}{c},\ u,\ v\right)dudv \tag{4.2}$$

Here, $\sigma(x,z)$ is the value of the scatter matrix, which is a measure of the amount of energy that is returned from a position at (x,z). $E(t,u,v)$ is the echo data collected at position v along the horizontal, using a virtual source at position u and a distance $\mathcal{Z}$ behind the aperture, as depicted in Figure 4.2. c is the velocity of the medium. An ultrasonic array samples the sound at discrete points, therefore the integral becomes a summation limited to the number of elements on the array and the number of virtual sources used. The TFM calculates the theoretical time of flight from the transmitting location to the pixel and back using the known velocity of the material. The amplitude of the corresponding time domain signal is then taken and summed for every transmit receive combination. For a region containing a reflector, the time domain signals at the calculated times corresponds to a peak in the amplitude of the signal; when summed these amplitudes constructively interfere and an indication can be seen. The amplitudes from regions that do not contain a reflector destructively interfere therefore an indication can be easily distinguished by a higher intensity value.

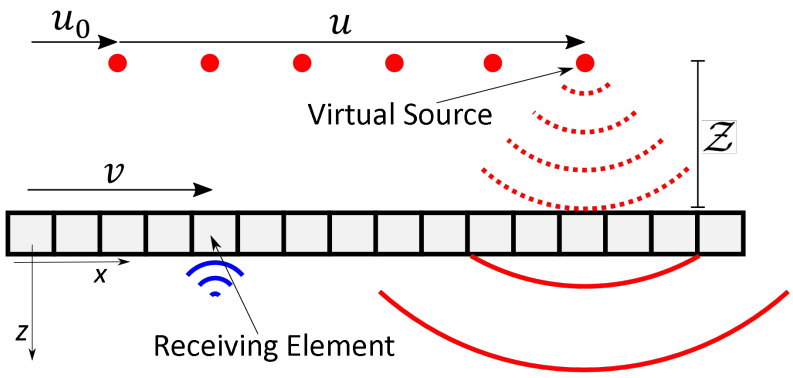


Figure 4.2: Depiction of the transmitting virtual source and receiving element.

4.2.2 Frequency Domain VSA

The advantage of using the frequency domain algorithm is that Fast Fourier Transforms (FFT) are efficiently used to quicken the post processing.

To start, it is assumed that the frequency domain echo data captured by the array, $E(k,u,v)$, can be predicted using a simplified forward propagation model [65], shown in Equation 4.3.

$$E'(k,u,v) = \int_{-\infty}^{\infty}\int \sigma(x,z)\, G(k, x-(u+u_0), z+\mathcal{Z})\, G(k, x-v, z)\, dx\, dz \quad (4.3)$$

Here, $E'(k,u,v)$ is the amplitude of the spatial frequency k, for an element with horizontal displacement v, a virtual source with horizontal displacement u and vertical displacement $\mathcal{Z}$, as shown in Figure 4.2. $E'(k,u,v)$ is obtained by performing a Fourier transform with respect to k on the recorded time domain signal $E(t,u,v)$ as distance and time are interchangeable ($x = ct$). The time domain $\sigma(x,z)$ is the scatter matrix of the region of interest. This is a measure of the amount of energy that is reflected at a position (x,z) due to an acoustic impedance mismatch, e.g. a flaw. It is the scatter matrix that is to be determined at the end of the process.

The imaging algorithm presented in this chapter assumes that data is recorded from the moment the sound leaves the virtual source at $t = 0$. The first element on the transducer is fired at $t = \mathcal{Z}/c$. However to avoid unnecessary firing delays the transducer begins recording data when the first element is fired. It is also sometimes useful to begin recording data sometime after the first element is fired in order to reduce processing later on. These delays must be accounted for in the imaging algorithm and can be done by padding the time domain signal with zeros such that the signal starts at $t = 0$. Alternatively the signal can be migrated in the frequency domain using:

$$E'(k, u, v) = E(k, u, v)\, exp\left(ik(\mathcal{Z} + t_0 c)\right) \tag{4.4}$$

Here, $E'(k, u, v)$ is the corrected signals modified for $t = 0$, $E(k, u, v)$ are the original signals recorded and t_0 is the time between the first element firing and echos being recorded.

Green's function $G(k, x, z)$ is a solution to the wave equation that gives a non zero value at a single point (delta function). It can be used when describing point sources in an acoustic field. The function used here, given in Equation 4.5, is the Green's solution for a 2D plane wave [79].

$$G(k, x, z) = \frac{-i}{4\pi} \int_{-\infty}^{\infty} \frac{exp\Big(ik_x x - i|z|\sqrt{k^2 - k_x^2}\Big)}{\sqrt{k^2 - k_x^2}} dk_x \tag{4.5}$$

This solution describes the frequency component phase shift when back propagating a signal. An assumption is made that the recorded wave is a plane wave, which introduces a small error. However the error diminishes the further away the reflector is from the transducer and is considered to be negligible. Here k is the wavenumber in the direction of propagation and k_x and $\sqrt{k^2 - k_z^2}$ are the directional components of the wavenumber in

the x and z directions. The wavenumber is a measure of how the phase of the wave changes with distance ($k = 2\pi/\lambda$). For a plane wave travelling in a given direction the wavenumber can be split up into the directional components as shown in Equation 4.6.

$$k = \sqrt{k_x^2 + k_z^2} = \sqrt{\left(\frac{2\pi}{\lambda_x}\right)^2 + \left(\frac{2\pi}{\lambda_z}\right)^2} \tag{4.6}$$

Here, k is the wavenumber in the direction of travel, k_x and k_z are the wavenumber components in the x and z direction and λ_x and λ_z are the wavelengths in the x and z direction as shown in Figure 4.3.

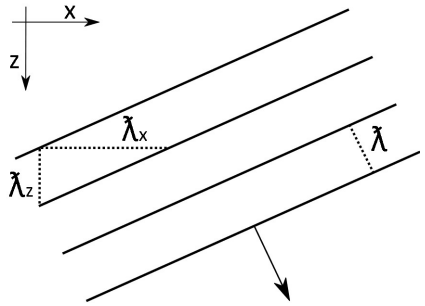


Figure 4.3: Depiction of the wavelength of a planar wave in the direction of propagation and the vertical and horizontal direction.

Substituting the Green's solution and Equation 4.4 into the forward propagation model we get:

$$\begin{aligned} E(k,u,v)\, exp\left(ik(\mathcal{Z}+t_0c)\right) = \\ \frac{1}{16\pi^2}\int_{-\infty}^{\infty}\int\sigma(x,z)\int_{-\infty}^{\infty}\frac{exp\big(\, ik_u(x-(u+u_0)) - i\sqrt{k^2-k_u^2}(z+\mathcal{Z})\,\big)}{\sqrt{k^2-k_u^2}} \\ \int_{-\infty}^{\infty}\frac{exp\big(\, ik_v(x-v) - i\sqrt{k^2-k_v^2}\,z\,\big)}{\sqrt{k^2-k_v^2}}\, dk_u dk_v dx dz \end{aligned} \tag{4.7}$$

Rearranging Equation 4.7 leads to:

$$E(k,u,v)\ exp\left(ik(\mathcal{Z}+t_0c)\right) = \int_{-\infty}^{\infty}\int exp(-ik_u u - ik_v v)$$
$$\left[\int_{-\infty}^{\infty}\int \frac{\sigma(x,z)\ exp\left(i(k_u+k_v)x - i(\sqrt{k^2-k_u^2}+\sqrt{k^2-k_v^2})\ z\right)}{16\pi^2\sqrt{k^2-k_u^2}\sqrt{k^2-k_v^2}}\right. \tag{4.8}$$
$$\left.\exp\left(i\sqrt{k^2-k_u^2}\ \mathcal{Z} - ik_u u_0 - ik(\mathcal{Z}+t_0c)\right) dxdz\right] dk_u dk_v$$

Then the 2D Fourier transform of both sides with respect to u and v is taken. This gives the data in terms of the spatial frequencies k_u and k_v: $FT(E(k,u,v)) \Rightarrow \bar{E}(k,k_u,k_v)$. The right hand of Equation 4.8 is the inverse Fourier transform of the term in square brackets. When the Fourier transform is performed on it only the term in square brackets remains. This results in:

$$E(k,k_u,k_v) = \left[\int_{-\infty}^{\infty}\int \frac{\sigma(x,z)\ exp\left(i(k_u+k_v)x - i\left(\sqrt{k^2-k_u^2}+\sqrt{k^2-k_v^2}\right)\ z\right)}{16\pi^2\sqrt{k^2-k_u^2}\sqrt{k^2-k_v^2})}\right.$$
$$\left. exp\left(i\sqrt{k^2-k_u^2}\ \mathcal{Z} - ik_u u_0 - ik(\mathcal{Z}+t_0c)\right)\ dxdz\right] \tag{4.9}$$

Rearranging we get:

$$16\pi^2\sqrt{k^2-k_u^2}\sqrt{k^2-k_v^2}\ E(k,k_u,k_v)\ exp\left(i(k-\sqrt{k^2-k_u^2})\mathcal{Z} + ik_u u_0 + ikt_0c\right) =$$
$$\left[\int_{-\infty}^{\infty}\int \sigma(x,z)\ exp\left(i(k_u+k_v)x - i\left(\sqrt{k^2-k_u^2}+\sqrt{k^2-k_v^2}\right)\ z\right)\ dxdz\right] \tag{4.10}$$

Define:

$$\begin{aligned}\xi(k, k_u, k_v) = 16\pi^2\sqrt{k^2 - k_u^2}\sqrt{k^2 - k_v^2}\; E(k, k_u, k_v) \\ exp\left(i(k - \sqrt{k^2 - k_u^2})\mathcal{Z} + ik_u u_0 + ikt_0 c\right)\end{aligned} \tag{4.11}$$

It can be seen that the right hand of Equation 4.10 is equal to the Fourier transform of the scatter matrix $\bar{\sigma}$ in terms of the wavenumber k_u and k_v. Therefore:

$$\bar{\sigma}(k_x, k_z) = \xi(k, k_u, k_v) \tag{4.12}$$

Where:

$$k_x = k_u + k_v \tag{4.13a}$$

$$k_z = \sqrt{k^2 - k_u^2} + \sqrt{k^2 - k_v^2} \tag{4.13b}$$

Equation 4.13a gives the total spatial frequency in the horizontal direction and likewise, Equation 4.13b gives the total spatial frequency in the vertical direction. The functions on the left and right hand side of Equation 4.12, $\bar{\sigma}(k_x, k_z)$ and $\xi(k, k_u, k_v)$ respectively, have different coordinates. A coordinate transform, known as Stolt Mapping [63], must be performed on $\bar{E}(k, k_u, k_v)$ in order to progress.

By rearranging using Equations 4.13a and 4.13b and making k_v and k respectively the subjects, we get:

$$k_v = k_x - k_u \tag{4.14a}$$

$$k = \pm\frac{\sqrt{k_z^4 + 2(k_u^2 + (k_x - k_u)^2)k_z^2 + k_u^4 + (k_x - k_u)^4 - 2k_u^2(k_x - k_u)^2}}{2k_z} \tag{4.14b}$$

Equation 4.14b is derived in Appendix A. The coordinate transform is done using the interpolation function described in the Appendix B. The

coordinate transform is performed on 2D slices of the 3D block of data while keeping k_u fixed for each slice:

$$\xi(k, k_v|k_u) \rightarrow \xi(k_x, k_z|k_u) \tag{4.15}$$

The final inverse of the scatter matrix can be found by summing each 2D slice:

$$\bar{\sigma}(k_x, k_z) = \int_{\infty}^{-\infty} \xi(k_x, k_z|k_u) dk_u \tag{4.16}$$

The final image or scatter matrix can then be found by performing an inverse 2D Fourier transform on this:

$$\sigma(x, z) = \int_{-\infty}^{\infty}\int \bar{\sigma}(k_x, k_z)\ exp(i(k_x x + k_z z))\ dk_x dk_z \tag{4.17}$$

Summary of the Implementation Process

1. Perform a 3D Fourier transform on the received data: $E(t, u, v) \overset{3Dft}{\Longrightarrow} \bar{E}(w, k_u, k_v)$.

2. Obtain $\xi(k, k_u, k_v)$ using Equation 4.11.

3. Keeping k_u constant, perform the coordinate change shown in Equation 4.15.

4. Obtain $\bar{\sigma}(k_x, k_z)$ through the summation of $\xi(k_x, k_z|k_u)$ over all k_u values (Equation 4.16).

5. Perform an inverse Fourier transform to obtain the image (Equation 4.17).

The basic concept of the difference between the time domain and the frequency domain imaging algorithms is depicted in Figure 4.4. In the time domain, the image is constructed by migrating the signals back along the

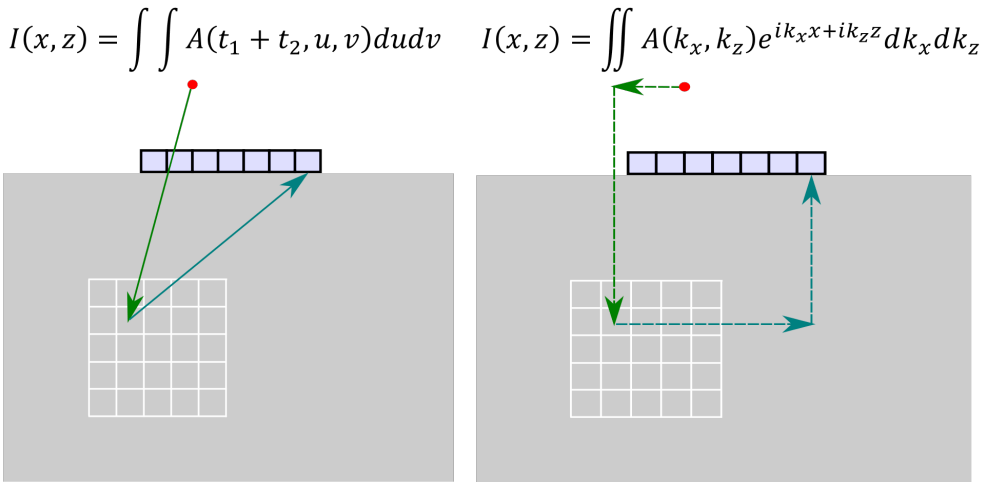


Figure 4.4: Left - Depiction of the time domain reconstruction. Right - Depiction of the frequency domain reconstruction.

direction of propagation. The signals for each pixel are migrated a depending on the distance of the pixel from the source and receiver. The frequency domain algorithm works in a similar way. However the horizontal and vertical frequency components of the data are obtained, these are migrated in the horizontal and vertical directions respectively in order to reconstruct the image.

The two algorithms were implemented in Matlab using in built functions. The frequency domain algorithm used the Matlab fast Fourier transform algorithms. Data was discretely sampled from $t = T_1 \rightarrow T_2$ at intervals related to the sampling frequency: f. N_t sample points are collected for each A-scan. Time and distance are interchangeable so the spatial frequency can be found by $k = \omega/c$. The Matlab fast Fourier transform applied to a single A-scan gives returns the spatial frequencies ranging from $k = -\pi f/c \rightarrow k = \pi f/c$ at intervals $2\pi f/cN_t$.

The data is collected in the form $E(t, u, v)$, where u and v are the transmit and receive points, discretely sampled in space. The virtual sources use a sup-aperture of the array, this aperture is incremented along the array by a number of elements until all elements have been used in transmission. Therefore the transmitters are sampled from

$u = 0 \rightarrow u = N_u p_u$. Here, N_u is the number of virtual sources and p_u is horizontal separation of the virtual sources. Each element receives, so the receivers are sampled from $x = 0 \rightarrow x = N_e p_e$. Here, N_e is the number of elements and p_e is the element pitch. The remaining spatial frequencies as a result of the shifted 3D Matlab Fourier transform range from $k_u = -1/2p_u \rightarrow 1/2p_u$ and $k_v = -1/2p_e \rightarrow 1/2p_e$ with a spacing of $1/N_u p_u$ and $1/N_v p_v$ for the transmit and receive respectively.

The entire coordinate transform as a result of the 3D Fourier transform can be seen here:

$$\begin{aligned} E(t = T_1 \rightarrow T_2, u = 0 \rightarrow N_u p_u, v = 0 \rightarrow N_e p_e) \overset{3dFT}{\Longrightarrow} \\ E(k = 0 \rightarrow 2\pi f/c, k_u = 0 \rightarrow 1/p_u, k_v = 0 \rightarrow 1/p_e) \end{aligned} \tag{4.18}$$

The interpolation values k_x and k_z are defined such that the inverse Fourier transform returns the image with the pixel spacing chosen for the image. Therefore the k_x and k_z are defined by $k_x = 0 \rightarrow 1/p_x$ and $k_z =\rightarrow 1/p_z$ with a spacing of N_x/p_x and N_z/p_z respectively. Here p_x and p_z is the spacing of the pixels and N_x and N_z is the number of pixels in the x and z direction respectively. A linear interpolation function is then used to perform the coordinate change $k, k_v | k_u \rightarrow k_x, k_z$ and the Matlab inverse Fourier transform is used to obtain the image.

4.3 Results and Discussion

In this section, the frequency domain algorithm is compared to the time domain algorithm for a variety of reflectors at a variety of different locations relative to the probe. The performance of each algorithm is measured using API and SNR.

4.3.1 Array Performance Indicator (API)

To measure the performance of an array for a given point in space, the API is used. The API [10] is given by:

$$API(x,z) = \frac{A(x,z)_{6dB}}{\lambda^2} \tag{4.19}$$

Here $A(x,z)$ is the area of indication within 6dB of the peak amplitude at the location (x,z). λ is the centre frequency of the array elements.

The API of the time and frequency domain algorithms was measured. The data was simulated using the CIVA software. An array with 64 elements and a pitch of 0.6mm was used. Each element had a centre frequency of 5MHz. The component was steel with an acoustic velocity of $5900ms^{-1}$. 25 virtual sources was used, each firing on 16 elements each and the transmission group was incremented by 2 elements along the array. The virtual sources were situated at 5mm behind the aperture.

A series of side drilled holes with a diameter of 1mm at different locations was imaged and used to map the API across a larger area. The SDHs were laid out in a square lattice, separated by 4mm, running horizontally from the centre of the array to 58mm out. The depth of the holes extended from 4mm deep to 80mm deep. To avoid masking and defect-defect interactions, each SDH was simulated and processed separately. Artificial noise was added into the data. This was done to test how well each algorithm managed to differentiate the signal from noise that would occur in a literal inspection. The noise was added by performing a Fourier transform on the data with respect to time. Random frequency components with random amplitude (between zero and some arbitrary value) and random phase (between 0 and 2π) were added before performing the inverse Fourier transform. Both time and frequency domain algorithms was then used to image a side drilled hole located at

30mm depth and 2mm from the centre axis of the transducer. The reference indication for the frequency domain was 6dB higher than that of the time domain.

The images of the SDH at different positions were combined by taking the maximum value of all the images at the different pixel positions. The results can be seen in Figure 4.5 for the time domain and Figure 4.6 for the frequency domain. Each image uses the SDH at 30mm depth and 2mm from the horizontal as the reference value. 6dB of soft gain has been added into Figure 4.6 to account for the greater noise SNR of the frequency domain algorithm.

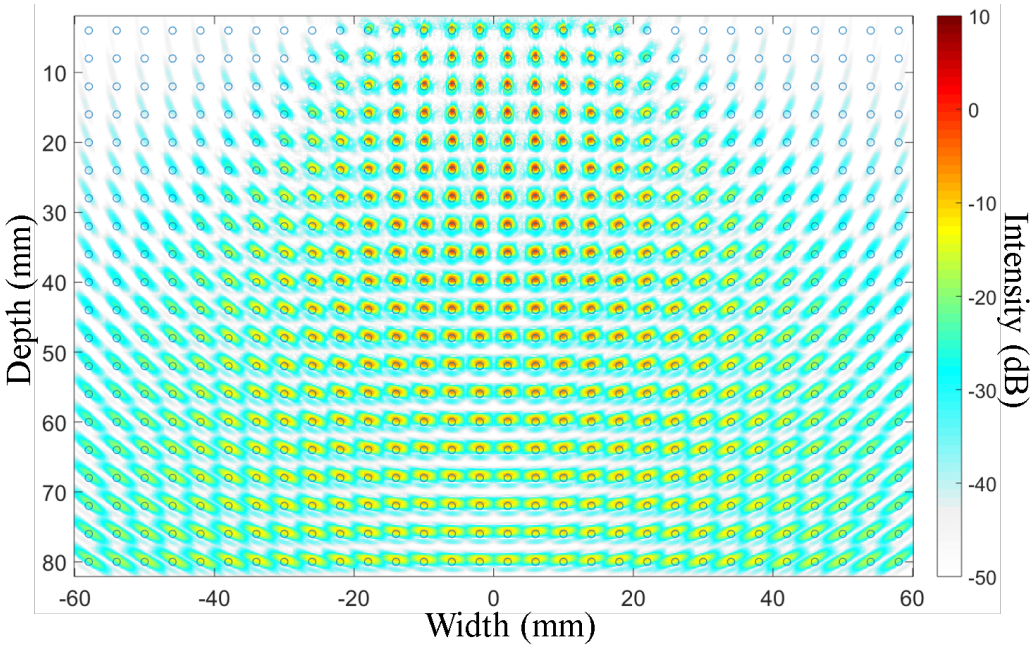


Figure 4.5: Image of the SDHs using the time domain TFM algorithm.

It can be seen that the indications closest to the transducer are stronger when imaged with the frequency domain algorithm. Indications further away from the transducer are stronger using the time domain algorithm. The time domain algorithm also images the holes that located away from the transducer normal axis, giving a wider field of view.

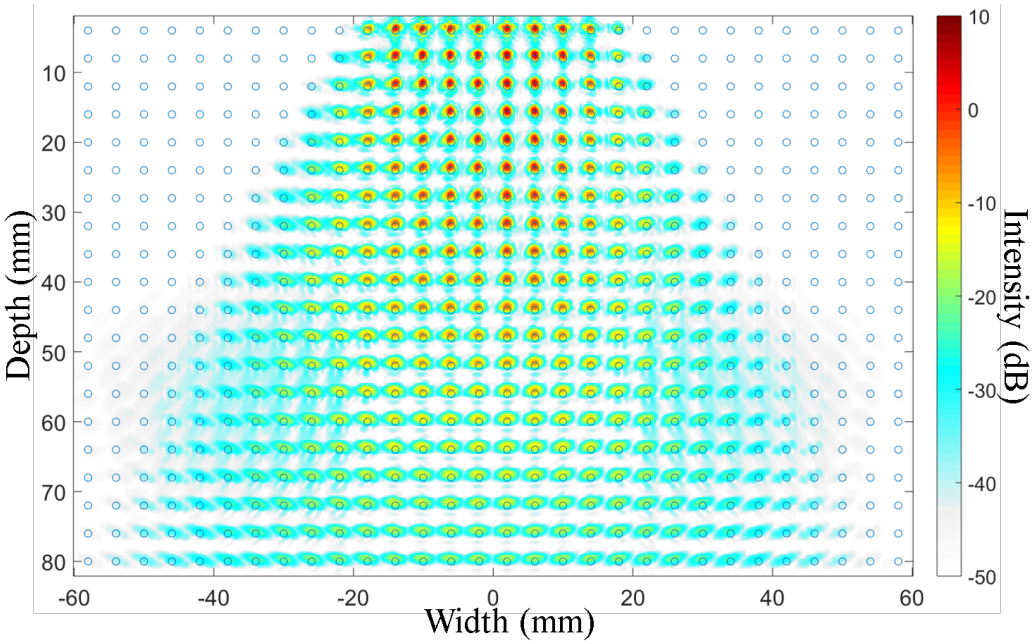


Figure 4.6: Image of the SDHs using the frequency domain TFM algorithm.

The API also was mapped for both the time and frequency domain, this can be seen in Figures 4.7 and Figure 4.8 respectively. The API is a measure of the size of an indication and is independent of the intensity of the peak amplitude. It can be seen that the performance of the array using the time domain algorithm is fairly uniform with angle, but gradually decreases with distance. By comparison, the frequency domain algorithm also decreases with distance, however a sharper decline can be seen with a wider angle.

To conclude the frequency domain algorithm is optimum for short range inspections in a noisy material. For longer range inspections with a wider steering angle, the time domain is preferred.

4.4 Implementation Complexity of the Time and Frequency Domain Algorithms

The main advantage of the performing the algorithm in the frequency domain is the theoretical decreased processing time due to efficient use of

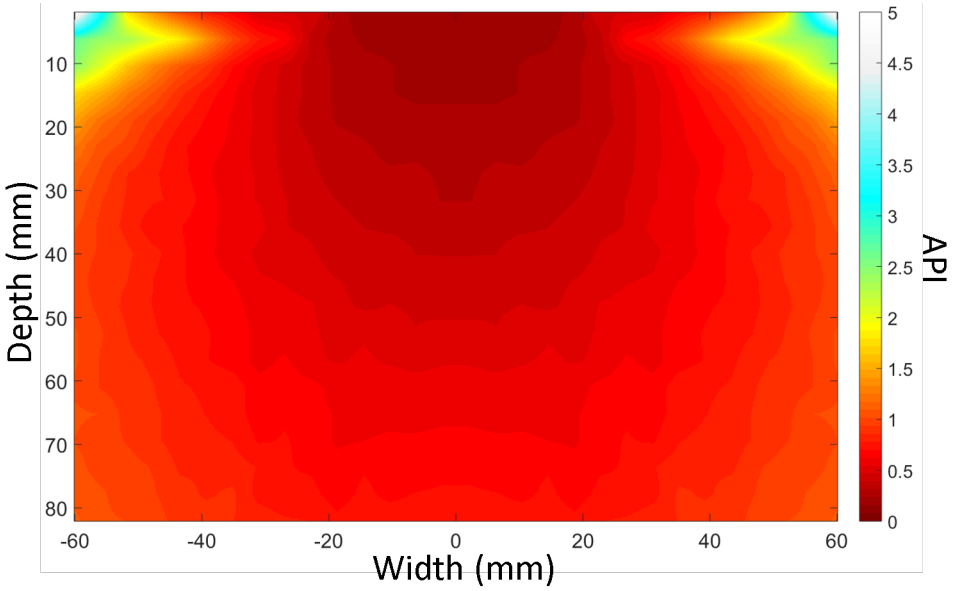


Figure 4.7: API map of the time domain TFM algorithm.

Fourier transforms. The purpose for this paper is to present the mathematics behind the implementation of the frequency domain algorithm in a comprehensible way. The two algorithms were implemented using MATLAB and in built functions within MATLAB. As the processing time depends heavily on implementation, a comparison of the time taken to process an image for the two techniques is unlikely to present any definitive results.

However, it can be said that the considerable majority of the image processing for the time domain algorithm is in calculating the TFM. For the purposes of this discussion, the order of processing will be considered to be the number of nested 'for' loops in the algorithm. For the TFM, an image of N_x by N_z pixels is used, and these are summed up over N_u transmitters and N_v receivers. The processing time therefore is of order $\mathcal{O}(N^4)$. The frequency domain algorithm uses a 3D Fourier transform, by conventional methods for a N by N by N data set, the processing time is of order $\mathcal{O}(3N^4)$. As this initial 3D transform in the most computationally expensive part of the process by far, other calculations are ignored in this

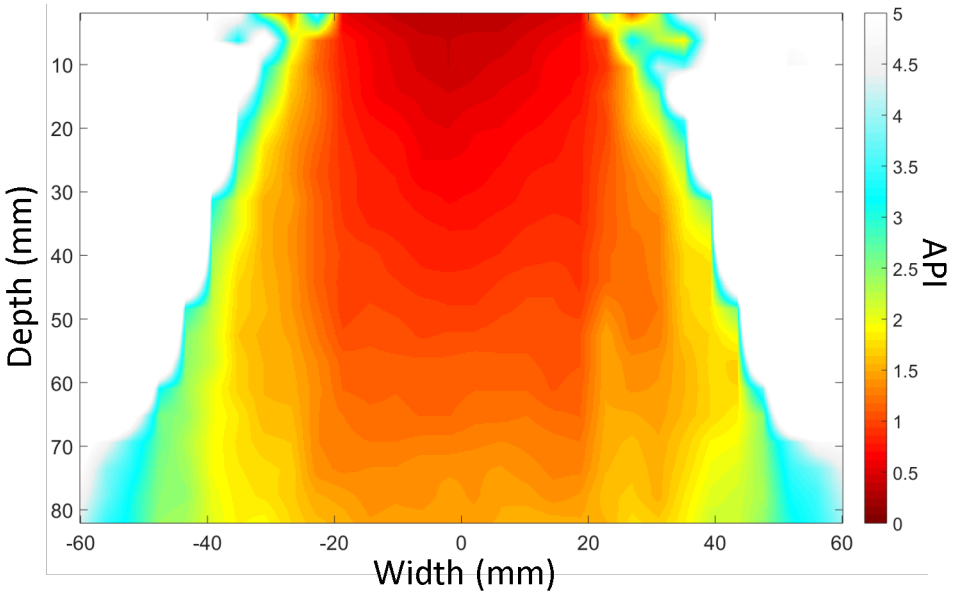


Figure 4.8: API map of the frequency domain algorithm.

discussion. Using Fast Fourier Transforms can reduce the processing time to an order of $\mathcal{O}(3N^3ln(N))$ [80], causing the frequency domain implementation to be significantly faster than the equivalent time domain providing that $3ln(N) < N$, which is true for the vast majority of inspection scenarios.

4.5 Conclusion

This chapter analyses both the time and frequency domain algorithms for ultrasonic array imaging using virtual sources. The time domain algorithm is well documented [13, 47] and fairly straightforward to implement. The implementation of the frequency domain algorithm is more complicated and difficult to implement [77]. This chapter discusses the implementation of the frequency domain algorithm used, detailing the frequency components used for the Fourier transforms and coordinate changes.

The two algorithms are tested and known reflectors are used at different locations to measure the performance. It is shown that the field of view of

the frequency domain algorithm is narrower than the time domain as the intensity of the image reduces quicker when moving away from the normal axis of the centre of the transducer. The SNR of indications closer to the probe is higher for the frequency domain algorithm, suggesting that it may be optimal for a short range inspection in noisy materials.

Due to the complexity of the algorithm, the frequency domain algorithm has not been developed as much as the time domain. A few publications describe using the frequency domain algorithm through a refractive boundary, but only these only exist for simple cases [68, 78].. Unfortunately, it is often required in NDT that inspections be carried out through some sort of refractive boundary, therefore it is not often practical to use it. Therefore for the remainder of this thesis, the time domain algorithm only has been investigated.

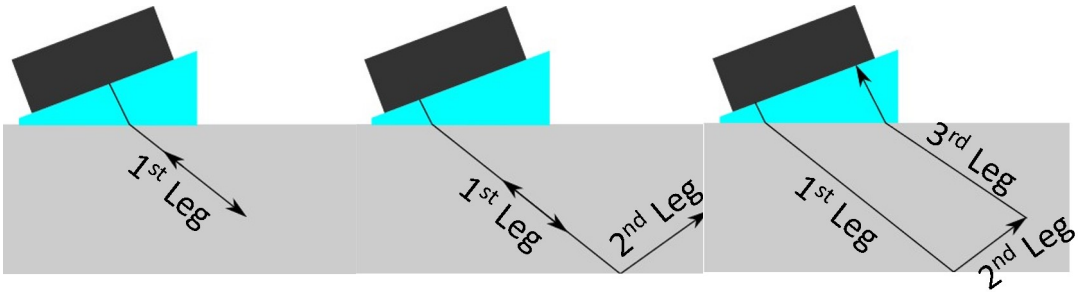
Chapter 5

Self Tandem and Multi-Mode Imaging

5.1 Introduction

The TFM algorithm may be used to consider a number of imaging views such as half-skip (where the sound travels directly from the transducer to the region of interest and directly back) [10], full-skip (where the sound skips off the known backwall of the component to the region of interst and back along the same route) [24] or a combination of the two (known as self-tandem) [47]. These inspection paths are depicted in Figure 5.1. Conventional UT and PAUT tend to only include half skip and full skip views [46], the self-tandem has since been introduced for use with the TFM [45].

The TFM self-tandem algorithm was developed to image vertically aligned flaws that were previously difficult to detect, such as vertically aligned flaws. This is because a sound wave hitting a flat surface reflects sound in a given direction, depending on the orientation of the flaw and the incident direction. This would mean that the sound is less likely to



(a) Half Skip Inspection (b) Full Skip Inspection (c) Self Tandem Inspection

Figure 5.1: Depicting different inspection paths that can be considered using the TFM.

return to the transducer compared to a point like reflector, that reflects sound at a range of different angles.

Due to the longer path length, and mode conversion, the self-tandem algorithm is more susceptible to imaging artefacts [45]. These are often caused from mode conversion. Ultrasound may propagate through a medium in a variety of modes. Three common modes of propagation have been described in the second chapter of this thesis (section 2.2.3). These are: longitudinal, transverse and surface. The main modes considered in this chapter are longitudinal and transverse, as these are the highest amplitude and most applicable for the type of imaging performed. It can be seen that behaviour of the particles in each mode is different. Specifically, the particles oscillate in the direction of wave propagation for longitudinal waves, and perpendicular to the direction of propagation for shear. Due to this, the velocity at which different modes travel is different, with transverse wave usually travelling at roughly half of the velocity of longitudinal.

If an incident planar wave passes over a boundary in which the speed of sound changes, the direction of the wave changes. This is called refraction. The angle of refraction relative to the angle of incidence and the relative velocity difference between the two mediums can be calculated using Snell's

law. Sound passing between a boundary between two materials may also mode convert, and the angle of refraction may be calculated by using the velocity of the new mode. Sound which has been reflected (rather than transmitted through) behaves in a similar way. The angle of incidence is equal to the angle of reflection if the velocity of the wave remains constant. However when a wave mode converts, the angle of reflection is different to the angle of incidence due to the velocity difference of the incident and reflected mode. This effect may cause imaging artefacts in some cases, as mode converted sound may be miss-plotted by the imaging algorithm, but may also be used to the advantage of the inspector providing an algorithm that accounts for this is used.

Studies have shown that the TFM algorithm may be adapted to consider sound that has mode converted [48]. This has been adapted such that a plane wave may be used on transmission [24]. These studies show the use of multi mode imaging algorithms for improving the detection of flaws and explaining imaging artefacts.

When mode conversion happens, the energy of the incidence wave is divided up between all of the resultant wave forms. Mode conversion, reflection and refraction happens whenever a wave comes into contact with an impedance difference. Figure 5.2 depicts this. The resultant waves also mode convert when hitting another impedance difference boundary. The proportion of energy of each wave mode is dependent on the incidence angle, refraction angle and the acoustical impedance of the two materials. The reflection and transmission coefficients for the simple 0^o case is shown in section 2.4.3, however for incident angles that are not perpendicular to the surface the proportion of energy can be found using the Fresnel weighting equations [81]. These equations are important in order to predict the useful wave modes for different imaging scenarios, as the energy produced in certain mode conversions may be so small that it

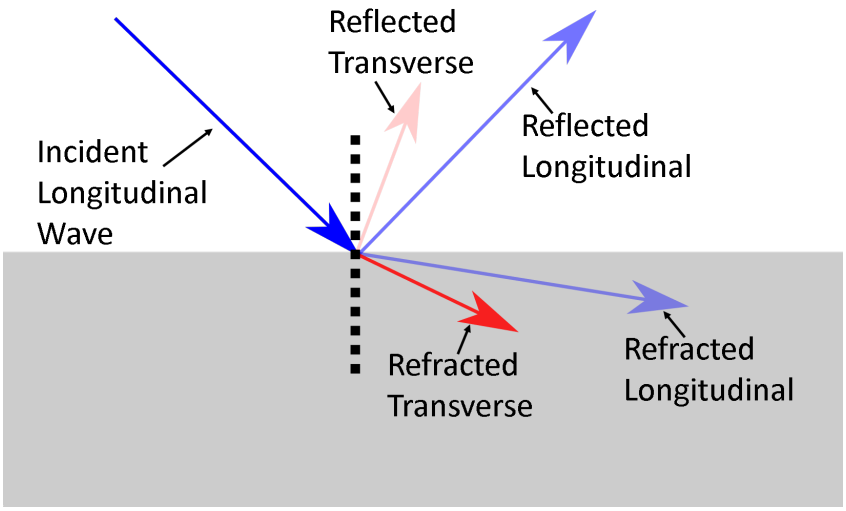


Figure 5.2: Depicting some of the resultant wave modes generated by an incident longitudinal wave crossing a refractive boundary.

can be disregarded. One example of this is when the angle of an incident wave is beyond the critical angle for longitudinal, but not for transverse. In this case only transverse waves will propagate through into the second material and so the longitudinal component can be ignored in the imaging algorithm.

In this chapter we present an imaging algorithm that accounts for multiple different wave modes using virtual sources on transmission. The algorithm implementation is discussed and experimental results show the possible advantages that the algorithm may bring in an inspection scenario.

5.2 Imaging Algorithm

The TFM algorithm is introduced in previous chapters. However it is revisited here for convenience. The algorithm is used to synthetically focus at every point in a defined region of interest. The intensity of a given pixel in that region is calculated by delaying and summing the A-scans to create

a synthetic focus point at every pixel in the image. The algorithm is shown in Equation 5.1.

$$\sigma(x,z) = \sum_{i=1}^{N_t} \sum_{j=1}^{N_r} A_{i,j}(a_i(x,z) + b_j(x,z)) \tag{5.1}$$

Here $\sigma(x,z)$ is the intensity of the TFM image at position (x,z), N_t is the number of transmitters and N_r is the number of receivers. $A_{i,j}(t)$ is the amplitude of the A-scan of the ith transmitter and jth receiver at time t, a_i is the time of flight from the ith sound source to the pixel and b_j is the return path to the jth receiving element.

The TFM algorithm can consider a number of different flight paths, such as half-skip, full-skip and self-tandem. This is done by calculating the time of flight a and b corresponding to the chosen paths. These paths may account for mode conversion. The time of flight between two points along any given path can be calculated by finding the distance for each leg of the flight path and dividing by the respective velocities. The correct flight path can be found by using Fermat's principle and minimising the time of flight for a given path.

5.2.1 Multi-Mode Time of Flight Calculation

In this chapter, vertically aligned reflectors are inspected using a VSA multimode imaging algorithm. A wedge designed to induce shear waves in the material is used to couple the transducer to the inspected component. This is depicted in Figure 5.3.

Equation 5.2 is used to calculate the time of flight for the multimode flight path.

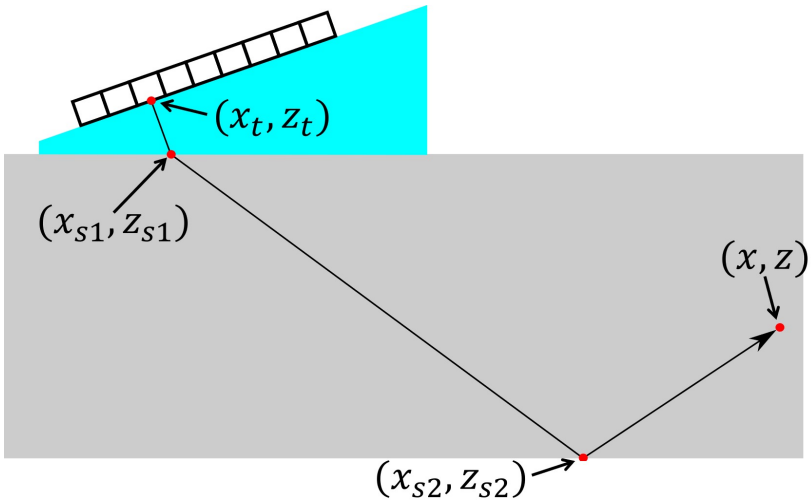


Figure 5.3: Depiction of the coordinates.

$$t = \frac{((x_{s1} - x_t)^2 + (z_{s1}(x_{s1}) - z_t)^2)^{\frac{1}{2}}}{c_0} + \frac{((x_{s2} - x_{s1})^2 + (z_{s2}(x_{s2}) - z_{s1}(x_{s1}))^2)^{\frac{1}{2}}}{c_1} + \frac{((x_p - x_{s2})^2 + (z_p - z_{s2}(x_{s2}))^2)^{\frac{1}{2}}}{c_2} \tag{5.2}$$

Here t is the time of flight, x_t and z_t are the coordinates of the sound source, x_{s1} and z_{s1} are the coordinates of the point at which the wavefront crosses the wedge-component boundary, x_{s2} and z_{s2} are the coordinates of the backwall surface from which the sound reflected, c_0 is the velocity of the wedge and c_1 and c_2 are the velocities of the mode of sound considered in the component.

For the purposes of this chapter it is assumed that $z_{s1}(x_{s1})$ and $z_{s2}(x_{s2})$ are constant and $z_{s1}(x_{s1}) = 0$ and $z_{s2}(x_{s2}) = \tau$, where τ is the thickness of the component. However, the algorithm may be adapted to account for components with a non flat surface and back wall. This gives Equation 5.3.

$$t = \frac{((x_{s1} - x_t)^2 + (-z_t)^2)^{\frac{1}{2}}}{c_0} + \frac{((x_{s2} - x_{s1})^2 + \tau^2)^{\frac{1}{2}}}{c_1} + \frac{((x_p - x_{s2})^2 + (z_p - \tau)^2)^{\frac{1}{2}}}{c_2} \tag{5.3}$$

The minimum time of flight could be calculated by minimising Equation 5.2 through an iterative process along the boundary. However this is computationally expensive. A quicker method would be to partially differentiate Equation 5.3 with respect to the variables x_{s1} and x_{s2} and find the point at which these are equal to zero:

$$\frac{\partial t}{\partial x_{s1}} = \frac{(x_{s1} - x_t)}{c_0\left((x_{s1} - x_t)^2 + (-z_t)^2\right)^{\frac{1}{2}}} + \frac{(x_{s1} - x_{s2})}{c_1\left((x_{s2} - x_{s1})^2 + \tau^2\right)^{\frac{1}{2}}} \tag{5.4a}$$

$$\frac{\partial t}{\partial x_{s2}} = \frac{(x_{s2} - x_{s1})}{c_1\ \left((x_{s2} - x_{s1})^2 + \tau^2\right)^{\frac{1}{2}}} + \frac{(x_{s2} - x_p)}{c_2\left((x_p - x_{s2})^2 + (z_p - \tau)^2\right)^{\frac{1}{2}}} \tag{5.4b}$$

To find the minimum, different values of the variables x_{s1} and x_{s2} are tested, to find the two points where the value of Equations 5.4a and 5.4b are equal to zero. The time of flight rises indefinitely when $|x_{s1}| \to \infty$ and $|x_{s2}| \to \infty$, with the minimum somewhere in between. Therefore it can be said that the gradient of the partially differentiated equations, Equations 5.4a and 5.4b, are negative when $x_{s1} \to -\infty\ x_{s2} \to -\infty$ and positive when $x_{s1} \to \infty\ x_{s2} \to \infty$. Assuming a single minimum, the direction of the minimum relative to the current iteration is determined using the sign of the gradient. This allows us to use a coarse iteration spacing to find x_{s1} and x_{s2} values giving the smallest gradient. Then a finer iteration spacing and the process repeated until the desired accuracy is achieved. This method

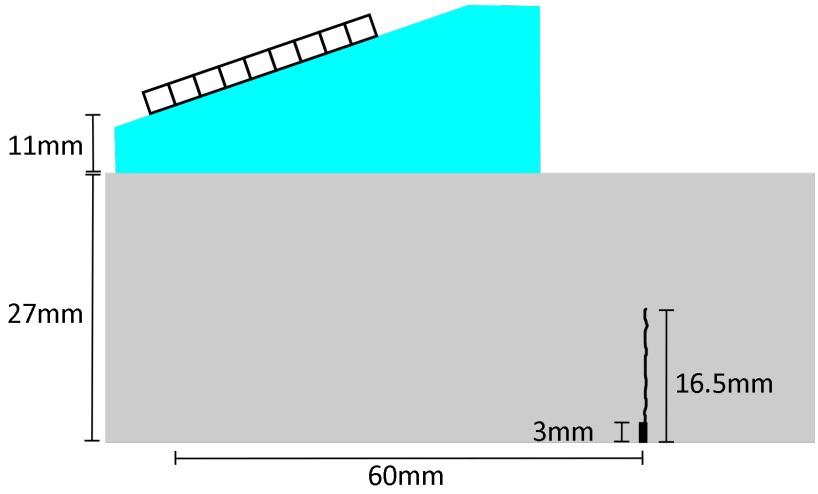


Figure 5.4: Image Depicting the Experimental Setup and the Fatigue Crack.

proves to be faster than iterating through every x_{s1} and x_{s2} combination in order to calculate the least time.

Using Equations 5.4a and 5.4b the x_{s1} and x_{s2} of the minimum flight path can be found. Then the time of flight for this path can be calculated using Equation 5.3 and inserted into the TFM algorithm to generate an image. It can be seen that different velocities may be inserted into the equation to account for mode converted sound.

The VSA multi-mode self-tandem algorithm was implemented in the TWI Crystal software in order to evaluate the performance.

5.3 Experimental Setup

A vertically aligned fatigue crack was used to test the algorithm. The fatigue crack was grown out of a notch that was cut out of the material. The fatigue crack had a height of 16.5mm. The part was turned upside down so that the same crack could represent a crack originating from the top and bottom surfaces of the component. The crack is depicted in Figure 5.4.

The experiment was run using an Olympus 5L64 array, attached to a perspex wedge. Due to the nature of the wedge material, any transverse

Imaging View	Modes Considered
Half Skip	T
Full Skip	T T
Self-Tandem	T T T
Self Tandem Multi Mode	T L T

Table 5.1: Modes Considered for different inspection views. T-Transverse, L-Longitudinal.

waves in the wedge attenuate quickly. This reduced the potential number of combinations of mode conversion that was considered in the algorithm, as the transverse waves in the wedge could be largely ignored. The angle of the wedge was 36^o, designed to induce transverse waves in the material. As this angle was beyond the critical incidence angle for longitudinal waves in the part, it can be said that the majority of the sound produced from the probe would be shear waves. This again helped limit the number of combinations to be considered for the algorithm.

The chosen combinations of modes for each leg of the journey (as depicted in Figure 5.1) for view can be seen in Table 5.1. The transverse was chosen for each leg of the half skip and full skip views as the transducer was designed to induce transverse waves in the material. The standard self-tandem algorithm as described in [47] was used as a reference, each leg of this was also chosen to be transverse. The multi mode algorithm was demonstrated using transverse for the first and third leg, however longitudinal was chosen for the second leg. The reasoning behind this was that the mode converted waves might be sensitive to higher regions of the component due to the angles of reflection in mode conversion, as depicted in Figure 5.5.

Figure 5.5 depicts the angles of reflections for mode converted and non mode converted signals. The reflection angles for the standard self-tandem algorithm are likely to be equal to the incident angles. The mode conversion angles are likely to favour a vertically aligned flaw. The

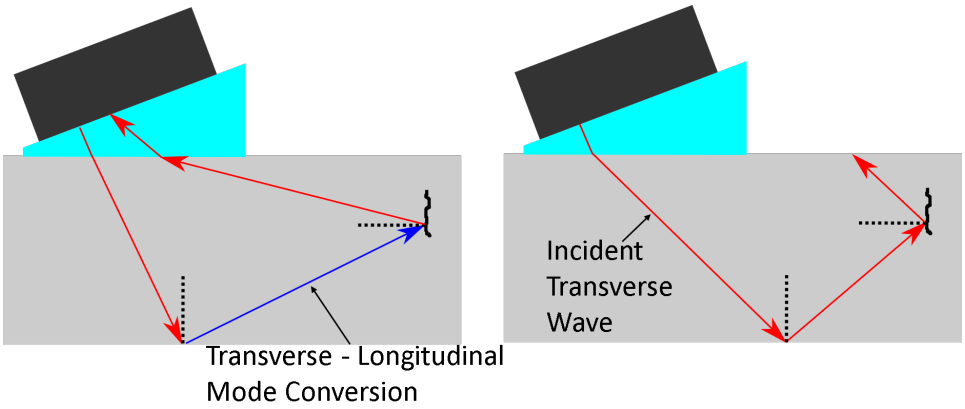


Figure 5.5: Figure Depicting the Potential Use of a Multimode Algorithm in Detecting a Vertically Aligned Flaw

reflection off the backwall causes a mode conversion from transverse to longitudinal and as longitudinal waves travel faster than transverse, the reflection angle is greater than the incident angle. When the wave interacts with the flaw, it may mode convert back from longitudinal into transverse. This causes the reflected angle to be smaller than the incidence angle. The mode converted sound seems more likely to return to the transducer because of this. This was investigated further using the vertically aligned flaw and the results shown.

Figures 5.6 shows the half skip algorithm imaging the flaw originating from the bottom of the component. The corner trap at the base of the flaw can be seen, along with low amplitude indications from facets along the length of the flaw. The tip diffraction can also be seen along with a high amplitude artefact beyond the flaw. This is due to sound that has followed a self-tandem path being plotted in the wrong place by the TFM image. Although the focussing of the artefact is poor, the high amplitude of the specular response means that the artefact can be seen. A similar response can be seen from the full skip image, shown in Figure 5.7. The tip is less visible and the artefact can be seen.

The self-tandem algorithm shown in Figure 5.8 distinguishes the flaw nicely. The base of the crack can be distinguished from the rest of the

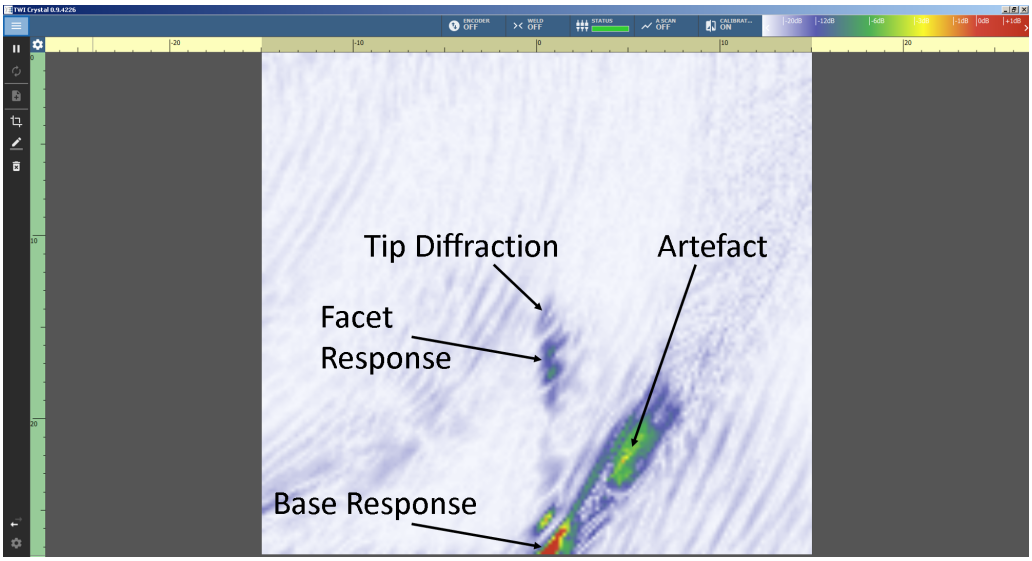


Figure 5.6: Half Skip Algorithm on the Vertical Fatigue Crack Originating from the Bottom of the Part.

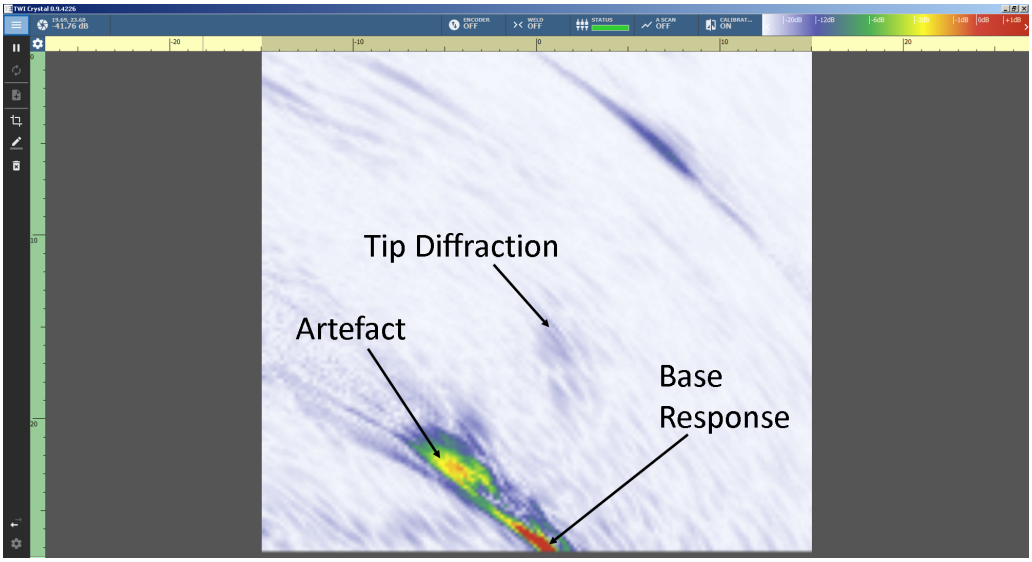


Figure 5.7: Full Skip Algorithm on the Vertical Fatigue Crack Originating from the Bottom of the Part.

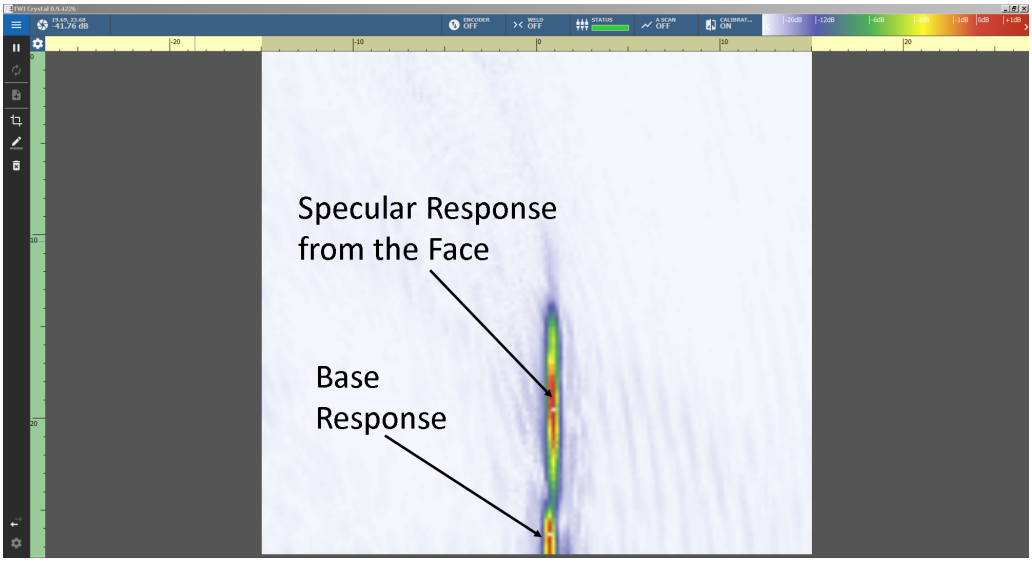


Figure 5.8: Self Tandem Algorithm on the Vertical Fatigue Crack Originating from the Bottom of the Part.

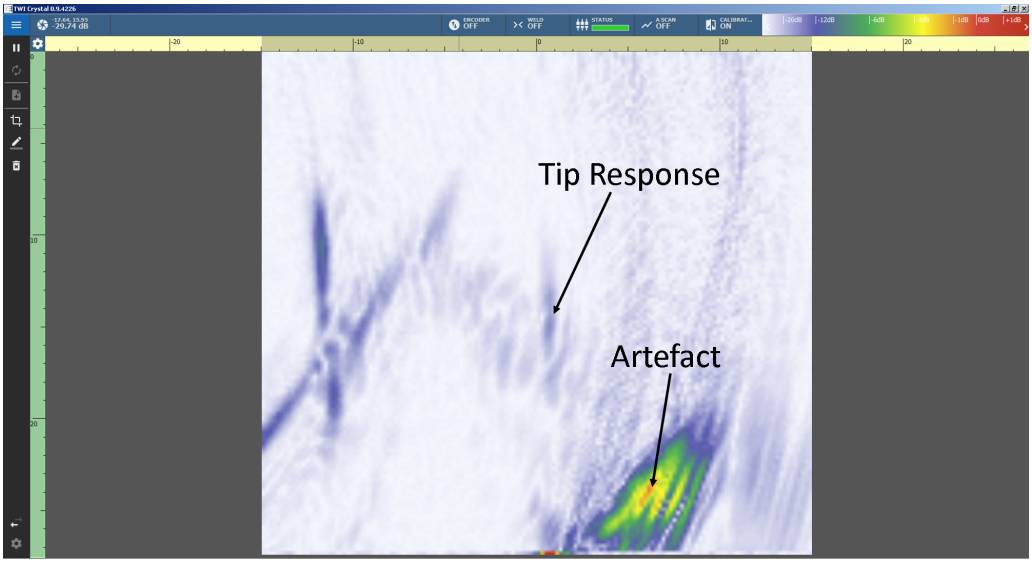


Figure 5.9: Multi-Mode Algorithm on the Vertical Fatigue Crack Originating from the Bottom of the Part.

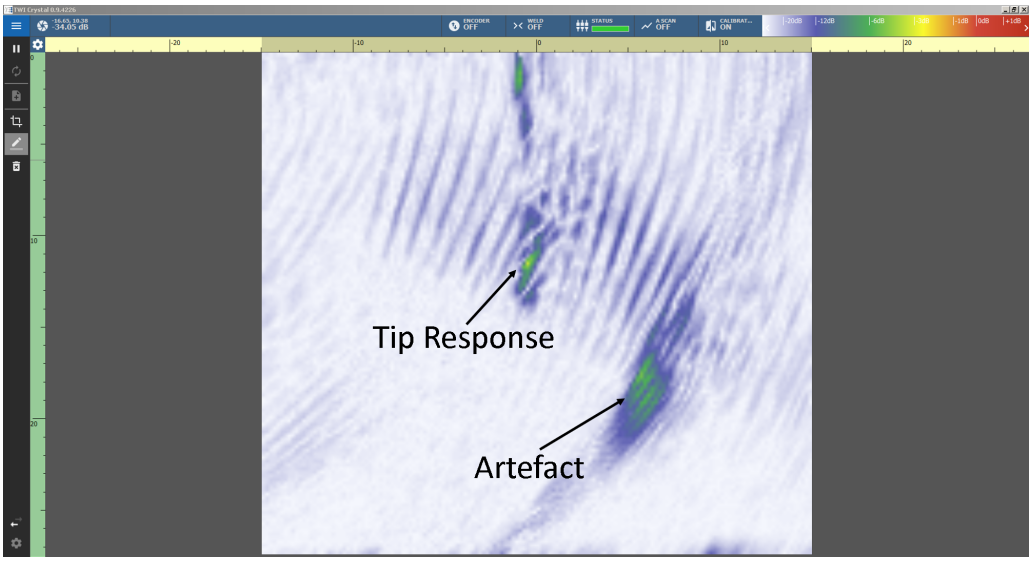


Figure 5.10: Half Skip Algorithm on the Vertical Fatigue Crack Originating from the Top of the Part.

remainder of the fatigue crack. The response is high amplitude and no artefacts appear in the image. This is because the high amplitude signals that caused an imaging artefact for the half and full skip techniques are being coherently summed by the self-tandem algorithm showing a strong indication.

The multimode image of the fatigue crack originating at the bottom of the component, shown in Figure 5.9, is poor. An imaging artefact, like the ones occurring in the half and full skip methods can be seen. No base indication can be seen and only a small amplitude tip response can be distinguished.

The sample was then flipped and imaged from the other side, such that the flaw was now originating from the ceiling. Figures 5.10 to 5.13 show the VSA algorithms imaging the surface breaking crack. The half skip algorithm shown in Figure 5.10 shows small amplitude responses from the facets along with an artefact. The full skip (Figure 5.11) shows only the response from the corner trap at the base of the flaw. The self-tandem algorithm, shown in Figure 5.12, is slightly clearer as the specular response from the deepest point of the flaw is be seen. However this indication

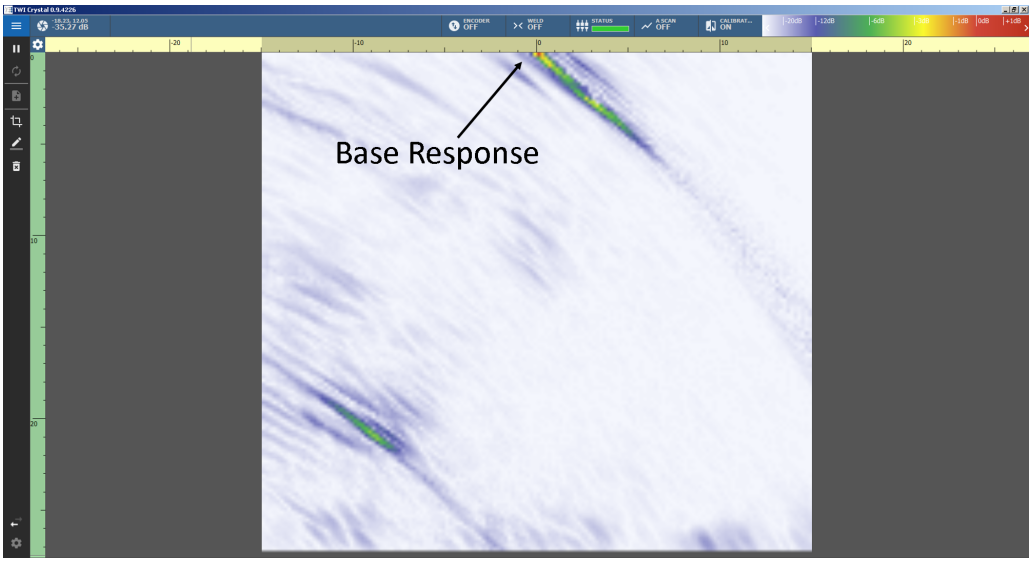


Figure 5.11: Full Skip Algorithm on the Vertical Fatigue Crack Originating from the Top of the Part.

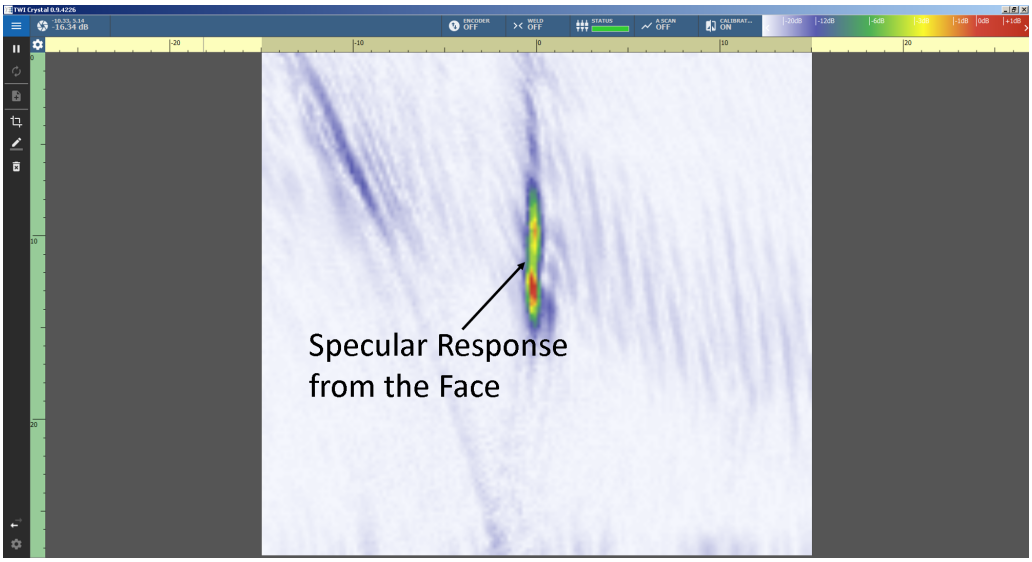


Figure 5.12: Self Tandem Algorithm on the Vertical Fatigue Crack Originating from the Top of the Part.

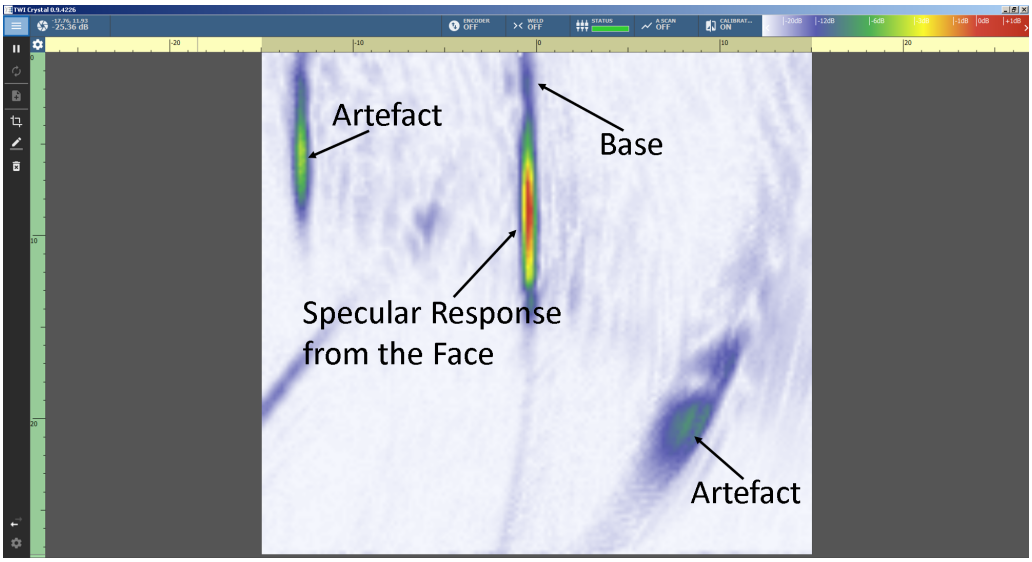


Figure 5.13: Multi-Mode Algorithm on the Vertical Fatigue Crack Originating from the Top of the Part.

cannot be seen further up the flaw because the single mode responses do not return to the transducer. The multi-mode algorithm (Figure 5.13) shows much more of the flaw than the self-tandem algorithm. Although low amplitude, the base of the flaw can be detected. Imaging artefacts occur due to high amplitude signals being plotted elsewhere. However a strong indication from the flaw can be seen coherently with the multi-mode algorithm. This highlights the importance of considering the the multiple modes for flaw detection, and this helps explain imaging artefacts as well.

The SNR relative to the SDH for each indication mentioned above can be seen in Table 5.2.

It can be seen that flaw detection can be improved upon by using the self-tandem and multi-mode algorithms. This is of great benefit in NDT as flaws that were previously ultrasonically invisible can be detected, and new regions can be reached through mode conversion.

Sizing using these methods is difficult, as the amplitude of the indication does not only depend on the size of the flaw, but the orientation and the size of the transducer relative to the beam path. Due to this, using specular responses may not be the most accurate method of sizing. For the

Indication Description	Bottom Flaw	Top Flaw
Half Skip Base	9	-5
Half Skip Tip	-8	-3
Artefact	-2	-5
Full Skip Base	10	1
Full Skip Tip	-18	-23
Artefact	0	-3
Self Tandem Flaw Face	2	-1
Self Tandem Tip	-6	-2
Self Tandem Base	2	N/A
Multimode Flaw Face	N/A	2
Multimode Tip	-15	-8
Multimode Base	7	-11
Artefact	0	3

Table 5.2: Table showing the Intensity (dB) of different Indications Relative to a Side Drilled Hole.

most accurate sizing, it is likely that tip diffracted or corner response signals showing either end of the flaw is the most accurate method, if these signals can be detected.

5.4 Conclusion

The chance that a reflector may be detected by ultrasonic methods depends strongly on whether an echo from the reflector returns to the transducer. Whether the sound returns from a planar reflector depends on the orientation of the surface and the incident and reflected angles of all the wave modes considered. Thus, imaging algorithms that consider mode conversions are much more likely to detect a reflector than one that does not. With prior knowledge of a component and the likely defects that occur, certain imaging modes can be carefully selected in order to increase the likelyhood of detection.

This chapter introduces a VSA multimode imaging algorithm. The algorithm was used to image a vertically aligned fatigue crack. It has been shown that the different modes considered are more sensitive in different

areas relative to the transducer. This depends on a number of parameters, such as the velocity of each mode in each material and the geometry parts of the component considered during the mode conversions.

Future work would involve further investigation into how to accurately determine what modes are applicable for what regions. An investigation is needed into how well certain reflectors, such as planar reflectors that do not reflect sound uniformly in all directions, behave for different mode types. This must be investigated in order to increase the technology readiness level (TRL) of the technique. A high value TRL must be obtained before the technique is used in industry.

Chapter 6

VSA Surface Mapping for Components with Complex Geometry

This chapter introduces a new surface mapping method for VSA when inspecting through dual layered media. This is useful for immersion testing or for when a wedge or a shoe is required to couple the array to the testing component. An overview of the literature can be seen in Section 6.1, then the VSA surface mapping method is introduced in Section 6.2. The focussing algorithm used for imaging through dual layered media is described in Section 6.3. A brief description of some current surface mapping methods is given in Section 6.4. Section 6.5 describes the testing components and the apparatus used to validate the technique and the results Section 6.6 provides a study on the reliability of the VSA surface mapping method compared to the existing methods.

6.1 Introduction

Often an array cannot be coupled directly to the surface of the testing component. It is possible to use flexible arrays that conform to the surface to account for this, however accurately knowing the element positioning can be an issue. In [53] an iterative process is performed where the positions of the elements on the surface is estimated using a cubic spline function. An image is generated using the TFM for each surface prediction. The contrast in the image is measured, and when it reaches its maximum, it is determined that the image is in focus and so the surface estimation is correct. A study done in 2008 [49] shows how phased array techniques can be adapted to work using conformable arrays.

An alternative to conformable arrays is to immerse the testing material in a coupling medium such as water [12], or use a fluid filled membrane [50]. Alternatively a shaped wedge/shoe [36] can be used to couple the array to the surface. In these cases, the refraction of sound as it enters the testing material must be taken into account, as this will change the path that the sound takes to travel from one place to another. The time of flight calculation is essential when computing the TFM and so the flight path must be known. For a flat surface, between two mediums an exact solution exists where the point of incidence (the point on the surface at which the flight path passes through) can be calculated from solving Snell's Law [34]. However, for more complicated geometries, Fermat's principle of least time is often used [37]. This states that the path taken between a point source of sound and receiver is the path of least time. The path is found by calculating the time of flight for a number of points along the boundary and taking the minimum. In [37], TFM is performed using the Fermat's principle approach for components with known complicated surface geometries. The iterative approach is often time consuming as multiple

points along the boundary have to be calculated. This can be reduced using a method shown in [41], where the derivative of the time of flight is calculated and a Newton Raphson based approach is used to find the point at which the function is equal to zero, which is often the minimum. However this method is unstable and frequently fails to converge.

In the majority of cases, the surface geometry relative to the array is not known. It is required to map the surface ultrasonically before an inspection is performed. This way the inspection is easier to perform as the surface estimation is modified automatically when the array is moved, and so the image is always in focus. Without surface mapping, the inspection is only focussed providing that the surface estimated matches with that of the actual physical surface. A small deviation away from this set up significantly reduces the focus of the image, reducing the chance that a critical defect is detected.

To estimate the profile surface relative to the array, a number of methods exist. One such method applies TFM in the coupling substance to find surface information [55]. The first response times may also be used to estimate the surface. The first echo that returns to the probe has typically reflected off the boundary between the coupling substance and the component surface. It is possible to estimate the surface using trigonometry and the element first response times. A variety of techniques exist in which to do this using either single element transmissions [54, 24] or plane wave transmissions [57]. The first response time is often determined at the time when the amplitude scan crosses a certain threshold. However, due to the long rise and fall times of the ultrasonic pulse, a simple threshold crossing technique causes errors [61]. Corrections to eliminate this error are discussed in [60].

Once the surface profile is known, different ways of imaging below exist. In [35], an inspection is performed on chain links from the Clifton

suspension bridge, Bristol. In this study, phased array techniques were compared to the TFM algorithm for imaging. It is shown that the two techniques produce images with comparable SNR, however the TFM has the advantage of producing a fully focussed image. In [56, 43], using a focal law similar to phased array focussing, an array of virtual sources and receivers are placed on the surface between the two mediums, and then TFM is performed in the second material for imaging. This approach requires two firing sequences, one for surface mapping and a second for imaging. It has also been shown that by optimising the post processing, time efficient TFM can be performed using the Fermat's principle approach [6].

In some approaches, the same data can be used to map the surface and image. However it is often the case that two firing sequences are used, one to map the surface profile and the second to image. To maximise inspection speed, a single firing is most efficient. In this chapter a virtual source method of surface estimation is discussed. This requires a single firing of the ultrasonic array for both surface mapping and imaging. The ultrasonic array is used with maximal efficiency by using virtual sources instead of firing single elements. By minimising the number of firings required to generate an image in this way, the speed of inspection can be increased.

6.2 Virtual Source Surface Mapping Method

The Virtual Source Surface Mapping Method (VSSM) is described here. The array transducer is coupled to the testing component with a complex surface using some coupling medium. This may either be through immersion or using a fitted shoe. The transducer transmits sound and the first response echo times are used to map the surface. Once the geometry of the surface is known, the TFM algorithm can be used to image underneath. The distance

that the response travelled can be calculated using:

$$r = t_1 c_1 \tag{6.1}$$

Here, r is the distance travelled, t_1 is the time of flight of the first response and c_1 is the velocity of sound in the first medium. The travelled distance of the first response can be used to find the position of the surface. Consider an ellipse: an ellipse is constructed around two focal points. The distance from a focus point to a point on the circumference and back to the other focal point is equal. If an ellipse were to be constructed using the virtual source position as the first focal point and the receiving element as the second, with the distance to the circumference and back equal to the first response distance, the point of the surface from which that response reflected will lie somewhere on the ellipse circumference. To find the actual surface point, two ellipses from receivers adjacent to each other must be constructed as depicted in Figure 6.1.

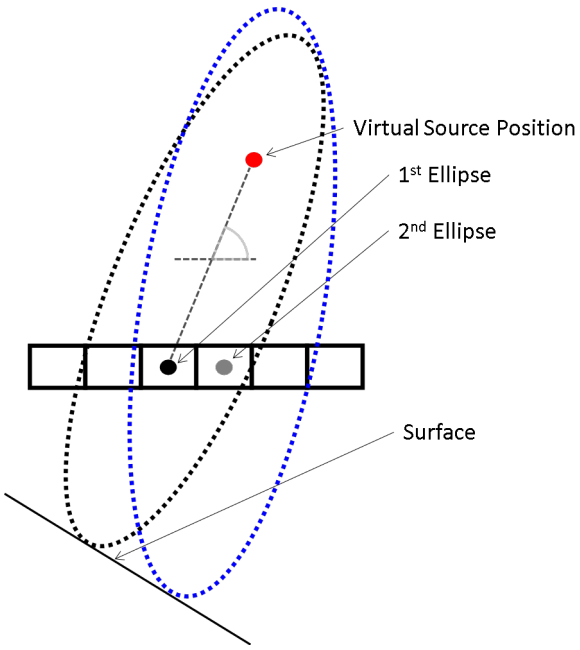


Figure 6.1: Depiction of how ellipses can be used to map the surface.

As the receivers are close together, it is assumed that the point on the surface from which the two echos are reflected are close together, and so the surface gradient of these two locations are equal. Therefore the surface can be found at the point at which the tangent of the first ellipse intercepts a point on the second ellipse with a tangent of the same gradient. This is illustrated in Figure 6.1.

With this knowledge it is possible to estimate a number of points along the surface using different pairs of receiving elements..

6.2.1 First Responses

Initially the first response times must be calculated. Simple threshold crossing methods have an error due to the long rise and fall times of the ultrasonic pulse [61, 60]. The firing latency is the firing delay due to the electronic circuit in the transducer. This differers depending on the transducers that are used. The firing latency is accounted for by calculating the delay caused by the latency and pulse width, and subtracting it from the first response times.

The error is calculated by setting the transducer on a sample with a known reflector that has its surface parallel to the surface of the transducer element. The transducer is fired and the time of the first and second peak response from the reflector are recorded. The travel path from the first response is exactly half that of the second response. This is because the sound bounces between the reflector and the element multiple times. The error time is calculated using:

$$t_0 = 2t'_1 - t'_2 \tag{6.2}$$

Here t_0 is the error due latency and pulse width, t_1' is the recorded time of the peak of the first response and t_2' is the recorded time of the peak of the second response.

The transducer can then be set adjacent to the inspected component with the complex surface. A coupling medium, such as a fitted perspex wedge or immersion of the part and transducer in water, must be used in order for sound to propagate into the inspected part. The first response can then be calculated using:

$$t_1 = t_1' - t_0 \tag{6.3}$$

Here, t_1 is the corrected first response time. Once the corrected first response times are obtained, the surface can be estimated using the ellipse method described above.

6.2.2 Constructing the Ellipses

The ellipses are constructed with focal points at the transmit and receive positions and first response distance from one focus point to the circumference and back. The ellipses are defined by a series of points. Two ellipses with adjacent receivers are chosen and every combination of two points on the two ellipses is tested. The surface is best described by the two points whos tangent intercepts each other. This section describes how these two points may be found.

Firstly, the ellipse is constructed from a series of points that satisfy Equation 6.4.

$$\frac{x_e}{a^2} + \frac{z_e}{b^2} = 1 \tag{6.4}$$

Here x_e and z_e are coordinates of points on the ellipse, and:

$$a = \frac{t_1}{2c_1} \tag{6.5a}$$

and

$$b = \sqrt{\frac{{t_1}^2}{c_1} + (x_v - x_t)^2 + (z_v - z_t)^2} \tag{6.5b}$$

However it is better to define the ellipse in polar coordinates, this ensures that the points are more evenly distributed. These are given by:

$$r_e(\alpha) = \sqrt{\frac{a^2 b^2}{a^2 cos^2(\alpha) + b^2 sin^2(\alpha)}} \tag{6.6a}$$

where:

$$x_e = r_e(\alpha) cos(\alpha) \tag{6.6b}$$

and:

$$z_e = r_e(\alpha) sin(\alpha) \tag{6.6c}$$

Here, α is the angle from the horizontal. α ranges from $0 \rightarrow 2\pi$ in increments that depend on how many ellipse points are generated.

The gradient of an ellipse is given by differentiating Equation 6.4:

$$\beta = tan^{-1}\left(\frac{dz}{dx}\right) = tan^{-1}\left(\frac{-b}{a^2}\frac{x_e}{\sqrt{1 - x_e^2/a^2}}\right) \tag{6.7}$$

Here dz/dx is the gradient and x_e is the x coordinate of the ellipse point. The gradient is changed into the angle from the horizontal β for simplicity.

Once the ellipse is constructed, the coordinates of the ellipses must be rotated and moved so that the focal points sit at the transmit and receive locations. The rotation is achieved using Equations 6.8a - 6.8c.

$$x'_e = x_e cos(\theta) - z_e sin(\theta) \tag{6.8a}$$

$$z'_e = x_e sin(\theta) + z_e cos(\theta) \tag{6.8b}$$

$$\theta = cos^{-1}\Big(\frac{x_v - x_a}{\sqrt{(x_v - x_a)^2 + (z_v - z_a)^2}}\Big) \tag{6.8c}$$

Here, θ is the angle of rotation, x'_e and z'_e are the new rotated coordinates, x_e and z_e are the coordinates original ellipse points, x_v and z_v are the coordinates of the virtual source, and x_a and z_a are the coordinates of the receiving element. Once the points have been rotated, they must be shifted so that they sit on the two focus points: This is done using:

$$x'_e = \frac{x_v + x_e}{2} \tag{6.9a}$$

$$z'_e = z_e + \frac{z_v}{2} \tag{6.9b}$$

It is important to calculate the new gradient of the ellipse once shifted, and is achieved by simply adding the angle of rotation to the angle of the tangent calculated in Equation 6.7:

$$\beta' = \beta + \theta \tag{6.10}$$

Here, β' is the angle of the rotated ellipse gradient to the horizontal, β is the angle of the gradient non rotated ellipse point and θ is the angle of a line between the two focal points to the horizontal.

6.2.3 Estimating the Surface

Once shifted, the two focus points of each ellipse should be sitting at the transmit and receive locations. The surface point is now estimated by

finding two points on each ellipse, both of which have a tangent that intercepts the other point.

To find the point which best represents the surface, the ellipses of two receivers are taken. Each combination of points on the two ellipses is tested. The intercept error for a point is the minimum distance between the tangent of the first point and the second point. The total intercept error is calculated by the summation of the error of the first tangent and the error of the second tangent. This is seen in equation 6.11a.

$$E_{tot} = E_1 + E_2 \tag{6.11a}$$

where:

$$E_1 = |sin(\beta_1 - \gamma)| \sqrt{(x_{e_2} - x_{e_1})^2 + (z_{e_2} - z_{e_1})^2} \tag{6.11b}$$

$$E_2 = |sin(\beta_2 - \gamma)| \sqrt{(x_{e_2} - x_{e_1})^2 + (z_{e_2} - z_{e_1})^2} \tag{6.11c}$$

$$\gamma = tan^{-1}\left(\frac{z_{e_2} - z_{e_1}}{x_{e_2} - x_{e_1}}\right) \tag{6.11d}$$

Here, γ is the angle of a line drawn between the two points with the horizontal and E is the error depicted in Figure 6.2.

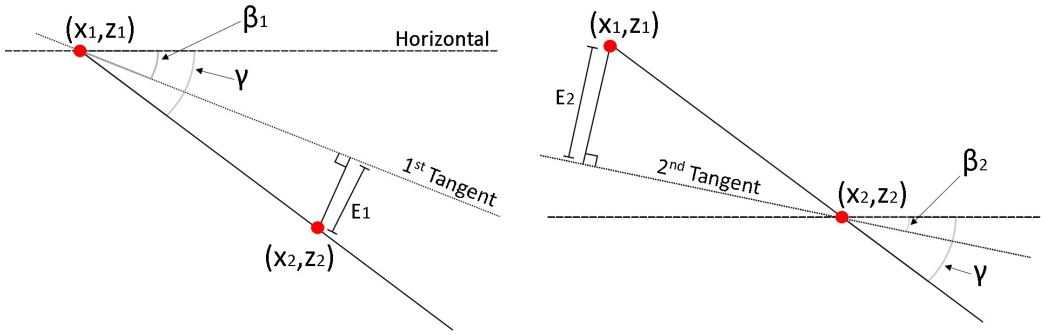


Figure 6.2: Figure Depicting the Intercept Error.

The points with the smallest combined error are selected. The middle point between these represents the surface:

$$(x_s, z_s) = \left(\frac{x_{e_1} + x_{e_2}}{2}, \frac{z_{e_1} + z_{e_2}}{2} \right) \tag{6.12}$$

The process is repeated for every adjacent receiver pair for each firing. For N_v virtual sources with an array containing N_r receivers, $N_r N_v - N_v$ surface points are generated. A least means squared technique is used to interpolate between these points to gain a more accurate representation of the surface.

To reduce computation time, it is useful to remove points on each ellipse that are known to not be surface points. For example, any points that are above the array can be removed, as sound is known to not travel in that direction. Points that are beyond the opening angle of the virtual source firing can also be removed for the same reason. Removing these points reduces the computation time required to map the surface.

6.2.4 Least Means Squared Interpolation

Once the surface is defined by a set of scatter points, a curve fitting algorithm is used to provide interpolation between points and to map the surface to a higher degree of accuracy. The surface is described by a 4th order polynomial as used in [6]:

$$z_s = \eta_0 + \eta_1 x_s + \eta_2 x_s^2 + \eta_3 x_s^3 + \eta_4 x_s^4 \tag{6.13}$$

Here, η_0, η_1 ... η_4 are the coefficients of the 4th order polynomial and z_s and x_s are the coordinates of the surface points. The aim of the least means squared method is to find the coefficients for the 4th order polynomial that gives the best fit line through the surface points generated by the surface

mapping algorithm. This is done by minimising the square of the separation between the line of best fit and the scattered points given in:

$$R^2 = \sum_{i=1}^{N} \left[z_i - (\eta_0 + \eta_1 x_i + \eta_2 x_i^2 + ... + \eta_4 x_i^4) \right]^2 \tag{6.14}$$

Here, x_i and z_i are the coordinates of the surface points generated by the surface mapping algorithm, and N is the total number of points. When the derivative of R^2 with respect to each coefficient is zero: $\frac{dR^2}{\eta_0} = 0$, $\frac{dR^2}{\eta_1} = 0$, ..., $\frac{dR^2}{\eta_4} = 0$, then the separation between the polynomial line and the each of the scatter points is at its minimum, and so this polynomial best represents the line of best fit. The derivative of R^2 with respect to the nth coefficient is given by:

$$\frac{dR^2}{d\eta_n} = \sum_{i=1}^{N} \left[z_i - \left(\eta_0 + \eta_1 x_i + ... + \eta_4 x_i^4 \right) \right] x_i^n \tag{6.15}$$

By setting $\frac{dR^2}{d\eta_n} = 0$ for all coefficients and rearranging we get:

$$\sum_{i=1}^{N} z_i x_i^n = \sum_{i=1}^{N} \left[\left(\eta_0 + \eta_1 x_i + ... + \eta_4 x_i^4 \right) \right] x_i^n \tag{6.16}$$

This can be shown in matrix form:

$$\begin{pmatrix} n & \sum_{i=1}^{N} x_i & \dots & \sum_{i=1}^{N} x_i^4 \\ \sum_{i=1}^{N} x_i & \sum_{i=1}^{N} x_i^2 & \dots & \sum_{i=1}^{N} x_i^5 \\ \vdots & \vdots & \ddots & \vdots \\ \sum_{i=1}^{N} x_i^4 & \sum_{i=1}^{N} x_i^5 & \dots & \sum_{i=1}^{N} x_i^8 \end{pmatrix} \begin{pmatrix} \eta_0 \\ \eta_1 \\ \vdots \\ \eta_4 \end{pmatrix} = \begin{pmatrix} \sum_{i=1}^{N} z_i \\ \sum_{i=1}^{N} z_i * x_i \\ \vdots \\ \sum_{i=1}^{N} z_i * x_i^4 \end{pmatrix} \tag{6.17}$$

By multiplying both sides of Equation 6.17 by the inverse of the matrix on the left hand side, the array of best fit polynomial coefficients can be found:

Using these coefficients, interpolation between the already existing surface points is achieved.

$$\begin{pmatrix} \eta_0 \\ \eta_1 \\ \vdots \\ \eta_4 \end{pmatrix} = \begin{pmatrix} n & \sum_{i=1}^{N} x_i & \dots & \sum_{i=1}^{N} x_i^4 \\ \sum_{i=1}^{N} x_i & \sum_{i=1}^{N} x_i^2 & \dots & \sum_{i=1}^{N} x_i^5 \\ \vdots & \vdots & \ddots & \vdots \\ \sum_{i=1}^{N} x_i^4 & \sum_{i=1}^{N} x_i^5 & \dots & \sum_{i=1}^{N} x_i^8 \end{pmatrix}^{-1} \begin{pmatrix} \sum_{i=1}^{N} z_i \\ \sum_{i=1}^{N} z_i * x_i \\ \vdots \\ \sum_{i=1}^{N} z_i * x_i^4 \end{pmatrix} \tag{6.18}$$

6.2.5 Outlying Points + Other Errors

Outlying points that do not represent the surface usually occur due to discontinuities in the first responses. The discontinuities are caused by the first response signals coming from different areas and so the surface assumption that the gradient off which they reflected is equal does not hold. These points must be removed or else they create outlying points that do not represent the surface and cause error when interpolating between the surface points.

The discontinuities in the first response can be found by using Equation 6.19.

$$dF = \left|2F_i - (F_{i-1} + F_{i-2})\right| \tag{6.19}$$

By calculating the difference between the two previous first response times (F_{i-2} and F_{i-1}) and adding it to the previous first response time F_{i-1}, the first response of the ith element can be approximated. By subtracting this prediction from the actual first response time F_i the difference between the predicted and real can be calculated dF. Assuming that the change in the first responses is smooth then dF is small. A discontinuity in the first response causes a large dF value.

The average magnitude at which dF changes depends on the surface geometry. For a planar surface $dF = 0$. For a more complex surface it is expected that dF has a non zero value. A large dF can be judged by values

outside of three times the standard deviation and surface points generated by discontinuities in the first response are removed.

Another source of outlying points is the error in the first response. The transducer records the amplitude with time discretely at a given sampling frequency set by the user. If the elements are close together, the difference in time between the first responses from adjacent elements is small and is greatly affected by any error caused by the sampling frequency. To minimise this error, instead of using adjacent element pairs to construct the ellipses, elements that are adjacent but one are selected. The same algorithm is then used to map the surface. This effectively doubles the element separation such that the difference in first response times is greater, reducing the error from the sampling frequency. However by doing this, the assumption that the surface gradient from which the two echoes reflected off is equal, is less likely to be true. Therefore care must be taken to ensure that doing this does not introduce other errors.

6.3 TFM Imaging Algorithm through Dual Layered Media

TFM is performed through a refractive boundary using Equation 6.20.

$$I(x,z) = \sum_{t=1}^{N_t} \sum_{r=0}^{N_r} A_{t,r}(p_1 + p_2) \tag{6.20}$$

This is the standard TFM algorithm. Here, $I(x,z)$ is the intensity of the pixel at a point defined by coordinates x and z, N_t and N_r are the number of transmitters and receivers respectively. $A_{t,r}(p)$ is the amplitude of the A-scan for the rth receiver and tth transmitter at time p. p_1 and p_2 are the time of flights for the paths to and from the pixel, through the refractive boundary, respectively. The time of flight for a given path can be calculated

using Fermat's principle. To find this path, a number of points on the surface are taken and an iterative process calculates the time of flight at each point to find the minimum. The time of flight for a given path is given in Equation 6.21.

$$p = \frac{\sqrt{(x_v - x_s)^2 + (z_v - z_s(x_s))^2}}{c_1} + \frac{\sqrt{(x_s - x)^2 + (z_s(x_s) - z)^2}}{c_2} \tag{6.21}$$

Here, p is the time of flight of the given path, x_v and z_v are the x and z coordinate of the virtual source, x_s and $z_s(x_s)$ are the x and z coordinate of the considered surface point, x and z are the coordinates of the pixel and c_1 and c_2 are the velocities of the first and second medium respectively.

6.3.1 Time of Flight Calculation - Gradient Method

When calculating the time of flight using Fermat's principle for the TFM algorithm, the approach of iterating through the boundary and calculating the least time at every point is computationally expensive. The gradient approach is used to eliminate the exhaustive search along a boundary to find the least time. Instead of calculating the time of flight at each point, the gradient of the time of flight function is found. The location at which the gradient is equal to zero is equal to the minimum point of the time of flight function. The gradient for the time of flight is easily differentiated from Equation 6.21 with respect to x_s and is given in Equation 6.22a. The $\frac{dz_s}{dx_s}$ term in Equation 6.22a is given by differentiating the 4th order polynomial, shown in Equation 6.13, that is used to describe the surface.

$$\frac{dt}{dx_s} = \frac{1}{c_1}\frac{(x_s - x_v) + (z_s - z_v)\frac{dz_s}{dx_s}}{\sqrt{(x_v - x_s)^2 + (z_v - z_s)^2}} + \frac{1}{c_2}\frac{(x_s - x) + (z_s - z)\frac{dz_s}{dx_s}}{\sqrt{(x_s - x)^2 + (z_s - z)^2}} \tag{6.22a}$$

where:

$$\frac{dz_s}{dx_s} = \eta_1 + 2\eta_2 x + 3\eta_3 x^2 + 4\eta_4 x^3 \tag{6.22b}$$

Equation 6.22a gives the change of the time of flight with position along the surface. The minimum time of flight is given when $dt/dx_s = 0$. It can be seen that the time of fight diverges: $t \to \infty$ as $x_s \to \pm\infty$. Therefore, the gradient of the time of flight function is negative as $x \to -\infty$ and positive as $x \to \infty$. The function passes through zero at the minimum point of the time of flight. Therefore the direction of the minimum point relative to an arbitrary location on the surface can be found by looking at the sign of the gradient.

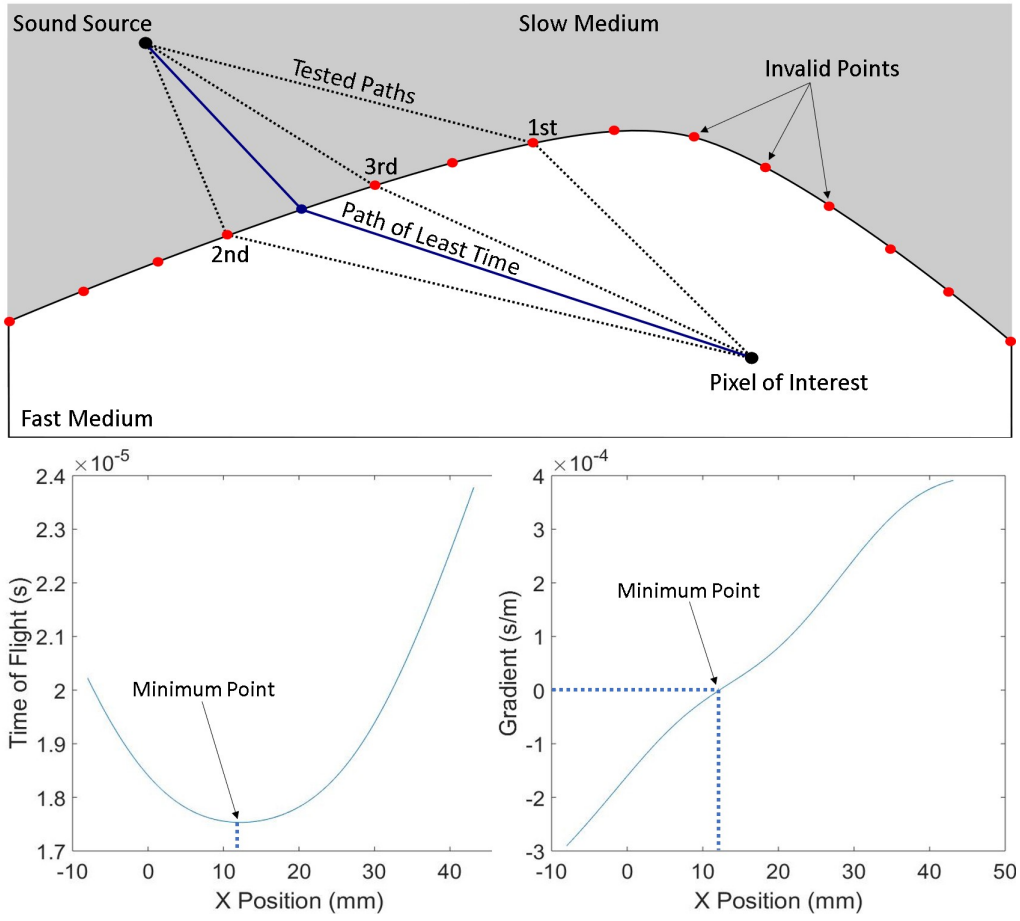


Figure 6.3: Depiction of the Fast Fermat method on an arbitrary surface.

The Fast Fermat's approach, depicted in Figure 6.3, works by defining a set of points that describe the surface, the number of which is an order

of two. The gradient of the middle point is taken and the direction of the minimum point can be found. Half of the points in the other direction are then disregarded. The gradient of the midpoint of the remaining points is then considered, and so half of the remaining points are then disregarded. This process is continually iterate until a single point remains where the gradient is closest to zero. Then, using this surface coordinate, the time of flight is calculated.

This process incurs an error: the surface point chosen has a 50% chance of being out by 1. This can occur if the iterations land on the minimum point before the end of the process. Thus the final surface point taken is adjacent to the real minimum point. To reduce this error, it is advantageous to calculate the surface point either side of the final point, and take the minimum. This way the fast Fermat method is as accurate as the iteration method but with a reduced number of calculations. If it is assumed that the time taken is directly proportional to the number of calculations required, the processing time is reduced from an order of $\mathcal{O}(N)$ to $\mathcal{O}(log_2(N))$ using this method, making real time focussing a possibility.

6.4 Other Surface mapping methods

This section briefly describes other surface mapping methods. These methods are compared to the VSSM method in the results section of this chapter.

6.4.1 Dipping Reflector Algorithm

The dipping reflector (DR) algorithm [6] is depicted in Figure 6.4. Each element transmits and receives individually. As with the VSSM method, it is assumed that for two adjacent receivers the surface off which the first

echo reflected has equal gradient. Using this assumption, the position of the surface can be calculated using Equations 6.23a and 6.23b.

$$x_s = \frac{t}{c}\, sin\left(sin^{-1}\left(\frac{dt}{2cp}\right)\right) \tag{6.23a}$$

$$z_s = \frac{t}{c}\, cos\left(sin^{-1}\left(\frac{dt}{2cp}\right)\right) \tag{6.23b}$$

Here, x_s and z_s are the x and z coordinates of the surface point for a receiver sat at the origin. t is the time of the first echo, c is the velocity of the medium, dt is the difference in time of flight between the two adjacent receiving elements and p is the spacing between elements.

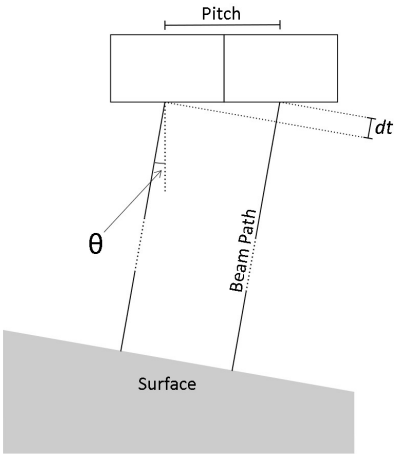


Figure 6.4: Depiction of how the Dipping Reflector Algorithm can be used to map the surface of an inspected component.

This method is commonly used as it is generally known to be the most accurate of the ultrasonic surface mapping methods [57]. The data used for this method is included in the full matrix of data, and therefore this method is useful when imaging using FMC-TFM [6].

6.4.2 Plane Wave Surface Mapping Algorithm

The plane wave surface mapping method (PWSM), involves a 0^o planar wave front as depicted in Figure 6.5. The algorithm, derived in [57], uses

the same assumption that the surface gradient reflecting sound for two adjacent receivers is equal. The surface coordinates can be given by:

$$x_s = x_i' = x_i + tan(\alpha_i)cT_i \tag{6.24a}$$

$$z_s = z_i' = \frac{(x_i' - x_i)^2}{2cT_i} \tag{6.24b}$$

$$tan(\alpha_i) = \frac{-p + \sqrt{p^2 - c^2(T_{i+1} - T_i)^2}}{c(T_{i+1} - T_i)} \tag{6.24c}$$

Here x_i' and z_i' are the surface coordinates for the receiver i, x_i is the x coordinate of the receiver i, R_i is the return path of the sound depicted in Figure 6.5. T_i is the total time of flight for the receiver i and α_i is the gradient of the surface off which the wave is reflected.

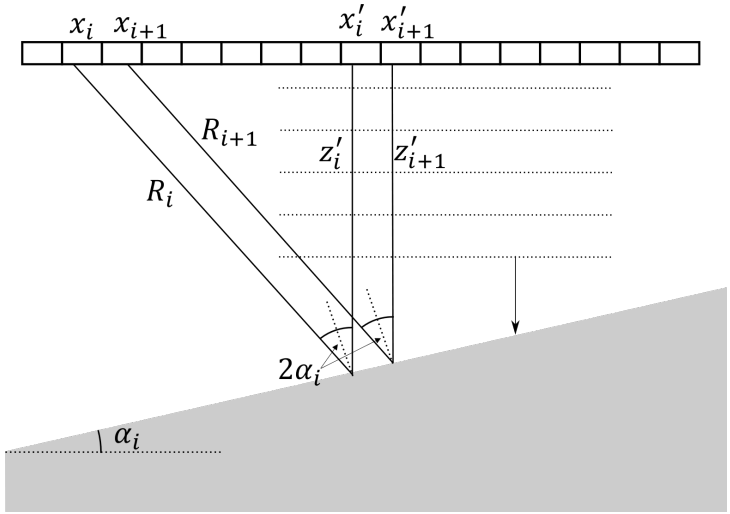


Figure 6.5: Depiction of how a planar wave may be used to map the surface of an inspected component.

6.5 Testing the VSA Surface Mapping Technique

The VSSM technique was tested on a series of components with complex geometry. Each component was mapped using the VSSM technique, but also the DR method and the PWSM method for comparison.

6.5.1 Setup

An Olympus 5L64 array transducer was used. The centre frequency of each element was 5MHz, with a pitch of 0.6mm and there were 64 elements in total. The DR method required each element to transmit and receive individually, collecting 64 amplitude scans. The plane wave surface mapping algorithm required all elements to be transmitted at the same time while individually receiving on all elements.

The virtual source transmissions used a 16 element sub aperture. For each sub aperture firing, all array elements would receive individually. The sub aperture was incremented by 8 elements after each firing, until all elements on the array were used in at least one transmission. This gave a total of 7 virtual source firings. The 6dB half angle of a 5MHz centre frequency element with a 0.6mm width in perspex (velocity $2750ms^{-1}$) is 28^o. The opening angle of the virtual source must be shallower than this in order for the beam properly to form. Setting the vertical position of the virtual source behind the aperture as 11mm gave an opening angle of 22^o. This was deemed sufficient for the inspection. The ellipses were constructed using the first responses. The sampling frequency used was 50MHz and the angular spacing of the ellipse points was 0.125^o.

Due to the nature of the transmit and receive paths, the difference in receive time between adjacent elements for a virtual source or plane wave transmission is likely to be less than the single element transmissions. Therefore the VSSM and PWSM algorithms are more likely to be affected by errors due to the sampling frequency than the DR algorithm. To account for this, it may be more efficient to use pairs of receivers separated by a single element. This was also investigated for VSSM and PWSM with only only adjacent elements pairs used for the DR algorithm.

The transducer was placed upon the test sample and the three transmission sequences were conducted in a short space of time to ensure that all three data types were acquired at the same location.

6.5.2 Testing Components

Each component had a fitted perspex wedge designed to couple the transducer to the component. Three components with a sinusoidal surface of wavelength of 40mm and amplitude of 1mm, 2mm, 4mm respectively were used. These can be seen depicted in Figure 6.6. The surface geometry of the sinusoidal surface is given by:

$$z_s = 25 + Asin\left(\frac{2\pi x_s}{40} + \theta\right) \tag{6.25}$$

Here, z_s is the depth of the surface at position x_s, A is the amplitude value for the deviation of the surface and θ is an arbitrary phase constant related to the horizontal position of the centre of the array relative to the surface.

Another component, depicted in Figure 6.7, was used and had a surface described by the quadratic equation:

$$z_s = 0.01(x_s - r)^2 \tag{6.26}$$

Here, r is the array centre distance relative to the shallowest part of the wedge.

The surface of each component was mapped using the DR, VSSM and PWSM techniques. For the sinusoidal components, the surface was mapped from above a peak, above the trough and somewhere in the middle. The quadratic component was inspected from above the shallowest part of the wedge.

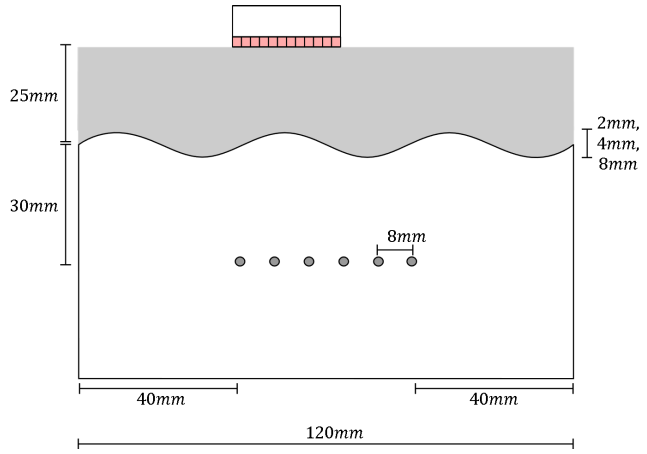


Figure 6.6: Depicting the component with the sinusoidal surface.

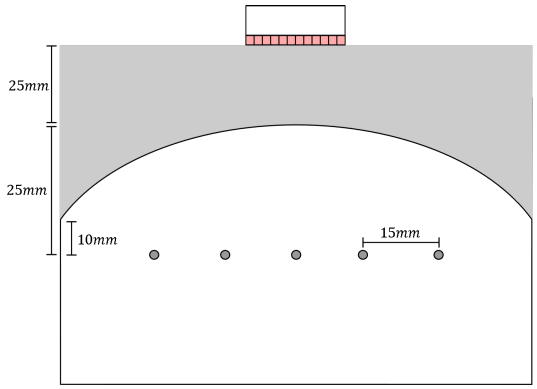


Figure 6.7: Depicting the component with the quadratic surface.

6.5.3 Accurately Determining the Surface Relative to the Transducer

Although the surface geometry and the dimensions of the fitted perspex wedge was known accurately, the horizontal position of the transducer relative to the surface was estimated only by eye. This introduced error. Validating the surface mapping techniques would require the surface geometry relative to the transducer to be known accurately. To do this, the constants θ and r must be found for the sinusoidal and quadratic components respectively.

To find θ for the sinusoidal components the TFM was used. The surface was estimated using an arbitrary value for θ, and a TFM image was generated in the region where the SDH were expected to be. Then the

value of θ was varied, taking a TFM image each for each change in θ. The surface was deemed to be when the SDHs were most focussed and the contrast between the peak value of the TFM image relative to the background highest. The method used is similar to the one described in [52] where the positions of a conformable array are found by maximising the contrast of a TFM image while varying the predicted positions of the array elements in space.

Once accurate surface information was acquired, the surface mapping techniques were tested against this.

6.6 Results

The results for the surface mapping techniques can be seen in Figures 6.8a and 6.8b. The error shown was calculated by taking the mean of the absolute value of the difference between the known geometry and the best fit curve interpolating between the surface points generated by each respective algorithm. It is shown that the DR method is consistently the most accurate of the three techniques across all of the samples tested. For relatively simple surfaces, the accuracy of the VSSM technique is similar to that of the DR. However the DR technique performs better than the VSSM on more complex surfaces. The results indicate that the PWSM technique performs more poorly than the VSSM and DR techniques.

In general, the simpler surfaces are mapped more accurately. The sinusoidal surface with an amplitude of ± 1mm is mapped to an accuracy of ± 0.05mm using the VSSM technique. As the amplitude of the sinusoidal surface increases, the error is also increased. The ± 2mm sinusoidal surface tends to be mapped to an accuracy of below ± 0.1mm using the VSSM technique and below ± 0.2mm for the ± 2mm sinusoidal surface. The DR

technique tends to be more accurate than the VSSM technique overall, while the PWSM tends to be less accurate.

The cause of the increasing error with surface amplitude is that the first echo recorded tends to return from the closest reflector. If the transducer array is moved above a deep trough, it is less likely that the first response will come from the deepest part of the trough. It is more likely that the first echoes recorded come from the peak or sides of the trough which is closer to the transducer. As less information is included in the deeper parts of the trough, the interpolation curve fitted to the points is less likely to be accurate. This is also supported by the fact that the most accurate surfaces mapped were the sinusoidal 1mm peak, the sinusoidal 2mm peak and the quadratic, where were all relatively shallow peaks. This where when the transducer was located closest to the surface.

Another cause of this error is that as the amplitude of the surface is increased, the gradient between the peak and the trough becomes steeper. This increases the likelyhood that sound hitting this part of the surface is reflected away from the transducer. As no sound from these areas return to the probe, no information on this part can be gathered, reducing the accuracy of the surface mapping technique.

Figures 6.9a and 6.9b show the standard deviation of the distance between the surface mapping points generated by each respective algorithm and the known surface geometry. The difference in surface mapping error between using adjacent receivers and non-adjacent receivers appears to be negligible by looking at the error in the interpolated line. However it can be seen in Figures 6.9a and 6.9b that the points generated by the algorithm using non-adjacent receivers has improved the accuracy of the surface mapping method because the points generated by the algorithm lie, on average, closer to the known surface geometry. By

using non-adjacent elements, the surface point fluctuation for VSSM and PWSM falls closer to the levels of the DR, and even below in some cases.

The individual cases for each of the results shown in Figures 6.8 and 6.9 can be seen in Figures 6.10, 6.11, 6.12, 6.13, 6.14, 6.15, 6.16, 6.17, 6.18 and 6.19. These figures show the original surface points generated by the algorithm, the line of best fit plotted to interpolate between these points and the known geometry of the surface. There are more plotted points for the VSSM techniques, this is because 7 transmissions are used while all elements receive giving $7 \times 64 = 448$ possible points. The PWSM uses a single transmission where all elements receive and the DR uses data from the individual element transmitting and receiving alone, both giving 64 points.

It can be seen that the part of the surface mapped by the algorithm favours the highest point on the surface, as large clusters of points accumulate around these points. The shallower troughs of the sinusoidal surface tends to be mapped more accurately than the deeper ones. This is because fewer points are generated in the deeper parts of the trough, making the interpolation line less accurate. This because the first response is more likely to come from the areas of the surface closest to the transducer.

The points between the trough and the peak are also poorly mapped in a number of locations. This is because the increasing surface gradient is more likely to reflect sound away from the transducer. This leaves large areas of the surface without any information at all, which is a cause of error. The peaks and troughs, where the component surface is normal to the transducer surface, have more information. This allows the best fit line to interpolate between the areas of the surface where no information was acquired.

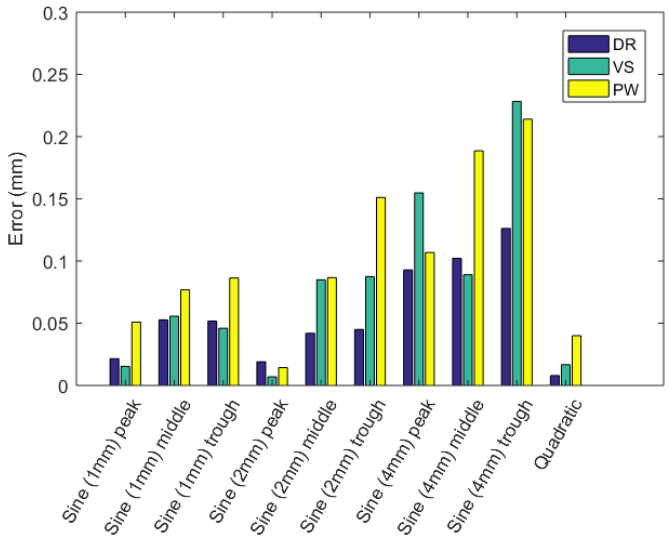
6.7 Conclusions

The results indicate that the VSSM technique is less reliable than the DR technique, but more reliable than the PWSM. For relatively simple surfaces, the VSSM performs comparably to the DR. As the complexity of the surface increases, the error increases for all techniques, however the error does seem to increase more substantially for the VSSM compared to the DR. The accuracy of the VSSM technique can be improved by using non-adjacent element receiver pairs in the algorithm.

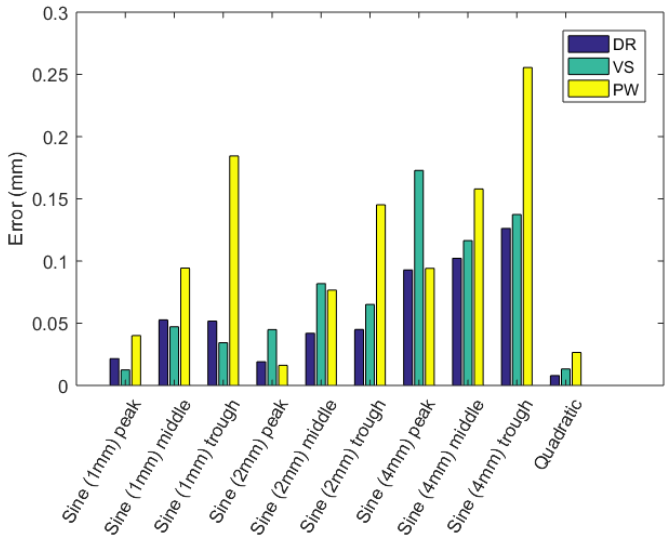
For relatively simple surfaces, the advantages of using VSA-TFM can be retained. For simple surfaces, the surface mapping technique is no less accurate than the DR used for with FMC-TFM. One firing sequence may be used to map the surface and image underneath, and as VSA may use less firings than FMC without detriment to the image quality. This heavily depends on the implementation. However in theory the overall inspection speed using VSA on complex parts may increase. This is an area for further research. The VSSM algorithm can be computationally expensive, especially when many ellipse points are considered. Further work must be conducted to see the effect that reducing the number of ellipse points has on the accuracy of the VSSM technique.

For more complicated surfaces, the DR is more suitable a technique. Therefore to use VSA, two firing sequences must be used, one for surface mapping and another for imaging. Whether the advantages of using VSA still exist in this case requires further investigation.

Figure 6.8: Showing the errors in the DR, VSSM and PWSM techniques using adjacent receivers (6.8a) and non-adjacent receivers (6.8b).

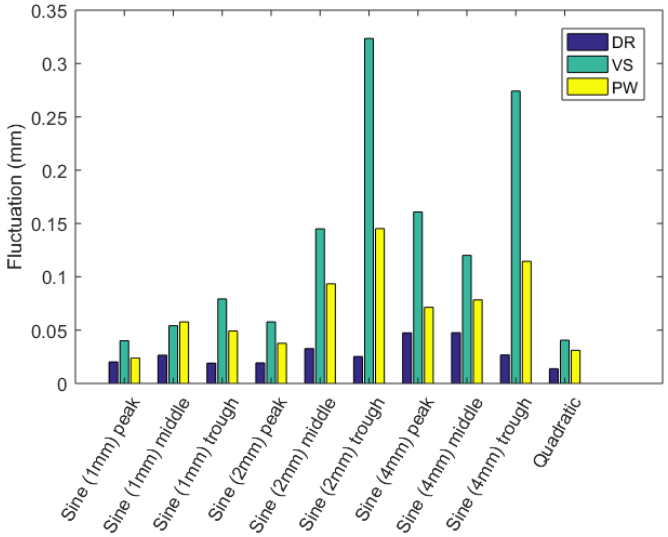


(a) Surface error for adjacent receivers.

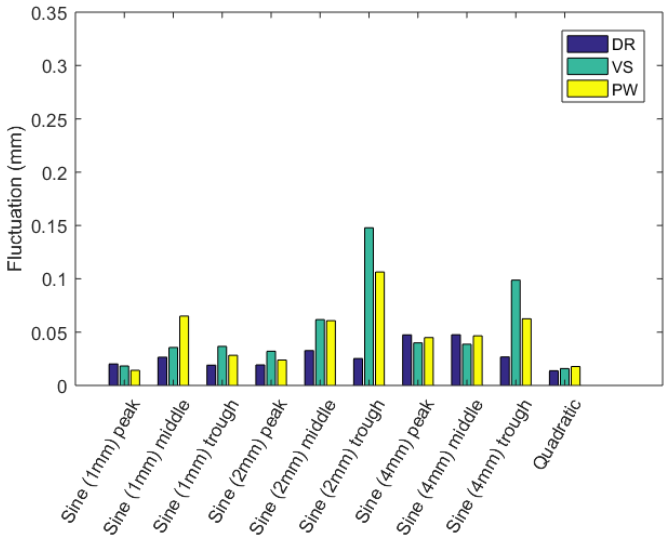


(b) Surface error for non-adjacent receivers for the VSSM and PWSM technique. The DR using adjacent element receivers is included for reference.

Figure 6.9: Figure showing the surface point fluctuation in the DR, VSSM and PWSM techniques using adjacent receivers (6.9a) and non-adjacent receivers (6.9b).



(a) Figure showing the surface point fluctuation in the DR, VSSM and PWSM techniques using adjacent receivers.



(b) Surface point fluctuation for the VSSM and PWSM techniques for receiver pairs separated by an element. Alongside is the DR using adjacent receivers for reference.

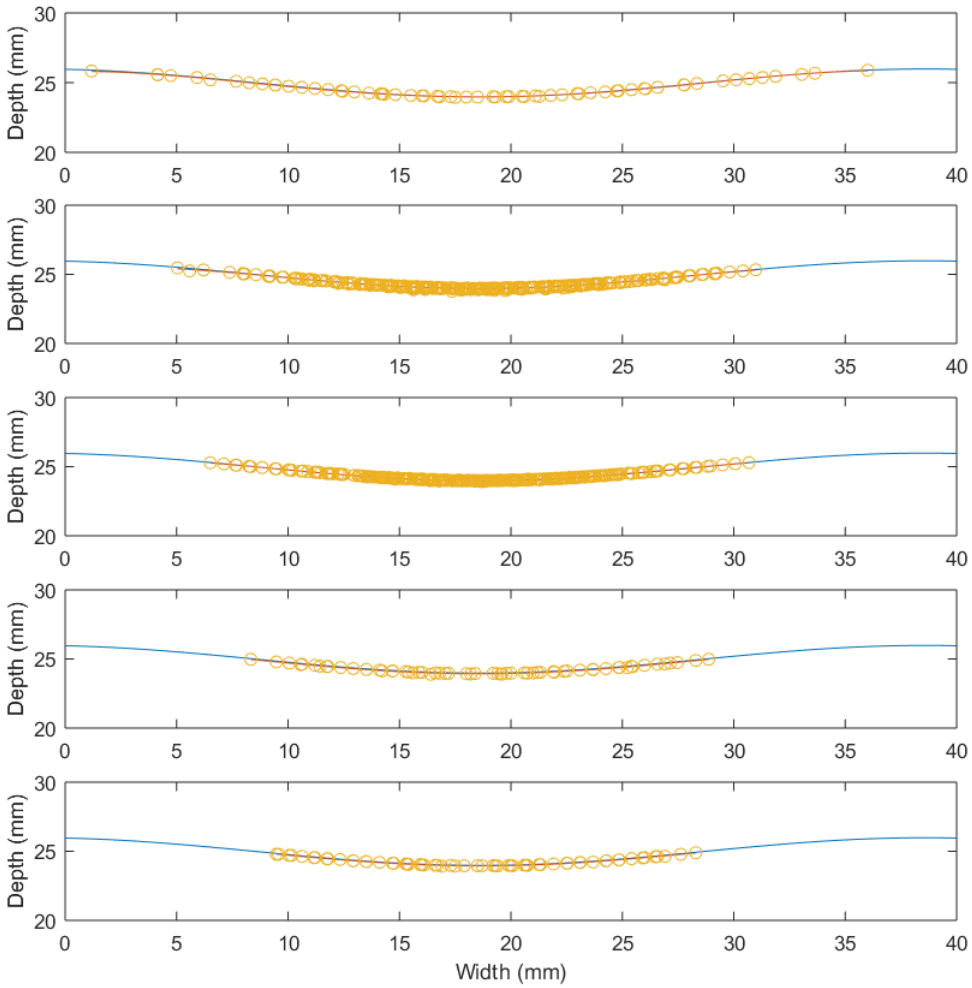


Figure 6.10: $\pm 1mm$ Sinusoidal Peak - Figure showing the surface mapping results for the sinusoidal surface with amplitude of 1mm. This was taken above the peak of the surface. The yellow plotted points are the points from the surface mapping algorithm. The orange line is the best fit curve interpolating between these points. The blue line is the known surface geometry. The top image shown is from the DR technique, the next is the VSSM with adjacent elements, then the VSSM with non-adjacent elements, then the PWSM with adjacent elements. The bottom image is the PWSM with non-adjacent elements.

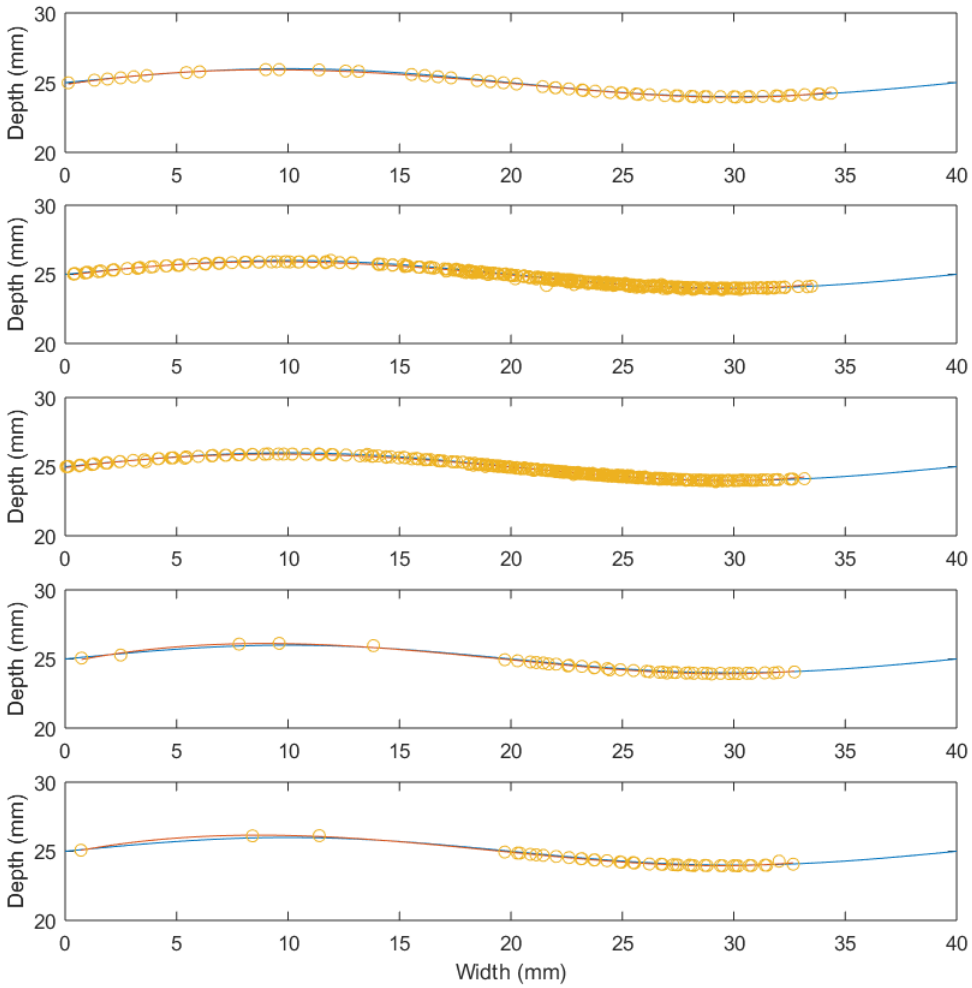


Figure 6.11: $\pm 1mm$ Sinusoidal Middle - Figure showing the surface mapping results for the sinusoidal surface with amplitude of 1mm. This was taken from somewhere between the peak and the trough. The yellow plotted points are the points from the surface mapping algorithm. The orange line is the best fit curve interpolating between these points. The blue line is the known surface geometry. The top image shown is from the DR technique, the next is the VSSM with adjacent elements, then the VSSM with non-adjacent elements, then the PWSM with adjacent elements. The bottom image is the PWSM with non-adjacent elements.

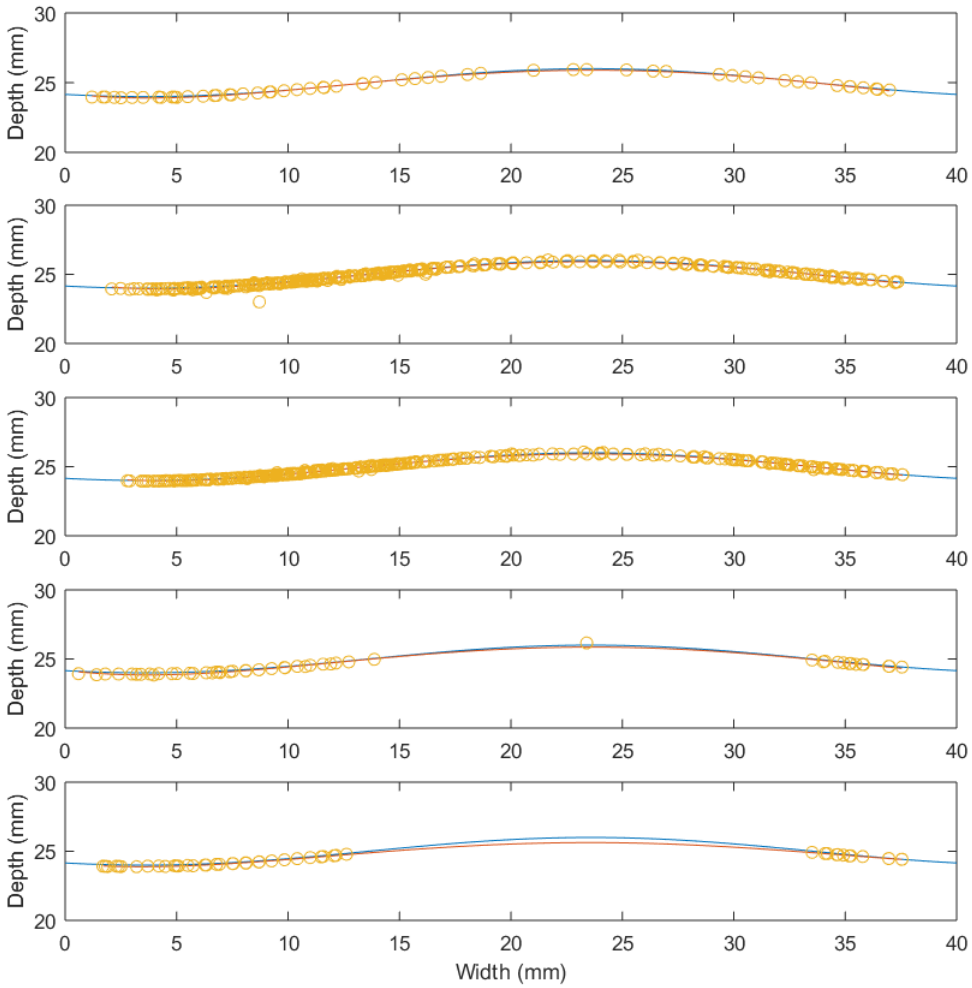


Figure 6.12: $\pm 1mm$ Sinusoidal Trough - Figure showing the surface mapping results for the sinusoidal surface with amplitude of 1mm. Here, the transducer was above the trough at when mapping the surface. The yellow plotted points are the points from the surface mapping algorithm. The orange line is the best fit curve interpolating between these points. The blue line is the known surface geometry. The top image shown is from the DR technique, the next is the VSSM with adjacent elements, then the VSSM with non-adjacent elements, then the PWSM with adjacent elements. The bottom image is the PWSM with non-adjacent elements.

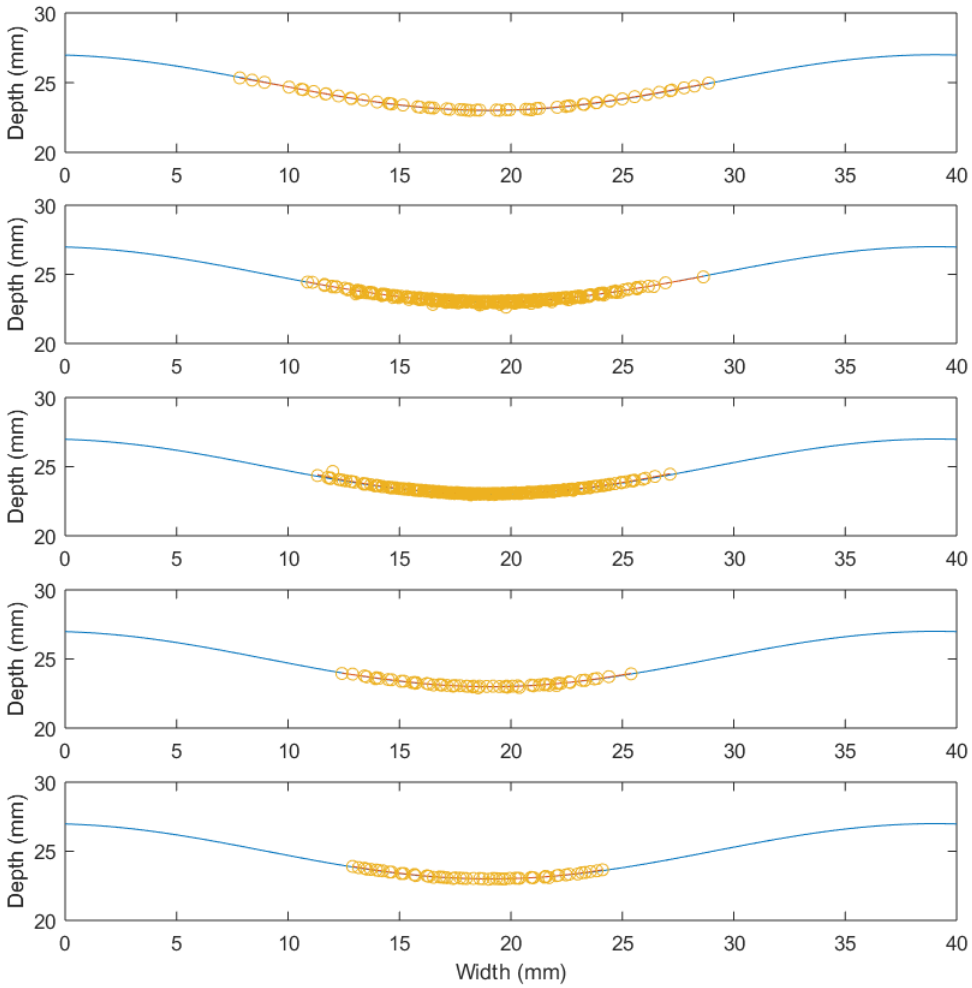


Figure 6.13: $\pm 2mm$ Sinusoidal Peak - Figure showing the surface mapping results for the sinusoidal surface with amplitude of 2mm. This was taken above the peak of the surface. The yellow plotted points are the points from the surface mapping algorithm. The orange line is the best fit curve interpolating between these points. The blue line is the known surface geometry. The top image shown is from the DR technique, the next is the VSSM with adjacent elements, then the VSSM with non-adjacent elements, then the PWSM with adjacent elements. The bottom image is the PWSM with non-adjacent elements.

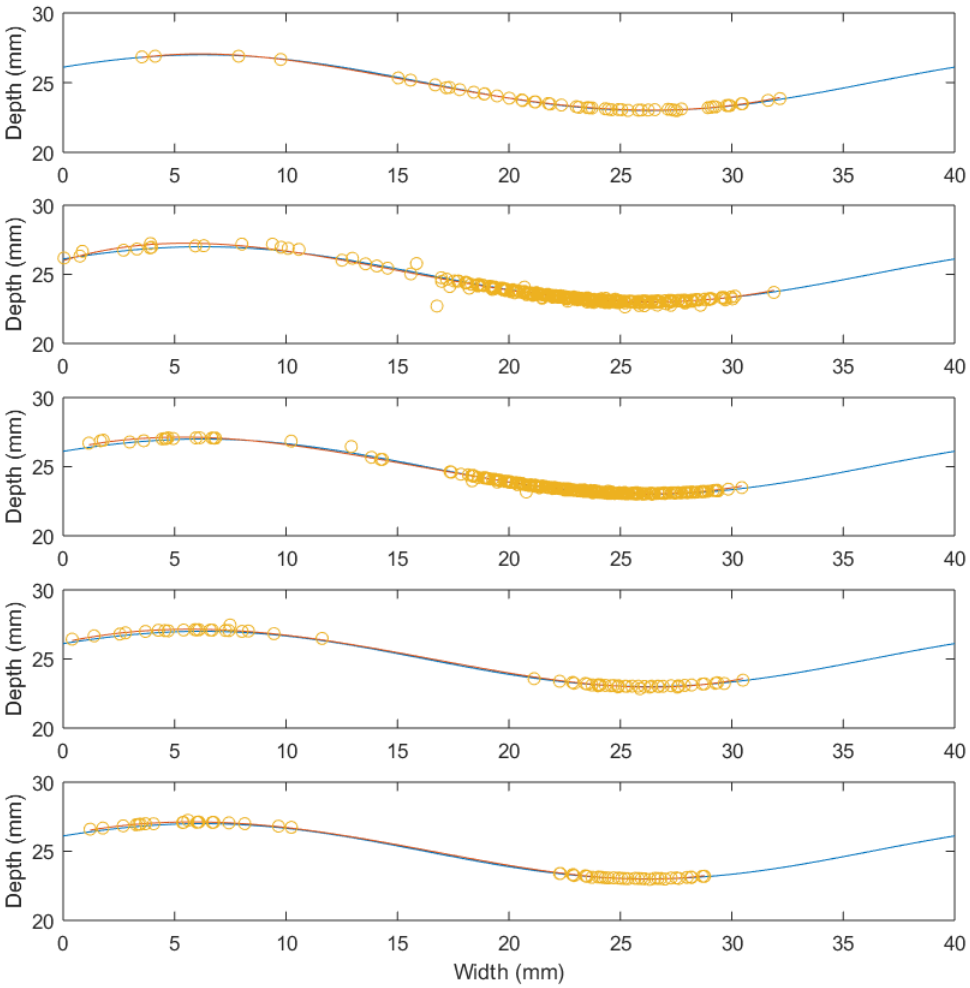


Figure 6.14: $\pm 2mm$ Sinusoidal Middle - Figure showing the surface mapping results for the sinusoidal surface with amplitude of 2mm. This was taken from somewhere between the peak and the trough. The yellow plotted points are the points from the surface mapping algorithm. The orange line is the best fit curve interpolating between these points. The blue line is the known surface geometry. The top image shown is from the DR technique, the next is the VSSM with adjacent elements, then the VSSM with non-adjacent elements, then the PWSM with adjacent elements. The bottom image is the PWSM with non-adjacent elements.

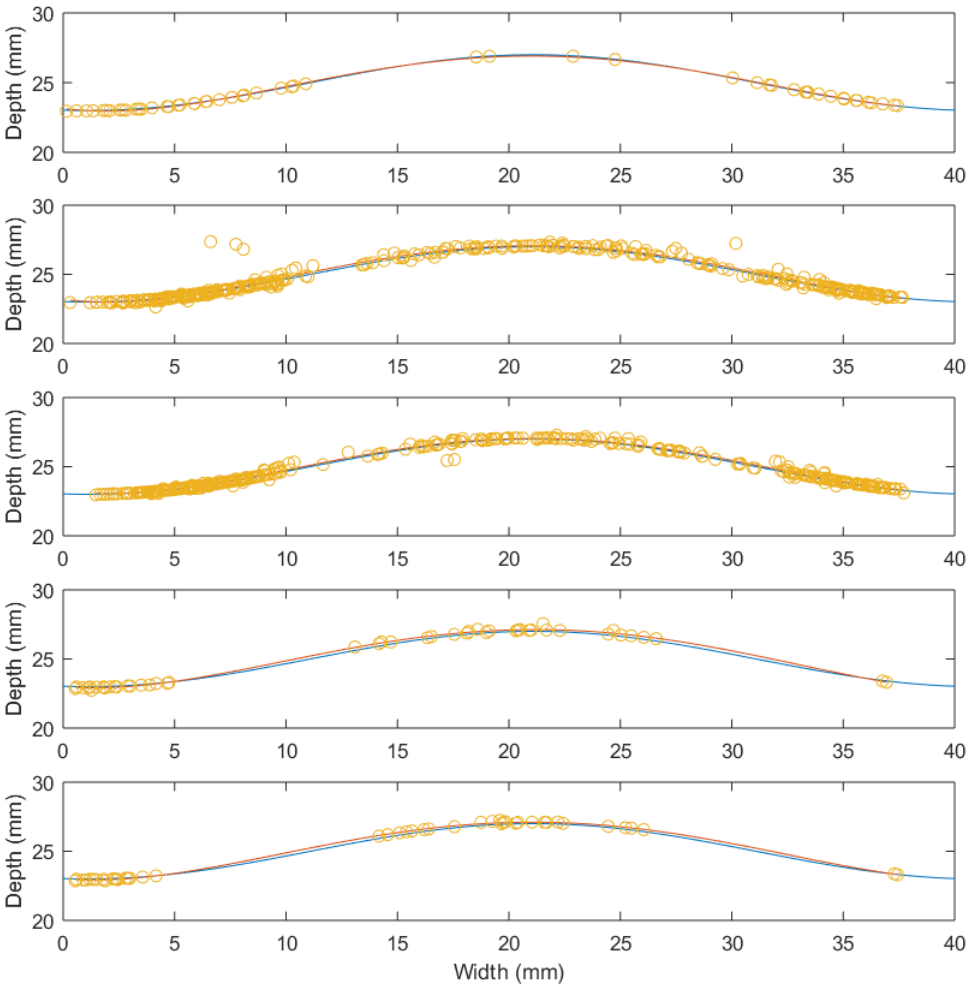


Figure 6.15: $\pm 2mm$ Sinusoidal Trough - Figure showing the surface mapping results for the sinusoidal surface with amplitude of 2mm. Here, the transducer was above the trough at when mapping the surface. The yellow plotted points are the points from the surface mapping algorithm. The orange line is the best fit curve interpolating between these points. The blue line is the known surface geometry. The top image shown is from the DR technique, the next is the VSSM with adjacent elements, then the VSSM with non-adjacent elements, then the PWSM with adjacent elements. The bottom image is the PWSM with non-adjacent elements.

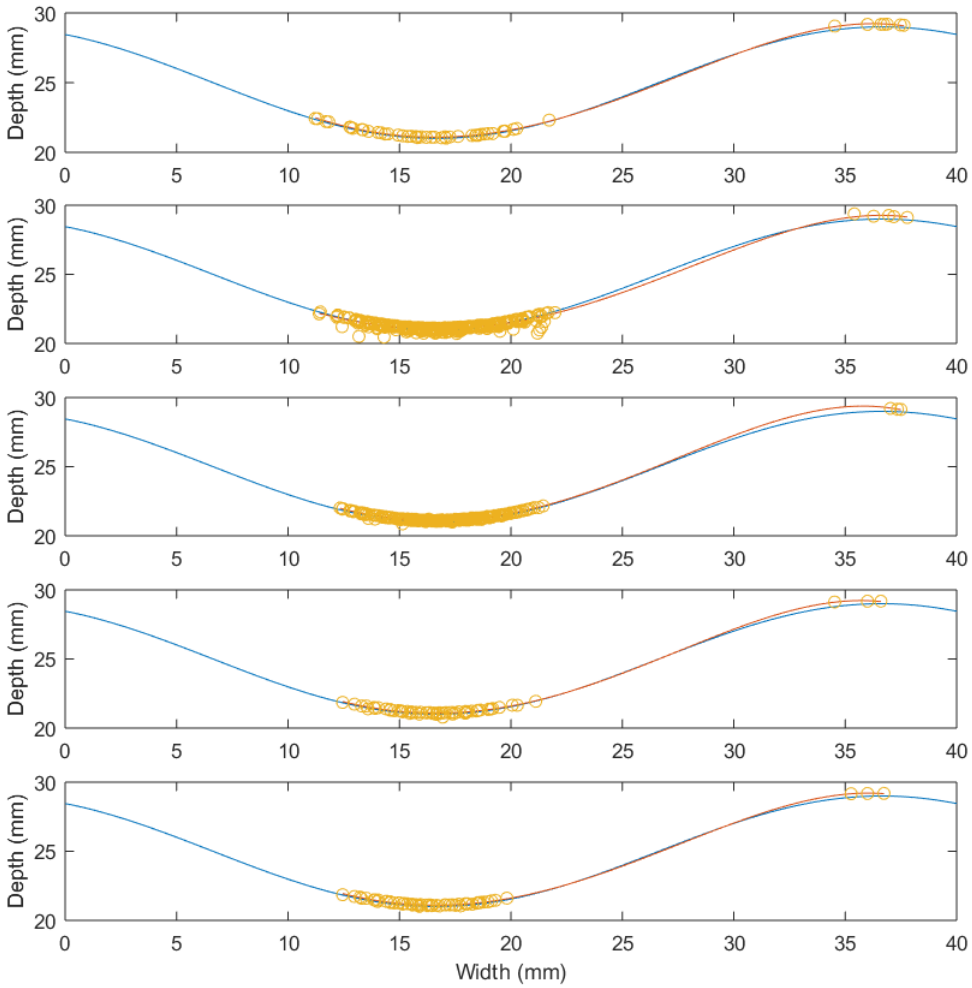


Figure 6.16: $\pm 4mm$ Sinusoidal Peak - Figure showing the surface mapping results for the sinusoidal surface with amplitude of 4mm. This was taken above the peak of the surface. The yellow plotted points are the points from the surface mapping algorithm. The orange line is the best fit curve interpolating between these points. The blue line is the known surface geometry. The top image shown is from the DR technique, the next is the VSSM with adjacent elements, then the VSSM with non-adjacent elements, then the PWSM with adjacent elements. The bottom image is the PWSM with non-adjacent elements.

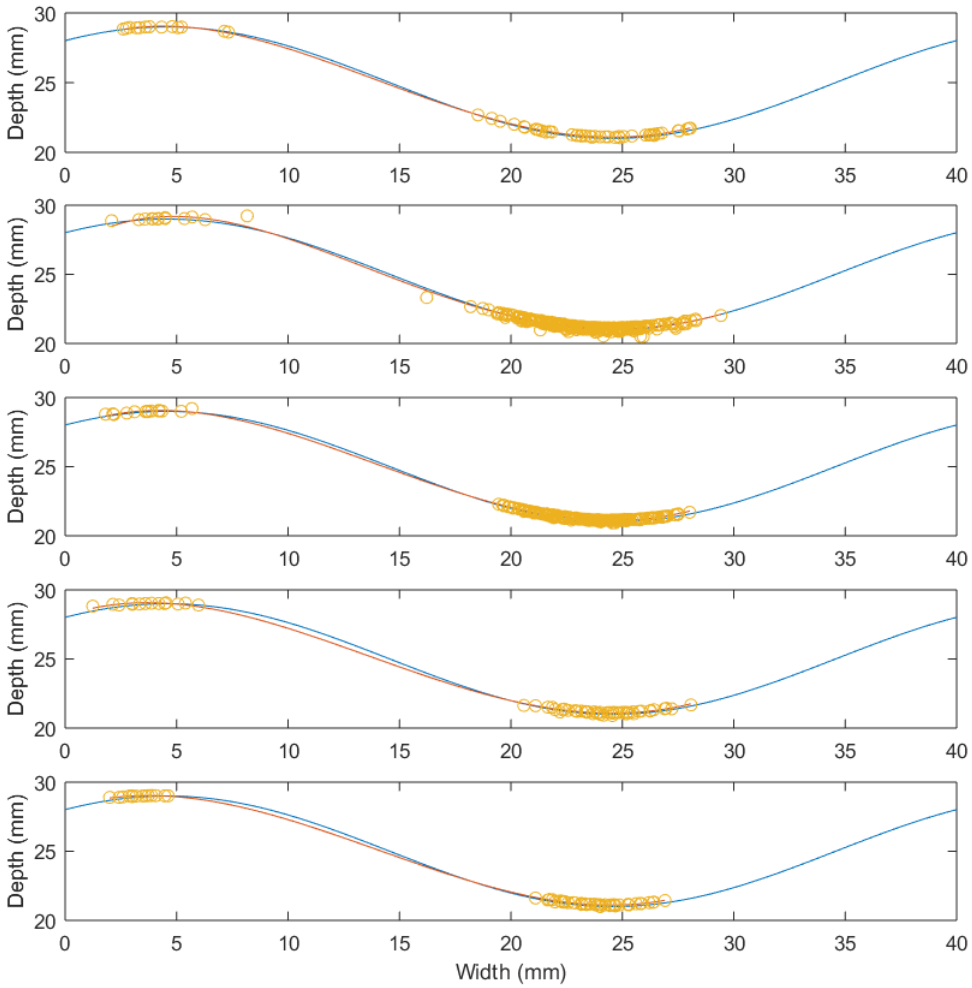


Figure 6.17: $\pm 4mm$ Sinusoidal Middle - Figure showing the surface mapping results for the sinusoidal surface with amplitude of 4mm. This was taken from somewhere between the peak and the trough. The yellow plotted points are the points from the surface mapping algorithm. The orange line is the best fit curve interpolating between these points. The blue line is the known surface geometry. The top image shown is from the DR technique, the next is the VSSM with adjacent elements, then the VSSM with non-adjacent elements, then the PWSM with adjacent elements. The bottom image is the PWSM with non-adjacent elements.

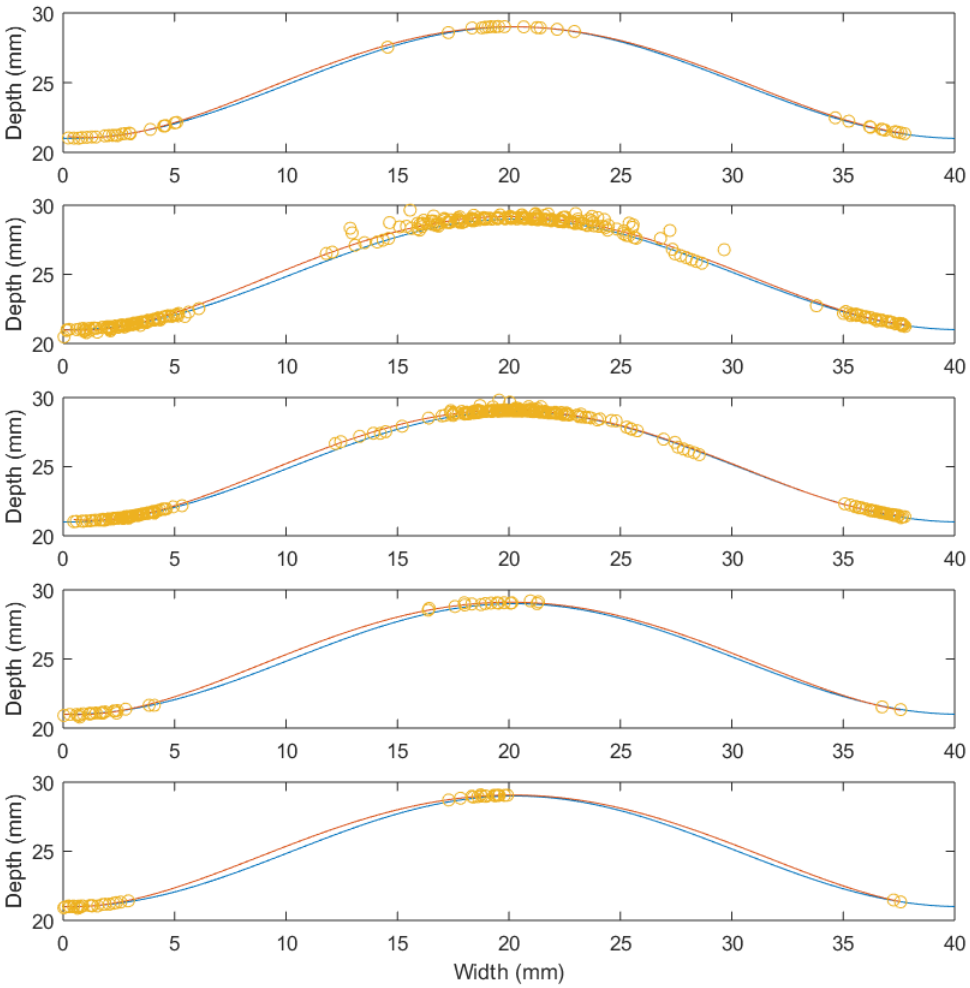


Figure 6.18: $\pm 4mm$ Sinusoidal Trough - Figure showing the surface mapping results for the sinusoidal surface with amplitude of 4mm. Here, the transducer was above the trough at when mapping the surface. The yellow plotted points are the points from the surface mapping algorithm. The orange line is the best fit curve interpolating between these points. The blue line is the known surface geometry. The top image shown is from the DR technique, the next is the VSSM with adjacent elements, then the VSSM with non-adjacent elements, then the PWSM with adjacent elements. The bottom image is the PWSM with non-adjacent elements.

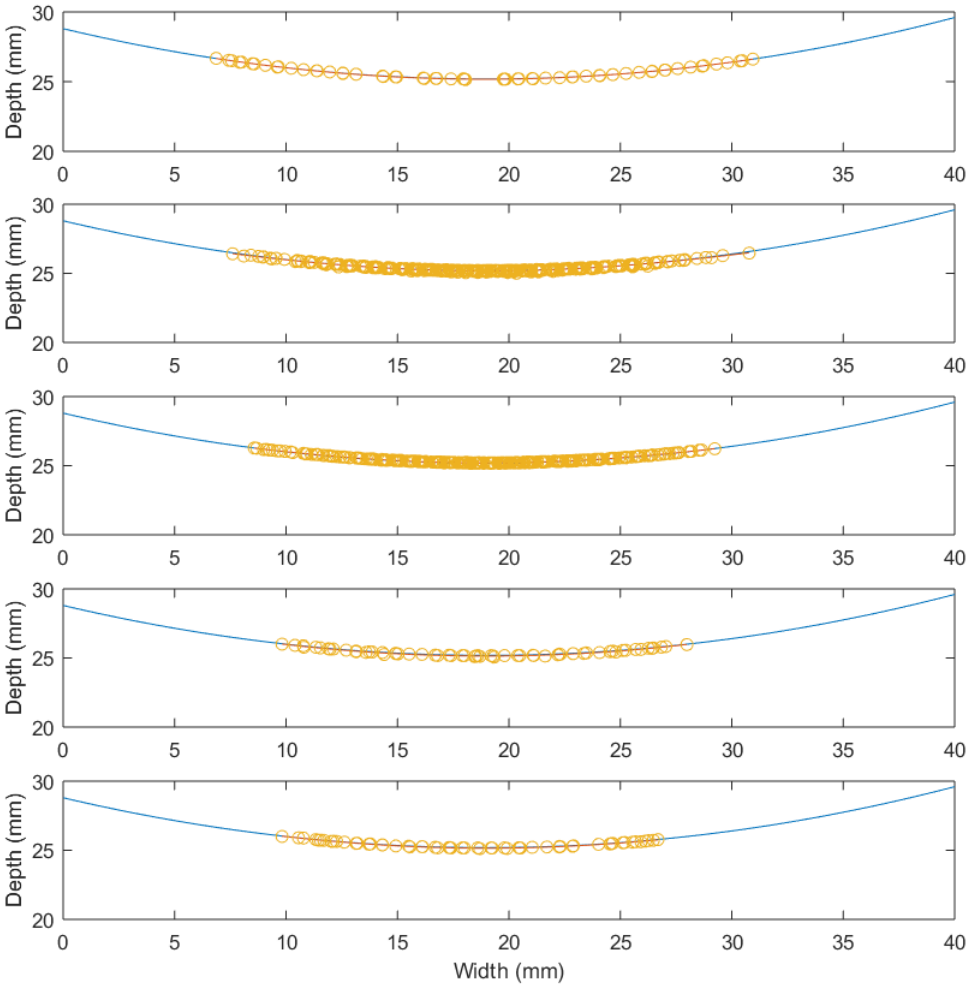


Figure 6.19: $\pm 4mm$ Sinusoidal Trough - Figure showing the surface mapping results for the quadratic surface. The yellow plotted points are the points from the surface mapping algorithm. The orange line is the best fit curve interpolating between these points. The blue line is the known surface geometry. The top image shown is from the DR technique, the next is the VSSM with adjacent elements, then the VSSM with non-adjacent elements, then the PWSM with adjacent elements. The bottom image is the PWSM with non-adjacent elements.

Chapter 7

Thesis Conclusion

7.1 Review of Thesis

Ultrasonic testing is vital for the integrity evaluation of components in many industries worldwide. PA is the most common method of UT, this is due to the fact that limited post processing is required for imaging and therefore it was one of the few methods that could achieve high frame rates at the time when UT originally became prominent in NDT. However, in the past decade or so, the development in advanced computer hardware has allowed post processing UT algorithms, in particular the TFM, to become increasingly popular in NDT. FMC generally is the most common acquisition strategy for TFM based imaging, due the the high quality images it produced. However FMC-TFM imaging, even with modern computer hardware, cannot achieve the frame rates achieved by phased array.

VSA and PWI have become increasingly more popular over the past five years as they combine the advantages of both PA and FMC-TFM. The TFM algorithm is used to form fully focussed images. PA like transmission sequences are used to improve the overall SNR of the Ascans such that a comparable image to FMC can be formed in fewer transmissions. Therefore the frame rate can be comparable to PA. VSA and PWI promise

to be the next generation of ultrasonic imaging due to the advantages they they provide over current existing algorithms such as ease of image interpretation and the ability to exploit more of the data by using imaging views such as self tandem and multimode.

Much research has been conducted on PWI algorithms, while VSA has largely been overlooked. It was shown in this work that VSA has advantages over PWI and may prove to be more more useful technique in certain situations. Therefore it was important to conduct further research in order to bring VSA to the same standard as PWI and FMC. The self tandem and multi-mode algorithms were investigated in this work, along with a surface mapping algorithm and a frequency domain VSA algorithm. This work has contributed to the overall development of the VSA testing technique, and brings it closer to being used by industry.

7.2 Main Conclusions

- It was found that FMC provides the highest quality images overall. For a small compromise in image quality, it is possible to achieve much higher frame rates using either VSA or PWI. FMC achieved 18fps while VSA and PWI could achieve up to 250fps, for a comparative, typical setup. There existed a linear relationship between the amount of data that was processed as the imaging algorithm was by far the largest computational burden.

- The PWI and VSA techniques gave comparable SNR values for the images, with VSA slightly higher. However both of these were a few dB less than FMC. The PWI performed better than VSA for the API, as the indications from the PWI algorithm were more tightly focussed. The measured values for SNR and API varied massively across the imaging region for PWI, and largely corresponded to how

many transmissions had covered each particular point in space. Where wavefronts overlapped, the images were higher intensity and more tightly focussed. To avoid this problem the number of transmissions must be higher such that the distribution of energy is more uniform. Therefore it is likely that VSA may be a better technique for certain circumstances as the API and SNR values for VSA were more uniform across the region of interest, closely resembling the values achieved by FMC.

- The VSA frequency domain algorithm was implemented and compared to the time domain. It was found that the frequency domain gave a narrower range of angular coverage compared to the time domain. Also the time domain was easier to implement through a refractive boundary. As inspection through refractive boundaries are common in NDT, such as when a wedge is used, or immersion testing is performed, this was a key limitation. Therefore the bulk of this research was carried out using the time domain algorithm.

- The VSA self tandem and multi-mode algorithms was investigated. It was found that the data acquired for a VSA acquisition strategy can be reprocessed in a number of ways to exploit all possible sound paths, including mode conversions, for imaging. Therefore, probability of detection and classification for certain defects can be improved. A few examples were shown of how the self tandem and multi-mode algorithms were used to image a vertically aligned flaw using the high amplitude specular responses rather than the low amplitude tip diffracted signals highlighted by the half skip and full skip algorithms.

- A VSA surface mapping method was introduced in this thesis. The method was compared to the existing dipping reflector and plane

wave surface mapping algorithms. It was shown that for less complex surface geometry, the VSA surface mapping algorithm was very comparable to the others. The advantage of using this algorithm is that VSA data can be used to extract surface information such that surface mapping and imaging can be performed with a single acquisition sequence.

7.3 Further Work

Further work is required to investigate inspection of composite components. The work carried out here was based on inspection of metals, where the velocity of sound is uniform in all directions. The algorithms would have to be edited to account for composites where the velocity of sound changes depending on the direction of travel through the material. It may also be beneficial to investigate the effect that rough surfaces have on the accuracy of the imaging algorithms, as this is a common issue in NDT. The frequency domain imaging algorithm through a complex geometry could provide benefits over current techniques, however this would have to be assessed.

Appendixes

Appendix A - Derivation of Equation 4.14b

The change of coordinates required for interpolation is shown here. We start with:

$$k_z = \sqrt{k^2 - k_u^2} + \sqrt{k^2 - k_v^2} \tag{7.1}$$

By squaring both sides and rearranging we get:

$$k_z^2 - 2k^2 + k_u^2 + k_v^2 = 2\sqrt{k^4 - k^2(k_v^2 + k_v^2) + k_u^2 k_v^2} \tag{7.2}$$

Squaring both sides again:

$$\begin{aligned} k_z^4 + k_z^2 k_u^2 + k_z^2 k_v^2 - 2k^2 k_z^2 + k_u^4 + k_u^2 k_v^2 - 2k^2 k_u^2 + k_u^2 k_z^2 + k_v^2 k_z^2 + k_v^2 k_u^2 + k_v^4 \\ -2k^2 k_v^2 - 2k^2 k_z^2 - 2k^2 k_u^2 - 2k^2 k_v^2 + 4k^2 = 4k^2 - 4k^2 k_u^2 - 4k^2 k_v^2 + 4k_u^2 k_v^2 \end{aligned} \tag{7.3}$$

Finally rearranging to make k the subject:

$$k = \pm \frac{\sqrt{k_z^4 + 2(k_u^2 + (k_x - k_u)^2)k_z^2 + k_u^4 + (k_x - k_u)^4 - 2k_u^2(k_x - k_u)^2}}{2k_z} \tag{7.4}$$

Appendix B - Interpolation Function

The interpolation function is given by Equation 7.5a.

$$\begin{aligned} f'(x,y) = \frac{z_2 - z}{z_2 - z_1}\left(f(x_1, z_1)\frac{x_2 - x}{x_2 - x_1} + f(x_2, z_1)\frac{x - x_1}{x_2 - x_1}\right) \\ + \frac{z - z_1}{z_2 - z_1}\left(f(x_1, z_2)\frac{x_2 - x}{x_2 - x_1} + f(x_2, z_2)\frac{x - x_1}{x_2 - x_1}\right) \end{aligned} \tag{7.5a}$$

where:

$$x_2, x_1 = round_{up,down}\left(\frac{x - x_{min}}{x_{max} - x_{min}} N_x\right) \tag{7.5b}$$

and:

$$z_2, z_1 = round_{up,down}\left(\frac{z - z_{min}}{z_{max} - z_{min}} N_z\right) \tag{7.5c}$$

Here a grid of a function $f(x_n, z_n)$ with known values at coordinates (x_n, z_n), with coordinate values between x_{min} and x_{max} and z_{min} and z_{max}, is linearly interpolated to give a new function $f'(x, z)$. The four closest coordinates around the point (x, z) are taken and the new value is the linear interpolation between these four coordinates. The time taken for this is of order $\mathcal{O}(N_x N_z)$ where $N_x N_z$ is the number of new coordinates that are interpolated.

Bibliography

[1] F. A. Firestone. The Supersonic Reflectascope, an Insturment for Inspection the Interior of Solid Parts by Means of Sound Waves. *The Journal of the Acoustical Society of America*, 17(3), 1946.

[2] J. C. Somer. Electronic sector scanning for ultrasonic diagnosis. *Elsevier*, 6(3):153–159.

[3] Olympus NDT. *Introduction to Phased Array Ultrasonic Technology Applications*. ISBN 0973593342, 2004.

[4] M. Sutcliffe, M. Weston, B. Dutton, P. Charlton, and K. Donne. Real-time full matrix capture for ultrasonic non-destructive testing with acceleration of post-processing through graphic hardware. *NDT&E International*, 51:16–23, 2012.

[5] B. W. Drinkwater and P. D. Wilcox. Ultrasonic arrays for non-destructive evaluation: a review. *NDT&E International*, 39:525–541, 2006.

[6] M. Sutcliffe, M. Weston, P. Charlton, K. Donne, B. Wright, and I. Cooper. Full matrix capture with time-efficient auto-focusing of unknown geometry through dual-layered media. *Insight: Non-Destructive Testing and Condition Monitoring*, 55(6):1–6, 2013.

[7] S. Yamamoto, J. Semboshi, A. Sugawara, M. Ochiai, K. Tsuchihashi, H. Adachi, and K. Higuma. Phased Array Ultrasonic Inspection

Technique for Cast Ausentic Stainless Steel Parts of Nuclear Power Plants. *ICONE24-60256*, pages 1–6, 2016.

[8] M. Moles, L. Wesley, and T. Sinclair. Accurate Defect Sizing using Phased Array and Signal Processing - Developments in Ultrasonic Inspection II. *Olympus NDT, University of Toronto*.

[9] P. D. Wilcox, B. W. Drinkwater, and J. Zhang. Defect Characterisation using ultrasonic arrays. In *Proceedings of SPIE*, 2008.

[10] C. Holmes, B. W. Drinkwater, and P. D. Wilcox. Post-processing of the full matrix of ultrasonic transmit-receive array data for non destructive evaluation. *NDT&E International*, 38:701–711, 2005.

[11] R. Long, J. Russell, and P. Cawley. Ultrasonic phased array inspection using full matrix capture. *Insight: Non-Destructive Testing & Condition Monitoring*, 54(7):380–385, 2012.

[12] L. Le Jeune, S. Robert, E. L. Villaverde, and C. Prada. Plane Wave Imaging for ultrasonic non-destructive testing: Generalization to multimodal imaging. *Ultrasonics*, 64:128–138, 2016.

[13] M. Sutcliffe, P. Charlton, and M. Weston. Multiple virtual source aperture imaging for non-destructive testing. *Insight: Non-Destructive Testing and Condition Monitoring*, 56(2):75–81, 2014.

[14] S. Mosey. Resolution Enhancement of B-Mode Ultrasound Images. *A thesis submitted to the University of Wales in partial fulfilment of the requirements for the degree of Doctor of Philosophy*, 2013.

[15] M. Weston, C. Nageswaran, M. Sutcliffe, A. Peyton, C. Davis, P. Mudge, and P. Wallace. Calibration of ultrasonic techniques using full matrix capture data for industrial inspection. 54(11):1–5, 2012.

[16] J. Zhang, B. W. Drinkwater, and P. D. Wilcox. Effects of array transducer inconsistencies on total focusing method imaging performance. *NDT&E International*, 2011.

[17] Jie Zhang, Bruce Drinkwater, and Paul D. Wilcox. Comparison of ultrasonic array imaging algorithms for nondestructive evaluation. *IEEE Transactions on Ultrasonics, Ferroelectrics, and Frequency Control*, 60(8):1732–1745, 2013.

[18] C. Frazier and W. D. O'Brien. Synthetic Aperture Techniques with a Virtual Source Element. *196 IEEE Transactions on Ultrasonics, Ferroelectrics, and Frequency Control*, 45(1), 1998.

[19] M. Sutcliffe, M. Weston, P. Charlton, B. Dutton, and K. Donne. Virtual source aperture imaging for non-destructive testing. *Insight: Non-Destructive Testing and Condition Monitoring*, 56(2):75–81, 2014.

[20] M. Sutcliffe, P. Charlton, and M. Weston. Virtual source aperture image processing methods for non-destructive testing. *Insight: Non-Destructive Testing and Condition Monitoring*, 58(2):1–5, 2016.

[21] M. Sutcliffe. *Time Critical Synthetic Transmit Aperture Ultrasound Imaging*. PhD thesis, University of Wales Trinity Saint David, 2012.

[22] Gabriel Montaldo, Mickaël Tanter, Jérémy Bercoff, Nicolas Benech, and Mathias Fink. Coherent plane-wave compounding for very high frame rate ultrasonography and transient elastography. *IEEE Transactions on Ultrasonics, Ferroelectrics, and Frequency Control*, 56(3):489–506, 2009.

[23] O. Couture, M. Fink, and M. Tanter. Ultrasound Contrast Plane Wave Imaging. 59(12):2676–2683, 2012.

[24] L. Le Jeune, S. Robert, E. L. Villaverde, and C. Prada. Multimodal plane wave imaging for non-destructive testing. *Physics Procedia*, 70(December):570–573, 2015.

[25] F. King. *Discrete Hilbert transforms. In Hilbert Transforms (Encyclopedia of Mathematics and its Applications, pp. 637-683)*. Cambridge University Press., 2009.

[26] J. Camacho, M. Parrilla, and C. Fritsch. Phase Coherence Imaging. *IEEE Transactions on Ultrasonics, Ferroelectrics and Frequency Control*, 56(5):1403–1404, 2009.

[27] J. F. Cruza, J. Camacho, and C. Fritsch. Plane-wave phase-coherence imaging for NDE. *NDT&E International*, 87(September 2016):31–37, 2017.

[28] S. Mosey, P. Charlton, and I. Wells. Resolution enhancement of ultrasonic B-mode images. *Insight: Non-Destructive Testing & Condition Monitoring*, 55(2), 2013.

[29] J. Camacho, D. Atehortua, J. F. Cruza, J. Brizuela, and J. Ealo. Ultrasonic crack evaluation by phase coherence processing and TFM and its application to online monitoring in fatigue tests. *NDT and E International*, 93(December 2016):164–174, 2018.

[30] P. D. Wilcox, C. Holmes, and B. W. Drinkwater. Advanced reflector characterization with ultrasonic phased arrays in NDE applications. *IEEE Transactions on Ultrasonics, Ferroelectrics, and Frequency Control*, 54(8):1541–1550, 2007.

[31] J. Zhang, B. Drinkwater, and P. D. Wilcox. Defect characterization using an ultrasonic array Defect Characterization Using an Ultrasonic

Array to Measure the Scattering Coefficient Matrix. *IEEE Transactions on Ultrasonics, Ferroelectrics and Frequency Control*, (October), 2008.

[32] J. Zhang, B. W. Drinkwater, and P. D. Wilcox. The use of Ultrasonic Arrays to Characterize Crack-Like Defects. *Journal of Non-Destructive Evaluation*, 29(4), 2010.

[33] M. Sutcliffe, P. Charlton, M. Weston, and S. Mosey. Virtual Source Aperture Imaging and Calibration for Ultrasonic Inspections through Dual Layered Media for NDT. *Insight: Non-Destructive Testing & Condition Monitoring*, 59(11), 2017.

[34] M. Weston, P. Mudge, C. Davis, and A. Peyton. Time efficient auto-focussing algorithms for ultrasonic inspection of dual-layered media using Full Matrix Capture. *NDT&E International*, 47:43–50, 2012.

[35] B. Drinkwater and W. Bowler. Ultrasonic Array Inspection of the Clifton Suspension Bridge chain-links. *Insight: Non-Destructive Testing and Condition Monitoring*, 51(9):491–498, 2009.

[36] E. Hoyle, M. Sutcliffe, P. Charlton, and J. Rees. Virtual Source Aperture with Real Time Focussing of Known Geometry Through Dual Layered Media. BINDT 56th Annual Conference 3B5 (freely available on Researchgate), 2017.

[37] M. Sutcliffe, M. Weston, B. Dutton, and I. Cooper. Real-time full matrix capture with auto-focussing of known geometry through dual layered media. *Birttish Institute of Non Destructive Testing Annual Conference*, 2012.

[38] L. Le Jeune, S. Robert, and C. Prada. Plane wave imaging for ultrasonic inspection of irregular structures with high frame rates. *42nd Annual*

Review of Progress in Quantitative Nondestructive Evaluation (AIP Conf. Proc. 1650), 020010:020010, 2016.

[39] J. Zhang, B. W. Drinkwater, and P. D. Wilcox. Efficient Immersion Imaging of Components with Nonplanar Surfaces. *IEEE International Ultrasonics Ferroelectrics and Frequency Control*, 61(8):139–142, 2014.

[40] M. Parilla, A. Ibañez, J. Camacho, and C. Fritsch. Fast focal law computing for Non-Destructive Testing with phased arrays. *International Congress on Ultrasonics*, 2007.

[41] M. Parrilla, J. Brizuela, J. Camacho, A. Ibáñez, P. Nevado, and C. Fritsch. Dynamic focusing through arbitrary geometry interfaces. *IEEE International Ultrasonics Symposium Proceedings*, 2008.

[42] J. F. Cruza, J. Camacho, L. Serrano-Iribarnegaray, C. Fritsch, and S. Member. New Method for Real-Time Dynamic Focusing Through Interfaces. 60(4):739–751, 2013.

[43] J. F. Cruza and J. Camacho. Total Focusing Method With Virtual Sources in the Presence of Unknown Geometry Interfaces. *IEEE Transactions on Ultrasonics, Ferroelectrics and Frequency Control*, 63(10):1581–1592, 2016.

[44] M. V. Felice, A. Velichko, and P. D. Wilcox. Accurate depth measurement of small surface-breaking cracks using an ultrasonic array post-processing technique. *NDT&E International*, 68:105–112, 2014.

[45] M. V. Felice, A. Velichko, P. D. Wilcox, J. Christopher, and L. Lane. Depth Measurement of Small Surface-Breaking Cracks Using the Half-Skip Total Focusing Method. *41st Annual Review of Progress in Quantitative Nondestructive Evaluation (AIP Conf. Proc. 1650)*, 994, 2015.

[46] E. Ginzel, O. Volf, and B. Brown. Next Generation Technology for Pipeline AUT TFM / FMC. *The e-Journal of Nondestructive Testing*, 20(8), 2015.

[47] E. Hoyle, M. Sutcliffe, P. Charlton, J. Rees, and M. Weston. Virtual Source Aperture Imaging for the Detection of Vertically Aligned Flaws in Non Destructive Testing . *Insight: Non-Destructive Testing and Condition Monitoring*, pages 1–7, 2017.

[48] J. Zhang, B. W Drinkwater, P. D. Wilcox, and A. J. Hunter. Defect detection using ultrasonic arrays : The multi-mode total focusing method. *NDT and E International*, 43(2):123–133, 2010.

[49] G. Toullelan, A. Nadim, O. Casula, P. Dumas, E. Abittan, and L. Doudet. Inspection of Complex Geometries using Flexible Phased-Array Transducers. *17th World Conference on Nondestructive Testing*, pages 25–28, 2008.

[50] J. Russell, R. Long, P. Cawley, and N. Habgood. Inspection of components with irregular surfaces using a conformable ultrasonic phased array. *AIP Conference Proceedings*, 1096:792–799, 2009.

[51] J. Russell, R. Long, D. Duxbury, and P. Cawley. Development and implementation of a membrane-coupled conformable array transducer for use in the nuclear industry. *Insight: Non-Destructive Testing & Condition Monitoring*, 54:386–393, 2012.

[52] A. J. Hunter, B. W. Drinkwater, and P. D. Wilcox. Autofocusing ultrasonic imagery for non-destructive testing and evaluation of specimens with complicated geometries. *NDT&E International*, 43(2):78–85, 2010.

[53] A. J. Hunter, B. W. Drinkwater, and P. D. Wilcox. Least-squares estimation of imaging parameters for an ultrasonic array using known geometric image features. *IEEE Transactions on Ultrasonics, Ferroelectrics, and Frequency Control*, 58(2):414–426, 2011.

[54] S. Robert, P. Calmon, M. Calvo, L. Le Jeune, and E. Iakovleva. Surface estimation methods with phased-arrays for adaptive ultrasonic imaging in complex components. *41st Annual Review of Progress in Quantitative Nondestructive Evaluation (AIP Conf. Proc. 1650)*, (2015):1657–1666.

[55] L. Le Jeune, S. Robert, P. Dumas, A. Membre, and C. Prada. Adaptive Ultrasonic Imaging with the Total Focusing Method for Inspection of Complex Components Immersed in Water. *AIP Conference Proceedings*, 1037:1037–1046, 2015.

[56] J. Camacho and J. F. Cruza. Auto-Focused Virtual Source Imaging With Arbitrarily Shaped Interfaces. *IEEE Transactions on Ultrasonics, Ferroelectrics and Frequency Control*, 62(11):1944–1956, 2015.

[57] J. Camacho, J. F. Cruza, J. Brizuela, and C. Fritsch. Automatic Dynamic Depth Focusing for NDT. *IEEE International*, 61(4), 2014.

[58] Ewan Hoyle, Mark Sutcliffe, Peter Charlton, and John Rees. Virtual source aperture imaging with auto-focusing of unknown complex geometry through dual layered media. *NDT and E International*, 98(November 2017):55–62, 2018.

[59] Billur Barshan and Deniz Backent. Comparison of two methods of surface profile extraction from multiple ultrasonic range measurements. *Measurement Science and Technology*, 11(6):833–844, 2000.

[60] B. Barshan. Fast processing techniques for accurate ultrasonic range measurements. *Measurement Science and Technology*, 11(1):45–50, 2000.

[61] M. Parrilla, J. J. Anaya, and C. Fritsch. Digital Signal Processing Techniques for High Accuracy Ultrasonic Range Measurements. *IEEE Transactions on Instumentation and Measurement*, 40(4):759–763, 1991.

[62] P. Gough and D. Hawkins. Unified Framework for Modern Synthetic Aperture Imaging Algorithms. *John Wiley & Sons Imaging Systems Technology*, 8:343–358, 1997.

[63] R. H. Stolt. Migration by Fourier Transform. *Geophysics*, 43(1):23–48, 1978.

[64] T. Stepinski. An Implementation of Synthetic Aperture Focusing Technique in Frequency Domain. *IEEE Transactions on Ultrasonics, Ferroelectrics, and Frequency Control*, 54(7), 2007.

[65] A. J. Hunter, B. W. Drinkwater, and P. D. Wilcox. The Wavenumber Algorithm for Full-Matrix Imaging Using an Ultrasonic Array. *IEEE Transactions on Ultrasonics, Ferroelectrics and Frequency Control*, 55(11):2450–2462, 2008.

[66] Niels Pörtzgen, Dries Gisolf, and Gerrit Blacquière. Inverse wave field extrapolation: A different NDI approach to imaging defects. *IEEE Transactions on Ultrasonics, Ferroelectrics, and Frequency Control*, 54(1):118–127, 2007.

[67] Niels Pörtzgen, Dries Gisolf, and Dirk J. Verschuur. Wave equation-based imaging of mode converted waves in ultrasonic NDI, with suppressed leakage from nonmode converted waves. *IEEE Transactions on Ultrasonics, Ferroelectrics, and Frequency Control*, 55(8):1768–1780, 2008.

[68] Nasim Moallemi and Shahram Shahbazpanahi. A New Model for Array Spatial Signature for Two-Layer Imaging with Applications to Nondestructive Testing Using Ultrasonic Arrays. *IEEE Transactions on Signal Processing*, 63(10):2464–2475, 2015.

[69] Tadeusz Stepinski and Fredrik Lingvall. Synthetic aperture focusing techniques for ultrasonic imaging of solid objects. *Synthetic Aperture Radar (EUSAR)*, (December 2013):438–441, 2010.

[70] T. Lukomski, T. Stepinski, and T. Kowal. Synthetic aperture focusing technique with virtual transducer for immersion inspection of solid objects. *Insight: Non-Destructive Testing & Condition Monitoring*, (October 2016), 2012.

[71] L. Levesque, A. Blouin, C. Neron, and J. P. Monchalin. Performance of Laser-Ultrasonic F-SAFT Imaging. *Ultrasonics*, 40:1057–1063, 2002.

[72] L. Levesque, A. Blouin, C. Neron, and J. P. Monchalin. Performance of Ultrasonic Imaging with Frequency Domain SAFT. *Journal of the Canadian Acoustical Association*, 32(3), 2004.

[73] L. J. Busse. Three-Dimensional Imaging Using a Frequency-Domain Synthetic Aperture Focusing Technique. *IEEE Transactions on Ultrasonics, Ferroelectrics and Frequency Control*, 39(2), 1992.

[74] D. Garcia, L. Le Tarnec, S. Muth, E. Montagnon, J. Porée, and G. Cloutier. Stolt ' s f - k Migration for Plane Wave Ultrasound Imaging. *IEEE Transactions on Ultrasonics, Ferroelectrics and Frequency Control*, 60(9):1853–1867, 2013.

[75] Synthetic aperture imaging for small scale systems. *IEEE Transactions on Ultrasonics, Ferroelectrics and Frequency Control*, 42(3):429–442, 1995.

[76] Hongwei Hu, Jian Du, Chengbao Ye, and Xiongbing Li. Ultrasonic phased array sparse-TFM imaging based on sparse array optimization and new edge-directed interpolation. *Sensors (Switzerland)*, 18(6), 2018.

[77] Elahe Moghimirad, Carlos A. Villagómez Hoyos, Ali Mahloojifar, Babak Mohammadzadeh Asl, and Jørgen Arendt Jensen. Synthetic Aperture Ultrasound Fourier Beamformation Using Virtual Sources. *IEEE Transactions on Ultrasonics, Ferroelectrics, and Frequency Control*, 63(12):2018–2030, 2016.

[78] Nasim Moallemi and Shahram Shahbazpanahi. A Novel Spatio-Temporal Frequency-Domain Imaging Technique for Two-Layer Materials Using Ultrasonic Arrays. *IEEE Access*, 6(February):8977–8989, 2018.

[79] Weng CHo Chew. *Waves and Fields in Inhomogeneous Media*. Wiley-IEEE Press, 1990.

[80] Ronald Brecewell. *The Fourier Transform and its Applications*. McGraw-Hill Book Company, 1963.

[81] J Krautkramer and H Krautkramer. *Ultrasonic Testing of Materials*. Springer - Verlag, 1983.

NDT and E International 98 (2018) 55–62

Contents lists available at ScienceDirect

NDT and E International

journal homepage: www.elsevier.com/locate/ndteint

Virtual source aperture imaging with auto-focusing of unknown complex geometry through dual layered media

Ewan Hoyle [a,*], Mark Sutcliffe [b], Peter Charlton [c], John Rees [d]

[a] University of Wales Trinity Saint David (UWTSD) associated with TWI ltd, UK
[b] TWI ltd, UK
[c] School of Engineering (UWTSD), UK
[d] School of Applied Computing (UWTSD), UK

A B S T R A C T

In this paper, a Virtual Source Aperture (VSA) surface mapping technique applicable for ultrasonic inspection of components with complex geometry through dual layered media is described. Assuming the first medium is free of significant discontinuities, the first echo arrives from the boundary between the two mediums. The surface is described by the tangent to a family of ellipses constructed using the time of the first echo from the VSA data set and the known positions of the transmitters and receivers. The Total Focusing Method, using Fermat's principle to account for refraction, is used to generate fully focused images of the test specimen interior. Using this technique, it is possible to obtain surface information and generate an image with as little as a single firing of the ultrasonic array, which will be of significance when ultra fast ultrasonic inspection is necessary. The method is tested on a series of surfaces with varying geometry and is shown to successfully image and position a series of side drilled holes within each specimen.

1. Introduction

The use of ultrasonic arrays for ultrasonic imaging in Non Destructive Testing (NDT) is prevalent [1]. The Total Focusing Method (TFM) is an advanced pulse echo technique that uses an array in contact with the testing material to produce fully focused images of flaws within [2]. It is often referred to as the 'gold standard' in ultrasonic imaging [3,4]. The TFM is often used with the Full Matrix Capture (FMC) of an ultrasonic array, which involves firing on each element individually and receiving on all [5]. However inspection using FMC-TFM is burdened by the need to acquire a vast amount of data and the large processing overheads that follow. Optimisation techniques with the use of graphic hardware [6] can be used to maximise the speed, however the large data sizes of can be a limiting factor in wide spread adoption of FMC-TFM.

Virtual Source Aperture (VSA) was first introduced in medicine [7] but has since been adapted to NDT [8]. The technique uses the TFM algorithm for imaging, however instead of each element being fired individually as is done with FMC-TFM, multiple elements are fired to create a beam profile as if it had come from a singular point behind the array (as depicted in Fig. 1). Each element then receives individually. As multiple elements are fired together rather than individually, VSA has been shown to increase the signal to noise ratio (SNR) of the returned A-scans [9]. The advantage of VSA over FMC-TFM is that a reduced amount of data is used to construct an image with a similar SNR, allowing higher inspection rates [10]. Multiple virtual source firings [8] can be used to widen the angle of inspection. However the virtual sources have to be carefully set up and care taken to ensure the beam front behaves as expected, as performance can be effected by element size and number of elements per firing [11]. VSA is a relatively new technique and consequently has not been as widely developed as FMC-TFM.

Often in NDT, the array cannot be coupled directly to the surface of the testing sample. Much research has been done into how to solve this problem. Flexible arrays have been used [12,13], but commonly the transducer and the sample are immersed in a coupling fluid such as water. A wedge/shoe or a fluid filled membrane [14] can also be used to couple the array to the testing sample [15–17]. If the geometry of the surface is unknown, the surface may first be be estimated using ultrasonic methods. The first response times are often used. Typically the first response is defined as the first time the ultrasonic response crosses a certain amplitude threshold, and is predominantly the response from the surface of the testing material. The long rise and fall times mean that simple crossing amplitude threshold techniques are subject to error [18], as the time at which the amplitude crosses threshold may not be the start of the signal, especially if the start of the signal is hidden by the low amplitude background noise. However methods exist to reduce or eliminate this error [19].

* Corresponding author.
E-mail address: ewan.hoyle@affiliate.twi.co.uk (E. Hoyle).

https://doi.org/10.1016/j.ndteint.2018.04.005
Received 16 November 2017; Received in revised form 22 March 2018; Accepted 9 April 2018
Available online 19 April 2018
0963-8695/© 2018 Published by Elsevier Ltd.

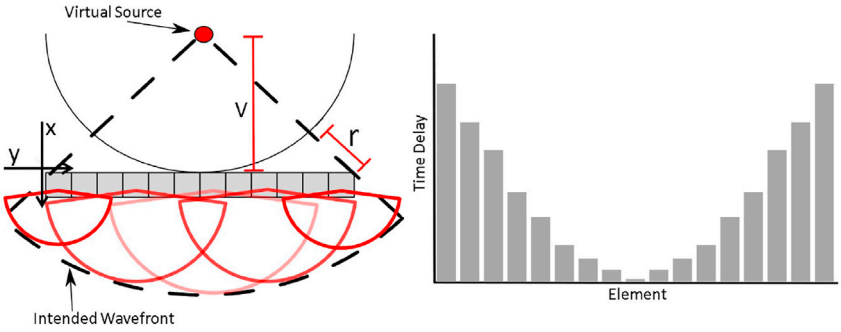


Fig. 1. Building a virtual source.

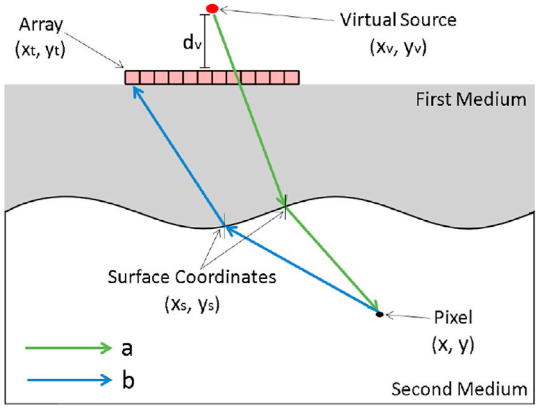


Fig. 2. Depiction of an arbitrary path from a given virtual source, to a given pixel and back to a given receiving element. This is typical of the paths considered when calculating the TFM algorithm.

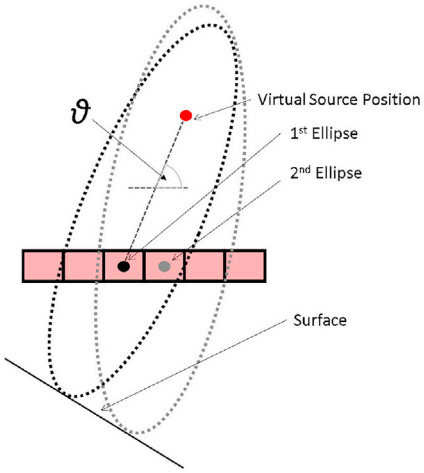


Fig. 3. Surface mapping method using ellipses. Here θ is the angle between the horizontal and a line drawn between the transmit point and the receive point.

Using a variety of techniques, the surface position can be calculated relative to the array. The so called 'dipping reflector' method can be used for time efficient surface mapping [20]. This uses the first response times from a scan where a single element transmits and receives individually, making it the optimum technique when using an FMC data set [21]. describes a 'pitch catch' method, like the 'dipping reflector' method a FMC data set can be used to obtain surface information and image. In Ref. [22], a method using a zero degree planar incident wave for surface mapping is described. The advantage of this is that a single transmission is used to obtain surface information, however a second transmission is

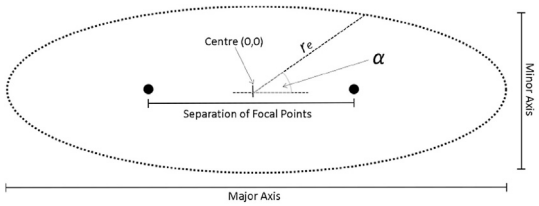


Fig. 4. Construction of an ellipse centred at the origin.

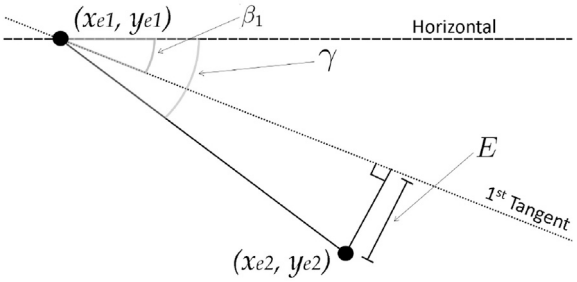
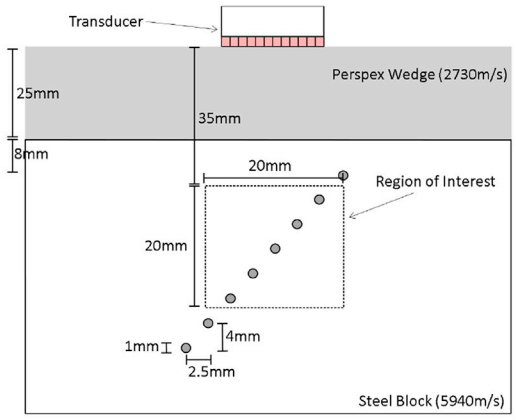


Fig. 5. Diagram depicting the calculation of the intercept.

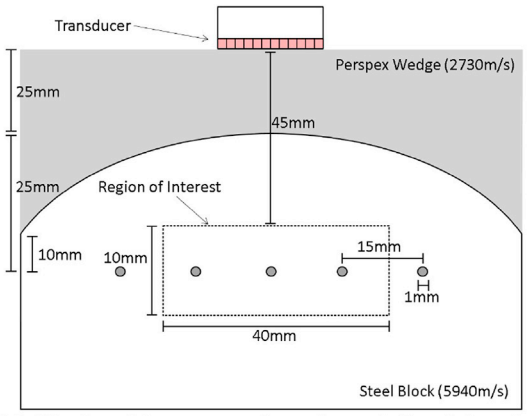
required for imaging as the plane wave breaks up when passing through a non flat boundary [23]. Barshan et al. [24] describes a method in which parabolas are drawn using the first response distance. By considering the beam profile, using sensible erosion techniques and considering the density of intersecting arcs in a given region to remove non applicable points, surface information is obtained. A similar method applies TFM in the coupling substance to find surface information [25,26].

Once surface information is obtained, a number of methods can be used to image. In Ref. [27], the surface information is obtained using an initial firing sequence. Then by applying focal laws to the array elements, an array of virtual sources and receivers are placed on the surface between the two mediums allowing TFM to be performed in the second material only [28] [23]. describes how delay laws can be applied to generate a plane wave within the material for imaging. However, most commonly, the TFM algorithm using Fermat's principle to account for refraction is used [20]. For a flat surface, Snellâ€™s Law [29] can be used to calculate an exact solution for the point of incidence in the path of least time. However, other surface geometries require an exhaustive traversal of the boundary to do this. It is possible to quicken this process by reducing the step size when close, or using a Newton Raphson based approach [30,31].

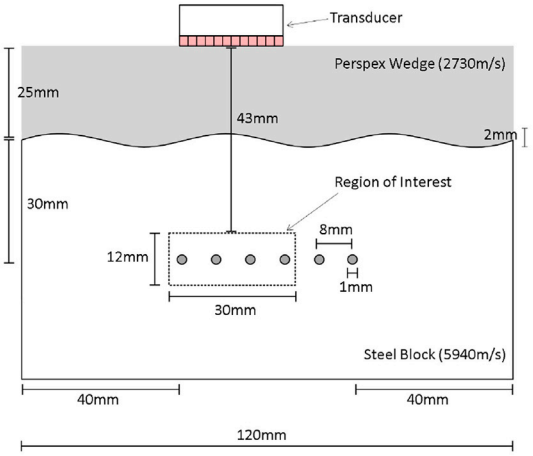
Current techniques for imaging through dual layered media tend to require multiple transmissions, as discussed above. In Ref. [32], it is shown that VSA can be used to produce fully focused images for materials with known complex geometry at high inspection rates. This paper develops a surface mapping technique using the VSA data set, the



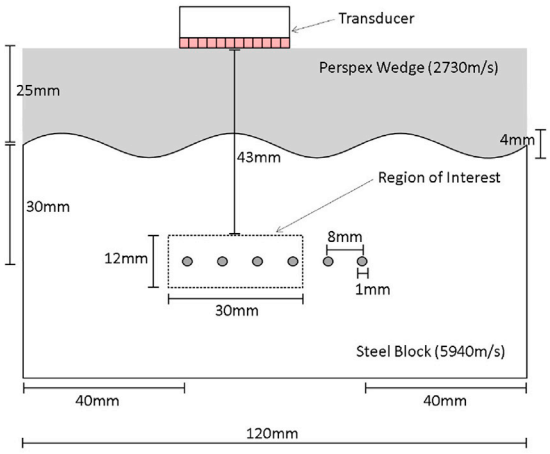
(a) Block with a planar surface with a series of diagonal SDH.



(b) Block with a curved surface defined by the quadratic: $z = 0.01x^2$, where x is measured in mm.



(c) Block with a surface following a sinusoidal curve, 40mm wavelength and an amplitude of 1mm.



(d) Block with a surface following a sinusoidal curve, 40mm wavelength and an amplitude of 2mm.

Fig. 6. Samples containing side drilled holes used to evaluate the method.

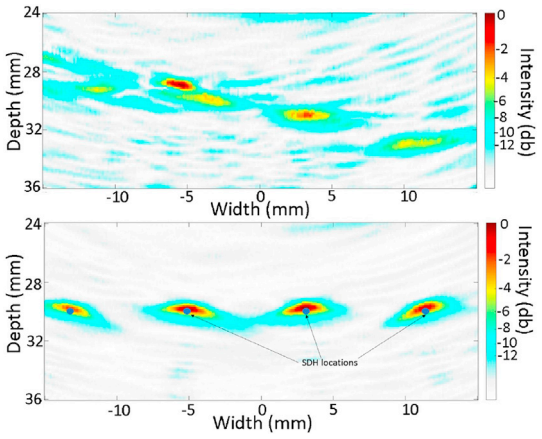


Fig. 7. Top - VSA image of the test block with a $\pm 2mm$ sinusoidal surface (SNR: 14 db), assuming a planar boundary. Bottom - VSA accounting for the $\pm 2mm$ sinusoidal surface (SNR: 24 db).

advantage of this is that surface mapping and imaging can be achieved with as little as a single firing of the ultrasonic array.

Table 1
Results table: shows the error in surface positioning, the error in the time of flight grid caused by this, the SNR of the image using the known geometry and the SNR of the image using the surface mapping.

Block	Surface error (mm)	TOF error (ns)	SNR known (db)	SNR unknown (db)
Planar	0.02	8	23	24
Quadratic	0.06	12	24	22
Sine ±1 mm Peak	0.02	34	28	26
Sine ±1 mm Trough	0.04	42	28	27
Sine ±2 mm Peak	0.04	45	25	25
Sine ±2 mm Trough	0.14	40	23	20

2. Background - virtual source aperture imaging through dual layered media

VSA uses an ultrasonic array fired with a transmission delay law to create a virtual source situated behind the aperture. All elements receive individually without any applied delays. Using the virtual source point as the transmission location and the element position as the receiving position, the TFM is used to generate a fully focused image of the specimen

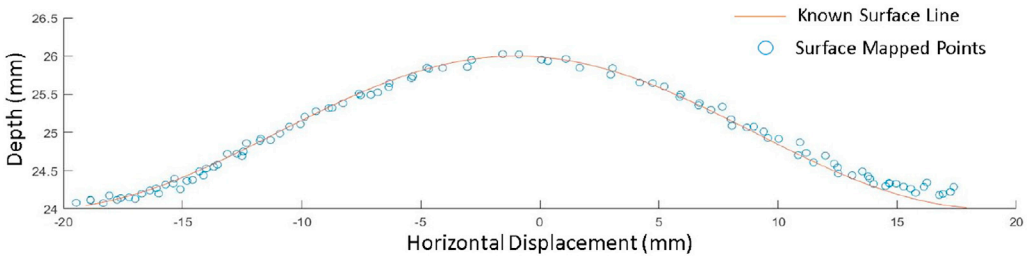


Fig. 8. Mapped points (blue) and the known geometry for the surface (orange) for a sine $\pm 1mm$ surface. (For interpretation of the references to colour in this figure legend, the reader is referred to the Web version of this article.)

interior, as shown in Ref. [32]. For dual layered media, Fermat's principle of least time is used to account for refraction.

The firing delay on each element required to generate a virtual source (depicted in Fig. 1) is shown in Equation (1).

$$dt_k = \frac{r_k}{c_1} = \frac{\sqrt{(x_v - x_{t_k})^2 + (y_v - y_{t_k})^2} - V}{c_1} \tag{1}$$

Here, dt_k is the time delay on the *kth* element, r_k is the delay distance from the virtual source to the *kth* element, x_v and y_v are the x and y co-ordinates of the virtual source, x_{t_k} and y_{t_k} are the x and y coordinates of the transmitting element, V is the perpendicular distance of the virtual source back from the array and c_1 is the velocity of sound in the coupling medium.

Once a virtual source is generated, the returned A-scans can be used to produce fully focused images using the TFM [2], shown in Equation (2).

$$I(x,y) = \left| \sum_{i=1}^{N_v} \sum_{j=1}^{N_e} A\left(a_i + b_j - \frac{V}{c_1}\right) \right| \tag{2}$$

Fig. 2 depicts an ultrasonic array coupled to an inspected part with a complex surface. The TFM works by defining an area of interest within the inspected specimen. This area is divided up into pixels. The intensity of a given pixel $I(x,y)$ is given by summing the amplitude of the real and imaginary parts of the Hilbert transform of the time domain signal, for each transmit-receive combination, at the corresponding time of flight. For each pixel N_v transmitting virtual sources and N_e receiving elements are considered, a total of N_vN_e signals in total. The time of flight is calculated by summing the time taken to reach a given pixel from the virtual source a_i, and the time taken to return to the receiving element b_j. The time V/c_1 is subtracted as sound is not actually emitted from the virtual source location but from the centre of the array. This process is repeated in every pixel in order to generate an image. If a flaw occurs in the region of a given pixel, the calculated times of flight will correspond to a peak in the amplitudes of the corresponding A-scans and therefore the intensity in that pixel will be higher than the pixels that do not contain a flaw.$A(t) = H(\varepsilon(t))$, where $H(\varepsilon(t))$ denotes the Hilbert transform of the time domain signal $\varepsilon(t)$. Typically the emitted pulse for the probe used was a 3–5 cycle Gaussian. The transform returns the envelope of the signal in its real and imaginary parts, improving the visualisation of the final image.

Using the Fermat's principle method to account for refraction, the time of flight of paths *a* and *b* can be calculated and a TFM image can be generated within the testing component with an arbitrary known surface geometry. This is described in more detail in Ref. [32]. This paper describes a surface mapping method using virtual sources in order to obtain knowledge of the surface geometry.

3. VSA surface mapping method

The VSA surface mapping method is depicted in Fig. 3. A family of ellipses is generated using the transmit and receive positions as the focal points. The distance from a given focal point to the circumference and back is given by the first response distance. The method considers two ellipses, and picks the two points that best represent the surface, as shown in Fig. 3. This process is repeated for every pair of receivers adjacent to each other and the surface profile is built up of these ellipse points.

3.1. Calculating the first responses

Firstly, the first response distance for each receiving element must be calculated in order to generate the ellipses. A signal generated from an ultrasonic element has relatively long rise and fall times, because of this, simple threshold crossing techniques are not sufficiently accurate to determine the surface profile [18]. The error in the first response can be removed using a variety of techniques discussed in Ref. [19], the best of which is a curve fitting method used here. The time at which the amplitude crosses two separate thresholds is recorded and a parabola is fitted in order to determine the first response. The corrected first response is given in Equation (3).

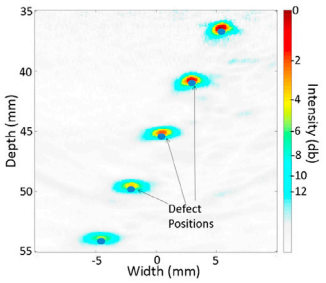
$$t_0 = \frac{\sqrt{\tau_2/\tau_1}t_1 - t_2}{\sqrt{\tau_2/\tau_1} - 1} \tag{3}$$

Here, τ_1 and τ_2 are the response thresholds set, t_1 and t_2 are the times at which the response threshold is crossed and t_0 is the corrected first response. Once the first response time is found, the first response distance can be calculated by multiplying it by the velocity of sound in the coupling medium. The thresholds τ_1 and τ_2 are set by the user, however it is suggested in Ref. [19] that a ratio of $\tau_2/\tau_1 = 2$ is acceptable and that both thresholds are set at least three standard deviations above the background noise level.

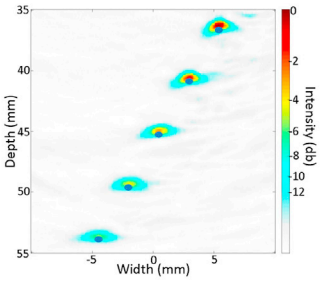
3.2. Ellipse mapping theory

For an ellipse constructed with the focal points at the transmit and receive locations, with the distance from one focal point to the circumference and back to the second focal point calculated using the time of flight from the first response, it can be said that all the possible locations from which that signal originated from are along the circumference. As the first response is assumed to be from the surface indication, the possible positions of the surface are along this line. The gradient of the surface is equal to the gradient of the ellipse at the surface point. However, the exact point along the circumference of the ellipse at which the surface is located is unknown. It can be found using two ellipses with receive points close together and making two assumptions which are common amongst many surface mapping techniques [22]:

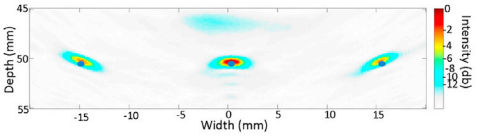
1. Surface Continuity - the surface is smooth with no sudden change in gradient.
2. Close Constant Gradient - for two A-scans with the same transmit position and receive positions close together, it can be assumed that the points at which they reflected off the surface are also close together. Therefore, the gradient of the surface at these two points are assumed to be equal.



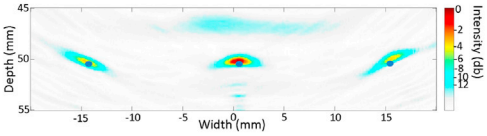
(a) Planar boundary image using the known geometry.



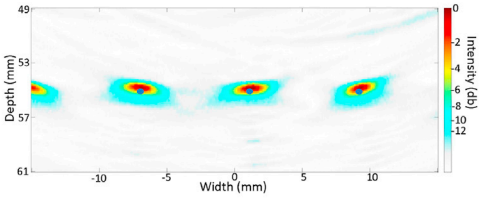
(b) Planar boundary image using surface mapping.



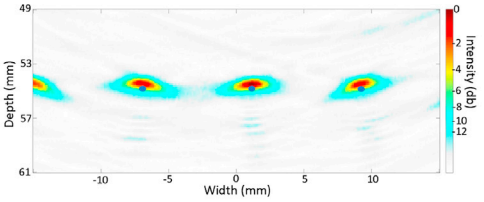
(c) Surface described by z = $0.01x^2$ using the known geometry



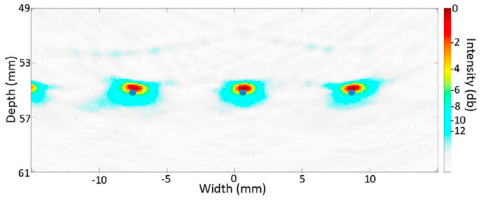
(d) Surface described by z = $0.01x^2$ using surface mapping



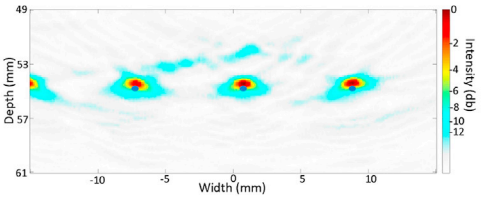
(e) Peak $\pm 1mm$ sinusoidal surface with known geometry.



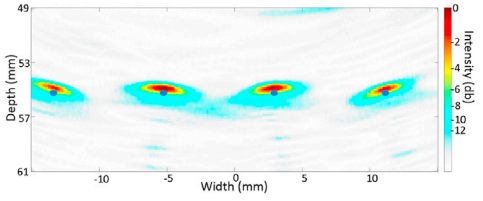
(f) Peak $\pm 1mm$ sinusoidal surface with surface mapping.



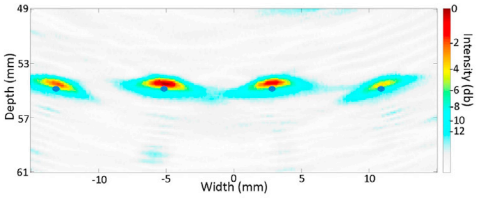
(g) Trough $\pm 1mm$ sinusoidal surface with known geometry.



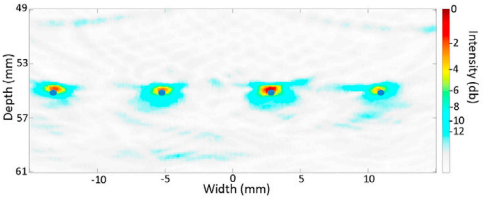
(h) Trough $\pm 1mm$ sinusoidal surface with surface mapping.



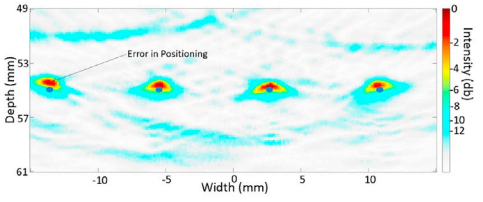
(i) Peak $\pm 2mm$ sinusoidal surface with known geometry.



(j) Peak $\pm 2mm$ sinusoidal surface with surface mapping.



(k) Trough $\pm 2mm$ sinusoidal surface with known geometry.



(l) Trough $\pm 2mm$ sinusoidal surface with surface mapping.

Fig. 9. Images of the SDH in a series of testing samples using the known geometry of the surface and the surface mapping technique.

The surface point for a given pair of receivers is calculated as follows. The process works through every combination of points on the two ellipses. The surface point is the point at which the tangent of the first ellipse intercepts with a point along the second ellipse that has a tangent of the same gradient (as depicted in Fig. 3). The two points have the same gradient and there is continuity in the surface, therefore the two conditions are met. The surface point is taken to be between these the two ellipse points. Once a number of scatted points that make up the surface are obtained, a least squares curve fitting algorithm is used to interpolate between points and obtain the surface position to higher degree of accuracy. The process is repeated for each adjacent pair of receivers and the surface profile is built.

As the surface is known to be below the array, only the ellipse points below the array are considered. It is also often useful to reduce processing time by roughly calculating the minimum depth of the surface using the minimum first response time, and only considering points below this.

3.3. Set up

An ellipse is depicted in Fig. 4.

The equations needed to generate an ellipse using polar coordinates are given in Equations (4a) – (4c).

$$r_e(\alpha) = \sqrt{\frac{a^2 b^2}{a^2 cos^2(\alpha) + b^2 sin^2(\alpha)}} \tag{4a}$$

$$a = \frac{t_0}{2c_1} \tag{4b}$$

$$b = \frac{1}{2}\sqrt{\left(\frac{t_0}{c_1}\right)^2 - s^2} \tag{4c}$$

Here, a is half of the long/major axis of the ellipse and b is half of the short/minor axis shown in Fig. 4, t_0 is the first response time, c_1 is the velocity of the first medium and s is the separation between the transmit and receive focal points. α is the angle between the horizontal and the coordinate vector of the point on the ellipse, as depicted in Fig. 4, and $r_e(\alpha)$ is the radius of the ellipse at this angle.

The tangent of the gradient of the ellipse is crucial for the surface mapping technique, this is given by:

$$\frac{dy}{dx} = \frac{-b}{a^2}\frac{x_e}{\sqrt{1 - x_e^2/a^2}} \tag{5a}$$

$$\beta = tan^{-1}\left(\frac{dy}{dx}\right) \tag{5b}$$

Here, $\frac{dy}{dx}$ is the gradient and x_e is the x coordinate of the ellipse.

A series of points is constructed for every receiving element and every transmitting virtual source. These points are rotated around the centre point and then shifted so that the focal points sit on the transmit and receive positions.

3.4. Mapping the surface

To find the surface point, each combination of points on the first and second ellipse is tested. The error for each combination is considered and the points with the minimum error is taken to be the best approximation for the surface. The intercept error, depicted in Fig. 5, is defined as the minimum distance between the tangent of the first point considered and the second point.

Equations (6a) and (6b) show how the intercept error is calculated.

$$E = \left| sin(\beta_1 - \gamma)\sqrt{(x_{e2} - x_{e1})^2 + (y_{e2} - y_{e1})^2} \right| \tag{6a}$$

$$\gamma = tan^{-1}\left(\frac{y_{e2} - y_{e1}}{x_{e2} - x_{e1}}\right) \tag{6b}$$

Here, E is the intercept error, γ is the angle between the horizontal and a line drawn between the two points, β_1 is the angle of the gradient of the first ellipse with the horizontal at the first testing point, x_{e1} and y_{e1} is the x and y coordinates of the first testing point and x_{e2} and y_{e2} the second testing point.

The minimum distance between the tangent of the second point and the first point is also considered and the total error is the summation of the two. This error is minimised to find the two points that best represent the surface. Once the two points defining the surface are found, the surface point is taken to be half way between the two chosen points on each ellipse. This process is repeated for every pair of elements on the array and so the surface is mapped.

3.5. Outliers

Outlying points that do not represent the surface occur due to discontinuities in the first responses. The discontinuities are caused by the first response signals coming from different areas and so the surface assumption that the gradient off which they reflected off is equal does not hold, or errors in calculating the first response. It is possible to detect discontinuities in the first response using Equation (7).

$$dF = |F_i - (2*F_{i-1} - F_{i-2})| \tag{7}$$

By calculating the difference between the two previous first response times (F_{i-2} and F_{i-1}) and adding it to the previous first response time F_{i-1}, the first response of the *ith* element can be roughly predicted. By subtracting this prediction from the actual first response time F_i the difference between the predicted and real can be calculated dF. Assuming that the change in the first responses is smooth then dF is small. A discontinuity in the first response causes a large dF value and can be judged by values outside of three times the standard deviation of all the dF values in the first response.

Once the surface is defined by a set of scattered points, a curve fitting algorithm is used to provide interpolation between points and to map to higher degree of accuracy.

4. Experimental setup

The technique was tested on a series of samples with known geometries, shown in Fig. 6. The surface geometries used were: a planar surface (Fig. 6a), a quadratic described by $z = 0.01x^2$ (Fig. 6b), and two blocks with surfaces described by a sine wave with an amplitude of $\pm$ 1*mm* and $\pm$2*mm* (Fig. 6c–d respectively). For the blocks with the sinusoidal surface, the transducer was placed above a peak and a trough on the surface for each block. 6 tests were done overall. A perspex shoe was used to couple the probe to the surface, this allowed the surface geometry relative to the transducer to be known accurately. A series of side drilled holes (SDH) were imaged and the positions recorded, this allowed the accuracy of the surface mapping method to be tested.

All data was acquired using a Micropulse 5 PA array controller manufactured by Peak NDT, Derby. The Micropulse was connected to a Windows 10 computer via Ethernet cable capable of transferring 45–50 MB/s according to the manufacturers specification. An Olympus 5L64-A2 - 64 element transducer with a pitch of 0.6 mm was used and a 5.1 $\pm$ 0.5 MHz central frequency (as per manufactures specifications). The duration of the excitation pulse was 100ns with an excitation voltage of 100 V. A 50 MHz sampling frequency was used. Data was acquired by the Micropulse at 16 bit resolution. All data processing was done using functions stored within MATLAB R2016b (MathWorks INC. Massachusetts, USA).

It was determined in Ref. [32] that the optimum set up for the 64 element probe used was to use a virtual linear array with 3 virtual

sources. This gave a wider angular coverage using a low number of firings. Each virtual source used a sub aperture of 32 elements, the first used elements 1–32, the second 17–48 and third 33–64. The virtual source was positioned in the centre of the sub-aperture at a distance of half the sub-aperture back.

5. Results

It was shown in Ref. [32] that VSA could be used to inspect materials with complex geometries if the geometry of the surface was known relative to the array. A modified VSA algorithm was used to image and position a series of side drilled holes (SDH) in materials with complex surfaces. The difference between the imaging algorithm that assumes a planar boundary and the algorithm when geometry accounted for is shown in Fig. 7. It can be seen that modifying the algorithm to account for the geometry allows the SDHs to be accurately positioned and the SNR is greatly improved.

In this paper a method is discussed in which the geometry of the surface is mapped ultrasonically. The accuracy of the mapping method is validated against the known geometry of the surface. The separation between the mapped surface and the known surface is averaged over the entire surface. The average difference between the time of flight grids generated by the known surface and the mapped surface is also considered. Table 1 shows the results. The surface error was taken to be the average difference between points on the known surface and the mapped points using the VSA ellipse technique. The surfaces of most of the components were mapped successfully with the error less than $0.1mm$. This was deemed sufficiently accurate, as the difference was less than quarter of the wavelength of sound in the first medium. An error greater than a quarter of the wavelength leads to a phase difference of higher than $\pi/2$, causing destructive interference when summing the values of the TFM algorithm.

Fig. 8 shows the surface points calculated for the trough of the sine wave component with a surface amplitude of $\pm 1mm$. It can be seen that fewer points are located within the trough, as the first responses are more likely to return from the peaks that are located closer to the probe. However enough information was collected for the surface to be mapped to an accuracy of $\pm 0.04mm$. Similar results are obtained for the other components and are shown in Table 1.

It can be seen in Fig. 9a – 9j that accurate images are produced with the planar, quadratic, sine ± 1 mm peak and trough and the sine ± 2 mm peak surfaces. These figures show the images obtained from knowing the geometry and the images obtained using the surface mapping. For these surfaces, the SDH are positioned in the correct places and are well defined with a high SNR using the surface mapping technique. This is to be expected as the errors for surface mapping for these images are small. The SNR of each image is shown in Table 1.

Fig. 9l shows the image obtained for the sinusoidal surface with an amplitude of ± 2 mm, with the transducer placed above the trough in the surface. The error in the surface mapped is above the other components and it can be seen that the indication of one of the SDH is slightly out of place. The SNR for this image is also lower than the other images, showing that it is not as tightly focused. This is due to the transducer position being above a trough deep enough that the responses from within the deepest parts of the trough do not come back quickly enough to be recorded as the first response. This causes fewer surface points are plotted in the depth of the trough, and the surface estimation is less accurate. This can be seen in the results Table 1, where the error in the mapped surface is 0.14 mm. This suggests a limit to what is ultrasonically possible to map using a first response method with a divergent beam in this way. However, the problem is not distinct to the VSA surface mapping method as it also occurs in other surface mapping methods that use the first response times [20].

6. Conclusion

A new virtual source aperture technique for ultrasonically mapping the surface of components when inspecting through dual layered media is presented. A family of ellipses is generated with the transmit and receive points at the focus points, with the first response time defining the circumference. The tangent of this family of ellipses describes the surface. This allows for virtual source aperture imaging of materials with complex geometry when a wedge/shoe or immersion is used to couple the transducer to the surface.

The surface information and imaging is obtained with as little as a single firing of the ultrasonic array, which if post processing can be optimised, will allow for the fastest inspection speed physically possible. However, probability of detection is increased with a few more firings as a wider viewing angle can increase the SNR [8], three firings have been used to image the components here.

The technique was tested on a series of surfaces, designed to exaggerate that which would be typically seen in industry. This was done to explore the boundaries of the VSA surface mapping technique and it was found that there exists a limit of what is ultrasonically possible to accurately map. However this is not just a limitation to the technique described in this paper, studies of other techniques have also found this [20].

To conclude the technique allows fully focused images of the material interior to be generated to a high degree of accuracy and if post processing is optimised then ultra fast inspection of components with complex geometry could be achieved. However, the surface mapping algorithm is implemented here in MATLAB and has not been written in the most efficient way to minimise post processing time. An area of future work required for the algorithm to achieve its potential is to apply optimisation techniques such as the ones discussed in Refs. [6,20], in order to maximise post processing efficiency and inspection speed.

Acknowledgements

“This work is as a result of a partnership between TWI ltd and the University of Wales Trinity Saint David (UWTSD), funded by the KESS 2 scholarship scheme”.

References

[1] Drinkwater BW, Wilcox PD. Ultrasonic arrays for non-destructive evaluation: a review. NDT&E Int 2006;39:525–41.
[2] Holmes C, Drinkwater BW, Wilcox PD. Post-processing of the full matrix of ultrasonic transmit-receive array data for non destructive evaluation. NDT&E Int 2005;38:701–11.
[3] Cruza JF, Camacho J, Fritsch C. Plane-wave phase-coherence imaging for NDE. NDT&E Int 2017;87:31–7 (September 2016).
[4] Wilcox PD, Holmes C, Drinkwater BW. Advanced reflector characterization with ultrasonic phased arrays in NDE applications. IEEE Trans Ultrason Ferroelectrics Freq Contr 2007;54(8):1541–50.
[5] Long R, Russell J, Cawley P. Ultrasonic phased array inspection using full matrix capture. Insight: Non-Destr Test Cond Monit 2012;54(7):380–5.
[6] Sutcliffe M, Weston M, Dutton B, Charlton P, Donne K. Real-time full matrix capture for ultrasonic non-destructive testing with acceleration of post-processing through graphic hardware. NDT&E Int. 2012;51:16–23.
[7] Frazier C, O'Brien WD. Synthetic aperture techniques with a virtual source element. In: 196 IEEE transactions on ultrasonics, ferroelectrics, and frequency controlvol.45; 1998 (1).
[8] Sutcliffe M, Charlton P, Weston M. Multiple virtual source aperture imaging for non-destructive testing. Insight: Non-Destr Test Cond Monit 2014;56(2):75–81.
[9] Sutcliffe M, Weston M, Charlton P, Dutton B, Donne K. Virtual source aperture imaging for non-destructive testing. Insight: Non-Destr Test Cond Monit 2014; 56(2):75–81.
[10] Sutcliffe M, Charlton P, Weston M. Virtual source aperture image processing methods for non-destructive testing. Insight: Non-Destr Test Cond Monit 2016; 58(2):1–5.
[11] Bannouf S, Robert S, Casula O, Prada C. Data set reduction for ultrasonic TFM imaging using the effective aperture approach and virtual sources. J Phys Conf 2013;457.
[12] Hunter AJ, Drinkwater BW, Wilcox PD. Autofocusing ultrasonic imagery for non-destructive testing and evaluation of specimens with complicated geometries. NDT&E Int 2010;43(2):78–85.

[13] Toullelan G, Nadim A, Casula O, Dumas P, Abittan E, Doudet L. Inspection of complex geometries using flexible phased-array transducers. In: 17th world conference on nondestructive testing; 2008. p. 25–8.
[14] Russell J, Long R, Duxbury D, Cawley P. Development and implementation of a membrane-coupled conformable array transducer for use in the nuclear industry. Insight: Non-Destr Test Cond Monit 2012;54:386–93.
[15] Drinkwater B, Bowler W. Ultrasonic array inspection of the clifton suspension bridge chain-links. Insight: Non-Destr Test Cond Monit 2009;51(9):491–8.
[16] Russell J, Long R, Cawley P, Habgood N. Inspection of components with irregular surfaces using a conformable ultrasonic phased array. In: AIP conference proceedingsvol.1096; 2009. p. 792–9.
[17] Le Jeune L, Robert S, Villaverde EL, Prada C. Plane Wave Imaging for ultrasonic non-destructive testing: generalization to multimodal imaging. Ultrasonics 2016;64:128–38.
[18] Parrilla M, Anaya JJ, Fritsch C. Digital signal processing techniques for high accuracy ultrasonic range measurements. IEEE Trans Instumentation Meas 1991;40(4):759–63.
[19] Barshan B. Fast processing techniques for accurate ultrasonic range measurements. Meas Sci Technol 2000;11(1):45–50.
[20] Sutcliffe M, Weston M, Charlton P, Donne K, Wright B, Cooper I. Full matrix capture with time-efficient auto-focusing of unknown geometry through dual-layered media. Insight: Non-Destr Test Cond Monit 2013;55(6):1–6.
[21] Robert S, Calmon P, Calvo M, Le Jeune L, Iakovleva E. Surface estimation methods with phased-arrays for adaptive ultrasonic imaging in complex components. In: 41st annual review of progress in quantitative nondestructive evaluation (AIP conf. Proc. 1650); 2015. p. 1657–66.
[22] Camacho J, Cruza JF, Brizuela J, Fritsch C. Automatic dynamic depth focusing for NDT. IEEE Int 2014;61(4).
[23] Le Jeune L, Robert S, Prada C. Plane wave imaging for ultrasonic inspection of irregular structures with high frame rates. In: 42nd annual review of progress in quantitative nondestructive evaluation (AIP conf. Proc. 1650); 2016. 020010:020010.
[24] Barshan Billur, Backent Deniz. Comparison of two methods of surface profile extraction from multiple ultrasonic range measurements. Meas Sci Technol 2000;11(6):833–44.
[25] Zhang J, Drinkwater BW, Wilcox PD. Efficient computation of delay law for imaging structure with a complex surface. IEEE Int Ultrason Ferroelectrics Freq Contr 2014;61(8):139–42.
[26] Le Jeune L, Robert S, Dumas P, Membre A, Prada C. Adaptive ultrasonic imaging with the total focusing method for inspection of complex components immersed in water. In: AIP conference proceedingsvol.1037; 2015. p. 1037–46.
[27] Camacho J, Cruza JF. Auto-focused virtual source imaging with arbitrarily shaped interfaces. IEEE Int Ultrason Ferroelectrics Freq Contr 2015;62(11):1944–56.
[28] Cruza JF, Camacho J. Total focusing method with virtual sources in the presence of unknown geometry interfaces. IEEE transactions on ultrasonics. Ferroelectrics Freq Contr 2016;63(10):1581–92.
[29] Weston M, Mudge P, Davis C, Peyton A. Time efficient auto-focussing algorithms for ultrasonic inspection of dual-layered media using Full Matrix Capture. NDT&E Int 2012;47:43–50.
[30] Parilla M, Ibañez A, Camacho J, Fritsch C. Fast focal law computing for Non-Destructive Testing with phased arrays. In: International congress on ultrasonics; 2007.
[31] Parrilla M, Brizuela J, Camacho J, Ibáñez A, Nevado P, Fritsch C. Dynamic focusing through arbitrary geometry interfaces. In: IEEE international ultrasonics symposium proceedings; 2008.
[32] Hoyle E, Sutcliffe M, Charlton P, Rees J. Virtual source aperture with real time focussing of known geometry through dual layered media. In: BINDT 56th annual conference 3B5 (freely available on researchgate); 2017.

DOI: 10.1784/insi.2018.60.7.XXX

Virtual source aperture imaging for the detection and sizing of vertically aligned flaws in non-destructive testing

E Hoyle, M Sutcliffe, P Charlton, J Rees and M Weston

In this paper, a modified virtual source aperture (VSA) technique that is used to detect, image and size vertically aligned flaws is described. The method is compared to the existing equivalent full matrix capture (FMC) technique. It is shown that by using the modified VSA technique it is possible to obtain much higher imaging frame rates, with little difference in image quality when compared to that obtainable with the equivalent FMC technique.

1. Introduction

Detecting vertically aligned flaws using ultrasonic methods has proven to be inherently difficult. This is because flaws with surfaces that are not orientated perpendicular to the direction of the incidence wave will cause the incidence wave to be reflected away from the probe. A number of diffraction methods have been developed and used to detect and size such defects but these are difficult to apply in practice[1].

In recent years, there has been a significant increase in the use of ultrasonic arrays for imaging in non-destructive testing (NDT)[2]. They offer more flexibility than single-element transducers, as a wider range of techniques can be used. If each element is fired individually while receiving on all elements, the full matrix capture (FMC) data of the array is collected. This means that for an N element array, N^2 time domain signals are collected. This data can be post-processed using the total focusing method (TFM)[3], which synthesises a focus point at every pixel in the region of interest to generate a fully-focused image. The basis of this is to calculate the time-of-flight from the transmitting element to a given pixel in the image and back to the receiving element. Then, the amplitude of the corresponding A-scan at that time is taken and summed for every transmit-receive combination. This process is repeated for every pixel in the image. Due to processing overheads, FMC-TFM is generally a slow technique. Optimisation techniques[4] must be used in order to make real-time inspection possible and even then it is unsuitable where large areas are required to be inspected quickly.

TFM can be modified for use through dual-layered media. Refraction will cause the ultrasonic beam to bend and, in order to calculate the time-of-flight, the point of incidence between the two media must be found. For flat surfaces, it is possible to obtain an exact solution for the position of incidence[5]; however, for more complex geometries, Fermat's principle of least time may be used[6]. Once the incidence point is known, an image can be generated. It is common in NDT for the inspected components to require the array to be coupled to the surface by either immersing the testing material in a couplant, such as water, or using a wedge/shoe, as demonstrated in[7]. Therefore, accounting for refraction is often necessary. TFM can be extended to image components with unknown and complex surface geometries[8].

Using TFM, the flight path considered does not necessarily have to be directly to the pixel and back. The FMC self-tandem technique (also referred to as the FMC half-skip TFM method[9]) is a modification of TFM that accounts for paths reflecting off a known backwall of the component before reaching a flaw and being received. This allows the user to inspect the part from a different angle so that flaws that were previously difficult to detect can be easily recognised[10-12].

The concept of focusing an array to create a virtual source was first developed for medicine[13]. This method involves a virtual source placed behind the ultrasonic array. By using delays on each array element firing, it is possible to create a beam profile as if it had come from this point in space, as shown in Figure 1. When applied for NDT, the virtual source aperture (VSA) technique[14,15] can be used to construct an image. VSA is similar to TFM but instead it uses the virtual source location as the transmitter location. The method has the advantage that it can significantly increase the signal-to-noise ratio (SNR) of the received A-scans. This allows a comparable image to FMC-TFM to be constructed using a reduced number of firings. The multiple virtual source aperture (MVSA) technique can be used to further increase the image quality and the area inspected[14].

This study investigated the self-tandem method using virtual sources. It can be seen that the flaws are easily detected and sizing using this technique is also investigated. The resulting images are compared to the FMC self-tandem technique as a reference.

1.1 Total focusing method

TFM is a post-processing imaging technique that can be implemented using data from the FMC of an ultrasonic array. The FMC-TFM requires that an area of interest be defined below the array (here, a 2D image grid is considered). For each pixel in this area, the time-of-flight is calculated from the transmitting position to the pixel and back to the receiving position using the known velocity of sound in the medium. The intensity of the image is calculated by taking the amplitude of the corresponding time

● ***Submitted 13.04.17 / Accepted 22.02.18***

Ewan Hoyle is with the University of Wales Trinity Saint David – Swansea Campus, Engineering.

Mark Sutcliffe and Miles Weston are with TWI Ltd.

Peter Charlton is with the School of Engineering, Manufacturing & Logistics, University of Wales Trinity St David.

John Rees is with the University of Wales Trinity Saint David – Swansea Campus.

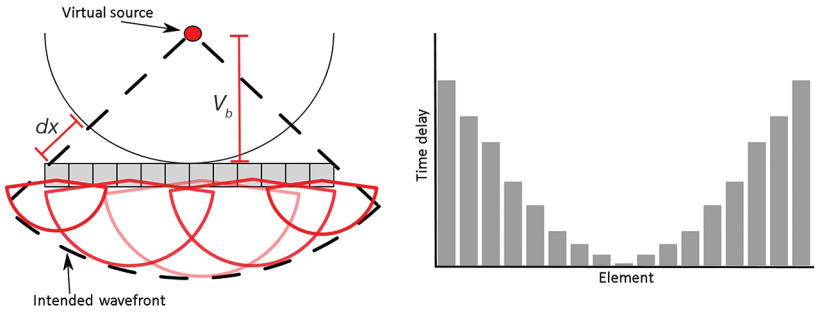


Figure 1. The element delay laws required to simulate a virtual source

domain signal at the calculated time and then summing this for each transmit-receive combination. This can be seen in Equation (1). Here, $I(x, z)$ is the intensity of the pixel at position (x, z), p_1 is the time taken for the ultrasound to travel along a path to the pixel and p_2 is the time taken for it to return back to the receiver. $A_{(t,r)}(t)$ is the amplitude of the A-scan received on the rth element for the tth transmitter. N_t is the number of transmitting virtual sources and N_r is the number of receiving elements on the array:

$$I(x,z)=\left|\sum_{t=1}^{N_t}\sum_{r=1}^{N_r}A_{(t,r)}(p_1+p_2)\right| \quad \text{..... (1)}$$

where:

$$p_1=\frac{\sqrt{(x_t-x)^2+z^2}}{c} \quad \text{..... (2)}$$

$$p_2=\frac{\sqrt{(x_r-x)^2+z^2}}{c} \quad \text{..... (3)}$$

Equations (2) and (3) show the time-of-flight calculations to and from the pixel. This is carried out using the known positions of the elements and pixels and the velocity of the medium. Here, x_t is the x-coordinate of the transmitting position, x_r is the x-coordinate of the receiving position (with the transmit and receive positions being the location of the elements for FMC) and c is the velocity of sound in the medium. The position of the array is defined at $z = 0$; therefore, there is no need to consider the z-coordinate of the element in the calculation. To improve visualisation on the image, a Hilbert transform is used on the returned A-scans and the amplitude of the real and imaginary parts are used for summation.

1.2 Virtual source aperture

Figure 1 depicts the generation of a virtual source. Each element is delayed in order to generate a beam profile as if it had come from this virtual transmission point. The delay law for a given element required to simulate a virtual source is shown in Equation (4). Here, the delay in the eth array element (dt_e) is given by the distance from the virtual source to that element, x_v is the x-coordinate of the virtual source and x_e is the x-coordinate of the eth element. To avoid unnecessary firing delays, the perpendicular distance of the virtual source from the transducer (v_b) is subtracted. The calculated distance, shown as dx_i in Figure 1, is divided by the velocity of sound in the first medium to obtain the delay of that element relative to the first element firing:

$$dt_e=\frac{dx_e}{c}=\frac{\sqrt{(x_e-x_v)^2+v_b^2}-v_b}{c} \quad \text{..... (4)}$$

Using these delay laws on transmit, a virtual source can be generated, as seen in Figure 1. As v_b is subtracted when generating the virtual source in Equation (4), it must also be accounted for when calculating the TFM image. Therefore, p_1 becomes:

$$p_1=\frac{\sqrt{(x_t-x)^2+(z_t-z)^2}-v_b}{c} \quad \text{..... (5)}$$

Here, p_1 is the time-of-flight along a path from the virtual source to the pixel and x_t and z_t are the x- and z-coordinates of the transmitting position, in this case the virtual source.

1.3 Time-of-flight through a refractive boundary

Refraction occurs when ultrasound travels through a boundary between two materials that differ in terms of acoustic impedance. For an array coupled to a surface using a wedge, the ultrasound will not necessarily take a straight path from the array element to the pixel in question, and the point of incidence, at which the sound enters the surface, is required to calculate the time-of-flight. Using Fermat's principle, the time-of-flight can be calculated by finding the path that takes the least time[8]. An iterative method is used to calculate the point of incidence in order to account for refraction, as depicted in Figure 2. An exact solution may be obtained[5], however, the implementation of Fermat's principle is simpler and sufficiently accurate, providing a small iteration step is used.

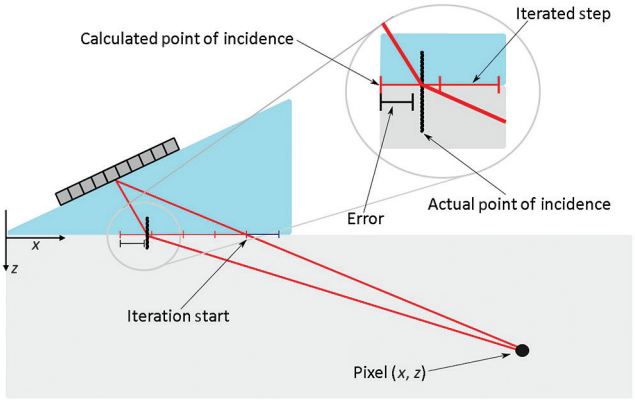


Figure 2. Calculating the point of incidence through a refractive boundary

The point of incidence is found by calculating the flight time for a number of points along the boundary and finding the minimum. The first tested position is the point on the boundary that intercepts a straight line between the transmitting element and the pixel (shown as 'Iteration start' in Figure 2) and the second is a point to the right of this. Using the time-of-flight of these two points, the sign of the gradient can be found. An iteration is then performed, in the direction of decreasing gradient, where the time-of-flight of each point along a line is calculated until the minimum time-of-flight is found. This will correspond to the point of incidence. This method of finding the point of incidence has an error relating to the size of the iterated step, as shown in the diagram; however, this error is insignificant providing a small enough step size is used $\ll\lambda$, where λ is the wavelength corresponding to the frequency of the probe and the coupling material. Once the point of incidence

is found, the time-of-flight is calculated and TFM is used to create an image.

Equation (6) shows the time-of-flight calculation through dual-layered media. Here, p is the time-of-flight of the path taken, x_t and z_t are the transmit coordinates, x and z are the coordinates of the pixel, c_1 and c_2 are the velocities of the first and second media, respectively, and x_s and z_s are an array of coordinates of points along the surface. Using this, the point of incidence is found and the corresponding time-of-flight is used in the TFM algorithm to generate an image.

$$p = \min\left[\frac{\sqrt{(x_t - x_s)^2 + (z_t - z_s)^2}}{c_1} + \frac{\sqrt{(x_s - x)^2 + (z_s - z)^2}}{c_2}\right] - \frac{v_b}{c_1} \quad \text{... (6)}$$

Equation (6) is used to calculate the time-of-flight of the transmit path and the receive path when calculating the TFM algorithm (on receive, however, there is no need to account for the firing delay, so $v_b = 0$).

2. VSA self-tandem technique

The FMC self-tandem is a technique that involves calculating the time-of-flight for an ultrasonic signal reflected off of the known backwall of the testing material before hitting the flaw and then returning to the receiver, as seen in Figure 3[9]. This study will apply this technique to VSA.

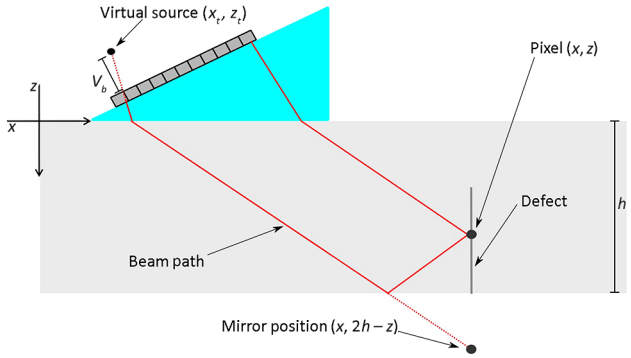


Figure 3. The self-tandem path considered using the new algorithm

The time-of-flight is calculated for every transmit-receive combination along a self-tandem flight path, depicted in Figure 3, and then used to create an image. A mirror image is used to calculate the time-of-flight from the virtual source to the pixel in question along a self-tandem path. This is mirrored around the backwall, as shown in Figure 3. The time-of-flight to the pixel will be the same as if the beam had continued through the backwall to this theoretical mirror position. The mirror position will be aligned with the pixel in the x-plane and the z-position of the mirrored pixel (z_m) can be calculated by subtracting the depth of the non-mirrored pixel (z) from twice the thickness of the material: $z_m = 2h - z$, as shown in Figure 3. The time-of-flight from the pixel back to the receiver is then calculated and the two summed for the total. The time taken for the sound to travel along this path is shown in Equation (7). Here, p_1 is the time-of-flight to the pixel and h is the known thickness of the material:

$$p_1 = \min\left[\frac{\sqrt{(x_t - x_s)^2 + (z_t - z_s)^2} - v_b}{c_1} + \frac{\sqrt{(x_s - x)^2 + (z_s - 2h + z)^2}}{c_2}\right] \text{.... (7)}$$

Equation (7) is then used to calculate the transmit time from the virtual source to the pixel along a self-tandem path. This is used in TFM (shown in Equation (1)) when calculating the transmit path.

2.1 Optimising the virtual source position

The optimal virtual source position is important when inspecting through a wedge. Ideally, the virtual source is set at the centre line of the transmitting array and at half the length of the aperture behind it. This will give the greatest divergence with a spherical beam front[14]. If placed closer than half aperture, the beam front created is more triangular and a poor comparison to a point-like source. If the source is further away than half aperture, the beam is less divergent and the possible area of inspection is reduced.

For an array coupled to the surface using a wedge, the virtual source position may be optimised to suit the wedge parameters, as depicted in Figure 4. The optimal position of the virtual source will maximise the ultrasonic energy going into the inspected material and minimise unwanted internal wedge reflections. This will give the highest SNR ratio possible for the constructed image. Figure 4 shows the optimal positioning of the virtual source. The ideal virtual source position is at the point of incidence between a line drawn from the edge of the wedge through the centre of the element at the edge of the array and projected back, and a line drawn perpendicular to the centre of the transducer. However, these lines may not intercept, or intercept too far away from the transducer to allow the creation of a divergent beam. In this case, the optimum transmission would be to fire on a smaller part of the array on transmit, as shown in Figure 4. All elements would still receive. Optimising the virtual source position in this way gives the most divergent beam possible so as the area inspected is maximised.

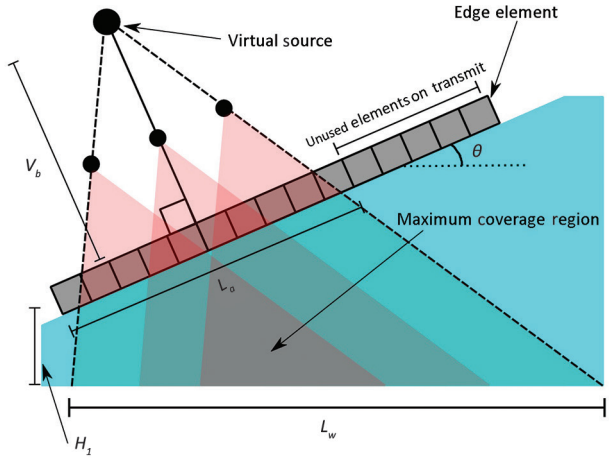


Figure 4. Optimal virtual source position

Equations (8) and (9) show the calculation of the optimum virtual source position. The equations are derived using trigonometry and the known wedge parameters. Here, v_b is the distance of the virtual source behind the aperture, θ is the wedge angle and L_w is the length of the wedge from the first element, as depicted in Figure 4. L_a is the length of the active aperture and H_1 is the height of the first element:

$$v_b = \frac{L_a}{2} * \tan\left(\frac{\pi}{2} + \theta - \tan^{-1}(\gamma)\right) \text{..... (8)}$$

where:

$$\gamma = \frac{L_w - L_a * \cos(\theta)}{H_1 + L_a * \sin(\theta)} \text{..... (9)}$$

Multiple virtual sources can be used if the firing aperture is reduced even further. Figure 4 also shows three virtual sources

and the coverage region they produce. Using more virtual sources improves the angle range at which the region of interest is inspected, further increasing image quality.

3. Validation of the technique

The technique was validated using a vertical flaw of known height. The flaw was sized using each technique and then compared to the FMC self-tandem.

3.1 Experimental set-up

All data was acquired using a Micropulse 5PA array controller manufactured by Peak NDT, Derby. The Micropulse was connected to a Windows 10 computer via an Ethernet cable capable of transferring 45-50 MB/s according to the manufacturer's specifications. An Olympus 5L64-A2 64-element transducer with a pitch of 0.6 mm was used and a 5.1 ±0.5 MHz central frequency (as per the manufacturer's specifications). A 50 MHz sampling frequency was used and the gain was kept constant for each technique. Data was acquired by the Micropulse at 16-bit resolution. All data processing was carried out using functions stored within MATLAB R2016b (MathWorks Inc, Massachusetts, USA). The inspected aluminium block, depicted in Figure 5, had a thickness of 38.1 mm. The flaw had a 16.5 mm shoulder, which was used for imaging and sizing, while the 2 mm high tip was ignored as the angle of the tip surface was such that it did not produce a response using the self-tandem method. The thickness and height of the flaw were measured using a digital caliper with an accuracy of ±0.01 mm. The wedge used to couple the transducer to the material had an angle of 35.6° and was designed to produce 50° shear waves in aluminium. The region of interest selected was optimal for the wedge design, such that the highest intensity of sound reached the area and any reflected signals could be detected. This was carefully selected using ray tracing techniques and Snell's Law[5].

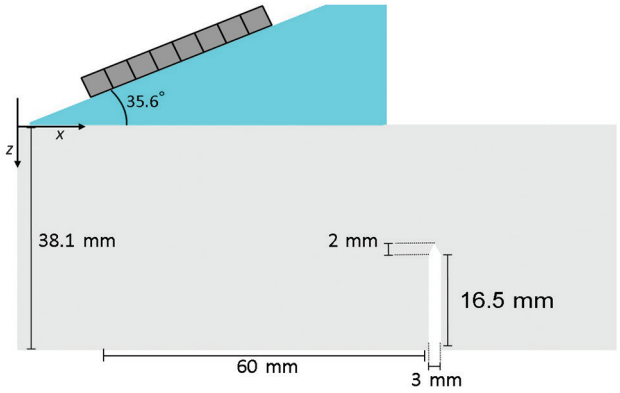


Figure 5. Experimental set-up

The images generated were 20 mm × 38.125 mm, with a pixel resolution of 0.125 mm. Experiments were run using one, three and five virtual sources, each placed at their optimum positions as determined by Equations (8) and (9). The first 32 elements of the array were fired for the single virtual source. 16 elements were fired for each of the three and five grouped virtual sources, with a separation of four and eight elements for each technique, respectively.

3.2 Defect sizing

Standard VSA is best suited for imaging flaws with a surface that is perpendicular to the direction of the beam. Surfaces that are not perpendicular to the beam reflect sound away from the transducer and can be missed. This causes only the tip of the flaw to be detected accurately. An imaging artefact can be seen, as shown in Figure 6. The data is captured by flooding the region of interest with sound. In this case, most of the returned signals are caused by sound bouncing off of the backwall before reaching the defect and returning to the probe. When using the standard algorithm, these signals are plotted at the wrong location on the image, causing an imaging artefact. When the tip diffraction is small, sizing can be difficult. Using the VSA self-tandem method, the flaw can be detected (shown in Figures 7(b)-7(d)) and sized. Sizing was carried out using both the −6 dB and the −20 dB sizing method.

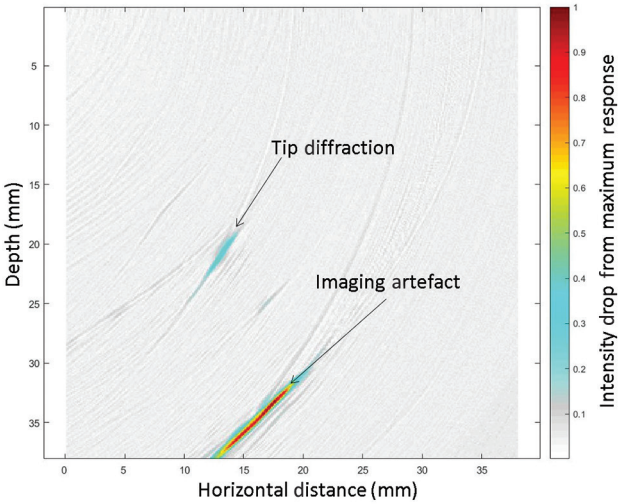


Figure 6. Standard VSA image on the 16.5 mm defect

The FMC and VSA self-tandem methods were investigated with one, three and five virtual sources. To validate the sizing accuracy of the VSA self-tandem, an aluminium block with a known vertically aligned flaw, 16.5 mm high, was used. The image was normalised to the peak response and anything within −6 dB or −20 dB (depending on the considered sizing method) of the peak response was considered to be a flaw indication. The results, seen in Table 1, show the size of each flaw using both the FMC and VSA self-tandem methods. The −6 dB sizing method undersizes the defect; this may be because conventional sizing methods are not adequate to size defects in the fully-focused images produced by TFM. This could be due to the proportion of energy that is returning to the probe from a given position. A wide variety of factors, such as the position of the probe relative to the region of interest and the size and orientation of the flaw, all affect the amount of energy returning to the probe. This causes certain types of flaws in optimal positions to be more illuminated than others in less optimal positions. For a flaw crossing a large region it may not be sufficient to use a simple −6 dB sizing method, as the tip of the flaw generally gives a weaker response to the base, which could cause undersizing. The calibration method described in[16] could be used to help account for this. Alternatively, a different sizing technique, such as looking at where the indication falls into the background noise of the image, may be used.

For this reason, the −20 dB sizing method was also considered. This tests where the indication of the flaw drops by 20 dB, which was closer to the background noise level. The −20 dB sizing method oversizes the defect, most likely due to the error caused by the pulse width. Ideally, the emitted wave would be the shape of a Dirac delta spike, as a single spike would give absolute resolution in the image. However, the emission of an infinitely thin pulse is impossible

with conventional equipment. The transducer elements were designed to typically emit a three-five cycle Gaussian. A 5.1 MHz central frequency shear wave in aluminium typically has a wavelength of approximately 0.5 mm and when multiple emitted wavelengths are considered the total pulse width can confidently be considered to be greater than 1 mm. The resolution of the image generated using TFM will be limited by this and, therefore, oversizing of the defect can be expected. This could be improved by using deconvolution methods on the returned time domain signals, as discussed in[17].

Table 1. Sizing results: measured size and error for each technique (VS = virtual source)

Technique	−6 dB (mm)	−20 dB (mm)	SNR (dB)	RMS (%)
1VS	15.75	17	27	0.36
3VS	15.875	17.375	25	0.3
5VS	15.875	17.375	25	0.23
FMC	15.5	16.75	30	0.04

The flaw appears shorter using the FMC technique compared to the VSA technique. This is because more signals are summed when creating the TFM image, the image is more tightly focused and the SNR is slightly higher, so the flaw is better defined. For a better defined flaw, the contrast between the indication and the background noise is greater and therefore accuracy is improved. This is shown, as the FMC −20 dB sizing method gives the most accurate reading.

The method is also sensitive to changes in the input parameters, especially the positions of the known backwall of the tested material, the angle of the probe and so on. Damage to the coupling wedge or different thicknesses in the gel used to couple the probe to the material can also introduce an error with both the FMC and VSA self-tandem techniques.

Figures 7(a)-7(d) show the images obtained when imaging the 16.5 mm-sized flaw using each technique. It is shown that the FMC self-tandem image has the highest image SNR of all the techniques, which is due to the large amount of firings and the coherent summations of all the signals. However, all VSA techniques show a high image SNR and the defect can easily be distinguished from the background noise.

3.3 Image comparison (RMS)

The images for each number of virtual sources were compared to the FMC self-tandem using a root mean square (RMS) method[18], as seen in Equation (10). In Equation (10), N_x and N_z are the number of pixels in the x- and z-direction, $I_{x,z}$ is the intensity of the pixel in the (x, z) position and $\bar{I}_{x,z}$ is the intensity of the pixel in the comparison image:

$$RMS = \sqrt{\frac{1}{N_x N_z}\sum_{x=1}^{N_x}\sum_{z=1}^{N_z}\left(I_{x,z} - \bar{I}_{x,z}\right)^2} \quad \text{..... (10)}$$

Each image, created using a different number of virtual sources, was compared with the FMC self-tandem image taken from the same transducer position. The average RMS variation in the intensity difference of each pixel for each technique is shown in Table 1 and none of the techniques exceeded 0.4% difference from the FMC self-tandem for any method. It is shown that the image becomes more comparable to the FMC self-tandem as the number of virtual sources is increased. For one virtual source the RMS variation was 0.36%, for three virtual sources it was 0.3% and for five virtual sources there was 0.23% variation. To calculate how much variation was expected between firings due to random electrical background noise, another FMC image was taken from the same location. The RMS variation due to noise was 0.04%.

The RMS results show that the virtual source techniques produce a comparable image to the FMC, although the FMC had a slightly higher signal-to-noise ratio than the virtual source techniques, which can be seen when comparing Figure 7(a) to Figures 7(b)-7(d).

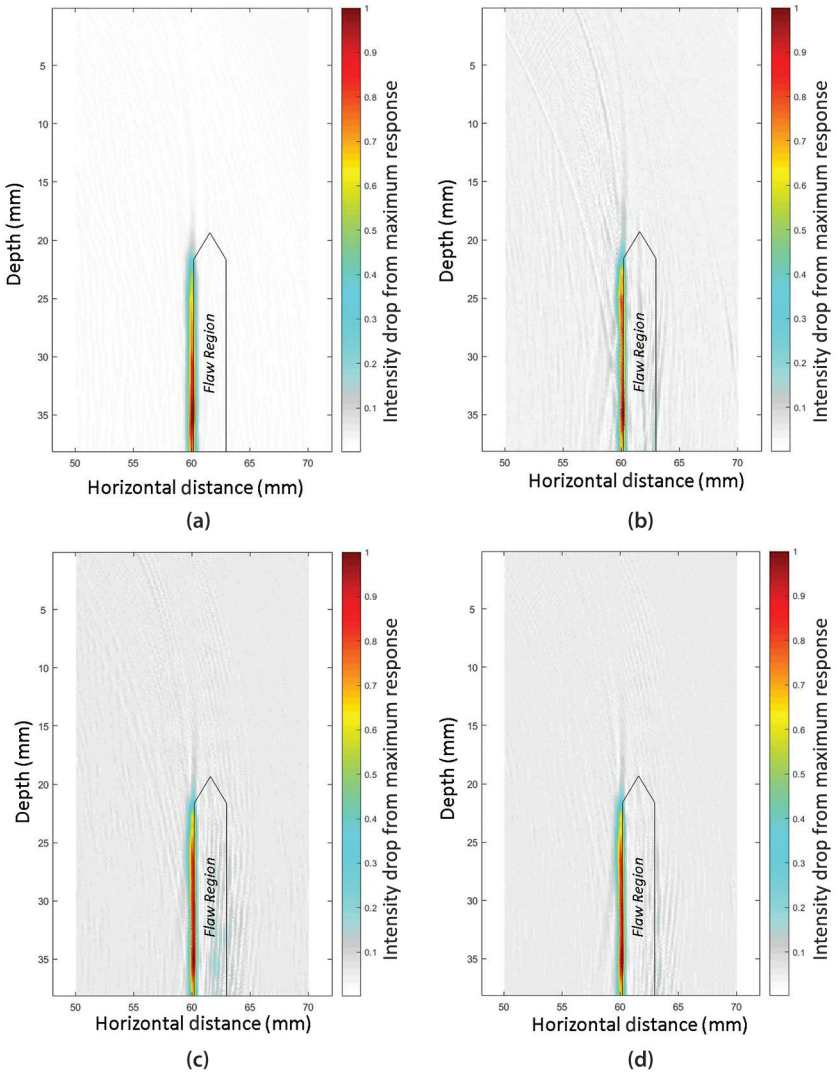


Figure 7. Images using various techniques. The horizontal distance corresponds to the *x*-axis while depth corresponds to the *z*-axis: (a) full matrix capture self-tandem; (b) flaw imaged using one virtual source; (c) flaw imaged using three virtual sources; and (d) flaw imaged using five virtual sources

3.4 Speed improvements

Table 2 shows the acquisition time, processing and rendering time and total time for each technique to generate an image. A sample image for each technique can be seen in Figures 7(a)-7(d). The number of frames generated per second is also shown in Table 2. The virtual source techniques have much higher frame rates than the FMC self-tandem, with one virtual source over 50 times faster. Images generated using higher numbers of virtual sources deviate less from the FMC, while the speed increase is still preserved; the use of three virtual sources is over 18 times faster and the use of five virtual sources is over 12 times faster.

Table 2. Timing table: acquisition time, processing and rendering time and total time to create an image for each technique and number of frames produced per second (VS = virtual source)

Technique	Acquisition (s) (±0.01)	Processing (s) (±0.01)	Total (s) (±0.02)	Frames/s
1VS	0.06	0.06	0.12	8.77
3VS	0.17	0.12	0.29	3.41
5VS	0.28	0.18	0.46	2.14
FMC	3.62	2.1	5.72	0.18

The inspection speeds achieved here are not so impressive when compared to what can be achieved with current FMC-TFM technologies[4] but, crucially, they do not reflect the full potential of VSA self-tandem. Technological advancements and optimisation techniques discussed in[4] allowed for inspection speeds of around 8 frames/s with FMC-TFM (compared to 0.18 frames/s achieved in MATLAB). These techniques include:

- Using the fast Fourier transform (FFT) in parallelisation allowed by the ancillary library CUFFT to speed up the Hilbert transform.
- Computing the focusing algorithm in parallel using a graphics processing unit (GPU).
- Using multi-threading so that the data acquisition and focusing algorithms are performed at the same time.
- Using smaller data sizes. 16-bit data might not be necessary and 8-bit could be used; however, this may degrade SNR and image quality.

The images in this paper are generated using MATLAB. Should the VSA algorithm be implemented in C++ and the same optimisation techniques used as those discussed in[4], it can be expected that VSA could achieve a dramatic increase compared with current inspection speeds. The amount of data processed for a VSA image is a fraction of what is used for FMC-TFM. A capable programmer using the optimisation techniques discussed above could develop a VSA system practical for fully-focused ultra-fast inspections. This could be of great benefit to industry.

4. Inspection of a fatigue crack

A fatigue crack sample was used to test the VSA self-tandem technique using a more realistic defect. A radiographic image of the fatigue crack was obtained for comparison (shown in the left-hand image in Figure 8). The radiographic image was generated using the computed tomography (CT) technique installed in the VG-studio 3.0 software (Volume Graphics GmbH, Heidelberg, Germany). The crack was grown out of a notch created in the bottom of the sample. The centre image in Figure 8 shows the fatigue crack imaged using standard VSA with a single virtual source. The image on the right-hand side shows the VSA self-tandem detecting the entire length of the flaw. Both the notch and the crack can be seen separately using the VSA self-tandem technique, where only the tip diffraction and an imaging artefact can be seen using standard VSA. VSA self-tandem offers comparability in terms of sizing the fatigue crack to that of the radiograph.

5. Conclusion

The research conducted here shows that images created with the adapted VSA technique can detect and size vertically aligned flaws that were previously difficult to detect with standard VSA. The technique was tested on two vertically aligned flaws of known height. An RMS image comparison method was used to compare the images with the equivalent FMC technique and it was shown that both techniques produce comparable images. The image SNR of the FMC technique was slightly higher than that of the VSA technique; this is simply because fewer firings are used to construct the image. However, the peak signal-to-noise ratio for VSA is still very high, at least 25 dB, so the indications are well defined, allowing flaws to be easily detected. The use of multiple virtual sources is also discussed. Using multiple virtual sources allows the region of interest to be inspected from a wider angle and images obtained using multiple virtual sources are shown to compare better to images obtained using the FMC self-tandem.

The VSA self-tandem technique was used to image a fatigue crack. It showed comparability in sizing to an image obtained using radiography. This shows that VSA self-tandem can be used to detect and size realistic flaws that one would come across in industry. Ideally, in a given inspection both the standard VSA algorithm and the VSA self-tandem would be considered, to give the operator a variety of viewing angles to improve flaw characterisation and increase the probability of detection in the first place.

Due to the vast amounts of data collected, the FMC technique proved to be slow. VSA requires a fraction of the data to generate a comparable image. VSA images using a single virtual source proved to be over 50 times faster, while three virtual sources proved to be over 18 times faster. An increase in speed of this magnitude could be of great benefit to industry.

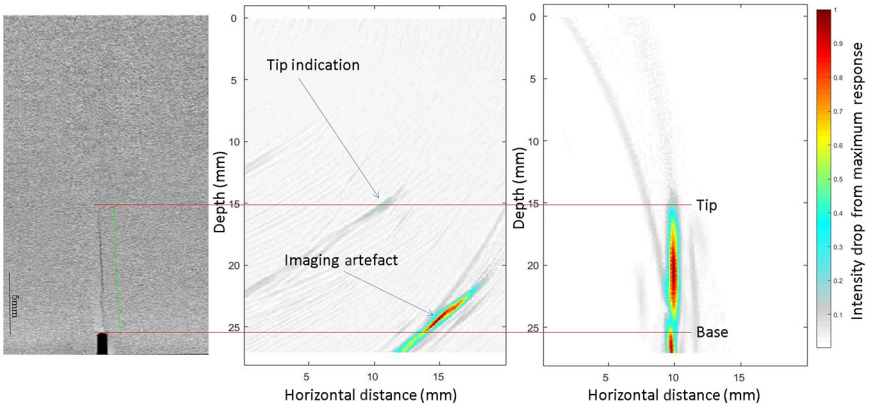


Figure 8. Inspection of a fatigue crack: radiographic image (left); standard VSA (middle); and VSA self-tandem (right)

References

1. M Moles, L Wesley and T Sinclair, 'Accurate defect sizing using phased array and signal processing – developments in ultrasonic inspection II', Olympus NDT, University of Toronto.
2. B W Drinkwater and P D Wilcox, 'Ultrasonic arrays for non-destructive evaluation: a review', NDT&E International, Vol 39, pp 525-541, 2006.
3. C Holmes, B W Drinkwater and P D Wilcox, 'Post-processing of the full matrix of ultrasonic transmit-receive array data for non-destructive evaluation', NDT&E International, Vol 38, pp 701-711, 2005.
4. M Sutcliffe, M Weston, B Dutton, P Charlton and K Donne, 'Real-time full matrix capture for ultrasonic non-destructive testing with acceleration of post-processing through graphic hardware', NDT&E International, Vol 51, pp 16-23, 2012.
5. M Weston, P Mudge, C Davis and A Peyton, 'Time-efficient auto-focusing algorithms for ultrasonic inspection of dual-layered media using full matrix capture', NDT&E International, Vol 47, pp 43-50, 2012.
6. M Parrilla, J Brizuela, J Camacho, A Ibáñez, P Nevado and C Fritsch, 'Dynamic focusing through arbitrary geometry interfaces', Proceedings of the IEEE International Ultrasonics Symposium, Beijing, China, 2-5 November 2008.
7. B Drinkwater and W Bowler, 'Ultrasonic array inspection of the Clifton Suspension Bridge chain-links', Insight: Non-Destructive Testing and Condition Monitoring, Vol 51, No 9, pp 491-498, 2009.
8. M Sutcliffe, M Weston, P Charlton, K Donne, B Wright and I Cooper, 'Full matrix capture with time-efficient auto-focusing of unknown geometry through dual-layered media', Insight: Non-Destructive Testing and Condition Monitoring, Vol 55, No 6, pp 1-6, 2013.
9. M V Felice, A Velichko and P D Wilcox, 'Accurate depth measurement of small surface-breaking cracks using an ultrasonic array post-processing technique', NDT&E International, Vol 68, pp 105-112, 2014.
10. E Ginzel, O Volf and B Brown, 'Next-generation technology for pipeline AUT TFM-FMC', The e-Journal of Non-destructive Testing, Vol 20, No 8, 2015.
11. J Zhang, B W Drinkwater, P D Wilcox and A J Hunter, 'Defect detection using ultrasonic arrays: the multi-mode total focusing method', NDT&E International, Vol 43, No 2, pp 123-133, 2010.
12. L Le Jeune, S Robert, E L Villaverde and C Prada, 'Plane wave imaging for ultrasonic non-destructive testing: generalisation to multimodal imaging', Ultrasonics, Vol 64, pp 128-138, 2016.
13. C H Frazier and W D O'Brien, 'Synthetic aperture techniques with a virtual source element', IEEE Transactions on Ultrasonics, Ferroelectrics and Frequency Control, Vol 45, No 1, pp 196-207, 1998.
14. M Sutcliffe, P Charlton and M Weston, 'Multiple virtual source aperture imaging for non-destructive testing', Insight: Non-Destructive Testing and Condition Monitoring, Vol 56, No 2, pp 75-81, 2014.
15. M Sutcliffe, P Charlton and M Weston, 'Virtual source aperture image processing methods for non-destructive testing', Insight: Non-Destructive Testing and Condition Monitoring, Vol 58, No 2, pp 1-5, 2016.
16. M Sutcliffe, P Charlton, M Weston and S Mosey, 'Virtual source aperture imaging and calibration for ultrasonic inspections through dual-layered media for non-destructive testing', Insight: Non-Destructive Testing and Condition Monitoring, Vol 59, No 11, pp 596-602, 2017.
17. S Mosey, P Charlton and I Wells, 'Resolution enhancement of ultrasonic B-mode images', Insight: Non-Destructive Testing and Condition Monitoring, Vol 55, No 2, pp 78-83, 2013.
18. S Mosey, 'Resolution enhancement of B-mode ultrasound images', A thesis submitted to the University of Wales in partial fulfilment of the requirements for the degree of Doctor of Philosophy, 2013.

©2018 TWI Ltd

46th Annual Review of Progress
in Quantitative Nondestructive Evaluation
QNDE2019
July 14-19, 2019, Portland, OR, USA

QNDE2019-6915

AN ULTRASONIC FREQUENCY DOMAIN IMAGING ALGORITHM USING VIRTUAL SOURCES

Ewan Hoyle, Peter Charlton, John Rees
University of Wales Trinity Saint David
Swansea, UK

Ewan Hoyle, Mark Sutcliffe
TWI ltd
Port Talbot, UK

ABSTRACT

In this paper a frequency domain implementation of the Virtual Source Aperture (VSA) ultrasonic array imaging technique is presented. Multiple elements are fired with a phased array like delay law in order to generate a beamform as if it had originated from a virtual source located behind the aperture. Each element individually receives. The time domain Total Focusing Method (TFM) and the frequency domain phase migration methods are used to image a series of reflectors and the performance of the two imaging algorithms are measured by mapping the response of a generic reflector over a range of positions and comparing the indication intensity of the two algorithms.

Keywords: Virtual Source Aperture, Ultrasonics, Non Destructive Testing, Fourier Beamforming

1. INTRODUCTION

The TFM is a post processing method was introduced to generate fully focused images of a test specimen interior [1]. Originally, the data from the Full Matrix Capture (FMC) of an ultrasonic array was used with the TFM to generate what is is often referred to as the 'gold standard' imaging method in NDT [2]. However, the large amounts of data that is required to capture and process has been a significant factor in restraining the wide adoption of the technique [3].

VSA was developed in order to reduce the amount of data that was required to form an image of the same standard as FMC but using fewer array transmissions [4]. Instead of firing individual elements, groups of element were fired with a phased array like delay law in order to generate a wave-front as if it had originated from a virtual point behind the aperture. As more energy is used to insonify the test specimen, the returned echoes have a higher signal to noise ratio than FMC, and so a TFM image can be formed using fewer firings.

The frequency domain algorithm originated from sonar and radar, where a single source was used to transmit and receive signals [5]. This algorithm was adapted to use with ultrasonic arrays in NDT [6]. Hunter *et al* [7] adapted the algorithm such that the transmitter and receiver could be at separate positions using a coordinate change known as Stolt mapping [8], originating from Geophysics. This allowed FMC imaging in the frequency domain to be achieved. The frequency domain algorithm makes efficient use of fast Fourier transforms which can allow for image forming through post processing [7]. Frequency domain imaging using virtual sources was later developed in [8].

In this paper, we investigate the time and frequency domain imaging methods using a series of reflectors and comparing the images generated by the two.

2. IMAGING METHODS

2.1 Virtual Source Generation.

A virtual source can be generated using a delay law applied to multiple elements of an ultrasonic array. This is depicted in Figure 1.

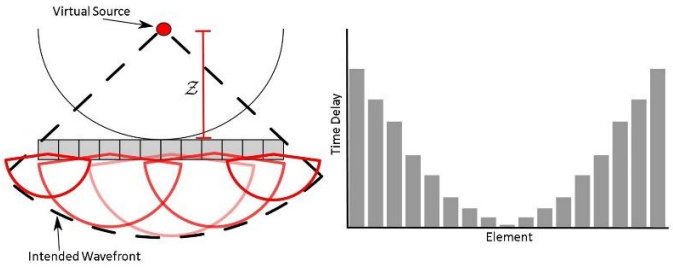


FIGURE 1: GENERATING A VIRTUAL SOURCE.

The delay applied to an element of index i in order to generate a virtual source is given by:

$$t_i = \frac{\sqrt{(i - i_0)p + z_v} - z_v}{c}$$

Here, t_i is the the delay applied to an element of index i, i_0 is the index of the center element, p is the element

© 2019 by ASME

pitch, z_v is the perpendicular distance of the source behind the aperture and c is the velocity of the medium.

2.2 TFM imaging (time domain)

The TFM imaging algorithm is a delay and sum approach [1] given by:

$$\sigma(x,z) = \int_0^{X_u}\int_0^{X_v} E(t(u,v),u,v)dudv$$

Where:

$$t(u,v) = \frac{\sqrt{(x-(u+u_0))^2+(z+z_v)^2}+\sqrt{(x-v)^2+z^2}-z_v}{c}$$

Here, $\sigma(x,z)$ is the intensity value of the image at the position (x,z), $E(t,u,v)$ is the amplitude of the signal at time t for a a virtual source at position u and receiver at v. This is depicted in Figure 2. $X_u$is the horizontal distance between the first and the last virtual source and X_v is the distance between the first and the last receiving element.

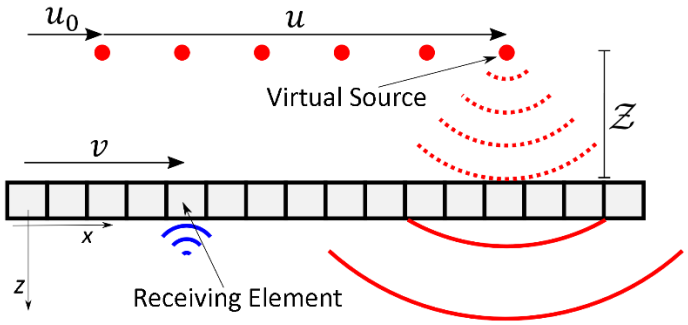


FIGURE 2: DEPICTING THE ARRAY SETUP.

2.3 Frequency Domain imaging

The frequency domain algorithm is derived for FMC in [7] and virtual sources in [9]. The summary of the implementation is seen here:

1. 3 dimensional Fourier Transform on the collected data: $E(t,u,v) \rightarrow E'(k,k_u,k_v)$ where k is the spatial frequency in the propagation direction and k_u and k_v are the spatial frequencies in the horizontal direction regarding the transmit and receive coordinates.
2. Frequency shift to account for the scan start gate and virtual source positions:
   $$E(k,k_u,k_v) = E'(k,k_u,k_v)e^{ik_uu_0+\frac{ikt_0}{c}-iz_v\sqrt{k^2-k_u^2}}$$
   Here, t_0 is the start gate of the scan.
3. Coordinate change known as Stolt mapping [8] to get the data from the transducer domain to the image domain. This is done by keeping k_u constant: $E(k,k_u,k_v) \rightarrow E(k_x,k_z|k_u)$ and using a linear interpolation function.
4. Sum over all k_u values: $E(k_x,k_z) = \int_{-\infty}^{\infty} E(k_x,k\_z|k_u)\,dk_u$
5. Inverse 2 dimensional Fourier transform to obtain the image $E(k_x,k_z) \rightarrow E(x,z)$

The coordinate change uses equations:

$$k_v = k_x - k_u$$

And

$$k = \pm\frac{\sqrt{k_z^4+2(k_u^2+(k_x-k_u)^2)k_z^2+k_u^4+(k_x-k_u)^4-2(k_x-k_u)^2k_u^2}}{2k_z}$$

The spatial frequencies k_x and k_z are real and satisfy the equation:

$$k = \sqrt{k_x^2+k_z^2}$$

3. RESULTS AND DISCUSSION

An array of 64 elements with a pitch of 0.6mm was simulated using the CIVA software. Each element had a center frequency of 5MHz. 25 virtual sources were used, each at the center of a smaller sub-aperture that was incremented along the array. The sub aperture consisted of 16 elements and was incremented by 2 elements between each transmission. The distance of the virtual source behind the aperture was 5mm.

The time domain signal recorded 4098 sample points for each transmit/receive pair, at a sampling frequency: f_s = 50MHz, with the first recording at when the first element was fired. The transmit and receive points were discretely sampled with a spacing of p_u and p_v. Therefore the spatial frequency components obtained from the initial 3D Fourier transform were ranging from: $k_u = -\frac{1}{2p_u} \rightarrow \frac{1}{2p_u}$, $k_v = -\frac{1}{2p_v} \rightarrow \frac{1}{2p_v}$ and $k = -\frac{f_s}{2c} \rightarrow \frac{f_s}{2c}$.). The data was padded with zeros such that the data in the k_u and k_v directions was double their original size. The spatial frequency components in the horizontal and vertical direction were respectively: $k_x = -\frac{1}{2p_x} \rightarrow \frac{1}{2p_x}$ and $k_z = -\frac{1}{2p_z} \rightarrow \frac{1}{2p_z}$, where p_x and p_z was the spacing of the image pixels in the horizontal and vertical direction (both 0.2mm).

A series of side drilled holes was simulated, each with a diameter of 1mm and were spaced in a square lattice 4mm apart in a steel test specimen with a longitudinal velocity of 5900 ms^{-1}. The data was simulated using the CIVA software, with artificial noise added in. Each hole was simulated and processed separately to avoid interfering signals. The images of all the side drilled holes were then combined in one image by displaying the maximum intensity of each pixel. Each image is normalized to the response of a side drilled located at 16mm depth and 2mm from the center axis.

The images of the side drilled holes from the time and frequency domain algorithms can be seen in Figures 3 and 4 respectively. It was found that the signal to noise ratio of the frequency domain algorithm was 6dB higher compared to that of the time domain. Therefore, 6dB of soft gain has been added into the frequency domain image for a fair comparison. The actual

© 2019 by ASME

location of the side drilled holes are displayed as blue circles overlaying the image for reference.

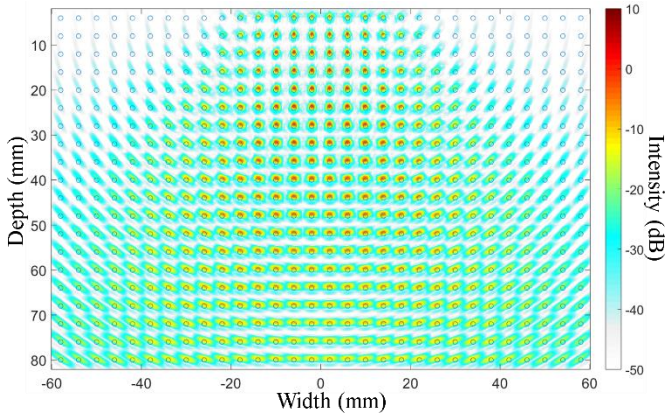


FIGURE 3: TIME DOMAIN ALGORITHM SDH IMAGE

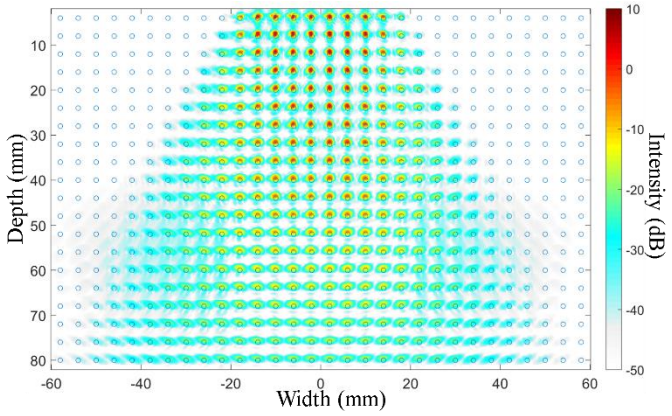


FIGURE 4: FREQUENCY DOMAIN ALGORITHM SDH IMAGE

Although the signal to noise ratio of the side drilled hole indication calibrated against was higher for the frequency domain than that of the time domain, it can be seen that the time domain algorithm provides a wider field of view than the frequency domain. The intensity of the indications from holes further away from the transducer and also at higher steering angles are comparatively higher. Therefore, the time domain algorithm is likely to be the more useful algorithm in general, unless a short-range inspection in a noisy material is performed.

Sampling a larger number of frequency components during the coordinate transform may help to improve the image. It could also be useful to use filtering to remove frequency components that only contribute noise to certain pixels, as this may help to improve the image contrast. Further work is required in order to investigate this and find the optimum implementation of the frequency domain algorithm.

4. CONCLUSION

The study indicates that the time domain algorithm gives a wider field of view and a higher intensity value for deeper indications when compared to the frequency domain. The signal to noise ratio of the indications from the frequency algorithm is higher closer to the transducer, making it ideal for short range inspections in noisy materials. However, the indications from the frequency domain algorithm attenuate quicker for a larger distance and a wider range of angles when compared to the time domain. Further work is required in order to confidently conclude these findings, as the implementation of the frequency domain algorithm could be improved with further investigation.

ACKNOWLEDGEMENTS

The work was funded by the European Social Fund through the KESS 2 scholarship scheme at the University of Wales Trinity Saint David, and supported by TWI ltd.

REFERENCES

[1] C. Holmes, B. W. Drinkwater, and P. D. Wilcox. Post-processing of the full matrix of ultrasonic transmit-receive array data for non-destructive evaluation. NDT&E International, 38:701–711, 2005.

[2] J. F. Cruza, J. Camacho, and C. Fritsch. Plane-wave phase-coherence imaging for NDE. NDT&E International, 87(September 2016):31–37, 2017.

[3] M. Sutcliffe, M. Weston, B. Dutton, P. Charlton, and K. Donne. Real-time full matrix capture for ultrasonic non-destructive testing with acceleration of post-processing through graphic hardware. NDT&E International, 51:16–23, 2012.

[4] M. Sutcliffe, P. Charlton, and M. Weston. Multiple virtual source aperture imaging for non-destructive testing. Insight: Non-Destructive Testing and Condition Monitoring, 56(2):75–81, 2014.

[5] P. Gough and D. Hawkins. Unified Framework for Modern Synthetic Aperture Imaging Algorithms. John Wiley & Sons Imaging Systems Technology, 8:343–358, 1997.

[6] T. Stepinski. An Implementation of Synthetic Aperture Focusing Technique in Frequency Domain. IEEE Transactions on Ultrasonics, Ferroelectrics, and Frequency Control, 54(7), 2007.

[7] A. J. Hunter, B.W. Drinkwater, and P. D.Wilcox. TheWavenumber Algorithm for Full-Matrix Imaging Using an Ultrasonic Array. IEEE Transactions on Ultrasonics, Ferroelectrics and Frequency Control, 55(11):2450–2462, 2008.

[8] R. H. Stolt. Migration by Fourier Transform. Geophysics, 43(1):23–48, 1978.

[9] Synthetic Aperture Ultrasound Fourier Beamformation Using Virtual Sources IEEE transactions on ultrasonics, ferroelectrics and frequency control, 63(11)

© 2019 by ASME

Virtual source aperture with real-time focussing of known geometry through dual-layered media.

Ewan Hoyle, Mark Surcliffe, Peter Charlton, John Rees

This paper was presented at the 56th Annual conference of the Brittish Institue of Non-Destructive Testing (BINDT) on the 6th September 2017.
http://www.bindt.org/events/ndt-2017/programme-6-september-2017/

Virtual source aperture with real-time focussing of known geometry through dual-layered media

Ewan Hoyle, Mark Surcliffe, Peter Charlton, John Rees

1 Abstract

A Virtual Source Aperture (VSA) method is presented that allows for real-time imaging through a non-planar surface where the geometry is known. For an identified complex geometric profile the point of incidence at the refractive interface is calculated with respect to the virtual source transmission. Fermat's principle of least time is used along with dynamic focussing applied to the inspection region allowing for fully-focussed images to be generated at high inspection speeds. To demonstrate this, a linear array transducer was coupled to the surface using an intermediate material. The technique was applied to a series of curved surfaces and its ability to image a series of side-drilled holes assessed. With further developments, this technique offers significant advantages over existing methods with the potential to be applied to a wide variety of industrial sectors.

2 Introduction

In recent years, the use of ultrasonic arrays has increased massively in Non Destructive Testing (NDT) [1]. The Total Focussing Method (TFM) is a pulse echo technique that uses an array coupled with the testing material to produce fully focussed images of flaws within [2]. TFM requires the Full Matrix Capture (FMC) of an ultrasonic array, which has the burden of huge processing overheads in terms of acquiring data and post processing. However, real time TFM is possible by using optimisation techniques [3]. TFM has been expanded to operate through dual layered media as direct contact between the array and inspected sample is often not possible. A wedge or shoe is required to couple the array to the testing material in this case [4] [5]. In simple cases, Snell's Law can be used to obtain an exact solution for the point of incidence when refraction occurs between media [6]. For geometries where an exact solution is not possible, the point of incidence can be derived using Fermat's principle of least time [7] [8].

Virtual Source Aperture (VSA) is a parallel technique to TFM except virtual sources, where multiple elements are fired instead of a traditional single element fired for TFM, are used [9]. By delaying element firings in a certain way, a beam profile can be formed as if it had come from a virtual source behind the aperture, as depicted in Figure 1. As multiple elements are fired, much more energy enters the material than if a single element was fired, causing a greater Signal to Noise Ratio (SNR) in the returned A-scans. VSA has this significant advantage over TFM because it allows a fully focussed image with a similar signal to noise ratio (SNR) to be generated in a fraction of the firings used for TFM. VSA can be expanded to the Multiple Virtual Source Aperture (MVSA) which uses multiple virtual sources allowing inspection from a wider angle, increasing the resolution of flaw indications [9].

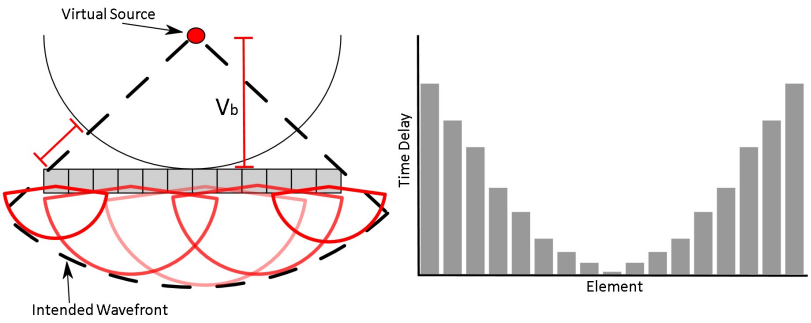


Figure 1: Depicted beam profile created using a virtual source.

This study investigates the potential for using Virtual Source Aperture to focus through dual layered media where the surface of the second media is known. Fermat's principle is used to account for refraction and determine the ultrasound path through the material.

3 Background

3.1 Virtual Source Delay Laws

The firing delay laws on each element (dt_k) required to simulate a virtual source are shown in Equation 1. Here, k is the element number, x_v and y_v are the x and y positions of the virtual source. The distance of the virtual source back from the centre of the transducer (v_b), depicted in Figure 1, is subtracted to avoid unnecessary delays as the sound is fired from the centre of the transducer rather than the virtual source position itself. The velocity of the medium that the ultrasound first propagates through is c_1, x_{a_k} and y_{a_k} are the x and y coordinates of the transducer element. dx_k is the distance depicted in Figure 1.

$$dt_k = \frac{dx_k}{c_1} = \frac{\sqrt{(x_v - x_{a_k})^2 + (y_v - y_{a_k})^2} - v_b}{c_1} \tag{1}$$

3.2 MVSA

The basic algorithm for creating an image using MVSA is shown in Equation 2. An area of interest is defined below the array. The time of flight from the virtual source position to each pixel in the area of interest and back to the receiving element is calculated using the known velocity of sound in the material. The theoretical time taken for the sound to reach the centre of the transducer from the virtual source (v_b/c_1) is subtracted as sound is emitted from the transducer rather than the actual virtual source. The amplitude (A_h) of the corresponding Ascan at this time is taken for each pixel. This process is repeated for every combination of virtual source and receiver element and the corresponding amplitudes are summed. Should a flaw occur in a given pixel, the time of flights for that pixel will correspond to peaks in each Ascan amplitudes, and so the sum of the amplitudes will indicate a flaw.

$$I(x,y) = \sum_{i=1}^{N_v} \sum_{j=1}^{N_e} A_h(t_i + f_j - v_b/c_1) \tag{2}$$

In Equation 2, $I(x,y)$ is the intensity of a pixel at the (x,y) location, N_v is the number of virtual sources used, N_e is the number of elements in the array, t_i is the time taken for the ultrasound to travel from the transducer to the pixel and f_j is the time taken for the ultrasound to travel from the pixel back to the transducer.

Typically, the emitted signal is a 3 to 5 cycle Gaussian, this can cause problems when generating an image. To account for this a Hilbert transform (h), used to acquire phase information for the envelope signal, is performed on the returned A-scans.

3.3 Time of Flight Calculation Through Refractive Boundary

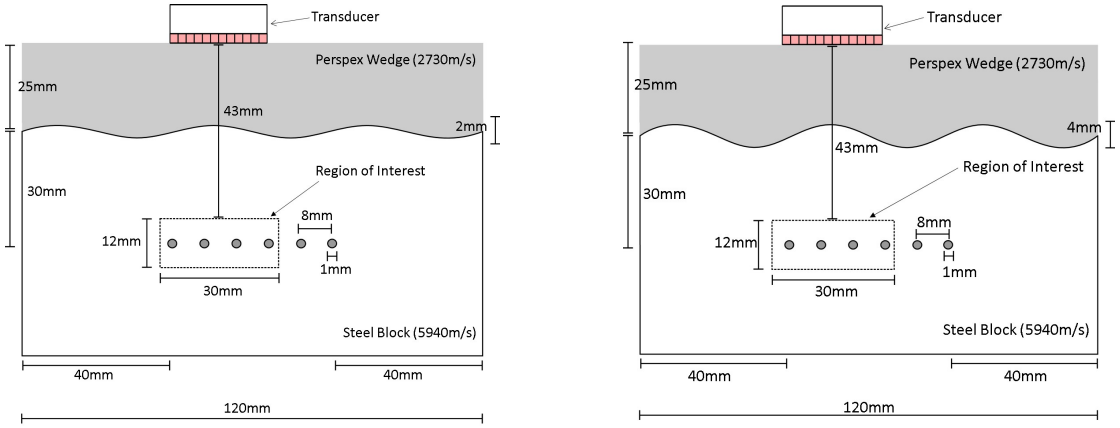
Fermat's principle states that the path of ultrasound between two points through a refractive boundary will be that that takes the shortest time. Therefore finding the ultrasound path using Fermat's principle requires calculating the time of flight for a number of points along the surface and selecting the least time as shown in Equation 3. Here, T_F is the time of flight between the two points, x_1 and y_1 are the positions of the transmission point in the first medium, x_2 and y_2 are the positions of the receive point in the second medium, x_s and y_s are all of the positions on the interface between the two mediums, c_1 and c_2 are the velocities of the first and second medium respectively.

$$T_f = min\Big[\frac{\sqrt{(x_1 - x_s)^2 + (y_1 - y_s)^2} - v_b}{c_1} + \frac{\sqrt{(x_s - x_2)^2 + (y_s - y_2)^2}}{c_2}\Big] \tag{3}$$

For a known geometry surface, it is possible to generate a fully focussed image, through a refractive boundary, using the MVSA Equation 2. Fermat's principle, as seen in Equation 3, is used to calculate the time of flights. Although to do this, positions of the surface relative to the transducer must be known.

4 Experimental Setup

The technique was tested on two steel blocks manufactured to have a surface following that of a sin wave with a wavelength of 40mm and amplitude of ±1mm and ±2mm as depicted in Figure **??**. Six side drilled holes (SDH) were placed at a 30mm depth with a separation of 8mm. A perspex shoe was used to couple the transducer to the testing sample.



Using Fermat's principle to work out the focal laws is time consuming due to the vast amount of calculations needed to find the minimum time of flight for each pixel. For this reason the time of flights for each transducer position along the boundary were pre calculated. An encoder with a resolution of 1mm was used to determine the transducer position relative to the surface. Once the position was determined, the pre calculated time of flights for that position were loaded so that an image could be generated. This allowed a real time inspection to be done of the sample.

All data was acquired using a Micropulse 5PA array controller manufactured by Peak NDT, Derby. The Micropulse was connected to a Windows 10 computer via Ethernet cable capable of transferring 45-50 MB/s according to the manufacturers specification. An Olympus 5L64-A2 - 64 element transducer with a pitch of 0.6mm was used and a 5.1 ± 0.5 MHz central frequency (as per manufactures specifications). The excitation pulse lasted for 100ns with an excitation voltage of 100 volts. A 50 MHz sampling frequency was used. Data was acquired by the Micropulse at 16 bit resolution. All data processing was done using functions stored within MATLAB R2016b (MathWorks INC. Massachusetts, USA).

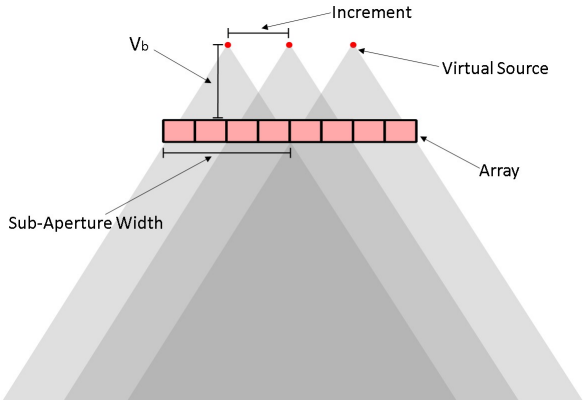


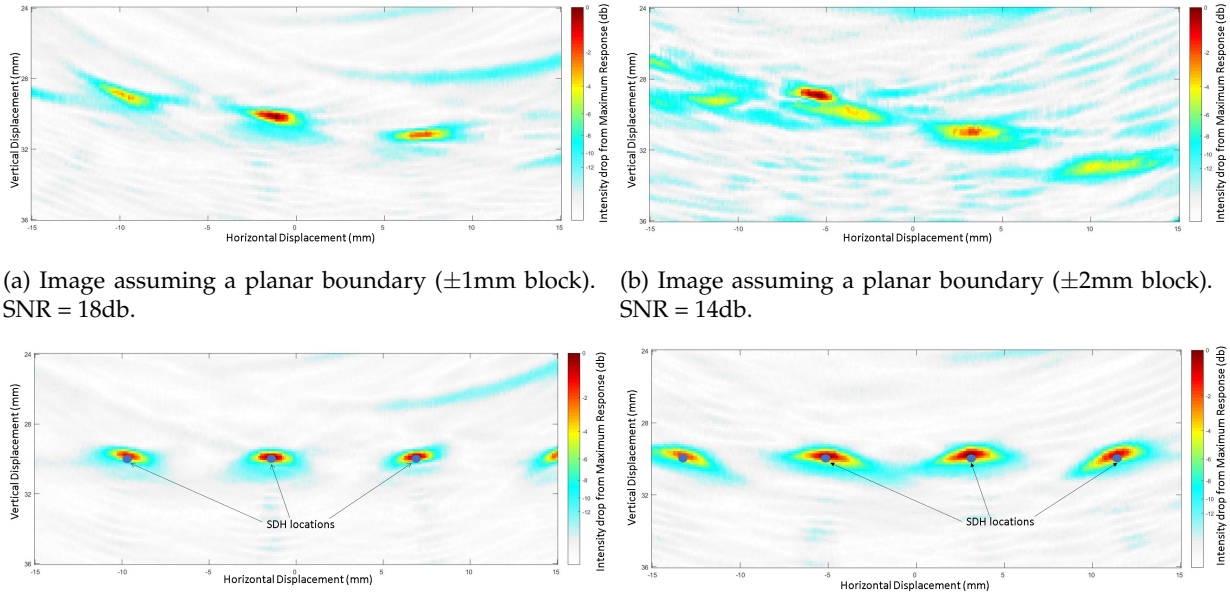
Figure 3: Firing sequence using three virtual sources.

It was determined that the optimum viewing coverage for the 64 element probe was to use a virtual array consisting of 3 virtual sources each to construct an image. Each virtual source was constructed using 32 elements with an increment of 16 elements, and each source was placed at half the sub-aperture width back from centre of the sub-aperture. The first virtual source used elements 1-32, the second 17-48 and the third 33-64. The positions of the virtual sources and their coverage region is depicted in Figure 3.

5 Results and Discussion

The technique was tested by measuring the positions of a series of side drilled holes, relative to the transducer, on two different testing samples depicted in Figure **??**. The depth of the holes relative to the

transducer were measured along with the separation. The peak intensity of the indication was taken to be the centre of the hole.



(a) Image assuming a planar boundary (±1mm block). SNR = 18db.

(b) Image assuming a planar boundary (±2mm block). SNR = 14db.

(c) Image focussing through the sine wave ±1mm boundary. SNR = 28db.

(d) Image focussing through the sine wave ±2mm boundary. SNR = 24db.

Figure 4: Imaging SDH using three virtual sources

Figure 4 shows the images taken while inspecting both test samples depicted in Figure **??**, the images are taken from the same transducer location. Figures 4a and 4b shows the focussing algorithm assuming a planar boundary. Flaw indications can be seen although the positions clearly do not represent the actual positioning of actual SDHs. The SNR of these images are also lower than what is expected from a fully focussed image. Figures 4c and 4d shows the images using the adapted MVSA technique that accounts for the surface geometry. The modified VSA algorithm using Fermat's principle managed to position the SDH accurately. The SNR ratio using three virtual sources exceeded 20db for each testing sample. However the complexity of the surface had a minor effect the as the simpler sinusoidal surface with an amplitude of $\pm 1mm$ tended to have a higher SNR than that of the $\pm 2mm$ amplitude (28db and 24db respectively). This suggests that there may be a limit as to what is ultrasonically possible to inspect, as more complex surfaces with stepper gradients will scatter the ultrasound at the surface, reducing the amount of energy that is transmitted into the material.

5.1 Real Time Inspection

Real time inspection was achieved here with up to three virtual sources with an image 30mm in length and 16mm width, with a resolution of 0.125mm. The highest theoretical frame rate depends on the acquisition time, the time taken for the ultrasound to propagate through the material and acquire the data. The rest is a post processing issue. By using a different programming language and optimising the processing required [3], the frame rate could be drastically increased from the value achieved here. However, by computing all the post processing in MATLAB and applying only basic optimisation techniques, a speed of 8fs^{-1} was achieved. The limits is because of the time taken to load the time of flights depending on the transducer position, the image processing time and the time taken to generate an image on the screen adding overheads. These timings are shown in Table 1.

	3 Virtual Sources
Acquisition (s)	0.028
ToF Loading Time (s)	0.017
Processing (s)	0.06
Image Generation (s)	0.017
Total (s)	0.12
Frames/Second (s^{-1})	8.2

Table 1: Total frames per second and the time taken for each stage for a single and three virtual sources

By using 3 virtual sources, the angle at which inspection is done is greatly increased (compared to a single virtual source) and therefore the flaws are better defined with a higher signal to noise ratio. However, adding multiple firings decreases the frame rate because of the increase in post processing.

6 Conclusion

In this work we have shown that real time inspection using MVSA through dual layered media with complex geometry is achievable. Fermat's principle is used to calculate the flight times of ultrasound through the refractive boundary. The inspection is done for known geometry, with an encoder used to find the position of the surface relative to the transducer.

Images of SDH in a series of testing blocks have been created and tested for positional accuracy using the virtual source technique. The high signal to noise value of the indications in the images shows that this technique gives a high probability of flaw detection.

Real time inspection speeds is achieved using 3 virtual sources ($8fs^{-1}$). Using multiple virtual sources allows for a wider viewing angle, causing the defects to be better defined. These inspection speeds could be further increased should the processing algorithm be implemented in a more efficient coding language and optimisation techniques used, as discussed in [3].

References

[1] Bruce W. Drinkwater and Paul D. Wilcox. Ultrasonic arrays for non-destructive evaluation: a review. *NDT&E International*, 39:525–541, 2006.

[2] Caroline Holmes, Bruce W. Drinkwater, and Paul D. Wilcox. Post-processing of the full matrix of ultrasonic transmit-receive array data for non destructive evaluation. *NDT&E International*, 38:701–711, 2005.

[3] Mark Sutcliffe, Miles Weston, Ben Dutton, Peter Charlton, and Kelvin Donne. Real-time full matrix capture for ultrasonic non-destructive testing with acceleration of post-processing through graphic hardware. *NDT&E International*, 51:16–23, 2012.

[4] M. Sutcliffe, M. Weston, P. Charlton, K. Donne, B. Wright, and I. Cooper. Full matrix capture with time-efficient auto-focusing of unknown geometry through dual-layered media. *Insight: Non-Destructive Testing and Condition Monitoring*, 55(6):1–6, 2013.

[5] Bruce Drinkwater and W. Bowler. Ultrasonic Array Inspection of the Clifton Suspension Bridge chain-links. *Insight: Non-Destructive Testing and Condition Monitoring*, 51, 2009.

[6] Miles Weston, Peter Mudge, Claire Davis, and Anthony Peyton. Time efficient auto-focussing algorithms for ultrasonic inspection of dual-layered media using Full Matrix Capture. *NDT&E International*, 47:43–50, 2012.

[7] M. Parilla, Alberto Ibañez, J. Camacho, and Carlos Fritsch. Fast focal law computing for Non-Destructive Testing with phased arrays. *International Congress on Ultrasonics*, 2007.

[8] M Parrilla, J Brizuela, J Camacho, A Ibáñez, P Nevado, and C Fritsch. Dynamic focusing through arbitrary geometry interfaces. *IEEE International*, 2(1):1195–1198, 2008.

[9] M. Sutcliffe, P. Charlton, and M. Weston. Multiple virtual source aperture imaging for non-destructive testing. *Insight: Non-Destructive Testing and Condition Monitoring*, 56(2):75–81, 2014.